



UvA-DARE (Digital Academic Repository)

Developing, optimizing and using FRET-based biosensors to elucidate G protein signaling

Mastop, M.

Publication date

2020

Document Version

Final published version

License

Other

[Link to publication](#)

Citation for published version (APA):

Mastop, M. (2020). *Developing, optimizing and using FRET-based biosensors to elucidate G protein signaling*. [Thesis, fully internal, Universiteit van Amsterdam].

General rights

It is not permitted to download or to forward/distribute the text or part of it without the consent of the author(s) and/or copyright holder(s), other than for strictly personal, individual use, unless the work is under an open content license (like Creative Commons).

Disclaimer/Complaints regulations

If you believe that digital publication of certain material infringes any of your rights or (privacy) interests, please let the Library know, stating your reasons. In case of a legitimate complaint, the Library will make the material inaccessible and/or remove it from the website. Please Ask the Library: <https://uba.uva.nl/en/contact>, or a letter to: Library of the University of Amsterdam, Secretariat, Singel 425, 1012 WP Amsterdam, The Netherlands. You will be contacted as soon as possible.

Developing, optimizing and using FRET-based biosensors to elucidate G protein signaling

Marieke Mastop



Developing, optimizing and using FRET-based biosensors to elucidate G protein signaling

Marieke Mastop

The research described in this thesis was funded by the Netherlands Organisation for Scientific Research (NWO).

The research was carried out at the Laboratory of Molecular Cytology, Swammerdam Institute for Life Sciences, Faculty of Science, University of Amsterdam.

ISBN

978-90-830704-1-4

Cover art by

Drenthedesigner via fiverr.com

Printed by

Proefschriftenprinten.nl

Editing and layout by

Proefschriftenprinten.nl

Developing, optimizing and using FRET-based biosensors to elucidate G protein signaling

ACADEMISCH PROEFSCHRIFT

ter verkrijging van de graad van doctor
aan de Universiteit van Amsterdam
op gezag van de Rector Magnificus
prof. dr. ir. K.I.J. Maex
ten overstaan van een door het College voor Promoties
ingestelde commissie,
in het openbaar te verdedigen in de Agnietenkapel
op woensdag 23 september 2020 , te 16:00 uur
door

Marieke Mastop

geboren te Ede

Promotiecommissie

Promotor: Prof. Dr. Th. W. J. Gadella (Universiteit van Amsterdam)

Co-Promotor: Dr. Ir. J. Goedhart (Universiteit van Amsterdam)

Overige Leden: Prof. Dr. H.W.H.G. Kessels (Universiteit van Amsterdam)

Prof. Dr. K. Jalink (Universiteit van Amsterdam)

Prof. Dr. J.D. van Buul (Universiteit van Amsterdam)

Prof. Dr. F.J. Bruggeman (Vrije Universiteit Amsterdam)

Dr. Ir. M.J.W. Adjobo-Hermans (Radboud UMC)

Dr. Ir. M.A. Hink (Universiteit van Amsterdam)

Faculteit: Faculteit der Natuurwetenschappen, Wiskunde en Informatica (FNWI)

Table of Contents

Summary	9
1. General Introduction	13
1.1 G-protein coupled receptor (GPCR) signaling	
1.2 Fluorescent proteins	
1.3 Förster Resonance Energy Transfer (FRET)	
1.4 Fluorescent proteins applied in FRET-based biosensors for monitoring events in GPCR signaling	
1.5 Thesis outline	
2. Characterization of a spectrally diverse set of fluorescent proteins as FRET acceptors for mTurquoise2	33
3. Effects of fluorescent protein dimerization and permutation on the performance of a FRET based RhoA sensor	77
4. A FRET based biosensor for measuring Gα13 activation in single cells	101



5. Optimization of FRET pairs based on large Stokes-shift fluorescent proteins (LSS-FPs) for application in multiplex FRET imaging	125
---	-----

6. Connecting S1P signaling to endothelial barrier regulation: a possible link between pRex1 and Cdc42	159
---	-----

7. General Discussion	177
7.1 Optimizing FRET based biosensors	
7.2 Developing novel FRET based biosensors	
7.3 Elucidating the regulation of GPCR signaling using FRET based biosensors	

References	188
-------------------	-----

Nederlandse Samenvatting	210
---------------------------------	-----

Dankwoord	214
------------------	-----

List of Publications	216
-----------------------------	-----

Summary

G protein-coupled receptors (GPCRs) represent the largest family of cell-surface receptors and a significant portion of the approved drugs acts through these GPCRs. The regulation of GPCR signaling is, however, not yet completely understood. Further elucidation of GPCR signaling is required in order to improve the specificity of drugs that target these receptors.

The aim of the research presented in this thesis was to gain a better understanding of how intracellular signaling by GPCRs is regulated. We used fluorescence microscopy to study GPCR signaling in live cells.

In order to study protein-protein interactions involved in GPCR signaling, a high spatiotemporal resolution is required. This because these interactions are often short-lived and occur at $<10\text{nm}$ proximities. The spatial resolution of conventional microscopy is maximum $\sim 250\text{nm}$. To enable visualization of protein-protein interactions at resolutions beyond the limits of conventional microscopy, the technique Förster Resonance Energy Transfer (FRET) is exploited, applied in fluorescent biosensors. FRET is energy transfer between two fluorophores. FRET occurs if the fluorophores exist in close proximity ($<10\text{nm}$). The fluorescent biosensors consist of two fluorescent proteins (FPs), called the FRET pair, and a sensing domain. The sensing domain should be specific for a certain biological event involved in GPCR signaling. Upon occurrence of the biological event, the sensing domain interacts, dissociates or changes conformation leading to a change in distance or orientation between the FRET pair, altering the efficiency of energy transfer. Thereby the FRET pair indirectly reports the occurrence of the specific biological event. It is of high importance that these biosensors report biological events truthfully. Therefore a substantial part of my research was directed towards the development and optimization of biosensors and the employed fluorescent proteins that constitute the FRET pair. Another part of my research was directed towards application of developed and optimized biosensors to gain more insight into the regulation of GPCR signaling.

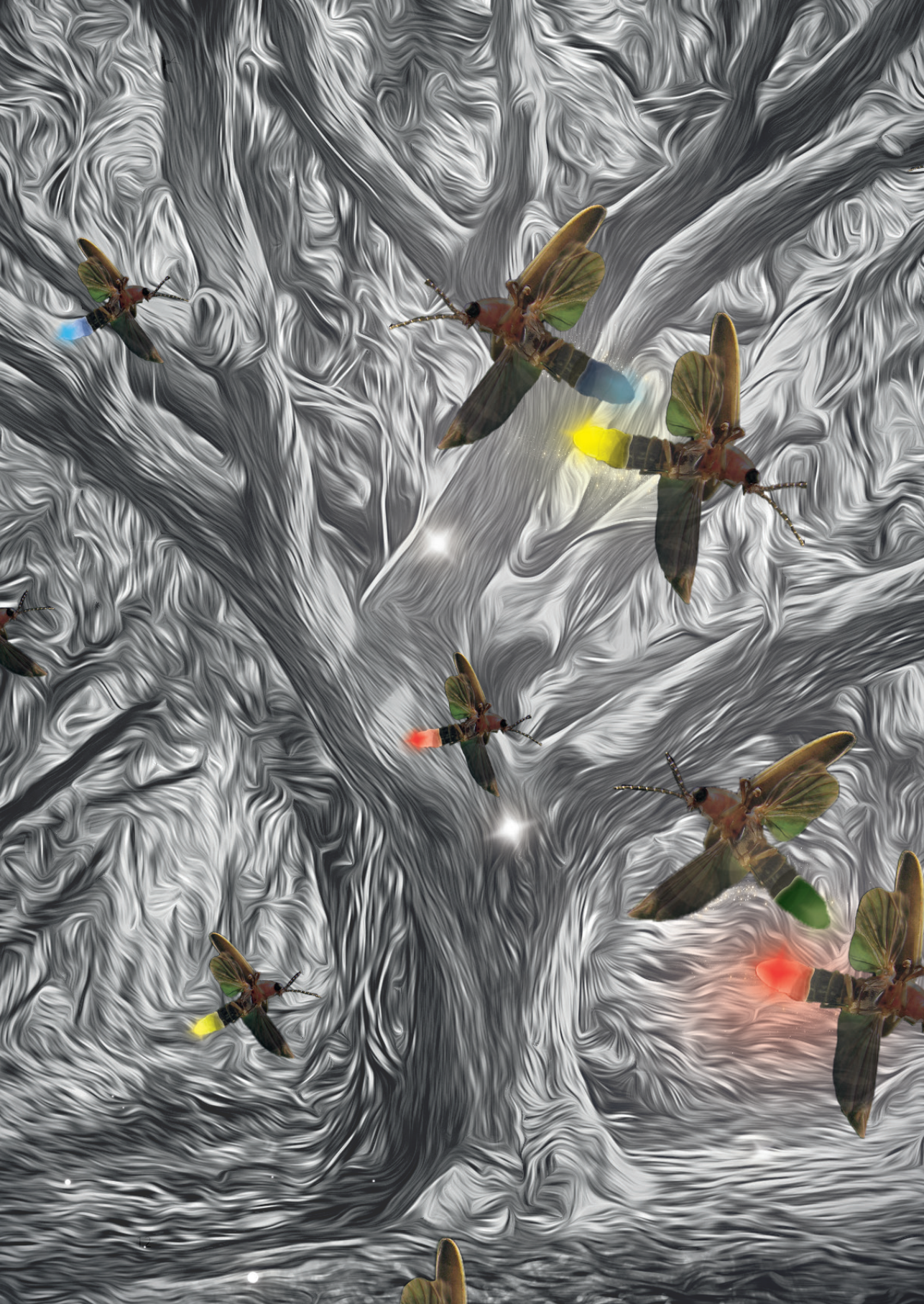
Chapter 2 includes a discussion on important characteristics of fluorescent proteins and their effect on the performance of a FRET pair, in terms of FRET contrast between the "on" state and the "off" state of the sensor, the brightness and the environmental sensitivity of the fluorescent proteins. A FRET pair consists of a FRET donor and a more red-shifted FRET acceptor. We evaluated the performance of several FRET acceptors combined with novel CFP, mTurquoise2, as FRET donor. The best performing FRET pair was mTurquoise2-mNeonGreen applied in a bimolecular FRET sensor for Gq activation. **Chapter 3** aimed to improve the performance of

a unimolecular FRET sensor. Novel FPs can contribute to increased brightness, FRET efficiency or photostability of a sensor. However, application of these novel FPs often leads to a decreased FRET contrast between the “on” state and the “off” state of the sensor, because the FPs are constrained to certain conformations in the unimolecular sensor format. Published unimolecular sensors often endured tedious optimization of relative orientations and distance. Changing one aspect of such a highly optimized sensor often results in a decrease in its FRET contrast. This study evaluated the effect of FP stickiness, a weak heterodimerization tendency, and the FPs’ relative orientations, on the FRET contrast of a unimolecular sensor, reporting RhoA activation. RhoA is a more downstream signaling effector in GPCR signaling, important in cytoskeleton regulation. The aim of the research discussed in **chapter 4** was to develop a FRET-based Gα13 activation biosensor. Gα13 represents one of the four classes of Gα subunits, part of a heterotrimeric G-protein. The heterotrimeric G-protein couples to the GPCR on the inside of the cell and transduces the signal to more downstream effectors. Multiple fluorescently tagged Gα13 variants were made and the functionality and localization was analyzed. Three G13 activation, single plasmid, biosensors were constructed and assessed. The sensor reports that P115 RGS domain was able to inhibit Gα13 activation in Human Umbilical Vein Endothelial cells (HUVECs). In addition, the sensor was used to evaluate which GPCRs activated the class of Gα13 heterotrimeric G-proteins. The Gα13 activation biosensor makes it possible to distinguish between Gαq and Gα13 signaling. These heterotrimeric G-protein classes are often activated by the same GPCRs and often lead to similar downstream signaling via different effectors. The development of a Gα13 activation biosensor was crucial in the path towards further elucidation of GPCR signaling.

In **chapter 5** sensors were developed, compatible with abundantly available CFP-YFP based sensors, aiming towards dual FRET imaging. As a FRET donor mT-Sapphire was further optimized to LSS-SGFP2, which was characterized and applied in a bimolecular Gq or G13 activation biosensor and a unimolecular RhoA activation biosensor, assessing mCherry and mScarlet-I as FRET acceptors. Preliminary dual FRET imaging was performed, simultaneously monitoring Gq and G13 activation. Further optimization of the unimolecular RhoA activation sensor included circular permutations of the FPs to tweak the relative orientation of the FPs’ dipoles.

Chapter 6 focusses on the barrier regulation in endothelial cells (EC). S1P activates GPCRs that couple to Gi or G13 heterotrimeric G-protein classes, respectively leading to barrier protection and barrier disruption. This chapter concerns the S1PR1-Gi-CDC42 signaling axis and aims to explore the molecular basis of CDC42 mediated EC spreading and to identify more involved signaling components. The study reveals that Gβγ signaling is required for CDC42 activation and pRex1 is suggested as CDC42 activating GEF.

The work described in this thesis contributes to the ongoing buildup of knowledge on how GPCR signaling is regulated. Moreover, the developed and optimized FPs, FRET based biosensors and other synthetic tools for unraveling signaling interactions could be applied in various future studies in GPCR signaling or related research fields.



1. General Introduction

1.1 G-protein coupled receptor (GPCR) signaling

All living organisms require communication for adaptation to environmental changes. Communication involves the sending and receiving of information and this is enabled by so-called signaling molecules. Signaling molecules bind receptors at the cell surface to elicit a response, thereby exerting control over processes such as metabolism, proliferation, differentiation and motility. The process of converting an extracellular signal into physiological responses, via membrane spanning cell-surface receptors, is called signal transduction (Lodish et al., 2007).

G-protein coupled receptors (GPCRs) represent the largest family of cell-surface receptors, with more than 800 different GPCRs expressed in humans (Gurevich and Gurevich, 2017). 25-40% of the approved drugs target GPCRs (Lagerström and Schiöth, 2008; Lappano and Maggiolini, 2011; Liu et al., 2016; O'Hayre et al., 2014; Roth and Kroeze, 2015). The value of GPCRs as drug targets underlines the importance of elucidating these complex signal transduction pathways in order to improve the specificity of drugs.

GPCRs consist of seven membrane-spanning α -helices with an extracellular amino-terminus and an intracellular carboxy-terminus (Lagerström and Schiöth, 2008; Palczewski et al., 2000; Rosenbaum et al., 2007). GPCRs respond to a diverse set of signaling molecules such as ions, lipids, hormones, peptides, odorants, photons and neurotransmitters. The family of GPCRs is subdivided into five or six classes, based on protein structure and mechanism of action (Fredriksson et al., 2003; Isberg et al., 2015; Lagerström and Schiöth, 2008). In this thesis only class A, rhodopsin-like, GPCRs are discussed. The vast majority of signaling molecules, interacting with class A GPCRs, bind to the extracellular loops of transmembrane domains due to the short amino terminus of these GPCRs (Jastrzebska, 2013).

Activation of GPCRs leads to a rearrangement of their transmembrane helices, particularly helices 3 and 6 (Villardaga et al., 2009) (figure 1). The rearrangements involve 1) the release of an ionic lock switch that secures the cytoplasmic sides of helix 3 and helix 6 in the inactive state of the receptor, 2) the rotamer toggle switch mechanism that modulates the conformation of helix 6 (Preininger et al., 2013; Shi et al., 2002; Xie and Chowdhury, 2013; Yao et al., 2006), or the transmission switch, which is a larger switch linking the agonist binding site with the movement of helix 5 and helix 6 through rearrangement of the helix 3-5-6 interface (Trzaskowski et al., 2012), 3)

the 3-7 lock switch which involves the disruption of a salt bridge between helix 3 and helix 7 upon receptor activation and 4) the tyrosine toggle switch where a rotation of helix 6 disrupts the water mediated link between helix 6 and helix 7, leading to the opening of a region called the hydrophobic barrier and subsequent rearrangements of helix 5 and 7 to fill the hydrophobic gap (figure 1) (Trzaskowski et al., 2012). These conformational changes of a GPCR relay the extracellular signal to the intracellular side. Heterotrimeric G-proteins are the primary signaling effectors of GPCRs.

Heterotrimeric G-proteins

A heterotrimeric G-protein consists of a $G\alpha$, $G\beta$ and $G\gamma$ subunit. Posttranslational lipidation is responsible for plasma membrane localization of the G-protein. The $G\alpha$ subunit is myristoylated ($G\alpha_i$) and/or palmitoylated ($G\alpha_i$, $G\alpha_s$, $G\alpha_{13}$ / $G\alpha_q$) and the $G\gamma$ subunit is prenylated (Jastrzebska, 2013; Wettschureck and Offermanns, 2005). The $G\alpha$ subunit consists of two conserved domains: a GTPase domain and helical domain (Lambright et al., 1994). The GTPase domain includes the guanine nucleotide binding site and intrinsic GTPase activity. Three flexible loops known as switch I, II and III in the GTPase domain are suggested to play a significant role in GDP/GTP exchange since these loops show the most significant conformational changes (Baltoumas et al., 2013; Jastrzebska, 2013). The $G\beta$ and $G\gamma$ subunits are tightly associated and serve as one functional unit. Active GPCRs function as guanine nucleotide exchange factors (GEFs) for heterotrimeric G-proteins, facilitating the GDP/GTP exchange (Dror et al., 2015). The active GPCR conformations reveal a binding pocket for interaction with the carboxy-terminus of the $G\alpha$ subunit. Binding of a G-protein to an activated receptor favors a conformational change that weakens interactions between GDP and the GTPase domain of the $G\alpha$ subunit, allowing GDP to escape. Loss of GDP shifts the equilibrium toward $G\alpha$ conformations with widely separated domains, provoking GTP to bind (Dror et al., 2015). Upon binding of GTP to the $G\alpha$ subunit, the heterotrimeric G-protein either dissociates in separate $G\alpha$ and $G\beta\gamma$ subunits or undergoes a conformational change, either way resulting in increased distance between $G\alpha$ and $G\beta\gamma$ and revealing binding sites for effectors to continue further downstream signal transduction (Lambert, 2008). The intrinsic GTPase activity of $G\alpha$, facilitates the hydrolysis of bound GTP to GDP, thereby inactivating $G\alpha$ and allowing the heterotrimeric G-protein to reassemble. Additionally, GTPase activating proteins (GAPs) bind $G\alpha$ to accelerate the intrinsically low GTPase activity of the $G\alpha$ subunit. The $G\beta\gamma$ signaling is terminated by reassociation with $G\alpha$ -GDP (figure 2) (Syrovatkina et al., 2016).

Four classes of $G\alpha$ subunits exist transducing the signal of >800 GPCRs: $G\alpha_s$ /olf (two members), $G\alpha_i$ /o (eight members) $G\alpha_q$ /11 (four members) and $G\alpha_{12/13}$ (two members) (Milligan and Kostenis, 2006).

$G\alpha_s$ /olf stimulates adenylyl cyclases (AC) to convert ATP to cyclic AMP (cAMP). cAMP activates, amongst others, protein kinase A (PKA) and cAMP gated channels (figure 3)

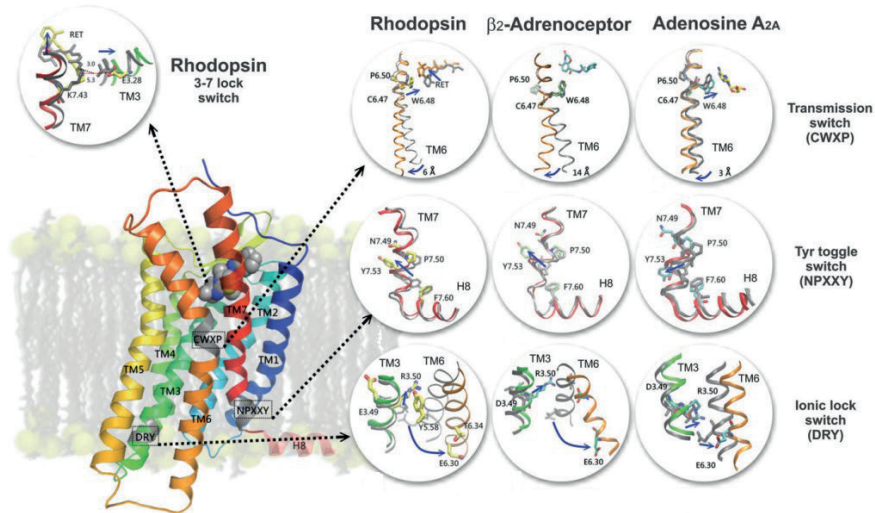


Figure 1. A GPCR, indicated are the conformational changes, molecular switches, leading to receptor activation. The figure zooms in on the four different molecular switches that constitute the conformational changes occurring during receptor activation. The molecular switches are shown for three different GPCRs. The inactive structures are depicted in gray and the active structures in color. Information on the different molecular switches is provided in the text. Adapted from Trzaskowski et.al. (Trzaskowski et al., 2012).

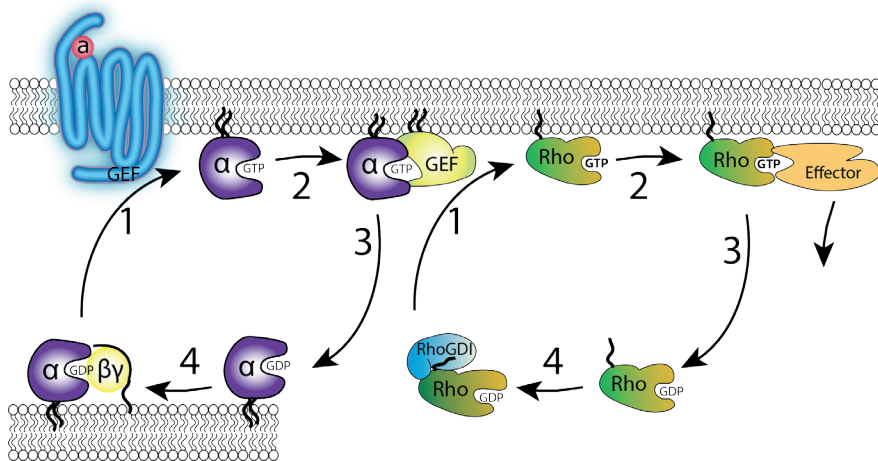


Figure 2. The activation cycle of the G proteins, heterotrimeric G protein and small RhoGTPases. G proteins cycle between an inactive GDP bound state and an active GTP bound state. Guanine exchange factors (GEFs) facilitate the exchange of GDP for GTP, activating the G protein (1). An activated GPCR is the GEF for a heterotrimeric G protein and an activated G protein is the GEF for small RhoGTPases. The active heterotrimeric G protein dissociates into two subunits, α and $\beta\gamma$, each activating downstream effectors, just as active RhoGTPases activate their downstream effectors (2). Guanine activating proteins (GAPs) hydrolyze GTP to GDP, thereby inactivating the G protein (3). The heterotrimeric G protein re-associates and the inactive RhoGTPase is bound by RhoGDI, keeping the RhoGTPases inactive in the cytoplasm (4), finishing one round of GTPase activation.

(Dorsam and Gutkind, 2007; Syrovatkina et al., 2016; Wettschureck and Offermanns, 2005). Gai/o inhibits the conversion of ATP to cAMP by inhibiting AC, thereby inhibiting further downstream signaling via cAMP. The Gai/o subunits are expressed at relatively high levels. As a consequence, activation of this class of G-proteins leads to substantial G $\beta\gamma$ mediated signaling, including the activation of G-protein coupled inwardly-rectifying potassium (GIRK) channels. Additionally, literature suggests that Gai and/or G $\beta\gamma$ can yield activation of RhoGEFs that activate small RhoGTPases. These small RhoGTPases are important in cell morphology and motility (Belcher et al., 2005; Chen et al., 2004; Li et al., 2003; Li et al., 2013; Smrcka, 2008; Vázquez-Prado et al., 2016; Wettschureck and Offermanns, 2005). Gq/11 activates phospholipase C β (PLC β), which hydrolyses phosphatidylinositol 4,5-biphosphate (PIP $_2$), producing diacylglycerol (DAG) and inositol-1,4,5-triphosphate (IP $_3$). Subsequently, DAG activates protein kinase C (PKC), and IP $_3$ causes calcium efflux from the endoplasmic reticulum (ER). Both events trigger further downstream effectors (Kamoto et al., 2015; Wettschureck and Offermanns, 2005). Additionally, Gq/11 activates RhoGEFs, p63RhoGEF and Trio, which in turn facilitate the activation of the small RhoGTPase, RhoA. RhoA is involved in cytoskeleton regulation, mainly via the formation of actin stress fibers and contraction of actomyosin (Lutz et al., 2005; Rojas et al., 2007; van Unen et al., 2016a). G $\alpha_{12/13}$ activates RhoGEFs (p115-RhoGEF, PDZ-RhoGEF and LARG) which facilitate the activation of RhoA. This leads to the activation of several downstream effectors such as Rho kinase (ROCK), protein kinase N (PKN), Jun kinase (JNK), citron kinase, phospholipase D (PLD), LIM kinase (LIMK), Diaphanous 1, raphilin, and rhotekin (figure 3) (Aittaleb et al., 2010; Jaffe and Hall, 2005; Meyer et al., 2008; Sah et al., 2000; Siehler, 2009).

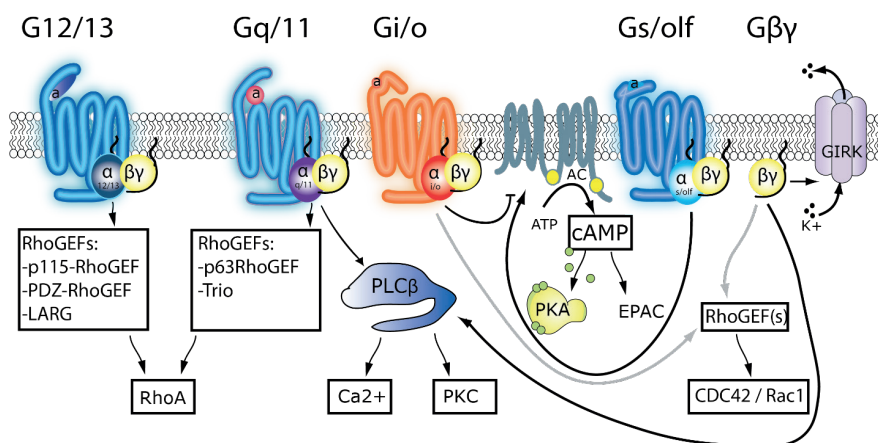


Figure 3. An overview of basic GPCR signaling induced by different G α classes and G $\beta\gamma$. Gray arrows represent unestablished connections in the signaling cascade, which will be investigated further in this thesis.

Rho GTPases

There is ample evidence that RhoGTPases are involved in GPCR signaling. The effects of RhoGTPases will be discussed in more detail in this section. RhoGTPases are important downstream effectors involved in regulation of the actin cytoskeleton, cell shape, cell polarity, microtubule dynamics, membrane transport pathways, gene transcription, neurite retraction, cell adhesion, migration and cell cycle progression (Etienne-Manneville and Hall, 2002; Meyer et al., 2008; Wennerberg and Der, 2004). RhoGTPases cycle between an inactive GDP-bound and an active GTP-bound state that can interact with specific downstream effector targets. RhoGTPases are activated by RhoGEFs, inactivated by GAPs and when inactive Rho guanine nucleotide dissociation inhibitors (RhoGDIs) bind RhoGTPases keeping them inactive in the cytoplasm, to prevent spontaneous activation (figure 2) (Jaffe and Hall, 2005; Olofsson, 1999).

The Rho GTPase family can be subdivided in the main families Rac, RhoA and Cdc42 (Boueux et al., 2007; Jaffe and Hall, 2005; Murali and Rajalingam, 2014). Rac is required at the front of migrating cells, promoting the actin polymerization that pushes the cell forward. Additionally, Rac mediates the formation of focal adhesions via JNK induced paxillin phosphorylation (Gardiner et al., 2002; Huang et al., 2003; Itoh et al., 2002; Jaffe and Hall, 2005; Kraynov et al., 2000). In *in vitro* cell culture, ectopic expression of Rac is associated with membrane ruffling due to the formation of lamellopodia (Murali and Rajalingam, 2014; Ridley et al., 1992; Sadok and Marshall, 2014). RhoA is active at the rear of the cell, generating contractile forces through ROCK mediated myosin light chain (MLC) phosphorylation (Jaffe and Hall, 2005; Riento and Ridley, 2003). In *in vitro* cell culture, ectopic expression of Rho is associated with the formation of actomyosin stress fibers (Murali and Rajalingam, 2014; Ridley et al., 1992). Cdc42 is essential for directional migration of macrophages in a gradient of chemoattractant, since inhibition of Cdc42 led to movement of these cells in random directions (Allen et al., 1998; Hall, 1998; Jaffe and Hall, 2005). In *in vitro* cell culture, ectopic expression of Cdc42 is associated with the formation of filopodia (Murali and Rajalingam, 2014; Nobes and Hall, 1995).

GPCR signaling beyond G-proteins

This concise overview of the signaling that can be induced by GPCRs still lacks the two other effectors of GPCRs, G-protein coupled receptor kinases (GRKs) and β -arrestins. They regulate GPCR signaling and contribute to the complex specificity of GPCR signaling. GRKs phosphorylate serine and threonine residues of the third intracellular loop and/or carboxy-terminus of activated GPCRs. β -arrestins bind to the phosphorylated sites and initiate receptor internalization and G-protein independent signaling (Ostermaier et al., 2014; Reiter and Lefkowitz, 2006; Vroon et al., 2006). Furthermore, GPCR (*hetero*-)dimerization, coupling of a GPCR to more than one G α class, biased signaling and specificity of GEFs and GAPs add to the complexity of GPCR signaling (Baltoumas et al., 2013; Chandrasekera et al., 2013; Hiller et al., 2013; Kasai

and Kusumi, 2014; Reiter et al., 2012; Satake et al., 2013; Saulière et al., 2012; Wisler et al., 2014; Yung et al., 2014).

1.2 Fluorescent proteins

Studying the tight spatiotemporal regulation of GPCR signaling demands a technique that allows high spatial ($< \mu\text{m}$) and temporal ($< 1\text{s}$) resolution with as little as possible perturbation of the cells. Techniques such as qPCR, western blot and mass spectrometry yield information about the average biochemical state of cells or cell populations. Data obtained with these techniques lack spatial information due to disruption of cellular integrity. Although this information is valuable, subcellular labeling techniques exist that offer higher spatial and/or temporal resolution. Immunolabeling yields high spatial resolution due to the small size of antibodies, nanobodies or aptamers, but the temporal resolution is often hampered by the need for fixation of the cells (Bauer et al., 2016; Chang et al., 2013; De Meyer et al., 2014; Virant et al., 2018). Fixation of cells is also often required for labeling with fluorescent dyes. However, small synthetic dyes and nanobodies exist for *in vivo* targeted labeling (Gautier et al., 2008; Griffin et al., 1998; Herce et al., 2017; Sun et al., 2011).

Fluorescent proteins derived from jelly fish and corals are entirely genetically encoded and can be functionally tagged to proteins of interest *in vivo* in heterologous systems without need for a cofactor, causing minimal perturbation of the cells (Chudakov et al., 2010; Tsien, 1998). This makes fluorescent proteins popular for *in vivo* subcellular labeling of proteins of interest.

The work described in this thesis uses fluorescent proteins as subcellular labels. The next paragraphs are used to give more information about how fluorescent proteins work, about the characteristics that differ amongst them and about their application in so-called biosensors used to study cellular signaling.

Compounds that exhibit fluorescence often contain conjugated double bonds providing appropriate energy states of the orbital electrons (Hochreiter et al., 2015). The absorption of a photon by a fluorophore, leads to the excitation of an electron from its ground state to an excited energy level (singlet state S_1 or S_2) (figure 4A). The excited state is instable, usually the electron relaxes back to its ground state within nanoseconds. The fluorophore can only emit a photon from the lowest S_1 energy level. Vibrational relaxation of the molecule towards the lowest S_1 energy level is called internal conversion, a non-radiative loss of energy, responsible for the Stokes shift. The Stokes shift of a fluorescent protein is the difference between excitation and emission wavelengths, the emission containing less energy and thus a longer wavelength. The absorption and emission do not occur only at a single wavelength, but rather within

a spectrum of a specific range, due to the variety in vibrational levels at which an electron can arrive in, respectively, the excited or the ground state. Alternatively, a molecule can also cross from the singlet state to the triplet state called intersystem crossing (figure 4A). Relaxation from the triplet state back to the ground state occurs through radiationless vibrational relaxation, emission of phosphorescence or delayed luminescence, which usually takes much longer (>1000-fold) than the transition from excited state to ground state (figure 4A) (Lichtman and Conchello, 2005; Toseland, 2013).

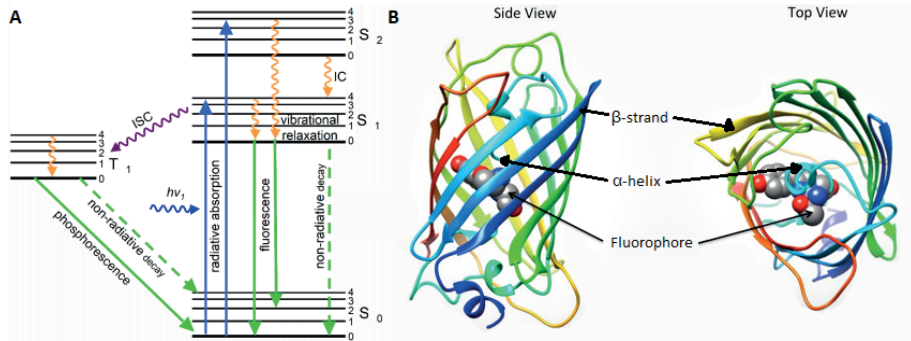


Figure 4. Fluorescence and the Green Fluorescent Protein (GFP) structure.

(A) A Jablonski diagram showing energy transitions that can occur when a fluorophore absorbs a photon ($h\nu_1$). The black solid lines represent singlet (S₀-S₂) and triplet (T₁) energy levels. Absorption and emission transitions are shown by solid blue and green lines. Dotted green lines represent non-radiative return to ground level (S₀). Curly orange and purple arrows show vibrational relaxations, internal conversion (IC) and intersystem crossing (ISC), respectively. Adapted from Patowary (Patowary, 2013).

(B) The structure of GFP, showing the β-strands that compose the β-barrel, the α-helix that runs through the β-barrel and the fluorophore halfway the α-helix, protected by the barrel. Adapted from rcsb.org (Berman et al., 2000).


Fluorescent proteins consist of a β-barrel, composed of eleven β-strands, and one α-helix that runs through the β-barrel and contains the chromophore (figure 4B). The chromophore is formed from three amino acids that autocatalytically react, to yield a functional chromophore via cyclization, dehydrogenation and oxidation steps (Cody et al., 1993; Cubitt et al., 1999). The chromophore is responsible for the ability to fluoresce and its composition determines the spectral class in terms of the range, in the visible spectrum, where it absorbs and emits light (Tsien, 1998). The amino acids composing the β-barrel interact non-covalently with each other, with amino acids from other fluorescent protein β-barrels and with the chromophore, influencing the characteristics of a particular fluorescent protein. Additionally, the β-barrel protects the chromophore from reactive oxygen species (ROS) in the environment that destroy the chromophore in a process called photobleaching (Greenbaum et al., 2000; Swaminathan et al., 1997).

Currently, a diverse set of fluorescent proteins is available (Miyawaki and Niino, 2015). The fluorescent proteins (FPs) vary in absorption and emission spectra, brightness, quantum yield, extinction coefficient, maturation speed and efficiency, fluorescence lifetime (τ), photostability, dimerization tendency and environmental sensitivity (for pH or halide concentrations).

The absorption and emission spectra depend on the amino acids that autocatalytically react to form the chromophore and on the amino acids within the beta barrel interacting with the chromophore. By mutagenesis of these amino acids, spectrally distinct fluorescent proteins can be obtained (Tsien, 1998). A special class of spectral variants are the large Stokes shift (LSS) FPs, which represent FPs with a Stokes shift of more than 100nm. The phenolate (tyrosine) containing chromophore of LSS-FPs is mostly protonated in the ground state. Protonated chromophores show a blue-shifted absorption spectrum. Excitation of a protonated chromophore highly increases its acidity, leading to a process called excited state proton transfer (ESPT). ESPT converts the chromophore into an intermediate state, via proton transfer over a hydrogen bonding network around the chromophore. The emission spectrum is similar to that of a non-LSS-FP from the same spectral class, because the chromophore becomes deprotonated in the excited state (Jung et al., 2005; Piatkevich et al., 2010; Tsien, 1998). Mutations in residues that alter the proton network around the chromophore may cause a large Stokes shift. Applications of LSS-FPs in FRET imaging will be discussed later.

The brightness of a fluorescent protein is important for its visibility during microscopy and it is determined by its quantum yield (QY), extinction coefficient (ϵ) and its maturation speed and efficiency. The extinction coefficient describes the efficiency of light absorption by the chromophore of the fluorescent protein. The quantum yield is defined as the ratio of photons emitted over photons absorbed. The more rigid and planar the chromophore the higher the quantum yield. Cis-/trans-isomerization of the excited chromophore causes loss of energy resulting in a lower quantum yield (Shanker and Bane, 2008; Toseland, 2013).

Additionally, the speed and efficiency of the autocatalytic maturation of the chromophore and correct folding of the protein influences the brightness, because for every non-functional fluorescent protein the overall brightness declines. Fluorescent protein timers make use of red fluorescent proteins with a slow maturation (Subach et al., 2009; Terskikh et al., 2000). Red fluorescent proteins mature via a blue fluorescent intermediate, visualizing how protein localization changes over time (Miyawaki et al., 2012; Subach et al., 2009; Terskikh et al., 2000).



The lifetime of a FP is the time the chromophore resides in an excited state before emitting a photon while going back to a ground state. The lifetime depends on the kinetics of all radiative and radiationless processes that bring the excited molecule back into the ground state, and is characteristic for each fluorophore (Goedhart et al., 2010). The fluorescence lifetime of a FP can be measured *in vivo* using frequency domain fluorescence lifetime imaging (FLIM) or time correlated single photon counting (TCSPC) FLIM (Becker, 2012; Becker et al., 2004; Van Munster and Gadella Jr, 2004; Van Munster and Gadella Jr, 2005).

The fluorescence lifetime is not dependent on concentration or maturation efficiency. The lifetime is proportional to the quantum yield and is therefore used for screening of the brightness of FPs (Bindels et al., 2017; Goedhart et al., 2010; Goedhart et al., 2012; Kremers et al., 2006).

Good photostability of an FP is required for *in vivo* timelapse imaging. Photobleaching is caused by irreversible (oxidative) damage to the chromophore due to the presence of ROS. The more the β -barrel structure protects the chromophore, the more photostable is the fluorescent protein. Additionally, some phenomena exist that might be confused with photobleaching, like photoconversion, photochromism and blinking (De Keersmaecker et al., 2016; Dickson et al., 1997; Kremers et al., 2009; Mizuno et al., 2008). Blinking is the frequent intersystem crossing towards the triplet state, which is a characteristic of FPs that are often used in superresolution microscopy techniques (Fölling et al., 2008).

In nature, FPs exist as dimers or tetramers (Baird et al., 2000; Tsien, 1998; Verkhusha and Lukyanov, 2004). Dimerization of FPs that are tagged to proteins of interest can lead to impaired functioning and/or localization of the proteins of interest (Piston and Kremers, 2007; Zacharias et al., 2002). In order to obtain monomeric FPs, positively charged amino acids were introduced at the dimer interface (Merzlyak et al., 2007; Zacharias et al., 2002). Furthermore, the environmental sensitivity of FPs should be considered since several FPs are sensitive to pH or halides (Griesbeck et al., 2001; Rekas et al., 2002; Wachter and Remington, 1999).

This overview gives some insight in how FPs function and how mutagenesis is used to further improve their characteristics. The large assortment of fluorescent proteins is optimized for multiple applications in fluorescence microscopy, including fluorescence recovery after photobleaching (FRAP), fluorescence lifetime imaging (FLIM), superresolution microscopy, fluorescence correlation spectroscopy (FCS) and Förster Resonance Energy Transfer (FRET) imaging (Crosby et al., 2013; Fölling et al., 2008; Schwille et al., 1999; Shrestha et al., 2015; Van Munster and Gadella Jr, 2005). The work described in this thesis focusses on FRET imaging to elucidate GPCR signaling.

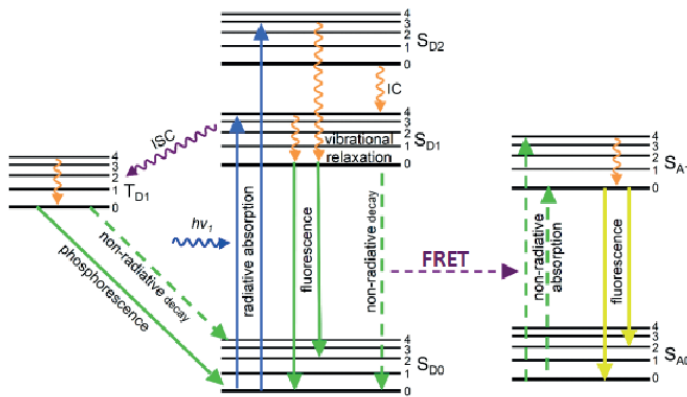
1.3 Förster Resonance Energy Transfer (FRET)

Studying interactions between molecules requires a resolution of <10nm, which conventional microscopy techniques are not able to convey. The diffraction limit sets the lateral (x,y) resolution of conventional microscopy at maximum ~250nm and the axial resolution (z) at maximum ~500nm. The resolution is dependent on the wavelength of the light, the refractive index of the imaging medium and the numerical aperture (NA) of the objective (Jares-Erijman and Jovin, 2003).

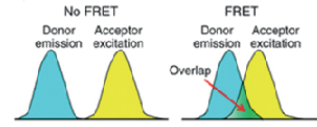
FRET can be used to visualize interactions at a distance of 1-10nm, making it extremely valuable in interaction studies. FRET is a radiationless transfer of energy from one excited state fluorophore (donor) to another fluorophore (acceptor) by direct dipole interactions (figure 5) (Shrestha et al., 2015). The efficiency of energy transfer is dependent on the distance between donor and acceptor (should be within 10 nm), the spectral overlap between the donor emission and the acceptor absorbance spectra, the quantum yield of the donor, the extinction coefficient of the acceptor and the relative orientation of the donor and acceptor dipoles (figure 5B, C) (Broussard et al., 2013; Wu and Brand, 1994). The relation between each of these parameters is shown in the formulas describing the FRET efficiency (E) and the Förster radius (R_0) (figure 5C). The Förster radius (R_0) is the distance at which the FRET efficiency of a particular donor and acceptor, FRET pair, is 50% (Goedhart et al., 2007; Wu and Brand, 1994).

In principle, any instrument that is capable of recording fluorescence can be used to measure FRET, provided that suitable fluorescent proteins are available and the corresponding filters and detectors are present. Methods used to measure FRET are based on: (1) fluorescence anisotropy; (2) fluorescence lifetime; or (3) fluorescence intensity. Fluorescence anisotropy based FRET measurements make use of the increase of donor anisotropy in the presence of FRET. In this thesis, this method of measuring FRET will not be thoroughly discussed, but the interested reader can read about it elsewhere (Pietraszewska-Bogiel and Gadella Jr, 2011; Piston and Rizzo, 2008). Fluorescence lifetime based FRET measurements (FLIM-FRET) require an advanced imaging system, able to record the lifetime of a fluorophore. When FRET occurs, the lifetime of the donor will be shortened due to the additional relaxation route, leading the excited fluorophore back to the ground state. The difference in lifetime in the presence and absence of FRET can be determined exactly, using the formula for the FRET efficiency (E) ($E = 1 - \left(\frac{\tau_{DA}}{\tau_D}\right)$, where τ_{DA} is the lifetime in presence of the acceptor and τ_D is the lifetime in absence of the acceptor)(Goedhart et al., 2007; Pietraszewska-Bogiel and Gadella Jr, 2011). Note that the quantum yield of the acceptor does not affect the lifetime of the donor and therefore is not important in FLIM-FRET experiments. FP variants were developed with very low quantum yield and high extinction coefficient, called dark acceptors or chromoproteins, used as acceptors in FRET pairs employed in FLIM-FRET experiments (Ganesan et al., 2006; Murakoshi et al., 2008).

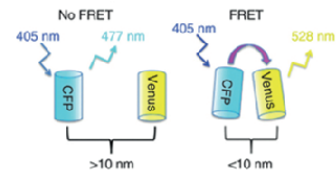
A



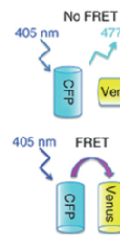
B Spectral Overlap



Distance



Orientation



C

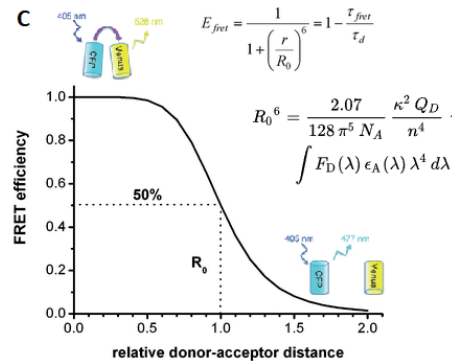


Figure 5. Fluorescence Resonance Energy Transfer (FRET) principle and requirements

(A) A Jablonski diagram showing energy transitions that can occur when a fluorophore absorbs a photon ($h\nu_1$), including the Förster resonance energy transfer (FRET) from a donor to an acceptor fluorophore (purple dotted arrow). The black solid lines represent singlet (S_{D0} - S_{D2} for the donor and S_{A0} - S_{A2} for the acceptor) and triplet (T_{D1}) energy levels. Absorption and emission of light are shown by solid blue, green and yellow lines. Dotted green lines represent non-radiative return to ground level (S_0). Curly orange and purple arrows show vibrational relaxations, internal conversion (IC) and intersystem crossing (ISC), respectively. Adapted from Patowary (Patowary, 2013).

(B) The FRET efficiency between two fluorescent proteins depends on: (1) the extent of the spectral overlap between the donor emission and acceptor excitation spectrum; (2) the relative orientation of the fluorescent proteins dipoles (adapted from Broussard 2013); and (3) the distance between the fluorescent proteins, which should be within 10nm for FRET to occur. Adapted from Broussard et al (Broussard et al., 2013).

(C) The graph shows the relation between the FRET efficiency and the distance between the FRET pair and the mathematical formula that describes the relation. The Förster radius (R_0), dotted lines, indicates the distance at which the FRET efficiency is 50%. The R_0 is used to theoretically assess the quality of FRET pairs and can be determined according to the given formula. Adapted from Broussard et. al and Festy et. al. (Broussard et al., 2013; Festy et al., 2007).

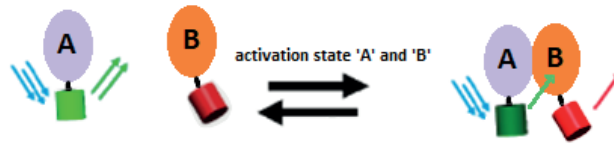
Fluorescence intensity-based FRET measurements can be performed on a spectrophotometer or wide-field microscope and do not require advanced imaging systems. Fluorescence intensity based methods for measuring FRET are: donor quenching, acceptor photobleaching, spectral imaging, ratiometric imaging and filter-FRET (Broussard et al., 2013; Goedhart et al., 2014; Pietraszewska-Bogiel and Gadella Jr, 2011; Piston and Kremers, 2007). Ratiometric FRET imaging is the most widely applied method for dynamic FRET measurements in cells. During ratiometric FRET imaging the intensity of the donor and sensitized emission of the acceptor are recorded in time and the ratio of both intensities is presented as quantitative output (Pietraszewska-Bogiel and Gadella Jr, 2011).

1.4 Fluorescent proteins applied in FRET-based biosensors for monitoring events in GPCR signaling

Biosensors are developed that use changes in FRET to report on molecular interactions, phosphorylation, changes in concentrations of ions or small molecules or the nucleotide loading state of a protein. The existing biosensors can be categorized based on their structural design. Bimolecular or intermolecular FRET sensors consist of two separate, FP-labeled domains. These labeled domains show FRET, dependent on the relative orientation of and the distance between the labeled domains and thereby can report on interaction and/or co-localization of these domains (figure 6) (Adjobo-Hermans et al., 2011).

Unimolecular or intramolecular FRET sensors consist of one construct encoding two FPs, linked with a sensory domain, which controls their orientation and distance and thus the degree of FRET (Hochreiter et al., 2015). This group of sensors can be subdivided based on their way of transforming a biological event into a change in FRET efficiency: (1) sensors based on a cleavable linker between the FRET pair, used to visualize the activity of certain enzymes. The reaction is irreversible and therefore not suitable for dynamic measurements (Sabariegos et al., 2009; Tyas et al., 2000; Xu et al., 1998); (2) sensors based on a linker of spider silk proteins between the FRET pair, translating mechanical force into changes in FRET (Grashoff et al., 2010); (3) sensors based on the environmental sensitivity of one of the FPs composing the FRET pair, used to measure changes in the environment such as pH or concentration of halides, oxygen or ROS (Kuner and Augustine, 2000); (4) sensors based on a conformational change of one or more sensor domain(s), via a linker connected with the FRET pair, used to measure for example phosphorylation, activation of effectors or concentration of ions or small molecules (figure 6). This category of biosensors is widely applied, due to its versatile nature.

Bimolecular sensor design strategy



Unimolecular sensor design strategies

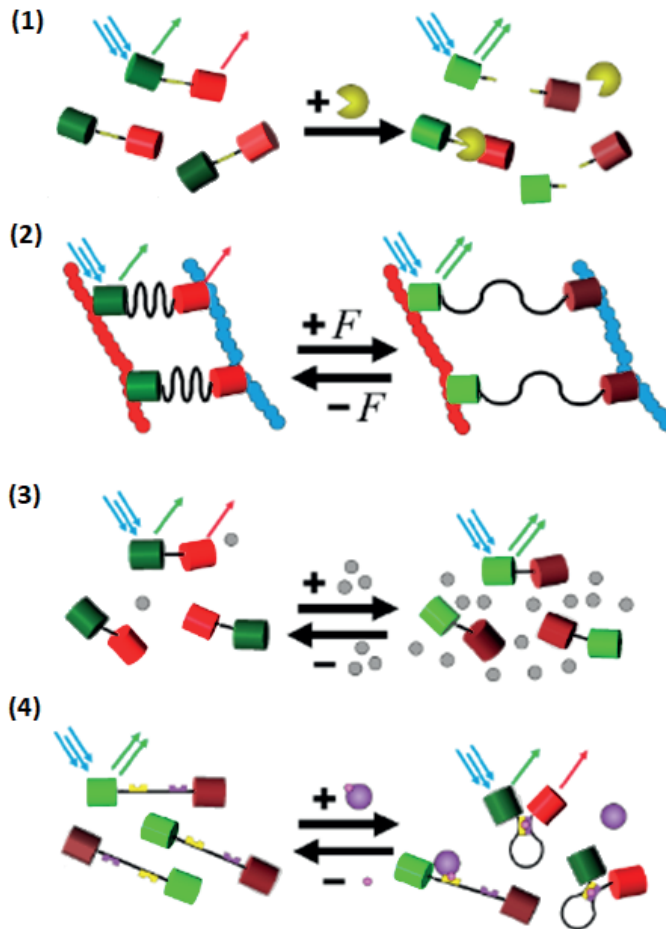


Figure 6. Overview of different FRET sensor design strategies.

The bimolecular or intermolecular sensor design strategy is based on interacting/co-localizing molecules 'A' and 'B' bringing the attached FRET pair together. The unimolecular or intramolecular sensor design strategies are based (1) on a cleavable linker to report on enzyme activity; (2) on a spider silk protein linker to report on mechanical force; (3) on environmental sensitivity of one FP of the FRET pair to report on changes in the cell's environment; or (4) on conformational changes of one or more sensor domains reporting on for instance phosphorylation, activation of effectors or concentration of ions or small molecules. Adapted from Hochreiter et. al. (Hochreiter et al., 2015).

An advantage of unimolecular sensors is that the conformations of the FRET “on” and FRET “off” states are structurally more confined. This implies that the sensor can be more extensively optimized for conformational changes that yield the largest FRET contrast, or dynamic range, between the “on” and “off” state of the sensor (Fritz et al., 2013; Nguyen and Daugherty, 2005). In addition, interference from endogenous cellular components is reduced in case of unimolecular sensors.

An advantage of bimolecular sensors is that their performance is less affected by small conformational changes in the sensor design and therefore the result of sensor optimization is more predictable and straightforward than for unimolecular sensors. A disadvantage of bimolecular sensors is that the FP-labeled domains are regularly expressed from different constructs or controlled by different promoters, resulting in an undefined stoichiometry that interferes with reliable FRET measurements. However, a set stoichiometry can be achieved by expressing both FP-labeled domains in one construct using an IRES or 2A sequence in the linker between the FP-labeled domains (Goedhart et al., 2011; Kim et al., 2011; Martin et al., 2006).

Proper functioning of a biosensor is of the utmost importance, because the data obtained with these biosensors contribute to a foundation of knowledge, aiming to elucidate cellular signaling. The correctness and quality of these data rely greatly on the functioning of the used biosensors.

If a biosensor is not functioning correctly, there is no guarantee that the observed changes in FRET efficiency are correlating with the occurrence of certain events in cellular signaling, for which the biosensor is used. The sensor may show false FRET changes, due to lack of selectivity of the sensing domain or due to employment of an unsuitable FRET pair composed of for example environmental sensitive or not photostable FPs. On the contrary, the sensor may not show changes in FRET efficiency even though the specific cellular signaling events are occurring, which could be due to a lack of affinity of the sensing domain or an unsuitable FRET pair. If the FRET pair shows a low Förster radius, the changes between FRET “on” and FRET “off” state might be indistinguishable. Additionally, a high dimerization tendency of the FRET pair might lock the sensor in the FRET “on” state.

The performance of a FRET based biosensor is determined by its selectivity, affinity and dynamic range. The first two factors are mostly defined by characteristics of the sensing domains, while the dynamic range is predominantly defined by spectroscopic characteristics of the FPs that form the FRET pair and, in case of unimolecular sensors, the relative orientation of the FPs’ dipoles and the linker length and composition (Fritz et al., 2013; Goedhart et al., 2007; van der Krogt et al., 2008).

Several studies have systematically tested several linkers (Komatsu et al., 2011; Schifferer and Griesbeck, 2012; Shimozone and Miyawaki, 2008), several FRET pairs (Goedhart et al., 2007; Nguyen and Daugherty, 2005), several sensor topologies (Ohta et al., 2016) and several dipole orientations of the FRET pair (Fritz et al., 2013; Nagai et al., 2004), resulting in the establishment of guidelines in biosensor development. However, transferring knowledge obtained during the optimization of one sensor to another sensor, often remains partially trial-and-error, because not all the effects of every FP residue on every position in a FP or linker are known and changing the sensing domain(s) affects the overall structure of a sensor.

Currently, numerous biosensors exist that can be used to monitor various events in GPCR signaling (Lohse et al., 2012). GPCR signaling is challenging to elucidate due to the interplay of numerous molecular players. Therefore, the simultaneous use of multiple biosensors, monitoring several events at the same time in the same cell, would contribute tremendously to a better understanding of the regulation of GPCR signaling and how it achieves its specificity. Dual/multiplex FRET imaging requires the employed sensors to be compatible, meaning that it should be possible to distinguish between the sensors based on localization, spectral properties or fluorescence lifetime. These different strategies for multiplex imaging will be detailed below.

Strategies for multiplex FRET imaging

Spatial separation of sensors is relatively straightforward. Signal peptides can be used to confine a sensor to a certain subcellular localization. An advantage is that the same FRET pair can be used in both sensors and therefore there is no need for additional imaging channels (DiPilato et al., 2004; Piljic and Schultz, 2008). A limitation of this approach is that it can only be used to study spatially resolved compartments.

The challenge to separate the sensors' emission signals based on their spectral properties, progresses with increasing spectral overlap between FRET pairs and decreasing FP quality.

The extensively optimized CFP-YFP FRET pair is most frequently used in single FRET experiments. However, in dual FRET applications, spectral separation is very important and the CFP-YFP pair occupies a substantial part of the spectrum. Additionally, the red-shifted FRET pairs, which are spectrally compatible with CFP-YFP, often lack in brightness, maturation speed and efficiency and frequently show dimerization or photoconversion (Chudakov et al., 2010; Kremers et al., 2009).

Nevertheless, these suboptimal FRET pairs have been successfully applied in multiplex FRET imaging (Piljic and Schultz, 2008).

In order to develop FRET pairs for successful multiplex experiments, Sun et.al. focused on combining a blue-shifted FRET pair with a slightly red-shifted FRET pair (Sun et al., 2009).

Another approach uses a single excitation wavelength for two FRET donors with resolvable emission spectra, employing previously mentioned large Stokes shift (LSS) FPs (Ai et al., 2008; Ding et al., 2011; Niino et al., 2009; Shcherbakova et al., 2012). This approach enables fast imaging acquisition due to the single excitation wavelength, while the differences in spectral properties facilitate spectral imaging and subsequent linear unmixing. Spectral imaging implies that as a reference, the contribution of each, separately expressed, fluorescent protein to each imaging channel is recorded. These 'spectral signatures' are used to assemble a matrix. Linear unmixing uses this matrix to determine the contribution of each fluorescent protein to each pixel of the FRET data recorded using the same imaging channels. The quality of linear unmixing is affected by the signal to noise ratio (SNR). The SNR decreases with the use of dim fluorescent proteins, with an increasing number of detection channels and with an increase of spectral overlap between FRET pairs (Niino et al., 2009; Woehler, 2013; Zimmermann, 2005; Zimmermann et al., 2003).

It is also possible to use the fluorescence lifetime to distinguish between FRET pairs. An advantage of this method is that FLIM-FRET occupies a smaller part of the visible spectrum, since only the donor lifetime is monitored (Laviv et al., 2016). Dark acceptors or chromoproteins can be applied to avoid FRET from the acceptor to another FRET pair (Ganesan et al., 2006; Lukyanov et al., 2000; Murakoshi et al., 2008). Drawbacks of FLIM-FRET are the required advanced imaging equipment, the slow image acquisition and the often lower FLIM-FRET contrast compared to the ratiometric FRET contrast of sensors.

Peyker et.al. measured the activation of different Ras proteins simultaneously, making use of a combination of lifetime and spatial separation (Peyker et al., 2005). Kremers et.al. reported a method for lifetime unmixing of spectrally indistinguishable fluorescent proteins, combining lifetime unmixing with simultaneous FLIM-FRET monitoring (Kremers et al., 2008). Furthermore, Grant et.al. combined ratiometric FRET with FLIM-FRET, using FLIM for the red-shifted FRET pair so the low quantum yield of the acceptor is of no concern (Grant et al., 2008).

Finally, single FRET pair experiments can be combined with a localization tag, single FP translocation reporter, intensimetric single FP sensor, bimolecular fluorescence complementation (BiFC) reporter or a synthetic calcium reporter (Carlson and Campbell, 2009; Miller et al., 2015; Schultz et al., 2005). These relatively simple experiments can already yield more information on the interplay between molecular players in regulating GPCR signaling.

Altogether, the more biochemical events can be monitored simultaneously, the more and better insights in the regulation of GPCR signaling can be obtained. The limitations in the amount of biosensors that can be measured simultaneously depends greatly on the imaging equipment and the qualities of the employed fluorescent proteins. Therefore, ongoing FP and sensor development and optimization are extremely important.

1.5 Thesis outline

The overall goal of our research is to understand how chemical states induced by GPCR activation control cellular decisions. Elucidation of GPCR signaling is challenging due to the interplay of numerous molecular players. To understand the complex interplay of signaling molecules in living cells, we use fluorescence microscopy techniques. Elucidating the chemical states induced by GPCR activation requires functional imaging at high spatial and temporal resolution. These requirements are met by genetically encoded FRET based biosensors. The research presented in this thesis aimed to gain more insight in the relation between fluorescent protein properties and its characteristics in FRET based biosensors, to develop and further optimize FRET based biosensors. The sensors are used to gather new insights into the regulation of GPCR signaling via dynamic FRET imaging in living cells.

Chapter 2 evaluates the performance of several FRET acceptors combined with novel CFP, mTurquoise2, as FRET donor. This chapter includes a discussion on important characteristics of fluorescent proteins and their effect on the performance of a FRET pair. The best performing FRET pair was mTurquoise2-mNeonGreen applied in a bimolecular FRET sensor for Gq activation. **Chapter 3** aimed to improve the performance of a unimolecular FRET sensor. Novel FPs can contribute to increased brightness, FRET efficiency or photostability of a sensor. However, application of these novel FPs often leads to a decreased dynamic range because the FPs are constrained to certain conformations. Published sensors often endured tedious optimization of relative orientations and distance. Changing one aspect of such a highly optimized sensor often results in a decrease in its dynamic range. This study evaluated the effect of FP stickiness, a weak dimerization tendency, and the FPs' relative orientations, on the dynamic range of a unimolecular sensor, reporting RhoA activation. The aim of the research discussed in **chapter 4** was to develop a FRET-based Gα13 activation biosensor. Multiple fluorescently tagged Gα13 variants were made and the functionality and localization was analyzed. Three G13 activation, single plasmid, biosensors were constructed and assessed. The sensor reports that P115 RGS domain was able to inhibit Gα13 activation in Human Umbilical Vein Endothelial cells (HUVEC). In addition, the sensor was used to evaluate which GPCRs activated the class of Gα13 heterotrimeric G-proteins. The Gα13 activation biosensor makes it possible to

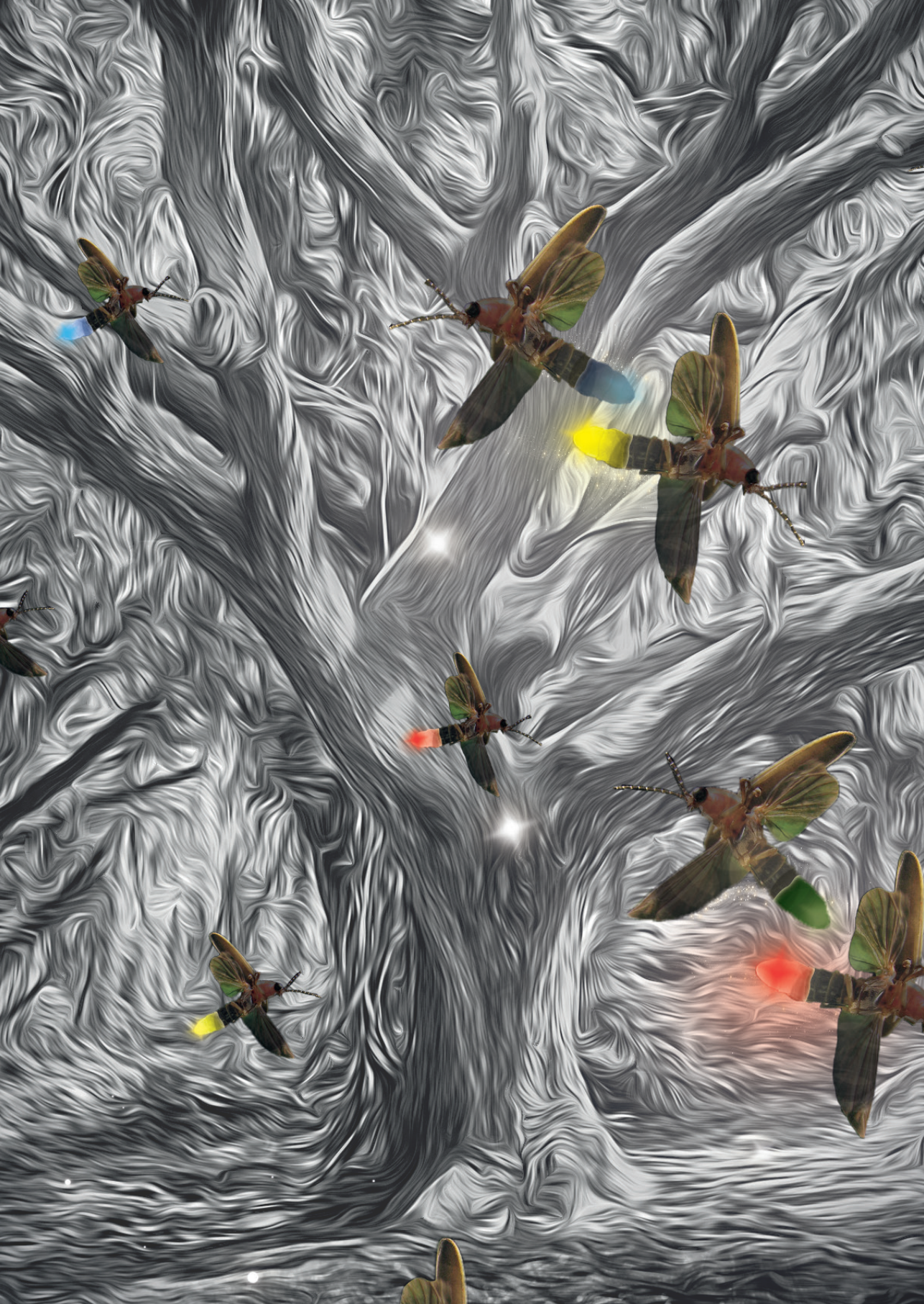


distinguish between Gαq and Gα13 signaling. These heterotrimeric G-protein classes are often activated by the same GPCRs and often lead to similar downstream signaling via different effectors. The development of a Gα13 activation biosensor was crucial in the path towards further elucidation of GPCR signaling regulation. In **chapter 5** sensors were developed, compatible with CFP-YFP based sensors, aiming towards dual FRET imaging. As a FRET donor mT-Sapphire was further optimized to LSS-SGFP2, which was characterized and applied in a bimolecular Gq or G13 activation biosensor and a unimolecular RhoA activation biosensor, assessing mCherry and mScarlet-I as FRET acceptors. Preliminary multiplex FRET imaging was performed, simultaneously monitoring Gq and G13 activation. Further optimization of the unimolecular RhoA activation sensor included circular permutations of the FPs to tweak the relative orientation of the FPs' dipoles.

Chapter 6 focusses on the barrier regulation in endothelial cells (EC). Sphingosine-1-phosphate (S1P) activates GPCRs that couple to Gi or G13 heterotrimeric G-protein classes, respectively leading to barrier protection and barrier disruption. This chapter concerns the S1PR1-Gi-Cdc42 signaling axis and aims to explore the molecular basis of Cdc42 mediated EC cell spreading and to identify more involved signaling components. The study reveals that Gβγ signaling is required for Cdc42 activation and pRex1 is suggested as Cdc42 activating GEF.

Finally, the general discussion debates and integrates the findings of all chapters in the light of the current literature.







2. Characterization of a spectrally diverse set of fluorescent proteins as FRET acceptors for mTurquoise2

Marieke Mastop¹, Daphne S. Bindels¹, Nathan C. Shaner², Marten Postma¹, Theodorus W.J. Gadella Jr.¹, and Joachim Goedhart¹

¹Swammerdam Institute for Life Sciences, Section of Molecular Cytology, van Leeuwenhoek Centre for Advanced Microscopy, University of Amsterdam, P.O. Box 94215, NL-1090 GE Amsterdam, The Netherlands.

²Department of Photobiology and Bioimaging, The Scintillon Institute, San Diego, California, United States of America



Abstract

The performance of Förster Resonance Energy Transfer (FRET) biosensors depends on brightness and photostability, which are dependent on the characteristics of the fluorescent proteins that are employed. Yellow fluorescent protein (YFP) is often used as an acceptor but YFP is prone to photobleaching and pH changes. In this study, we evaluated the properties of a diverse set of acceptor fluorescent proteins in combination with the optimized CFP variant mTurquoise2 as the donor. To determine the theoretical performance of acceptors, the Förster radius was determined. The practical performance was determined by measuring FRET efficiency and photostability of tandem fusion proteins in mammalian cells. Our results show that mNeonGreen is the most efficient acceptor for mTurquoise2 and that the photostability is better than SYFP2. The non-fluorescent YFP variant sREACH is an efficient acceptor, which is useful in lifetime-based FRET experiments. Among the orange and red fluorescent proteins, mCherry and mScarlet-I are the best performing acceptors. Several new pairs were applied in a multimolecular FRET based sensor for detecting activation of a heterotrimeric G-protein by G-protein coupled receptors. Overall, the sensor with mNeonGreen as acceptor and mTurquoise2 as donor showed the highest dynamic range in ratiometric FRET imaging experiments with the G-protein sensor.

Introduction

Fluorescent proteins derived from jellyfish and corals are fluorescent probes that are entirely genetically encoded and do not require a co-factor (Chudakov et al., 2010; Tsien, 1998). These probes are important tools for fluorescence imaging of cellular processes (Chudakov et al., 2005; Miyawaki and Niino, 2015). A specific application of fluorescent proteins is their use in Förster resonance energy transfer (FRET) studies (Gadella Jr et al., 1999; Miyawaki, 2011; Piston and Kremers, 2007; Pollok and Heim, 1999). FRET is the radiationless transfer of energy from an excited donor to a nearby acceptor. The FRET efficiency depends on several parameters, including the quantum yield of the donor, the extinction coefficient of the acceptor, the spectral overlap of donor emission and acceptor absorbance and the dipole orientation (Jares-Erijman and Jovin, 2003; Pietraszewska-Bogiel and Gadella Jr, 2011). The aforementioned parameters determine the Förster distance, R_0 , which is the distance between donor and acceptor that will result in 50% FRET (Hamers et al., 2014; Wu and Brand, 1994).

FRET can be used to determine the interaction between biomolecules and is also the basis for so-called biosensors. Biosensors are designed to report on chemical states and can be used to measure concentrations of ions or small molecules, phosphorylation of peptides or the nucleotide loading state of a protein (Mehta and Zhang, 2011; Okumoto et al., 2012). The performance of FRET based biosensors depends on their brightness and dynamic range, which are highly dependent on the characteristics of the applied fluorescent proteins (Goedhart et al., 2007; Scott and Hoppe, 2015; van der Krogt et al., 2008). Both FRET efficiency and brightness depend on extinction coefficient and quantum yield and therefore a general recommendation is to use the brightest fluorescent proteins available (Scott and Hoppe, 2015). For FRET imaging in living cells, several other parameters should be considered including maturation, photostability, oligomeric state and sensitivity to environmental changes (Hamers et al., 2014; Piston and Kremers, 2007; Scott and Hoppe, 2015).

The maturation is a critical factor for effective brightness of a fluorescent protein and for efficient FRET (Miyawaki, 2011). The maturation efficiency is the fraction of produced protein that results in a correctly folded protein with a functional, fluorescent chromophore. Ideally, the maturation of a fluorescent protein approaches 100%. When a protein incorrectly folds or does not form a correct chromophore, the FRET pair will lack a functional donor or acceptor and this will prevent FRET, thereby diluting the number of functional FRET pairs and decreasing the dynamic range (Scott and Hoppe, 2015).

In *Aequorea victoria* derived fluorescent proteins, amino acid residues 65–67 of the folded protein undergo several chemical reactions necessary for chromophore formation, including cyclization, oxidation and dehydration (Tsien, 1998).



Characteristics of residues in the vicinity of the chromophore can influence the efficiency of protein folding and chromophore formation. Mutations leading to more efficient chromophore formation (F64L, V68L) or protein folding (S72A, V163A, S175G) were identified (Cormack et al., 1996; Cubitt et al., 1999; Fukuda et al., 2000; Kremers et al., 2006; Patterson et al., 1997; Siemering et al., 1996). However, other mutations may lead to inefficient or slow maturation, resulting in dim fluorescence and only a small fraction of fluorescent cells (Nagai et al., 2002; Wachter et al., 2010). In red fluorescent proteins (RFPs), the maturation process is more complex. After the cyclization and oxidation steps the chromophore can be dehydrogenated in two alternative ways. One leads to a blue fluorescent intermediate that upon another oxidation step results in a mature RFP, while the other leads to a non-reversible GFP form (Miyawaki et al., 2012). Thus in the case of RFPs, inefficient or slow maturation may result in substantial green or blue fluorescence next to dim and inefficient RFP expression, hindering their use in multi-color labeling experiments (Chudakov et al., 2010).

Furthermore, it is important that the fluorescent proteins used in biosensors are not sensitive to environmental changes other than the one you want to measure. For example, yellow fluorescent protein (YFP) variants are sensitive to halide concentrations, but this problem was addressed by mutagenesis resulting in YFP variants Citrine and Venus (Griesbeck et al., 2001; Nagai et al., 2002; Rekas et al., 2002). In addition, changes in intracellular pH may affect the absorbance and hence change the FRET efficiency (mainly in GFP, YFP and mOrange). The pH sensitivity is dependent on the pKa of a fluorescent protein and depending on the acidity of the experimental environment, this characteristic should be taken into account when choosing or constructing a biosensor.

In nature, fluorescent proteins usually exist as dimers or tetramers (Baird et al., 2000; Tsien, 1998; Verkhusha and Lukyanov, 2004). It is important that fluorescent proteins that are tagged to proteins of interest are not oligomerizing, because this can lead to impaired functioning and/or localization of the protein of interest and it can lead to false positives in interaction studies (Piston and Kremers, 2007; Zacharias et al., 2002). The latter issue is more critical for intermolecular sensors as compared to intramolecular sensors. In fact, a weak tendency of *hetero*-dimerization can be beneficial for FRET contrast for unimolecular sensors (Lindenburg et al., 2014; Nguyen and Daugherty, 2005; Vinkenburg et al., 2007). Monomeric variants of *Aequorea victoria* fluorescent proteins were obtained by replacing hydrophobic residues at the dimer interface with positively charged residues (A206K, L221K, or F223R) (Zacharias et al., 2002). The engineering of bright, monomeric RFP variants is more difficult, since mutations disrupting dimer interfaces also affect other characteristics such as the quantum yield (Campbell et al., 2002). A recent engineering effort has resulted in a truly monomeric red fluorescent protein, mScarlet-I, with good maturation. Because of its relatively high quantum yield, the level of sensitized emission surpasses that of mCherry in a FRET pair (Bindels et al., 2017).

The monomeric nature of fluorescent proteins is often analyzed via *in vitro* ultra centrifugation or gel filtration of purified proteins (Baird et al., 2000; Pédelacq et al., 2006; Zacharias et al., 2002) and this is not a good predictor for the tendency to dimerize in living cells. Costantini et al. developed an *in vivo* dimerization assay in which fluorescent proteins are fused to an endoplasmic reticulum (ER) signal anchor membrane protein (CytERM)(Costantini et al., 2012). Homo-oligomerization of this CytERM-FP with the same construct in opposing membranes causes the formation of organized smooth ER (OSER) structures, which can be quantitatively evaluated in this OSER assay (Costantini et al., 2012; Costantini et al., 2015). Recently, Cranfill et al. assessed the oligomeric state of a large number of fluorescent proteins in cells using the OSER assay (Cranfill et al., 2016), providing a useful guide in choosing fluorescent proteins for certain applications.

FRET based sensors are mostly used in dynamic systems that are examined by timelapse imaging and therefore, photostability is an important characteristic. During timelapse imaging, it is crucial that only the actual changes in FRET are reported, since differences in photobleaching characteristics between the fluorescent proteins in a sensor will result in false FRET changes, complicating data analysis. Since FRET by itself changes photobleaching rates (Van Munster et al., 2005), changes in FRET will result in altered photobleaching kinetics. Hence, the photobleaching rate may change during a timelapse experiment and therefore it is close to impossible to correct for photobleaching. Consequently, it is important to choose photostable fluorescent proteins, enabling FRET imaging with little photobleaching.

The photostability of fluorescent proteins is only poorly understood. The photostability differs even between fluorescent proteins with very similar optical properties (Goedhart et al., 2012; Shaner et al., 2008). The β -barrel around the chromophore protects the chromophore against oxidative damage so perhaps slight changes in the β -barrel architecture account for these differences (Cody et al., 1993; Cubitt et al., 1995; Greenbaum et al., 2000; Swaminathan et al., 1997). Recently, it was reported that many fluorescent proteins show supralinear photobleaching (Cranfill et al., 2016). Consequently, if the excitation light power doubles, the photobleaching rate increases with a factor of more than two (Cranfill et al., 2016). Therefore, photostability depends on the illumination power this should be taken into consideration when choosing fluorescent proteins for a FRET pair. In addition, photochromic behavior and photoconversion can also drastically change the intensity of a fluorophore over time and therefore should be evaluated as well (Bindels et al., 2017; Goedhart et al., 2007).

The photostability of fluorescent proteins is usually determined at the excitation wavelength that is close to the absorbance maximum (Cranfill et al., 2016; Shaner et al., 2008). However, in FRET experiments, either FLIM or ratio-imaging, FRET acceptors are usually excited far from their absorbance maximum. In addition, they receive



energy from the excited donor. Exactly, how these different modes and wavelengths of excitation affect the photostability or photoconversion of acceptor fluorophores, and consequently the FRET pair, has not been thoroughly investigated.

At the moment cyan fluorescent protein (CFP) or teal fluorescent protein (TFP) combined with yellow fluorescent protein (YFP) is the most frequently used as FRET pair in biosensors (Adjobo-Hermans et al., 2011; Fritz et al., 2013; Klarenbeek et al., 2015; Nagai et al., 2004). The CFP variant mTurquoise2 is an attractive FRET donor because of its high quantum yield (of 93%), monomeric behavior and good photostability (Cranfill et al., 2016; Goedhart et al., 2012). As for acceptors, optimized variants of YFP: mCitrine, mVenus, YPet and SYFP2 (mVenus-L68V), are reported (Griesbeck et al., 2001; Kremers et al., 2006; Nagai et al., 2002; Nguyen and Daugherty, 2005). These YFPs exhibit a high extinction coefficient, optimized folding, a large spectral overlap with the emission spectrum of mTurquoise2 and a good quantum yield. However, current YFPs lack photostability and pH-stability. In addition, acceptors that provide an even higher FRET efficiency might yield biosensors that have improved contrast. Therefore, in this study, we evaluated the properties of a diverse set of acceptor proteins in combination with mTurquoise2 as donor.

Many studies have reported improvements of FRET sensors by changing the distance between the fluorescent proteins, varying linker length (Komatsu et al., 2011; Peroza et al., 2015; Shimozono and Miyawaki, 2008) and/or composition (Schifferer and Griesbeck, 2012) or changing the relative orientation of the fluorescent proteins by using circularly permuted fluorescent protein variants (Fritz et al., 2013; Nagai et al., 2004). Recently, it was reported that even the order of fluorescent proteins in a sensor alters its dynamic range (Ohta et al., 2016).

Here, we aspired to examine which of the current bright fluorescent proteins would have favorable properties for FRET-based imaging, not taking into account linkers and relative orientation. To this end, we evaluated the FRET efficiencies of FRET pairs consisting of mTurquoise2 as donor and acceptors varying from green to far-red. The Förster distance was determined for every pair, followed by experimental determination of FRET efficiencies of tandem fluorescent protein constructs in living cells. The FRET efficiencies were determined by fluorescence lifetime imaging (FLIM) and spectral imaging microscopy of tandem fusions. In addition, the photostability under FRET conditions was determined. The most promising pairs were applied in a FRET based biosensor for heterotrimeric G-protein activation.

Results

Absorption and emission spectra of purified fluorescent proteins

Due to the long emission tail of mTurquoise2, fluorescent proteins red-shifted relative to mTurquoise2 are potentially efficient FRET acceptors. We selected a number of promising acceptor candidates based on two criteria: (i) reported monomeric, (ii) bright in their spectral class. The list of selected proteins covers the visible spectrum, with fluorescent protein emission colors ranging from green to far-red. To judge the theoretical quality of the FRET pairs, we determined the Förster radius (R_0) (Goedhart et al., 2007; Wu and Brand, 1994).

In order to do so, we purified a selection of fluorescent proteins and determined the absorbance and emission spectra. The absorbance and emission spectra of the proteins employed in this study are depicted in figure 1 and the spectral data is published elsewhere (<http://doi.org/10.5281/zenodo.580169>). We note that the absorbance spectra of all the fluorescent proteins, even the most red-shifted variant, mKate2, overlap with the emission of mTurquoise2.

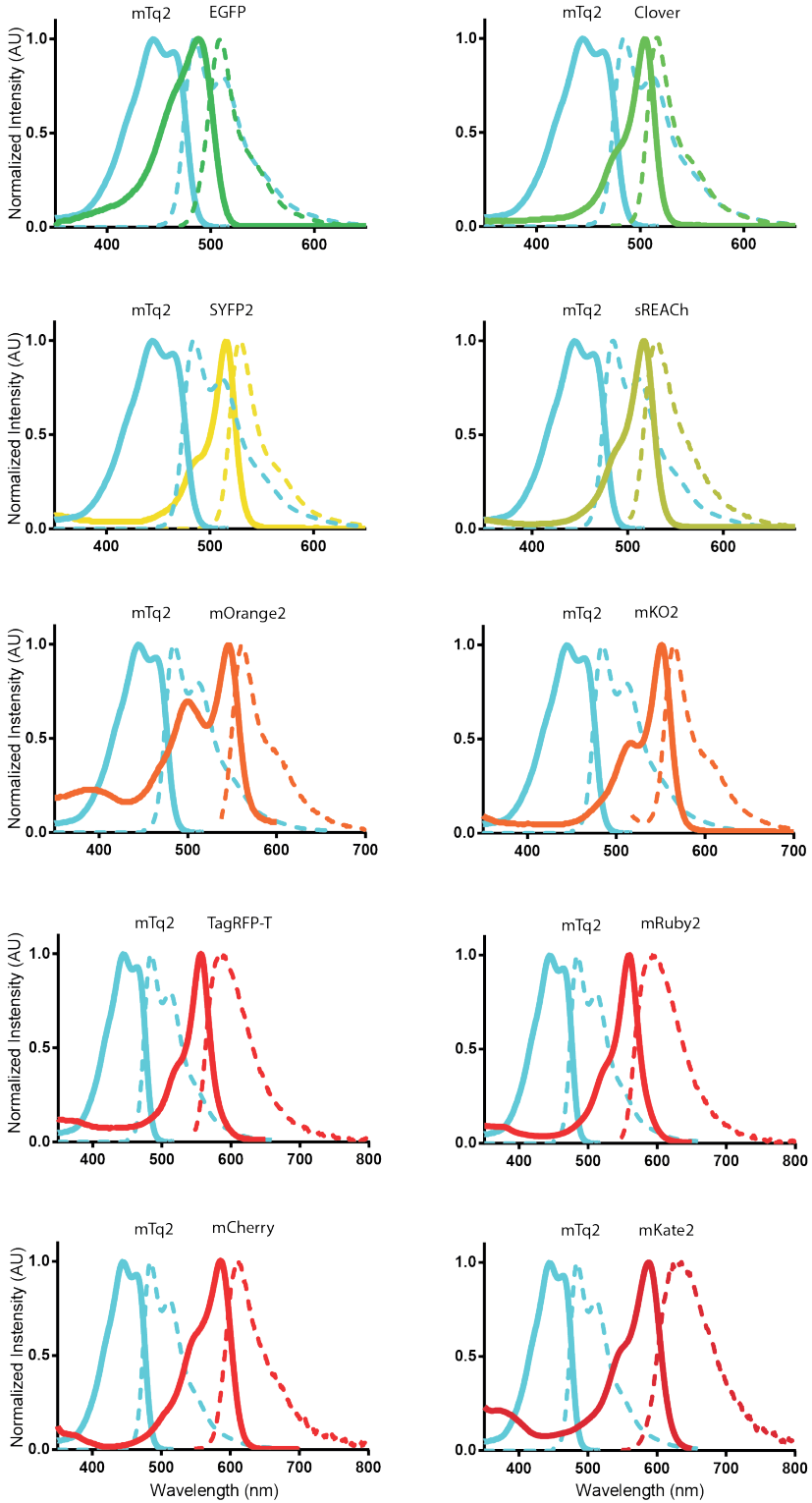
Next, we determined the overlap integral, $J(\lambda)$, for mTq2 emission with the absorbance, based on the spectra that we acquired, the quantum yield of the donor ($QY_D = 0.93$) and the published extinction coefficient of the acceptors (table 1). The overlap integral was used to calculate the Förster radius R_0 , assuming a refractive index (n) of 1.33 and κ^2 of 2/3 (Goedhart et al., 2007; Wu and Brand, 1994). Of note, n and κ^2 are usually unknown in cells, but alternative R_0 values can be calculated if n and κ^2 are known from the reported overlap integral.

The calculated R_0 values show a declining trend when the absorbance peak shifts to the red part of the spectrum. The standard cyan-yellow pair has a R_0 of 59Å. In theory, the best green acceptor is mNeonGreen with a R_0 of 62Å. The orange and red fluorescing fluorescent proteins with the highest R_0 values are mKOK, mOrange and mRuby2 with a value of 58Å.

In summary, from the Förster radii it can be concluded that the selected fluorescent proteins are promising as FRET acceptors.



Characterization of a spectrally diverse set of fluorescent proteins as FRET acceptors for mTurquoise2



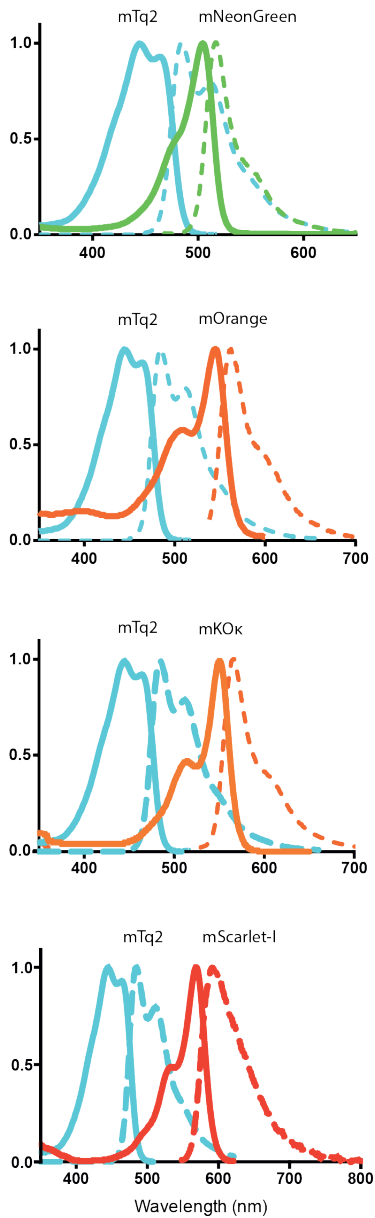


Figure 1. Absorption and emission spectra of the FRET pairs investigated in this study. The spectra were recorded from purified proteins and were normalized to their peak values. Solid lines indicate absorption spectra and dashed lines indicate emission spectra. All lines are colored according to the emission wavelength of the fluorescent protein. All spectra show the donor mTurquoise2 (mTq2) and the indicated acceptor. Data available at <http://doi.org/10.5281/zenodo.580169>.



Table 1. Spectroscopic parameters of fluorescent proteins employed in this study as acceptor for mTurquoise2. The overlap integral was determined from spectra acquired in this study and extinction coefficients taken from literature. The Förster radius was calculated from $J(\lambda)$ and quantum yield of the donor ($QY_D=0.93$, $n=1.33$ and $k^2 = 2/3$).

FRET Acceptor	Absorption peak (nm)	Molar extinction coefficient ($M^{-1}cm^{-1}$)	$J(\lambda)*10^{15} M^{-1} cm^{-1} nm^4$	QY_A	R_0 (Å)
EGFP	488	55000 (Patterson et al., 1997)	1.53	0.6 (Patterson et al., 1997)	55
Clover	505	111000 (Lam et al., 2012)	2.7	0.76 (Lam et al., 2012)	60
mNeonGreen	505	116000 (Shaner et al., 2013)	3.15	0.8 (Shaner et al., 2013)	62
SYFP2	515	101000 (Kremers et al., 2006)	2.31	0.68 (Kremers et al., 2006)	59
sREACH	517	100000 (Ganesan et al., 2006; Murakoshi et al., 2008)	2.53	-	59
mOrange	548	71000 (Shaner et al., 2004)	2.19	0.69 (Shaner et al., 2004)	58
mOrange2	549	58000 (Shaner et al., 2008)	2.05	0.60 (Shaner et al., 2008)	57
mKO2	551	63800 (Sakaue-Sawano et al., 2008)	1.44	0.57 (Sakaue-Sawano et al., 2008)	54
mKOok	551	105000 (Tsutsui et al., 2008)	2.08	0.61 (Tsutsui et al., 2008)	58
TagRFP-T	557	81000 (Shaner et al., 2008)	1.62	0.41 (Shaner et al., 2008)	55
mRuby2	560	113000 (Lam et al., 2012)	2.12	0.38 (Lam et al., 2012)	58
mScarlet-I	569	102000 (Bindels et al., 2017)	1.84	0.54 (Bindels et al., 2017)	56
mCherry	587	72000 (Shaner et al., 2004)	1.24	0.22 (Shaner et al., 2004)	53
mKate2	588	62500 (Shcherbo et al., 2009)	1.15	0.40 (Shcherbo et al., 2009)	52

Fluorescence lifetime analysis of FRET pairs

The R_0 values can be used as a theoretical measure for the quality of a FRET pair. However, it is important to evaluate the FRET pairs experimentally *in cyto*, to reveal cellular parameters that affect the FRET efficiency. To judge the quality of the FRET acceptors in cells, we constructed plasmids encoding fusion proteins incorporating mTurquoise2 as the donor and one of the candidate fluorescent proteins as the acceptor (figure 2).

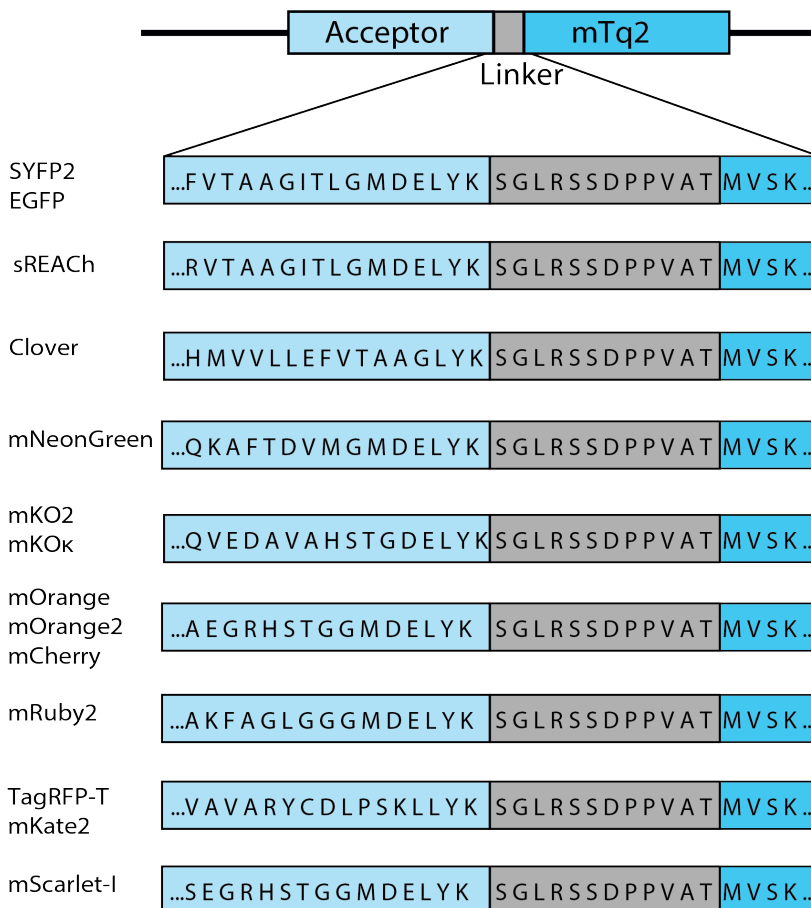


Figure 2. Schematic overview of the fusion constructs used in this study.

The differences in the amino acid sequence of the C-termini of the acceptor fluorescent proteins are depicted. The size of the acceptors is 158 amino acids for mKO2 and mKOκ, 163 amino acids for mOrange, mOrange2, mScarlet-I and mCherry, 164 amino acids for Clover, 166 amino acids for mNeonGreen, TagRFP-T and mKate2, 168 amino acids for mRuby2 and 171 amino acids for EGFP, SYFP2 and sREACH. The acceptors are followed by a small linker, which is the same for each construct, separating it from the donor mTurquoise2 (mTq2).

These plasmids were transfected in mammalian cells and fluorescence lifetime imaging microscopy (FLIM) was performed. In order to calculate the FRET efficiency, the donor lifetimes of cells in FRET and non-FRET conditions were measured. We used cells expressing untagged mTurquoise2 as non-FRET condition. These show a donor phase lifetime of 3.8ns, as reported before (Goedhart et al., 2012). The fusion constructs are used for FLIM measurements in FRET condition. All FRET pairs show a decrease in donor lifetime compared to untagged mTurquoise2 indicating that FRET occurred. For



a complete overview of phase and modulation lifetime values and the FRET efficiency based on lifetime see table 2. We focused on the FRET efficiencies based on phase lifetime rather than modulation lifetime, because it shows a higher dynamic range meaning that differences in FRET efficiency will be more noticeable (Goedhart et al., 2007). The phase lifetimes are graphically depicted in figure 3. From figure 3, it can be inferred that mNeonGreen shows the largest reduction in fluorescence lifetime and consequently the highest FRET efficiency *in cyto*. The other yellow-green acceptor fluorescent proteins, including the non-emitting variant sREACH, display lifetimes similar to the standard mTurquoise2-SYFP2 pair. As can be appreciated from figure 3, SYFP2 shows high cell-to-cell variation compared to the other green and yellow acceptors. Among the orange acceptors, mKOκ shows the largest lifetime change, whereas mOrange and mOrange2 show only moderate changes in fluorescence lifetime and also display quite some cell-to-cell variability. The tandems that comprise red acceptors display similar lifetime reductions, with mRuby2 as the most efficient FRET acceptor. In summary, mNeonGreen shows the highest FRET efficiency and mKOκ stands out amongst the orange acceptors.

Table 2. Fluorescence lifetime data of mTurquoise2 as FRET donor in a tandem construct with the different FRET acceptors and corresponding FRET efficiency (figure 3).

Acceptor	n ¹	τ_{ϕ} (ns) ²	τ_M (ns) ³	$E_{\tau_{\phi}}$ (%) ⁴	E_{τ_M} (%) ⁴
-	89	3.77 ±0.01	4.01 ±0.01	-	-
EGFP	26	2.60 ±0.01	3.21 ±0.01	31 ±0.26	20 ±0.21
Clover	18	2.59 ±0.02	3.28 ±0.02	31 ±0.60	18 ±0.62
mNeonGreen	14	2.02 ±0.01	2.70 ±0.01	46 ±0.33	33 ±0.21
SYFP2	72	2.59 ±0.02	3.16 ±0.02	31 ±0.57	21 ±0.48
sREACH	27	2.53 ±0.01	3.13 ±0.01	33 ±0.26	22 ±0.20
mOrange	21	3.13 ±0.03	3.63 ±0.03	17 ±0.92	9 ±0.76
mOrange2	27	3.10 ±0.04	3.61 ±0.02	18 ±0.99	10 ±0.61
mKO2	17	2.59 ±0.02	3.11 ±0.02	31 ±0.52	22 ±0.44
mKOκ	17	2.31 ±0.01	2.77 ±0.01	39 ±0.42	31 ±0.28
TagRFP-T	20	2.70 ±0.02	3.15 ±0.02	28 ±0.62	22 ±0.44
mRuby2	17	2.63 ±0.02	3.30 ±0.02	30 ±0.45	18 ±0.45
mScarlet-l	30	2.67 ±0.02	3.21 ±0.01	29 ±0.64	15 ±0.37
mCherry	24	2.83 ±0.02	3.26 ±0.01	25 ±0.42	19 ±0.19
mKate2	22	2.74 ±0.01	3.23 ±0.02	27 ±0.42	19 ±0.40

¹n is number of cells used for lifetime determination, ² τ_{ϕ} average phase lifetime ± SEM, ³ τ_M average modulation lifetime ± SEM, ⁴E is average FRET efficiency calculated from the change in τ_{ϕ} or τ_M ± SEM.

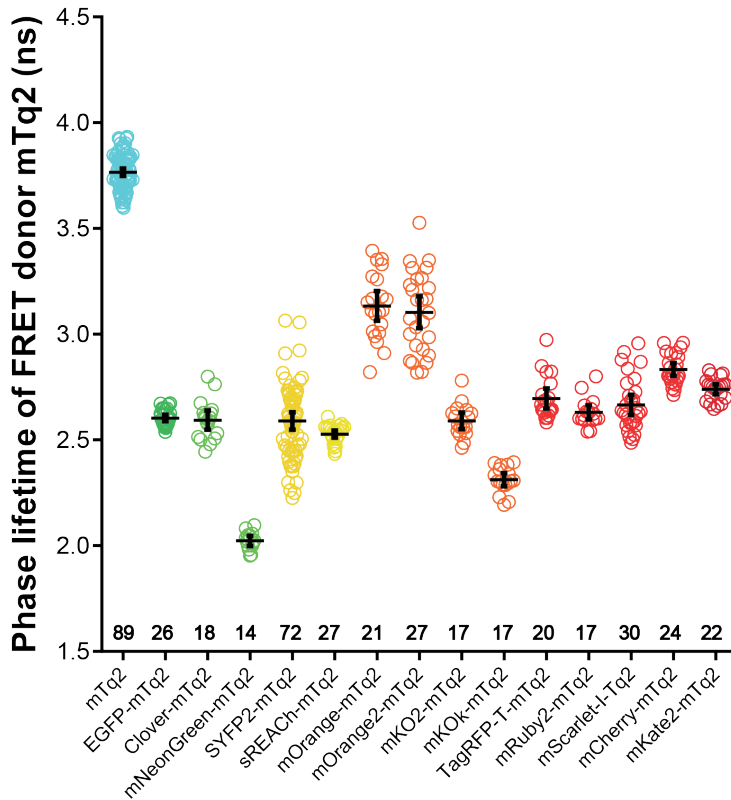


Figure 3. Fluorescence lifetime of the FRET donor mTurquoise2 fused to different FRET acceptors.

The phase lifetime of mTurquoise2 (mTq2) when paired with different acceptors is depicted. As a reference the lifetime of untagged mTurquoise2 is shown. The dots indicate individual cells and the error bars show 95% confidence intervals. The number of cells imaged is mTq2 n=89, EGFP n=26, Clover n=18, mNeonGreen n=14, SYFP2 n=72, sREACH n=27, mOrange n=21, mOrange2 n=27, mKO2 n=17, mKO2 n=17, TagRFP-T n=20, mRuby2 n=17, mScarlet-I n=30, mCherry n=24, mKate2 n=22.

Spectral imaging of FRET pairs

The FLIM data of FRET pairs gives insight in the importance of spectral overlap and extinction coefficient of the acceptor, while the quantum yield of the acceptor does not matter in FLIM measurements. Most of the currently applied biosensors are, however, analyzed by ratiometric imaging which relies, besides donor quenching, on sensitized emission (Goedhart et al., 2014; Piston and Kremers, 2007). The sensitized emission depends on the FRET efficiency (spectral overlap and extinction coefficient) and the quantum yield of the acceptor. A higher sensitized emission results in a better contrast in ratiometric FRET imaging. To examine the amount of sensitized emission for each FRET pair, we acquired spectral images of single cells producing fusion proteins



(figure 4). Corrected spectra were obtained by correcting for spectral sensitivity (tail of long-pass (LP) filter and camera). From these data, we isolated the pure sensitized emission component by unmixing the donor spectrum and the amount of direct acceptor excitation (figure 4).

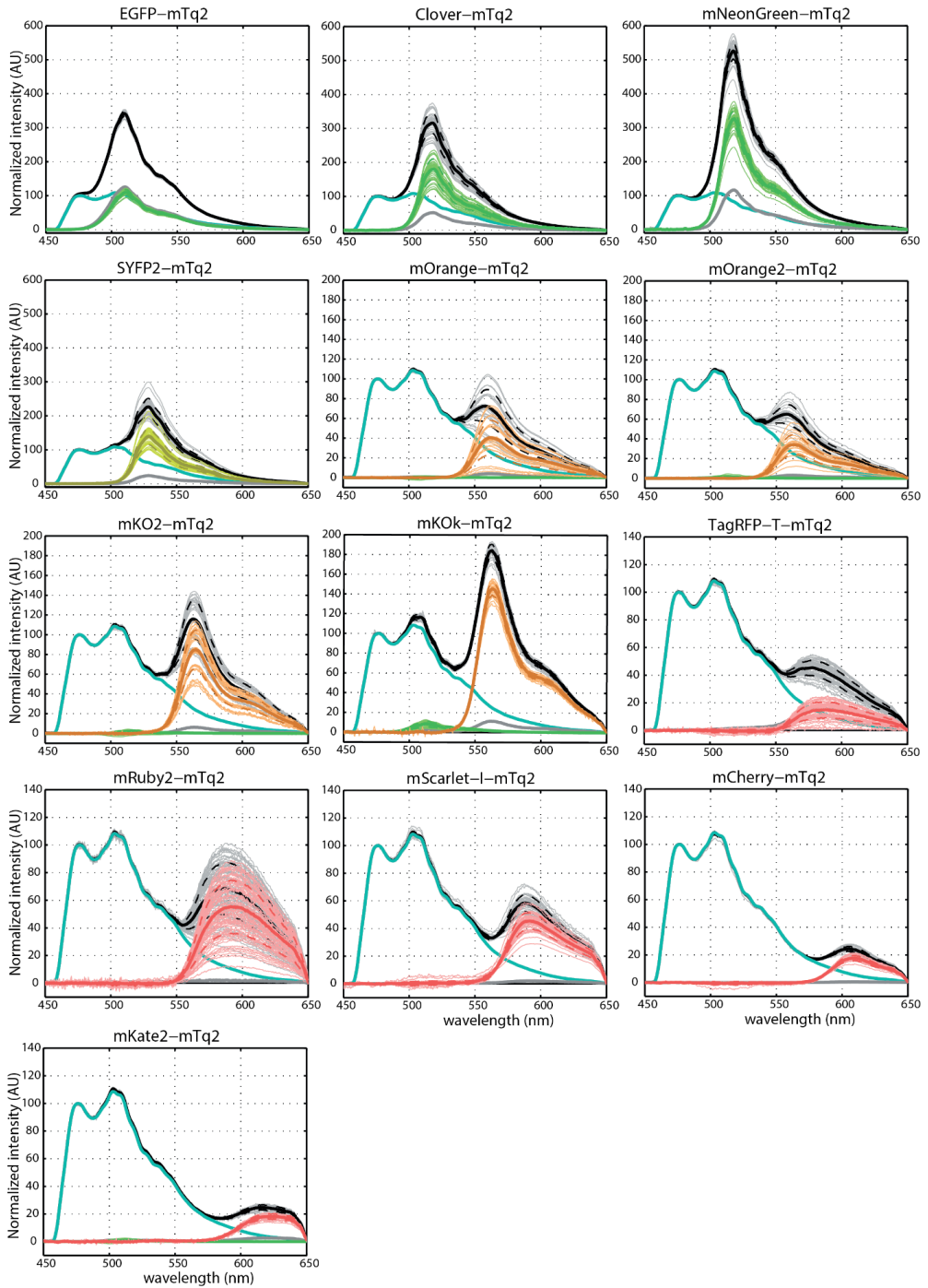
As can be inferred from figure 4, there is a large variation in the amount of sensitized emission between the fusion proteins. Overall, the strongest sensitized emission signal is observed for the fusion with mNeonGreen. In the orange spectral class, the fusion with mKOκ shows the highest level of sensitized emission and in the red spectral class, we observed relatively high sensitized emission for the fusions with mRuby2 and mScarlet-I. We also note that the cell-to-cell variation differs between FRET pairs. For instance, there is enormous variation between cells in the amount of sensitized emission for the FRET pair with mRuby2. In contrast the amount of sensitized emission for the FRET pair with mScarlet-I is well-defined.

The differences among the FRET pairs with orange fluorescent proteins were striking. The FRET pair with mKOκ showed much stronger sensitized emission than mKO2 which is surprising given the single amino acid difference. In addition, the modest sensitized emission for FRET pairs with mOrange and mOrange2 is unexpected given their high intrinsic brightness (Shaner et al., 2004; Shaner et al., 2008). Based on the spectral imaging and FLIM data, we do not consider mOrange(2) as promising FRET acceptors for mTurquoise2.

To further examine the properties of the orange fluorescent proteins, we determined their brightness in cells. We used a previously established assay that measures the fluorescence of transfected cells relative to a quantitatively co-expressed control, in this case mTurquoise2 (Goedhart et al., 2012). The results show that the brightness in cells is in the order mKOκ > mKO2 = mOrange > mOrange2 (supplemental figure S1), showing that mKOκ is by far the brightest orange fluorescent protein in cells.

> Figure 4. Spectral images of the FRET donor mTurquoise2 fused to different FRET acceptors.

The emission spectra of FRET pairs were recorded from single living cells. The sensitized emission component was calculated by unmixing the donor spectrum and the direct acceptor excitation. Black lines represent the FRET-pair spectra. Cyan lines represent the donor emission spectra. Grey lines represent direct acceptor excitation spectra. If orange or red fluorescent proteins show an evident green component, this is represented by a green line. Lines in color of the acceptor emission represent the unmixed sensitized emission. Thick lines show the average emission spectrum, dashed lines represent the standard deviations and thin lines show individual measurements. Based on these data the FRET efficiency was calculated (table 3). The number of cells imaged is EGFP n=37, Clover n=36, mNeonGreen n=46, SYFP2 n=39, mOrange n=24, mOrange2 n=22, mKO2 n=35, mKOκ n=24, TagRFP-T n=50, mRuby2 n=66, mScarlet-I n=47, mCherry n=28, mKate2 n=27.





The data depicted in figure 4 was used to calculate the FRET efficiency based on the assumption that every photon emitted by the acceptor stems from a quenched donor photon (see materials and methods). The FRET efficiency value for each FRET pair is listed in table 3. The mTurquoise2-SYFP2 pair showed a FRET efficiency of 42%, in line with the FLIM results. The pair with mNeonGreen as acceptor showed the highest FRET efficiency of 59%, with little cell-to-cell variation. The pair with mKOκ shows a relatively high FRET efficiency of 47%. The FRET pair with mRuby2 shows a high FRET efficiency of 43% but this is accompanied by substantial cell-to-cell variability. The FRET efficiency of FRET pairs with mScarlet-I and mCherry is comparable with values of 34% and 32% respectively. Based on the spectral imaging data and R_0 values, we prepared an animation of the spectral changes that occur as function of distance for the mTurquoise2-SYFP2 and –mNeonGreen pair (supplemental movie S1) and the mTurquoise2-mCherry and –mScarlet-I pair (supplemental movie S2).

In summary, the FRET efficiencies calculated from the spectral imaging data are corresponding to the FRET efficiencies calculated from the FLIM data. mNeonGreen shows the highest FRET efficiency and a dominant sensitized emission peak. mKOκ shows the highest FRET efficiency and sensitized emission peak of the orange variants. The TagRFP-T and mRuby2 show high cell-to-cell variability. In contrast, mScarlet-I and mCherry show little variation and mScarlet-I shows a higher amount of sensitized emission than mCherry which is explained by the higher quantum yield of mScarlet-I.

Table 3. FRET efficiencies of mTurquoise2 paired with the different acceptors, calculated from spectral imaging results (Figure 4).

Acceptor	Number of cells	FRET efficiency (%) ¹
EGFP	37	44 ±0.3
Clover	36	47 ±0.7
mNeonGreen	46	59 ±0.3
SYFP2	39	42 ±0.7
mOrange	24	20 ±1.5
mOrange2	22	21 ±1.0
mKO2	34	35 ±0.9
mKOκ	24	47 ±0.2
TagRFP-T	50	17 ±0.8
mRuby2	66	43 ±1.2
mScarlet-I	47	34 ±0.4
mCherry	28	32 ±0.4
mKate2	27	28 ±0.4

¹E is the average FRET efficiency ± SEM

Based on the FLIM and spectral imaging data shown in the previous two paragraphs a selection was made of the most promising FRET acceptors. This selection includes mNeonGreen, mKO_k, mRuby2 and mScarlet-I, with as reference commonly used acceptors SYFP2 and mCherry. Since mKate2 showed a substantial reduction of the mTurquoise2 lifetime and moderate sensitized emission in the spectral imaging experiments, mKate2 was included as well.

Photostability of FRET pairs

Photostability is a crucial parameter for the reliable and robust detection of FRET, especially in timelapse imaging. We evaluated the photostability of a selection of fusions with mTurquoise2 that was made based on FRET efficiency. In order to stay close to the purpose of the fluorescent proteins as acceptor in FRET experiments we used the fusion constructs and bleached them under the conditions that are normally used for recording ratiometric FRET data. To determine photostability we continuously excited the donor, while alternatingly measuring donor emission and acceptor emission. The only difference compared to recording FRET data of biosensors is that the photostability measurements are done under continuous illumination instead of 200ms exposure per frame and for a longer duration than usual FRET measurements. The photostability curves for the fusion constructs are depicted in figure 5 and supplemental figure S2. Under these conditions unfused, unquenched mTurquoise2 shows a decrease in intensity over time (Goedhart et al., 2012). For the tandem fusions, an increase in the CFP channel is observed, which is accompanied by a decrease of acceptor fluorescence. These observations indicate acceptor bleaching, either by FRET or direct excitation, resulting in dequenching of the donor due to diminished FRET.

mNeonGreen and SYFP2 are bleached in a similar fashion after 900s continuous illumination, but mNeonGreen bleaches in a more linear fashion while SYFP2 bleaches more rapidly at the start of the experiment. When performing a typical FRET experiment, corresponding to a total exposure time of 48s (240 images of 200ms exposure time) (van Unen et al., 2016b), mNeonGreen would be more photostable than SYFP2 (supplemental figure S3). In line with a previous report (Klarenbeek et al., 2015), we observed good photostability of the mTurquoise2-sREACH pair (supplemental figure S2).

A striking result is the fast bleaching of mKO_k under our conditions. After 48 seconds, which equals a typical FRET measurement, 79% of the initial intensity is left (supplemental figure S3). These results are in line with a previous observation that the related mKO can be photoconverted to a green species by blue light (Goedhart et al., 2007). When directly exciting mKO_k with 570nm light, instead of 420nm, the fluorescent protein is rather photostable (83% of initial intensity left after 900s continuous illumination), and outperforms mKO2 (supplemental figure S4).



Characterization of a spectrally diverse set of fluorescent proteins as FRET acceptors for mTurquoise2

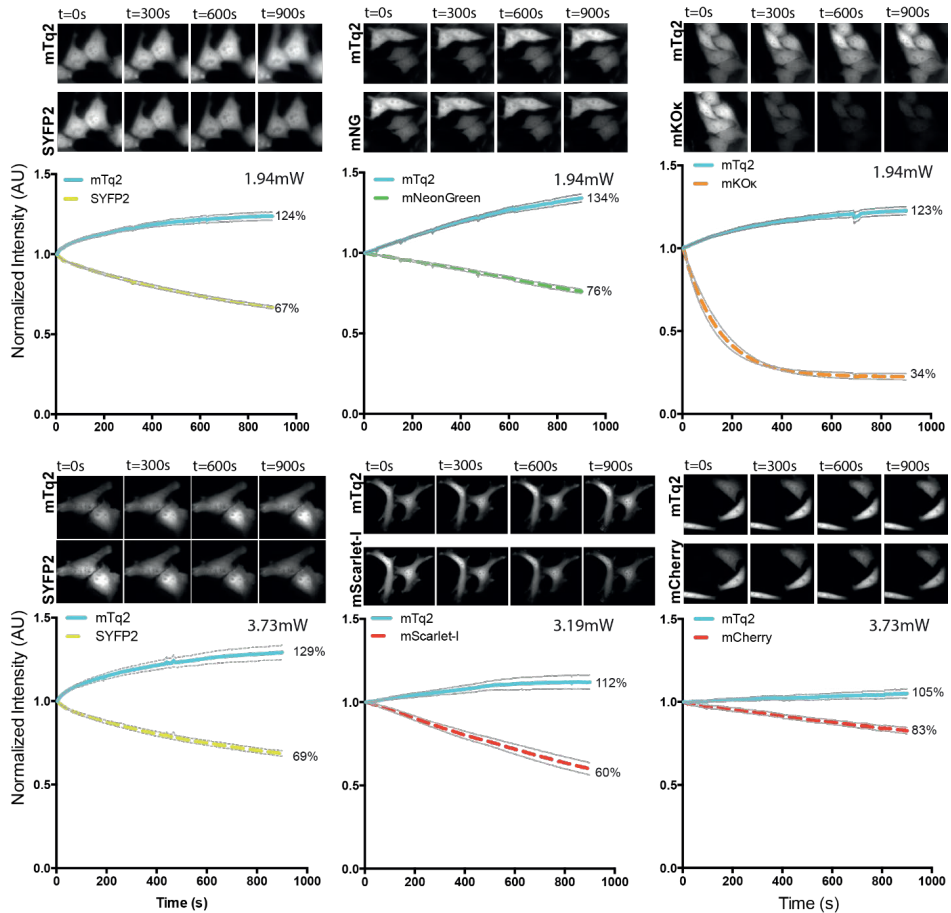


Figure 5. Photostability of tandem pairs during ratiometric FRET measurements.

Fusion constructs of mTurquoise2 and acceptor fluorescent protein were used in this experiment. The power is shown in the graphs. The thin lines display the 95% confidence intervals. The photostability of the fusion constructs is shown under continuous illumination with 420nm light for 900s. Images of cells after 0s, 300s, 600s and 900s illumination show the fluorescence intensity. The width of the images are 58.14µm for SYFP2-mTurquoise2 (1.94mW), 87.21µm for mNeonGreen-mTurquoise2, 80.07µm for mKOK-mTurquoise2, 116.28µm for SYFP2-mTurquoise2 (3.73mW), 147.56µm for mScarlet-l-mTurquoise2 and 116.28µm for mCherry-mTurquoise2. For the graph the initial fluorescence intensity was set on 100% and it is stated what percentage of the initial fluorescence is left after 900s illumination. The number of cells imaged is: SYFP2-mTq2 (1.94mW) $n=23$; mNeonGreen-mTq2 $n=21$; mKOK-mTq2 $n=15$; SYFP2-mTq2 (3.73mW) $n=23$; mScarlet-l-mTq2 $n=11$; mCherry-mTq2 $n=15$.

mRuby2 shows relatively slow and linear bleaching and after 900s 55% of the initial intensity is left, which is comparable to the photostability of mTurquoise2-SYFP2 with the same excitation power (supplemental figure S2). mKate2 is less photostable than

mCherry after 900s of continuous illumination (supplemental figure S2). From figure 5, it can be inferred that the photostability of mScarlet-I is lower than that of mCherry under FRET imaging conditions. Still, under typical conditions for a dynamic FRET experiment (supplemental figure S3), the mScarlet-I hardly loses its intensity.

Recently, a more photostable YFP was reported, generated by one mutation resulting in Y145L (Bogdanov et al., 2016). We mutated SYFP2 and confirmed highly improved photostability (supplemental figure S5). However, next to the reported reduction in brightness, the mTurquoise2-SYFP2(Y145L) pair shows hardly any FRET as compared to the mTurquoise2-SYFP2 pair (supplemental figure S5).

In summary, mNeonGreen is a relatively photostable acceptor under FRET ratio-imaging conditions. mKOok bleaches rapidly when illuminated with 420nm light and is therefore unfit as FRET acceptor for timelapse imaging.

Emission ratio-imaging with novel biosensors to measure heterotrimeric G-protein activation

We used a well-characterized FRET biosensor that measures heterotrimeric G-protein activation to examine how the selection of FRET pairs would perform in terms of dynamic range (Adjobo-Hermans et al., 2011; Goedhart et al., 2011; van Unen et al., 2016b). Since it is of importance to use only monomeric fluorescent proteins for our multimeric membrane located biosensor we evaluated oligomerization by the OSER assay (Costantini et al., 2012).

The OSER assay is based on a fusion with the CytERM signal sequence. Monomeric FPs will show ER localization in this assay, whereas non-monomeric proteins will show OSER structures.

A recent thorough OSER analysis of fluorescent proteins that was published during the course of our experiments (Cranfill et al., 2016), fits largely with our observations. The notable exception is mRuby2, which in our hands shows predominant localization at the Golgi when it is fused to the ER-localization signal, CytERM as shown in supplemental figure S6. This observation is documented in more detail recently (Bindels et al., 2017). Since the OSER assay reveals aberrant localization, we decided to exclude mRuby2 as acceptor.

The original FRET sensor consists of three subunits that are co-expressed from a single plasmid, including a Gα tagged with mTurquoise, an untagged Gβ subunit and a Gγ tagged with acceptor (Goedhart et al., 2011). We modified this plasmid in several ways. First, we replaced mTurquoise by mTurquoise2. The second modification is the removal of the untagged Gβ which turned out to be non-essential (supplemental figure S7). Finally, the Gγ subunit was tagged with the acceptors SYFP2, mNeonGreen, mScarlet-I



and mCherry. The resulting plasmid encoded Acceptor-Gy-IRES-Gaq-mTurquoise2. The localization of the sensor with different acceptor fluorescent proteins is shown in supplemental figure S8.

To examine the FRET response upon activation, we co-expressed the histamine-1 receptor (H1R), which activates the heterotrimeric G-protein, resulting in a loss of FRET. The response is de-activated with the H1R antagonist pyrilamine. As can be inferred from figure 6, the activation of the H1R results in a loss of FRET as inferred

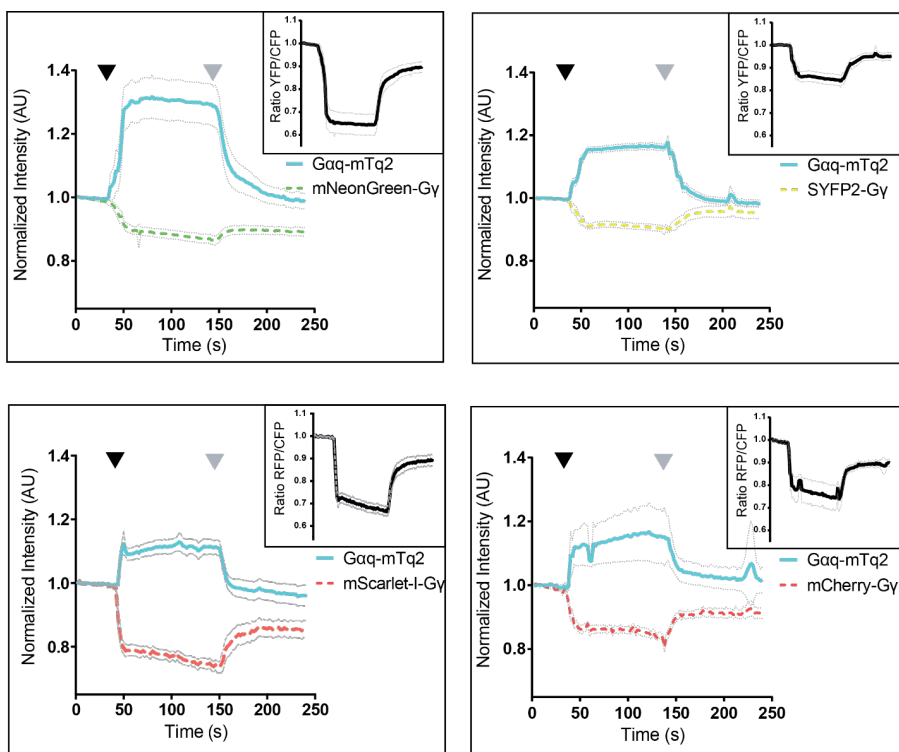


Figure 6. Ratiometric FRET imaging of Gq-activation biosensors equipped with novel FRET pairs.

FRET ratio-imaging was performed on HeLa cells over-expressing the histamine-1 receptor and a FRET biosensor for Gq activation. The blue, solid lines show the mTurquoise2 fluorescence intensity over time, the dashed lines show the acceptor emission level over time. The initial fluorescence intensity is normalized to the average intensity of the first 5 frames. The black graph in a separate upper right window shows the FRET ratio over time. The thin lines indicate the 95% confidence intervals. 100 μ M histamine was added after 42-50s (black arrowhead) and 10 μ M pyrilamine was added after 140-150s (grey arrowhead).

The number of cells analysed is: Gqsensor-mTq2-mNeonGreen $n=32$ (out of 34 in total), Gqsensor-mTq2-SYFP2 $n=42$ (out of 44 in total), Gqsensor-mTq2-mScarlet-I $n=24$ (out of 26 in total) and Gqsensor-mTq2-mCherry $n=19$ (out of 26 in total)

from a donor increase and a concomitant acceptor intensity decrease. The sensor with mNeonGreen excels compared to the other acceptors with an increase in donor intensity of up to 30%, when the G α subunit is activated, while the sensor with SYFP2 showed an increase of approximately 16%. From the acceptor/donor ratio traces it can be concluded that the dynamic range of the sensor with mNeonGreen is higher than that of sensor with SYFP2.

The same sensor with mCherry as acceptor showed a robust change in FRET. Strikingly, the change in both CFP and RFP fluorescence resulted in a similar dynamic range compared with that of the CFP-YFP variant. The G α sensor that employs mScarlet-1 as the acceptor, shows a more robust decrease of the RFP signal, resulting in a higher dynamic range than the mCherry variant.

Often, ratiometric measurements are corrected for CFP bleed-through in the acceptor channel. This is straightforward for the CFP-YFP pair, since the YFP emission is absent in the CFP channel. However, whether this is true for other combinations is unknown. Since chromophore formation of RFP requires several reactions possibly resulting in a fraction of blue or green emitting structures, we expressed RFPs and measured their emission spectra (supplemental figure S9). We noted different extents of blue/green emission when the RFPs were excited at 436nm, showing that bleedthrough-correction for CFP-RFP pairs is not straightforward. Our data shows that full filter FRET analysis, as reported previously (Bindels et al., 2017), is required to calculate the amount of sensitized emission. In summary, employing mNeonGreen as acceptor in the ratiometric FRET sensor for G α activation yields an improvement of the dynamic range compared to YFP.

Fluorescence lifetime analysis of heterotrimeric G-protein activation

Since our FLIM analysis showed that sREACH is an efficient FRET acceptor, we evaluated the performance of the G-protein biosensor for FLIM. To this end we constructed a sensor with sREACH as the acceptor. Next, we repeated the GPCR activation/deactivation experiment for sensors incorporating mNeonGreen, SYFP2 or sREACH based sensors with FLIM (figure 7).

The initial lifetime values differed between the three sensors, reflecting a difference in the initial FRET efficiency. Still, all three sensors showed a robust increase in lifetime upon GPCR stimulation, which agrees with the dequenching of the donor observed by ratio-imaging. The increase in lifetime observed for the sensor with sREACH of about 0.2ns is in line with previous data (Raspe et al., 2016). Addition of pyrilamine, which switches the receptor off, results in a decrease in donor lifetime.

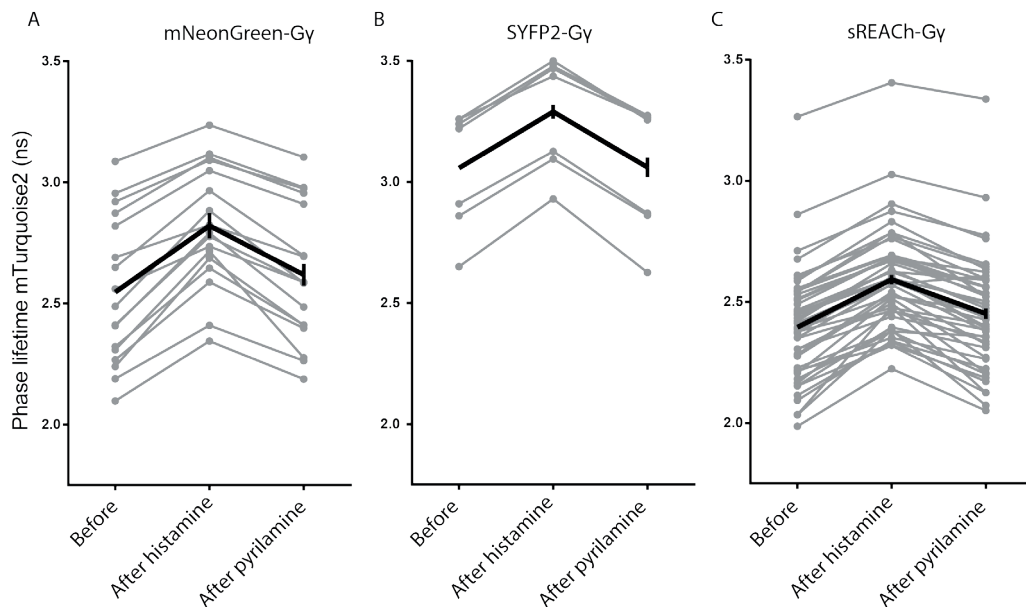


Figure 7. FIIM-FRET of Gq activation biosensors equipped with novel FRET pairs.

The fluorescence lifetime of mTurquoise2 was recorded from the biosensor for Gq activation containing mNeonGreen, SYFP2 or sREACH as FRET acceptor. The phase lifetime was recorded before addition of (ant)agonist, 20-60s after addition of 100 μ M histamine and 20-60s after addition of 10 μ M pyrilamine. The changes in phase lifetime are shown in the graphs. The grey lines represent individual cells and the black graph represents the average of which the error bars indicate the 95% confidence intervals. The number of cells used for the graph is for mNeonGreen as FRET acceptor $n=17$ (out of a total of 26 cells), for SYFP2 as FRET acceptor $n=7$ (out of a total of 23 cells) and for sREACH as FRET acceptor $n=46$ (out of a total of 60 cells).

The donor lifetime after addition of pyrilamine is similar to the lifetime observed at the start of the experiment, suggesting that the deactivation of the receptor is complete. This is in agreement with the ratio-imaging data (figure 6). Together, these results show that both sREACH and mNeonGreen are suitable acceptors for FLIM in combination with mTurquoise2.

Discussion

In this study, we have evaluated the performance of FRET pairs consisting of mTurquoise2 as donor and acceptors varying from green to far-red in mammalian cells. In all our experiments the acceptor mNeonGreen consistently showed the highest FRET efficiency and dynamic range, accompanied by strong sensitized emission. This can be explained by the large spectral overlap, high extinction coefficient and

high quantum yield of mNeonGreen. It also implies that the maturation efficiency of mNeonGreen is high. Another beneficial feature of mNeonGreen is that it shows increased photostability under FRET conditions relative to SYFP2. However, since photostability is generally power-dependent (Cranfill et al., 2016), the photostability will differ when experimental conditions are different. We conclude that mTurquoise2-mNeonGreen is the optimal FRET pair for live cell imaging application in mammalian cells and we demonstrate that the mTurquoise2-mNeonGreen pair can be used to generate biosensors with high dynamic range and photostability.

The superior performance of mNeonGreen in FRET pairs with mTurquoise2 relative to Clover is surprising, given their equal spectroscopic properties (Cranfill et al., 2016). We did not analyze the performance of mClover3 (Bajar et al., 2016), which may be an improvement over Clover for FRET with mTurquoise2.

We compared the cellular brightness of Clover and mNeonGreen and did not find striking differences (supplemental figure S10). Next, to verify dimerization tendency of mNeonGreen, we performed an OSER assay. The results indicate that mNeonGreen shows no strong tendency to dimerize, in line with previous findings (Cranfill et al., 2016; Shaner et al., 2013). Therefore, the better performance of mNeonGreen may be explained by better maturation in the context of fusion proteins.

It is of note that the FRET efficiency may be cell-type and certainly will be organism dependent, since the protein maturation can vary in different systems. The set of fluorescent protein fusions, and accompanying controls that we have generated, provides a way to systematically determine the performance of FRET pairs in other biological contexts.

The detection of Gq activation with biosensors based on sREAcH or mNeonGreen using FLIM resulted in a similar contrast. Since the blue-shifted emission of mNeonGreen requires a narrow band-pass (BP) filter for exclusive detection of CFP fluorescence in FLIM, the donor emission intensity will be reduced (supplemental figure S11). Therefore, it may be more desirable to use the non-emitting acceptor sREAcH for FRET based biosensors that are dedicated for FLIM.

Although the properties of the mTurquoise2-mNeonGreen pair are favorable and we demonstrate good performance in an intermolecular FRET sensor, it remains to be determined whether this pair will beat the CFP-YFP or TFP-YFP pair in intramolecular biosensors. We have replaced YFP with mNeonGreen in two unimolecular sensors and have observed that the dynamic range of these sensors is not improved (supplemental figure S12). These preliminary studies suggest that in addition to probe properties, other factors such as linker length, weak *homo*-dimerization and probe orientation, determine FRET contrast. Optimization of unimolecular sensors with the mTurquoise2-



mNeonGreen pair will benefit from strategies that generate and screen a large number of different variants (Fritz et al., 2013; Thestrup et al., 2014). Perhaps circular permutation of mTurquoise2 and mNeonGreen would be a viable way to generate high-contrast intramolecular FRET biosensors.

Based on theory, i.e. R_0 values, all pairs should display considerable FRET efficiency, but this is not observed in cells for all pairs. We suspect that this is due to inefficient maturation of the acceptor fluorescent protein, affecting the FRET efficiency (Scott and Hoppe, 2015; Shaner et al., 2004). Additionally, slight differences in orientation between different acceptors due to small changes in acceptor fluorescent protein length and sequence might also influence the FRET efficiency (Jares-Erijman and Jovin, 2003; Shimozono et al., 2006).

Our photostability analysis of FRET pairs shows a donor increase due to photobleaching of the acceptor. This demonstrates the superior photostability of mTurquoise2 as compared to the employed acceptors. We did not pursue the origin of acceptor photobleaching, which is either due to direct excitation or due to FRET. Regardless of the mechanism, the kinetics of the donor intensity increase will depend on the FRET efficiency of the fluorescent protein pair. In dynamic FRET ratio-imaging, the FRET efficiency can change in time and space and effects of photobleaching will be difficult to correct for. Hence, it is essential for reliable FRET ratio-imaging experiments to avoid photobleaching and to employ the most photostable donor-acceptor pair.

In general, the relatively low quantum yields of the red fluorescent proteins result in a low level of sensitized emission, which is a disadvantage for the acquisition of ratiometric FRET data. Although mRuby2 combines efficient FRET with a high sensitized emission, several properties argue against the use in FRET experiments combined with mTurquoise2. First, the fusion with CytERM shows Golgi localization, rather than the ER localization, making it impossible to reliably determine monomeric behavior (supplemental figure S6). Second, a large fraction of blue fluorescence of mRuby2 is detected in the CFP emission band (supplemental figure S9). Finally, the FRET efficiency is variable between cells, which can likely be attributed to variable maturation (Scott and Hoppe, 2015) or photochromism (Bindels et al., 2017). Similar cell-to-cell variation is observed for tagRFP-T. The recently developed monomeric RFP, mScarlet-I, with good maturation and high quantum yield has optimal properties for ratiometric FRET. Our results show that mScarlet-I exhibits high sensitized emission amongst the RFPs tested when paired with mTurquoise2. We conclude that mScarlet-I is the preferred acceptor in the red part of the spectrum since (i) it shows consistent FRET in cells, with substantial sensitized emission, (ii) it has little blue fluorescence when excited at 436nm, (iii) it shows good photostability when excited at the CFP excitation wavelength and (iv) it is monomeric (Bindels et al., 2017). In addition, we demonstrate that it can be used in a biosensor to report on the activation of a GPCR.

In summary, the results obtained in this study point out that mTurquoise2-mNeonGreen is an optimal FRET pair for ratiometric detection of cellular processes with genetically encoded intermolecular FRET based biosensors.

Methods

Cloning / plasmid construction

All fluorescent proteins (FPs) that were used as FRET acceptor, were cloned in clontech-style C1 mammalian expression vectors and RSET bacterial expression vectors with flanking AgeI and BsrGI restriction sites. RSET bacterial expression vectors were used for protein production and isolation while the C1 vectors were used to construct the fusion constructs (figure 2).

TagRFP-T was made by introducing the S158T point mutation into tagRFP (Shaner et al., 2008). Clover and mRuby2 were derived from a plasmid obtained from addgene (#40255), mCherry-C1 and mOrange-C1 were previously described (Goedhart et al., 2007). mOrange2 was a kind gift of M. Ouyang (Ouyang et al., 2010). mKO2 was a kind gift of R.N. Day (Sun et al., 2009). mKOκ (Tsutsui et al., 2008) was obtained by introducing the point mutation M176F (Fw: 5'-GGCAATCACAATGCCAATTCAAGACTACTTACAAGGCG-3'; Rv: 5'-CGCCTTGTAAGTAGTCTTGAATTGGCATTGTGATTGCC-3') in the mKO2 coding sequence. sREAcH was obtained from addgene (plasmid #21949) (Murakoshi et al., 2008). mKate2 was a kind gift of D.M. Chudakov (Shcherbo et al., 2009). mNeonGreen was as reported before (Shaner et al., 2013). mScarlet-1 has been reported by Bindels et al (Bindels et al., 2017).

All tandem fusions were based on the SYFP2-mTurquoise2 construct that was previously described (Goedhart et al., 2012); addgene #60493). The SYFP2 in the plasmids SYFP2-mTurquoise2 was replaced by the acceptor fluorescent protein of interest cut from the clontech-style C1 plasmids using NdeI/Kpn2I restriction enzymes.

The brightness of fluorescent proteins was analyzed using tandem FP constructs with a T2A linker resulting in equal expression of two fluorescent proteins (Kim et al., 2011). These constructs were produced by cutting the SYFP2-mTurquoise2 with BamHI/Kpn2I and inserting two hybridized oligonucleotides (5min, 95°C) (Goedhart and Gadella Jr, 2005) (Fw: 5'-ccgagagagggcagaggaagtcttctaacaatcggtgacgtggaggagaatcccgccctgt-3'; Rv: 5'-gatccaggggcgggattctctccacgtcaccgcatgttagaagacttctctgcctct-3'), resulting in SYFP2-T2A-mTurquoise2. mTurquoise2 is used as reference in the brightness assay to correct for protein concentration. The SYFP2 is replaced by a FP of which the brightness is to be characterized, cut from the clontech-style C1 plasmids using NdeI/Kpn2I restriction enzymes.



The multimeric biosensors for Gq activation are based on the published FRET biosensor that is encoded on a single plasmid; G β 1-2A-YFP-Gy2-IRES-Gaq-mTurquoise Δ 6 (Goedhart et al., 2011). In order to make the Gq activation biosensors with the desired FRET pairs, first, mTurquoise Δ 6 was exchanged for mTurquoise2 Δ 6 in a pcDNA3.1 vector containing the Gaq-mTurquoise Δ 6 sequence, where the fluorescent protein is inserted at the 125th amino acid residue of the Gaq sequence. A PCR was performed on a clontech-style C1 vector containing the mTurquoise2 sequence using primers Fw 5'-TTGAGGATCCAAGCGGAGGCGGAGGCAGCATGGTGAGCAAGGGCG-3' and Rv 5'-GTATATGCCGAGAGTGATCCCGGC-3'. The PCR product and the pcDNA3.1 Gaq-mTurquoise Δ 6 vector were both digested with BamHI and SnaBI (PCR product digested with only BamHI since half the SnaBI site is present in the reverse primer, which can be directly ligated in the SnaBI cut vector) and the digested mTurquoise2 Δ 6 PCR product was ligated in the Gaq pcDNA3.1 vector. Subsequently, the Gaq-mTurquoise2 Δ 6 vector and the G β 1-2A-YFP-Gy2-IRES-Gaq-mTurquoise Δ 6 sensor were both digested with BamHI and EcoRI. Then, the Gaq-mTurquoise2 Δ 6 was ligated in the sensor replacing the original Gaq-mTurquoise Δ 6, leading to G β 1-2A-YFP-Gy2-IRES-Gaq-mTurquoise2 Δ 6 sensor. In order to exchange the YFP- Gy2 in the sensor for other acceptor fluorescent proteins (FP), first, acceptor FP-Gy2 fusions were constructed. A PCR was performed on clontech-style C1 vector containing the Gy2 sequence using primers Fw 5'-AGCTGTACATGGCCAGCAACAACACC-3' and Rv 5'-TCTACAAATGTGGTATGGC-3'. The Gy2 PCR product and clontech-style C1-FP plasmids were digested with BsrGI and SacII and the Gy2 sequence is ligated behind the fluorescent protein in the clontech-style C1 vector. Next, these acceptor FP-Gy2 fusions and the G β 1-2A-YFP-Gy2-IRES-Gaq-mTurquoise2 Δ 6 sensor were digested with NheI and SacII and the FP-Gy2 sequence was ligated into G β 1-2A-YFP-Gy2-IRES-Gaq- mTurquoise2 Δ 6 replacing the original G β 1-2A-YFP-Gy2. Finally, this resulted in a pcDNA vector encoding acceptorFP-Gy2-IRES-Gaq-mTurquoise2 Δ 6.

The intramolecular FRET sensors for RhoA activation are based on the published sensor (DORA-RhoA) (Pertz et al., 2006; van Unen et al., 2015b). First a PCR is performed on a clontech-style C1-Tq2(206A) (nTq2) plasmid using the primers Fw 5'-AACGGATCCGTGAGCAAGGGCGAGG-3' and Rv 5'-AGCGCTAGCCCCGGCGGCG-TCAC-3'. The PCR product and the original RhoA sensor were digested with BamHI and NheI and the nTq2 was ligated in the sensor construct replacing the original donor Cerulean3. A BglII restriction site is introduced in the sensor plasmid, behind the acceptor FP sequence and simultaneously the original acceptor is swapped for mNeonGreen via overlap-extension PCR (Heckman and Pease, 2007; Horton et al., 1989). The first PCRs were performed on the clontech-style C1 plasmid containing mNeonGreen using primerA Fw 5'-CTACCGGTGCCACCATG-3' and primerB Rv 5'-CTCGATGTTAGATCTGAGTCCGGACTGTGACA-3' and on the RhoA activation sensor containing the correct donor FP using primerC Fw 5'-CTCAGATCTAACATCGAGGAAGCACAAAAG-3' and primerD Rv 5'-TGCACGTGTATACAG-

CTGTGC-3'. The second PCR was performed on a mix of both PCR products using primerA and primerD. This second PCR product and the RhoA sensor are digested with AgeI and HindIII and the PCR product containing the BglIII restriction site and mNeonGreen is ligated into the sensor. To swap the acceptor from mNeonGreen to SYFP2 a PCR was performed on a clontech-style C1 vector containing SYFP2 using Fw 5'-CTACCGGTGCCACCATG-3' and Rv 5'-TCTACAAATGGTATGGC-3' and both PCR product and sensor (containing mNeonGreen) were digested with AgeI and BglIII and the SYFP2 is ligated in the sensor replacing mNeonGreen.

The intramolecular FRET sensors for calcium are based on the published Twitch2B sensor addgene (#49531) (Thestrup et al., 2014). In order to swap the fluorescent proteins the calcium binding domain and the acceptor FP were transferred to a RSET bacterial expression plasmid, using SphI and EcoRI, resulting in RSET-Minimal Calcium Binding Domain-cpmCitrine. A PCR was performed on a RSET vector containing mTurquoise2 using the primers: Fw 5'-TAATACGACTCACTATAGGG-3' and Rv 5'-GGTCATGCATGCGGGCGGGTCACGAAC-3'. The PCR product and RSET- Minimal Calcium Binding Domain -cpmCitrine vector were both digested with NcoI and SphI and mTurquoise2 was inserted prior to the calcium binding domain sequence. A mutagenesis PCR is performed on the Twitch2B RSET plasmid introducing a XhoI restriction site (by introducing 3 nucleotides) using primers Fw 5'- CCCATCTACCCCGAGCTCGAGATGGGTGGGGTC-3' and Rv 5'-GACCCACCCATCTCGAGCTCGGGGTAGATGGG-3'. Then a PCR is performed on a clontech-style C1 vector containing either mNeonGreen or SYFP2 using Fw 5'-GAGTCTCGAGATGGTGAGCAAGGGCG-3' and Rv 5'- GAGCTGAATTCTCACTTGTACAGCTCGTCCATGC-3'. The PCR product and mutagenized Twitch2B RSET plasmid are both digested with XhoI and EcoRI and ligated, exchanging the acceptor FP for mNeonGreen or SYFP2. With NheI and EcoRI the whole sensor module is transferred from the RSET vector to a clontech-style C1 vector for mammalian expression. Plasmids generated in this study will be available through addgene at https://www.addgene.org/Dorus_Gadella/

Spectroscopy of purified fluorescent proteins

His6-tagged proteins were produced in *E. coli* and purified on Hisbind resin (Novagen, Darmstadt, Germany), according to Bindels et.al. (Bindels et al., 2014). After elution by imidazole the proteins were dialyzed 2x against 20mM Tris. Spectral measurements were done in 20mM Tris (Goedhart et al., 2007), unless indicated otherwise. Absorption spectra were recorded on a Libra S70 double-beam spectrophotometer (Biochrom) (Goedhart et al., 2012). Emission spectra were recorded on a Perkin Elmer LS55 fluorimeter. Emission spectra were recorded with following settings: mKOk ex525nm, slit 5nm; em530-750nm slit 5nm; scan speed 150nm/min; pmt 750V. mOrange ex530nm, slit 5nm; em540-750nm slit 2.5nm; scan speed 150nm/min; pmt 750V. mOrange2 ex530nm, slit 5nm; em540-750nm slit 2.5nm; scan speed 150nm/



min; pmt 760V. mKO2 ex520nm, slit 5nm; em535-750nm slit 5nm; scan speed 150nm/min; pmt 750V. mNeonGreen ex460nm, slit 5nm; em470-675nm slit 5nm; scan speed 150nm/min; pmt 760V. Clover ex465nm, slit 5nm; em475-650nm slit 5nm; scan speed 150nm/min; pmt 760V. sREAcH ex505nm, slit 5nm; em515-675nm slit 5nm; scan speed 150nm/min; pmt 810V. mCherry, mScarlet-l, mRuby2, tagRFP-T and mKate2 ex540nm slit 2.5nm; em550-800nm slit 2.5nm; scan speed 150nm/min in PBS (50mM PO₄, 136mM NaCl, 2.7mM KCl, pH7.4).

Emission spectra were corrected for instrument response factors after calibration with emission spectra of established fluorophores. The emission spectra of SYFP2 and EGFP were acquired previously (Kremers et al., 2006; Kremers et al., 2007).

The R_0 values were calculated as described previously (Goedhart et al., 2007; Wu and Brand, 1994).

Cell culture and transfection

HeLa cells (CCL-2, American Tissue Culture Collection; Manassas,VA, USA) were cultured in Dulbecco's modified Eagle's medium (DMEM) (Gibco, cat# 61965-059) supplemented with 10% fetal bovine serum (Invitrogen, cat# 10270-106), 100U/ml penicillin and 100µg/ml streptomycin at 37°C in 7% CO₂. For microscopy experiments cells were grown on 24mm Ø round coverslips, 0.13 - 0.16mm thick (Menzel, cat# 360208) to 50% confluency and transfected with 500ng plasmid DNA, 1µL Lipofectamin 2000 (Invitrogen, cat# 11668-019), 2µl Polyethylenimine (PEI) (1mg/ml) in EtOH, or 4.5µl PEI (1mg/ml) in water (pH 7.3) and 100µl OptiMEM (Gibco, cat# 31985-047) per 35mm Ø dish holding a 24mm Ø coverslip. Two days after transfection the coverslip was mounted in a cell chamber (Attofluor, Invitrogen). Microscopy medium (20mM HEPES (pH = 7.4), 137mM NaCl, 5.4mM KCl, 1.8mM CaCl₂, 0.8mM MgCl₂ and 20mM glucose) was added to the coverslip in the cell chamber. The OSER assay, Ratiometric FRET, bleaching and brightness experiments are performed at 37°C.

Fluorescence lifetime imaging microscopy

Fluorescence lifetime imaging was performed using the wide-field frequency domain approach on a home-build instrument (Van Munster and Gadella Jr, 2004) using a RF-modulated AOM and a RF-modulated image intensifier (Lambert Instruments I118MD) coupled to a CCD camera (Photometrics HQ) as detector. A 40x objective (Plan NeoFluar NA 1.3 oil) was used for all measurements. The modulation frequency was set to 75.1MHz. At least twelve phase images with an exposure time of 20-100ms seconds were acquired in a random recording order to minimize artifacts due to photobleaching (van Munster and Gadella Jr., 2004). A picoquant directly modulated diode laser was used for excitation at 442nm, passed onto the sample by 455dclp dichroic and emission light was filtered by a BP480/40 emission filter. When imaging with GFP as FRET acceptor, a second emission filter BP447/60 was combined with the

BP480/40 filter (supplemental figure S11). Each FLIM measurement is calibrated by a reference measurement of the reflected laser light using a modified filter cube (Van Munster and Gadella Jr, 2004) for correcting the phase and modulation drift of the excitation light. The reference is calibrated by averaging five FLIM measurements of cells expressing mTurquoise2 (mTq2), which has a known phase lifetime of 3.8ns and a modulation lifetime of 4.0ns (Goedhart et al., 2012). This extra calibration corrects for path-length differences and possible optics-related reflections that are different between the FLIM and reference measurements. At least twelve phase sequences were acquired from each sample. From the phase sequence, an intensity (DC) image, phase and modulation lifetime images were calculated (Van Munster and Gadella Jr, 2005) using Matlab macros.

Alternatively, we performed the fluorescence lifetime measurements with a Nikon Eclipse Ti-E inverted microscope equipped with a LIFA system (Multi-Led illumination and LI2CAM; Lambert Instruments). The modulated 446nm LED excitation light passed through a 448/20 excitation filter (FF01-448/20, Semrock), reflected towards the sample by a 442nm dichroic mirror (Di02-R442, Semrock) and focused using a 60x objective (Nikon, CFI Plan Achromat NA 1.4 oil, MDR01605). The emission was filtered by a BP482/20 (FF01-482/25, Semrock). The LI-FLIM software (LI-FLIM 1.223 Lambert Instruments) recorded 18 phase steps (with three times averaging) in pseudorandom order at a frequency of 40MHz. Erythrosin B (198269, Sigma-Aldrich) dissolved in ddH₂O was used as reference dye (fluorescence lifetime 0.086 ns; ten times averaging for reference stack). After background subtraction and 3x3 blurring, the lifetimes were calculated by the LI-FLIM software.

The FRET efficiency E was calculated according to: $E = (1 - (\tau_{DA} / \tau_D)) * 100\%$, in which τ_{DA} is the fluorescence lifetime of the donor in presence of the acceptor and τ_D is the fluorescence lifetime of the donor in absence of the acceptor. Since frequency domain FLIM yields a phase lifetime and a modulation lifetime, the FRET efficiency can be calculated based on both (Goedhart et al., 2007).

For the fluorescence lifetime analysis of heterotrimeric G-protein activation the same methods were used to measure the fluorescence lifetime before adding 100uM histamine, 20-60s after adding histamine and 20-60s after adding 10uM pyrilamine.

Spectral imaging microscopy of FRET pairs

Spectral imaging of living cells was performed with hardware as described (Vermeer et al., 2004), two days after transfection using an imaging spectrograph-CCD detector.

For each cell transfected with a construct of interest a spectral image was acquired using donor excitation at 436/20nm, an 80/20 (transmission/reflection) dichroic and a 460LP (long-pass) emission filter. Subsequently a spectral image was acquired using



acceptor excitation without exciting the donor. For EGFP, mNeonGreen, Clover and SYFP2 (green/yellow) excitation at 500/20nm and for detection a BP534/20 filter was used, for mKO2, mKO κ , mOrange, mOrange2 (orange) excitation at 500/20nm and for detection a 530LP filter was used, and for mScarlet-I, mRuby2, mCherry, TagRFP-T and mKate2 (red) excitation at 546/10nm and for detection a 590LP filter was used. Using a custom made Matlab script, cells were selected from the spectral images and each sample spectrum obtained with donor excitation settings was normalized to the peak intensity of the spectrum obtained using acceptor excitation settings. In general, the donor excitation setting also leads to direct excitation of the acceptor. Using cells transfected with an acceptor only construct the direct acceptor excitation contribution could be estimated. The donor-only spectrum was obtained by using cells transfected with mTurquoise2. Prior to unmixing, all spectra were aligned and the wavelength axis was calibrated. From each sample spectrum, $F(\lambda)$, the direct acceptor excitation spectrum, $F_A(\lambda)$, was subtracted in order to remove the contribution of direct acceptor excitation. For the green/yellow acceptors, the donor component, $F_D(\lambda)$ and the sensitized emission component, $F_S(\lambda)$ were obtained from the spectrum with linear regression using the donor-only spectrum and acceptor-only spectrum, both obtained with donor excitation settings. In this case the whole wavelength range (450-650nm) was used. For the orange and red variants with a green component the donor and green contribution, $F_G(\lambda)$ were obtained by unmixing the sample spectrum in the wavelength range of 450-525nm using the donor-only spectrum and the EGFP-only spectrum. The sensitized emission was then obtained by subtracting the unmixed donor and green component from the spectrum. For red variants without a discernable green component in the spectra a similar approach was used, but now only using the donor-only spectrum applied to a wavelength range of 450-500nm. All sample and unmixed spectra $F(\lambda)$, $F_D(\lambda)$, $F_S(\lambda)$ and $F_G(\lambda)$ were subsequently normalized to the first peak value of the donor.

Using the unmixed donor and sensitized emission spectrum the apparent energy transfer, E_D can be estimated using the following equation (Wlodarczyk et al., 2008):

$$E_D(\lambda) = 1 - \frac{F_D(\lambda)}{\frac{Q_D f_D(\lambda)}{Q_A f_A(\lambda)} F_S(\lambda) + F_D(\lambda)}$$

Where Q_D and Q_A denote the quantum yields of the donor and acceptor respectively, and $f_D(\lambda)$ and $f_A(\lambda)$ denote corrected and area normalized reference spectra of the donor and acceptor respectively. The numerator represents the quenched donor and the denominator represents the total donor emission reconstructed using the ratio of quantum yields and reference spectra. In principle the E_D value should be the same for each wavelength, hence it should follow a flat line, however at the edge of spectra this can deviate and therefore a flat region was selected and a weighted average was calculated using weights $w(\lambda) = f_D(\lambda)f_A(\lambda)$, hence $E_D = \frac{\sum_i w(\lambda_i)E_D(\lambda_i)}{\sum_i w(\lambda_i)}$.

Photostability

Photostability of fluorescent proteins in fusion constructs was measured on a wide-field fluorescence microscope (Axiovert 200 M; Carl Zeiss GmbH) equipped with a xenon arc lamp with monochromator (Cairn Research, Faversham, Kent, UK). Measurements were performed under continuous illumination for 900s with 420nm light (slit width 30nm) to excite mTurquoise2. Supplemental figure S3 shows the photobleaching results for the first 48s continuous illumination (corresponding to the total illumination time during a FRET experiment with 200ms exposure time and 121 time frames) of the same experiments as shown in figure 5 and supplemental figure S2. The power was measured at the 20x objective (Zeiss LD-A-plan 20x Air/0,30 ph1 ∞) using a coherent power meter (FM Fieldmaster Power Energy Meter, 0210-761-99). Each 4s, fluorescence intensity of FRET donor and acceptor was recorded with an exposure time of 200ms using a 40x objective (oil-immersion Plan-Neo- fluor 40x/1.30; Carl Zeiss GmbH). mTurquoise2 emission was detected with a BP470/30 filter, GFP/YFP emission was detected with a BP535/30 filter and OFP/RFP emission was detected with a BP620/60 filter (Adjobo-Hermans et al., 2011). Image analysis was done in ImageJ. After subtraction of background signal, the mean fluorescence intensity of the cells was calculated for each time point.

Ratiometric FRET measurements

FRET ratio-imaging was performed on a wide-field fluorescence microscope (Axiovert 200 M; Carl Zeiss GmbH) (Adjobo-Hermans et al., 2011) equipped with a xenon arc lamp with monochromator (Cairn Research, Faversham, Kent, UK) for 240s and with a time interval of 2s. The fluorescence intensity of the donor and acceptor were recorded with an exposure time of 200ms per image using a 40x objective (oil-immersion Plan-Neo- fluor 40x/1.30; Carl Zeiss GmbH). HeLa cells were used expressing Gq-sensors, comprising Gαq-mTq2 and acceptor FP-Gγ, and histamine-1 receptor-2A-mCherry (van Unen et al., 2016b) or in the case of orange or red acceptors in the Gq-sensor untagged histamine-1 receptor (Adjobo-Hermans et al., 2011). Fluorophores were excited with 420nm light (slit width 30nm), mTq2 emission was detected with the BP470/30 filter, GFP/YFP emission was detected with the BP535/30 filter and OFP/RFP emission was detected with BP620/60 filter by turning the filter wheel (supplemental figure S11). After 42-50s HeLa cells were stimulated with 100μM (final concentration) histamine (Sigma-Aldrich) and after 140-150s 10μM (final concentration) pirlamine (mepyramine) (Sigma-Aldrich) was added as antagonist. The curves were corrected for shifts in time point of adding drugs. The curves were normalized to the average intensity of the first five frames that were recorded. ImageJ was used to perform a background correction and calculation of mean intensity of each cell for each time point. Cells that did not show a visible response were not used for the analysis. The total number of cells imaged and the number of cells analyzed (“the responders”) are indicated in the figure legends.

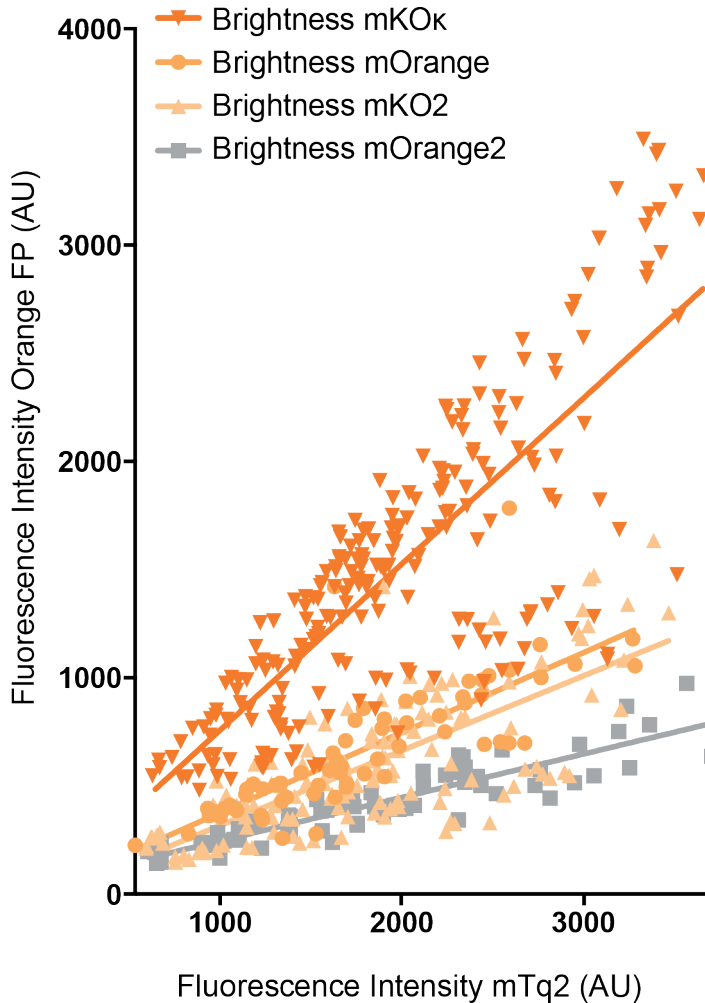


For the FRET measurements using the RhoA activation biosensors or the calcium sensors, the same time lapse, filter settings, exposure times and analysis methods are used. For the calcium sensor, HeLa cells are stimulated with 100 μ M histamine at t=44s (black arrow) and at t= 150s with 10 μ g/ml Ionomycin (Cayman chemical #10004974) (gray arrow). For the RhoA sensor, cells are stimulated with 100 μ M histamine at t=44s (black arrow) and antagonized at t= 150s with 10 μ M Pyrilamine (gray arrow). In these cells, a GEFT-mCherry construct was overexpressed next to the FRET sensor (van Unen et al., 2016a).

Brightness analysis

Cells were transfected with Tandem FP constructs containing a T2A linker, mTurquoise2 as reference and a fluorescent protein of interest. Cells expressing two separate FPs in equal amounts were imaged on a widefield fluorescence microscope (Axiovert 200 M; Carl Zeiss GmbH) equipped with a xenon arc lamp with monochromator (Cairn Research, Faversham, Kent, UK), using a 40x objective (oil-immersion Plan-Neo- fluor 40x/1.30; Carl Zeiss GmbH). Orange FPs were excited with 510nm light and emission was detected with a BP572/25 filter. As reference, mTurquoise2 was excited with 420nm light and emission was detected with a BP470/30 filter. Clover and mNeonGreen are excited with 500nm light and emission was detected with a BP535/30 filter. To prevent cross excitation, reference mTurquoise2 was excited with 405nm light and emission was detected with a BP470/30 filter. After subtraction of background signal, the mean fluorescence intensity of the cells was calculated. The fluorescence intensity of the protein of interest relative to the fluorescence intensity of the reference mTurquoise2 reveals the relative brightness of the protein of interest (Goedhart et al., 2012).

Supplemental Figures

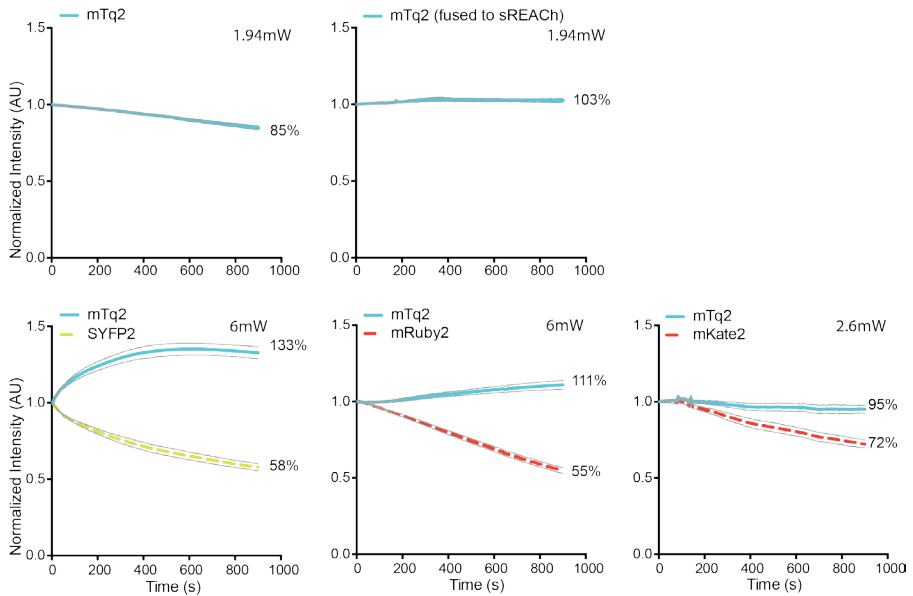


S1. The brightness of orange fluorescent proteins (FPs).

The brightness of the orange FPs relative to mTurquoise2 by employing a T2A construct with both FPs resulting in the separate expression of both fluorescent proteins in equal amounts. Cells were imaged on a widefield fluorescence microscope (Axiovert 200 M; Carl Zeiss GmbH) equipped with a xenon arc lamp with monochromator (Cairn Research, Faversham, Kent, UK), using a 40x objective (oil-immersion Plan-Neo-fluor 40x/1.30; Carl Zeiss GmbH). Orange FPs were excited with 510nm light and emission was detected with a BP572/25 filter. As reference, mTurquoise2 was excited with 420nm light and emission was detected with a BP470/30 filter. After subtraction of background signal, the mean fluorescence intensity of the cells was calculated. Each dot represents a cell. The lines show the fit with a linear regression, the steeper the line the higher the brightness. The number of cells analyzed are: mOrange-T2A-mTq2 $n=65$, mOrange2-T2A-mTq2 $n=67$, mKO2-T2A-mTq2 $n=147$ and mKOκ-T2A-mTq2 $n=239$.

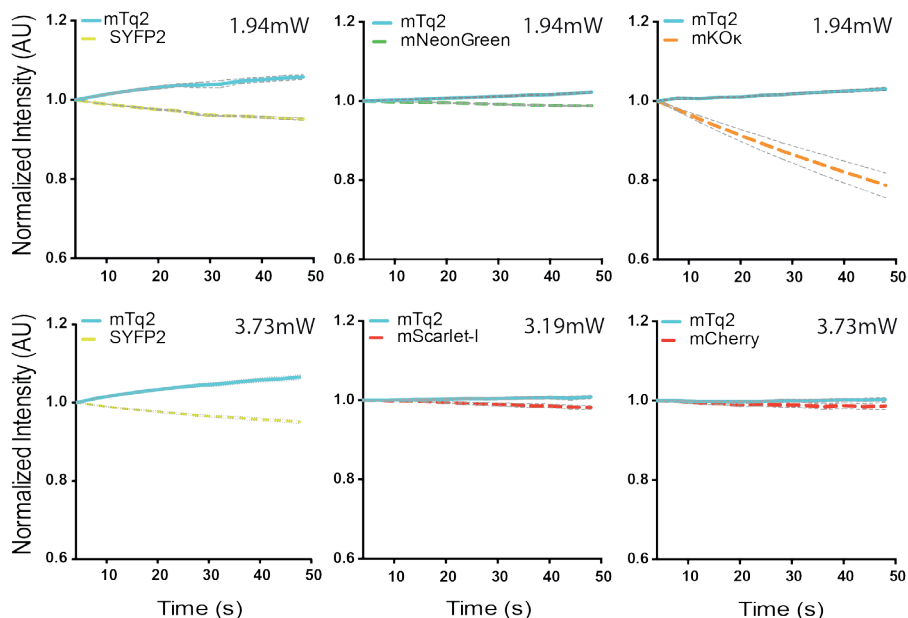


Characterization of a spectrally diverse set of fluorescent proteins as FRET acceptors for mTurquoise2



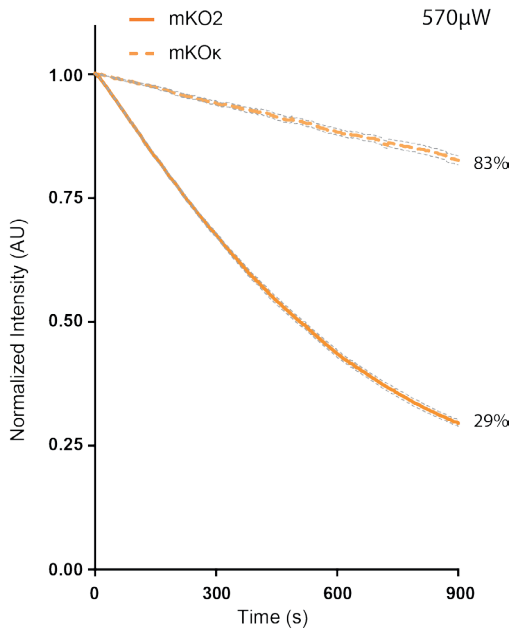
S2. Photostability under FRET conditions.

Fusion constructs of mTurquoise2 and acceptor FP were used in this experiment. As control a construct only expressing mTurquoise2 is measured (upper left). The power is shown in the graphs. The error is indicated with grey lines and corresponds to 95% confidence interval. The photostability of the fusion constructs is shown under continuous illumination with 420nm light for 900s. Each 4s, fluorescence intensity of FRET donor and acceptor was recorded with an exposure time of 200ms using a 40x objective (oil-immersion Plan-Neo- fluor 40x/1.30; Carl Zeiss GmbH). mTurquoise2 emission was detected with a BP470/30 filter, GFP/YFP emission was detected with a BP535/30 filter and OFP/RFP emission was detected with a BP620/60 filter. After subtraction of background signal, the mean fluorescence intensity of the cells was calculated for each time point using ImageJ. The initial fluorescence intensity was set on 100% and it is stated what percentage of the initial fluorescence is left after 900s illumination. The number of cells imaged is: mTq2 n=18; sREACH-mTq2 n=12; SYFP2-mTq2 n=25; mRuby2-mTq2 n=36; mKate2-mTq2 n=18.



S3. Photostability under FRET conditions for a duration that equals a typical FRET experiment.

This experiment shows in more detail the bleaching in the first 48s of the experiments shown in figure 5 and supplemental figure S2. Fusion constructs of mTurquoise2 and acceptor FP were used in this experiment. The power is shown in the graphs. The error is indicated with grey lines and corresponds to 95% confidence interval. The photostability of the fusion constructs is shown under continuous illumination with 420nm light for 48s. Each 4s, fluorescence intensity of FRET donor and acceptor was recorded with an exposure time of 200ms using a 40x objective (oil-immersion Plan-Neo- fluor 40x/1.30; Carl Zeiss GmbH). mTurquoise2 emission was detected with a BP470/30 filter, GFP/YFP emission was detected with a BP535/30 filter and OFP/RFP emission was detected with a BP620/60 filter. After subtraction of background signal, the mean fluorescence intensity of the cells was calculated for each time point using ImageJ. The initial fluorescence intensity was set on 100%. The number of cells imaged is: SYFP2-mTq2 $n=23$; mNeonGreen-mTq2 $n=21$; mKOκ-mTq2 $n=15$; SYFP2-mTq2 (3.73mW) $n=23$; mScarlet-I-mTq2 $n=11$; mCherry-mTq2 $n=15$.



S4. Photostability of mKO2 and mKOκ.

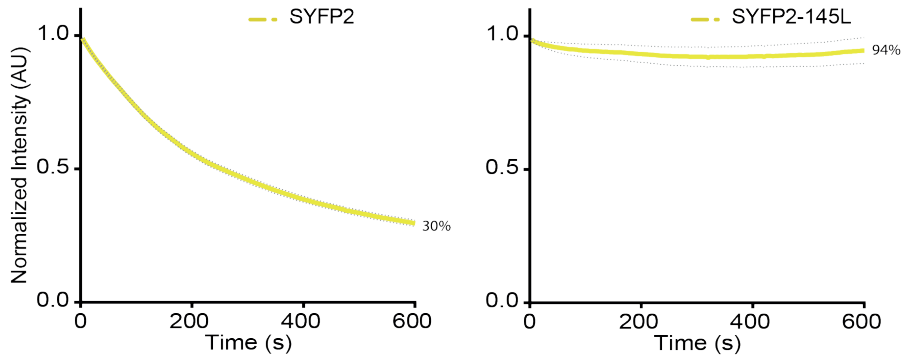
The graph shows the photostability of mKO2 and mKOκ, directly excited with 570nm light at a power of 570µW. Each 4s, fluorescence intensity of the orange fluorescent protein was recorded with an exposure time of 200ms using a 40x objective (oil-immersion Plan-Neo- fluor 40x/1.30; Carl Zeiss GmbH). The emission was detected with a BP620/60 filter. After subtraction of background signal, the mean fluorescence intensity of the cells was calculated for each time point using ImageJ. The initial fluorescence intensity was set on 100% and it is stated what percentage of the initial fluorescence is left after 900s continuous illumination. The error is indicated with grey lines and corresponds to 95% confidence interval. The number of cells imaged is: mKO2 $n=7$; mKOκ $n=9$.

> S5. Photobleaching and FLIM-FRET of SYFP2 compared to SYFP2-145L.

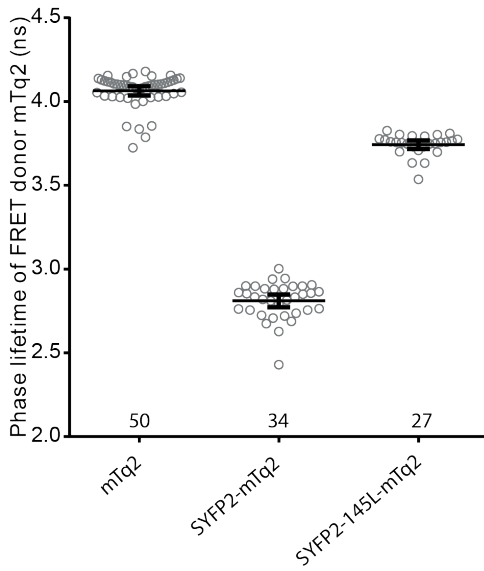
The upper graphs show the photobleaching of HeLa cells expressing yellow fluorescent protein variants SYFP2 or SYFP2-145L, under continuous illumination for 600s with 500nm light at a power of 1.39mW. Cells were imaged on a widefield fluorescence microscope (Axiovert 200 M; Carl Zeiss GmbH) equipped with a xenon arc lamp with monochromator (Cairn Research, Faversham, Kent, UK), using a 40x objective (oil-immersion Plan-Neo- fluor 40x/1.30; Carl Zeiss GmbH). Each 4s, fluorescence intensity of the yellow fluorescent protein was recorded with an exposure time of 200ms using a 40x objective (oil-immersion Plan-Neo- fluor 40x/1.30; Carl Zeiss GmbH). The emission was recorded with a BP535/30 filter. The initial fluorescence intensity was set on 100% and it is stated what percentage of the initial fluorescence is left after 600s continuous illumination. The error bars display the 95% confidence interval. The number of cells imaged is: SYFP2 $n=19$; SYFP2-145L $n=29$.

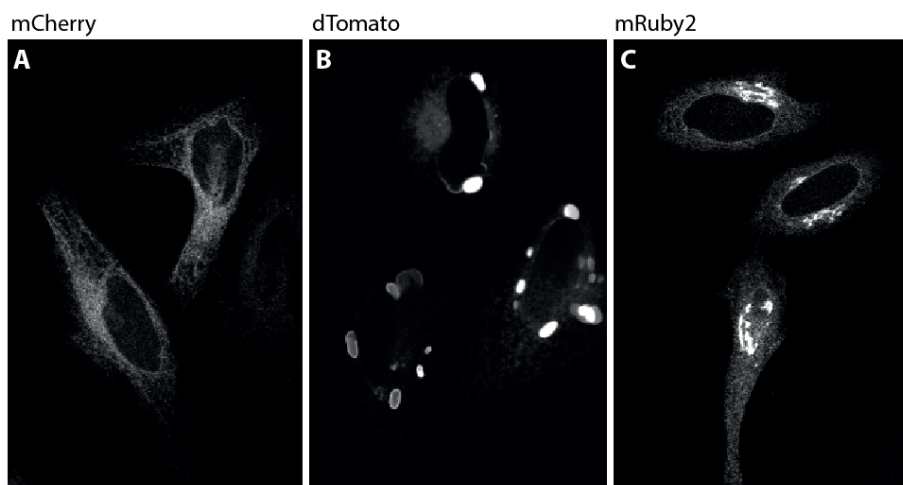
In the lower graph the phase lifetime of mTurquoise2 (mTq2) when paired with either SYFP2 or SYFP2-145L as acceptor is depicted. Cells were imaged with a home-build instrument (Van Munster and Gadella, 2004) using a RF-modulated AOM and a RF-modulated image intensifier (Lambert Instruments I18MD) coupled to a CCD camera (Photometrics HQ) as detector, using a 40x objective (Plan NeoFluar NA 1.3 oil). The modulation frequency was set to 75.1MHz. At least twelve phase images with an exposure time of 20–100ms seconds were acquired in a random recording order (van Munster and Gadella Jr., 2004). As a reference the lifetime of untagged mTurquoise2 is shown. The dots indicate individual cells and the error bars show 95% confidence intervals. The number of cells imaged is mTq2 $n=50$; SYFP2-mTq2 $n=34$; SYFP2-145L-mTq2 $n=27$.

Photobleaching of SYFP2 and SYFP2-145L



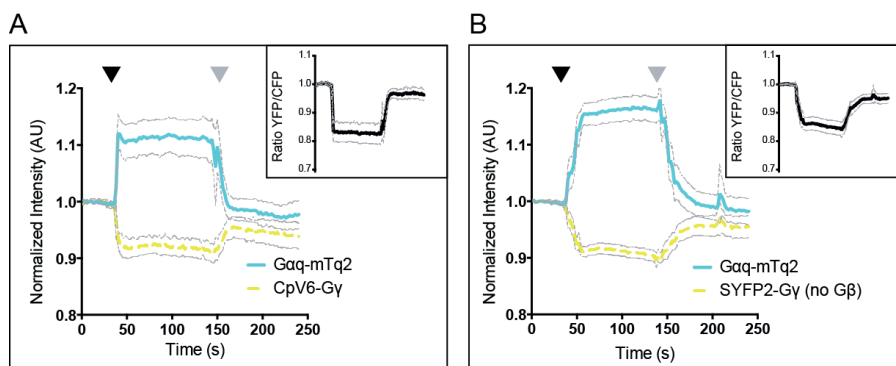
Fluorescence lifetime imaging of FRET pairs comparing SYFP2 and SYFP2-145L as FRET acceptor with donor mTurquoise2





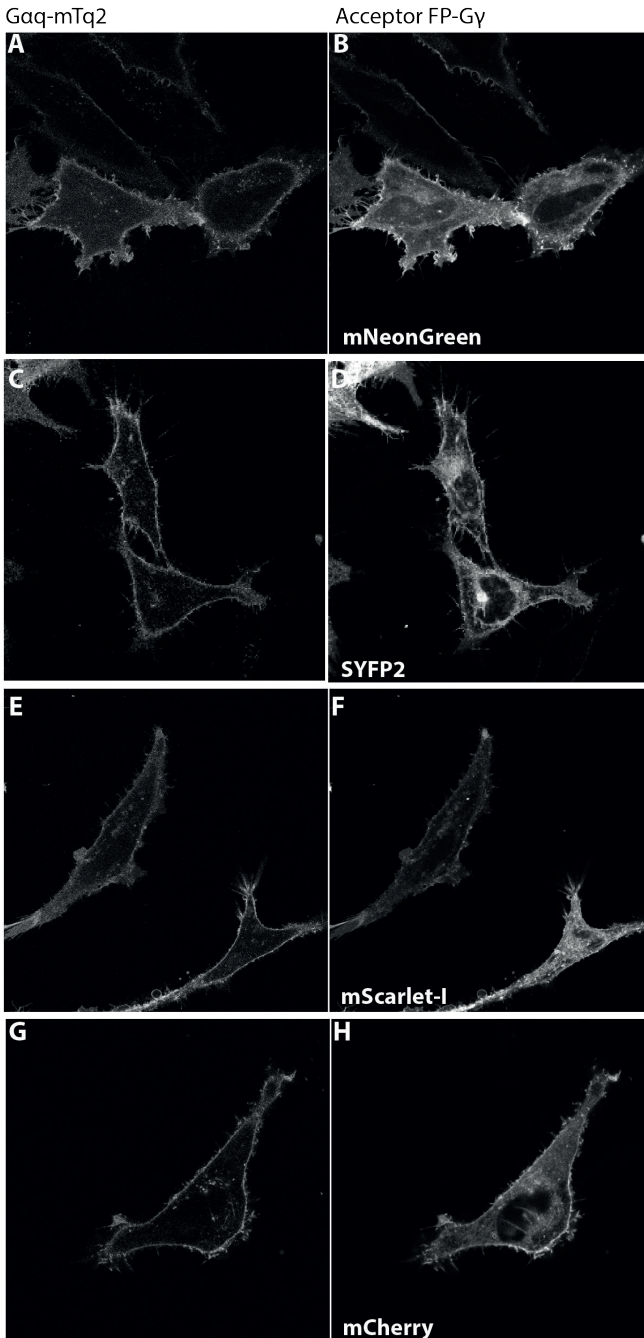
S6. mRuby2 shows abnormal localization in the OSER assay.

This graph shows CytErm-FP fusion constructs that are used in the OSER assay to determine the dimerization tendency of an FP. Cells were imaged with a Nikon A1 confocal microscope equipped with a 60x oil immersion objective (Plan Apochromat VC, NA 1.4), with the pinhole size set at 1 Airy Unit. The FPs were excited with a 561 nm laser and a BP595/50 emission filter was used. A monomeric FP such as mCherry (A) shows ER localization. If a FP has a high dimerization tendency, ER membranes fuse and form OSER structures, which is shown here for dTomato (B). It was impossible to perform this assay on mRuby2 since it showed what seemed Golgi localization instead of the expected ER and it is unknown what causes this abnormal localization. The width of the images is: 140 μ m.



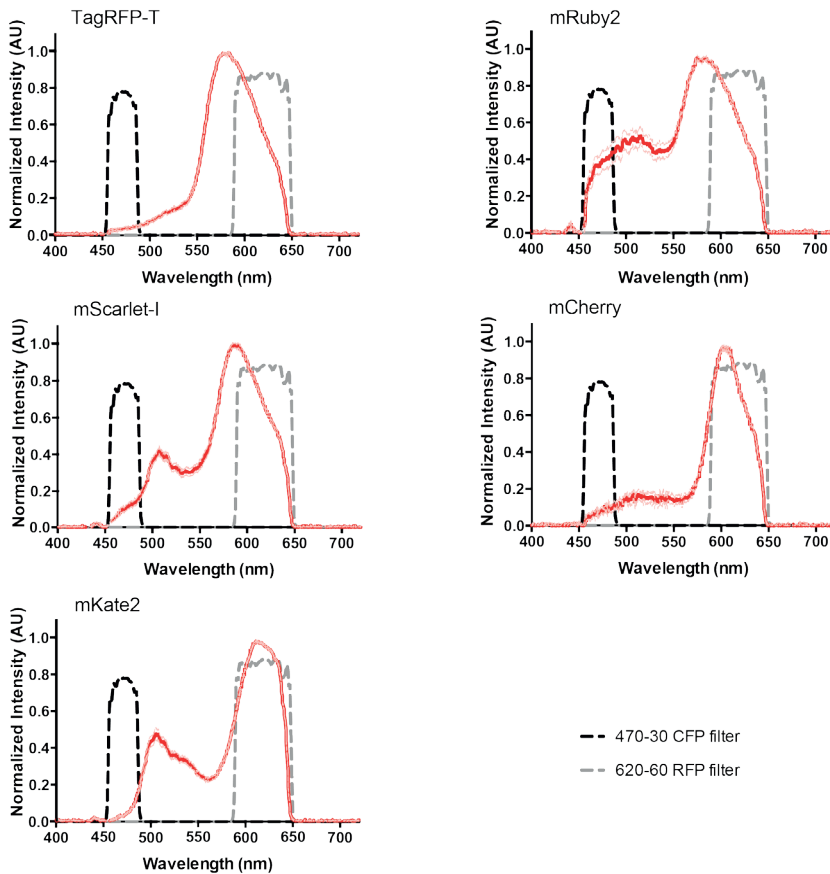
S7. Comparison of a Gq activation biosensor with and without the G β subunit.

Hela cells over-expressing the histamine₁ receptor and Gqsensor were stimulated with 100 μ M histamine after 42s (black arrow) and antagonized with 10 μ M pyrilamine after 146s (grey arrow). Cells were imaged on a widefield fluorescence microscope (Axiovert 200 M; Carl Zeiss GmbH) equipped with a xenon arc lamp with monochromator (Cairn Research, Faversham, Kent, UK), using a 40x objective (oil-immersion Plan-Neo-fluor 40x/1.30; Carl Zeiss GmbH). The blue and solid lines show the mTurquoise2 fluorescence intensity over time, the interrupted lines show the sensitized emission level over time. The black graph in a separate upper right window shows the FRET ratio (YFP/CFP) over time. The error is indicated with grey lines and corresponds to 95% confidence interval. A) Shows the FRET graphs for a Gqsensor including a G β sequence and mTurquoise2-cpVenus6 as FRETpair, $n=13$ (and 2 non-responding cells were imaged) B) Shows the FRET graphs for a Gqsensor without a G β sequence and mTurquoise2-SYFP2 as FRETpair, $n=42$ (and 2 non-responding cells were imaged).



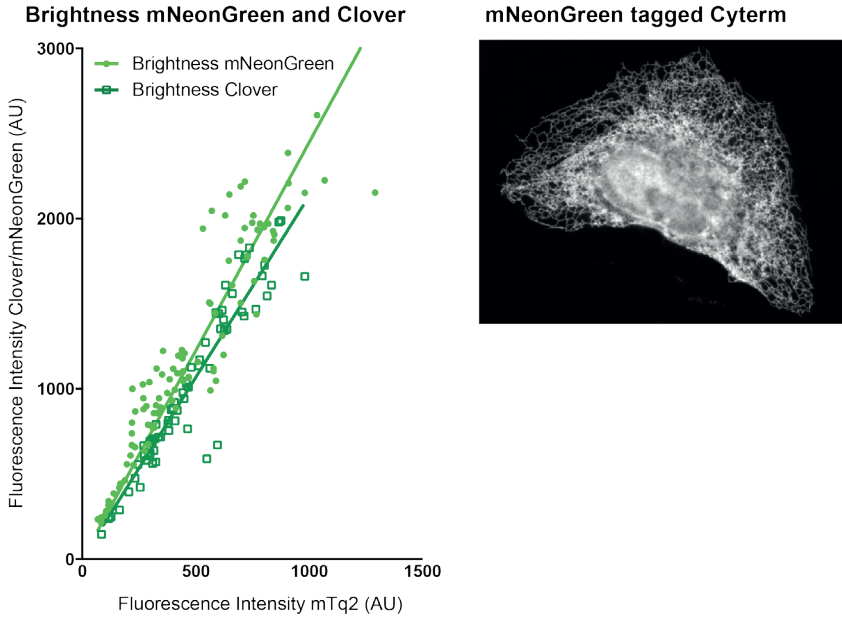
S8. Localization of Gq activation biosensors.

This figure shows images of the localization of the Gq-sensors containing a Gq-mTurquoise2 (A, C, E, G) and a Gy tagged with either mNeonGreen (B), SYFP2 (D) mScarlet-I (F) or mCherry (H). Cells were imaged with a Nikon A1 confocal microscope equipped with a 60x oil immersion objective (Plan Apochromat VC, NA 1.4), with the pinhole size set at 1 Airy Unit. For recording the images of mTurquoise2 the 457nm laser and BP480/30 emission filter were used, for mNeonGreen and SYFP2 the 514nm laser and BP537/26 emission filter were used and for mCherry and mScarlet-I the 561nm laser and BP595/50 emission filter was used. All images were recorded sequentially to minimize the amount of bleedthrough. The width of the images is 131.35 μ m for Gq-sensor-mTq2-mNeonGreen, 116.28 μ m for Gq-sensor-mTq2-SYFP2, 98.32 μ m for Gq-sensor-mTq2-mCherry and 160.23 μ m for Gq-sensor-mTq2-mScarlet-I.



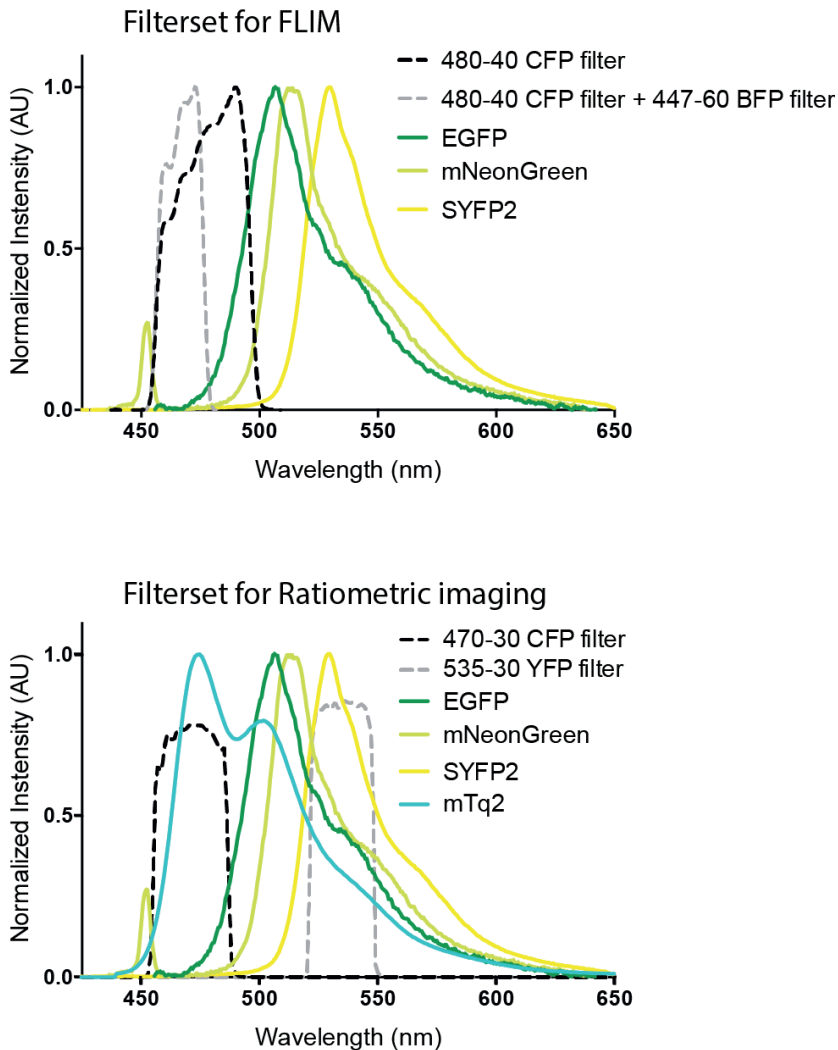
S9. Bleedthrough of RFPs in the CFP emission channel during ratiometric FRET measurements.

These graphs show the spectral imaging data recorded for RFPs excited with 436/20nm light, using a 80/20 cube and a 460LP emission filter (red line). The error is indicated with pink lines and corresponds to 95% confidence interval. The emission filters for CFP (BP470-30) (black intermittent line) and RFP (BP620-60) (grey intermittent line) used in ratiometric FRET imaging are shown in the graphs in order to show the bleedthrough of RFPs in the CFP channel and how well certain RFPs fit to the RFP emission filter that we used. Of note, very long exposure times were needed to obtain these spectra since the RFPs are hardly excited with 436/20nm light. The number of cells analyzed is: TagRFP-T $n=15$; mRuby2 $n=16$; mScarlet-I $n=14$; mCherry $n=8$; mKate2 $n=16$.



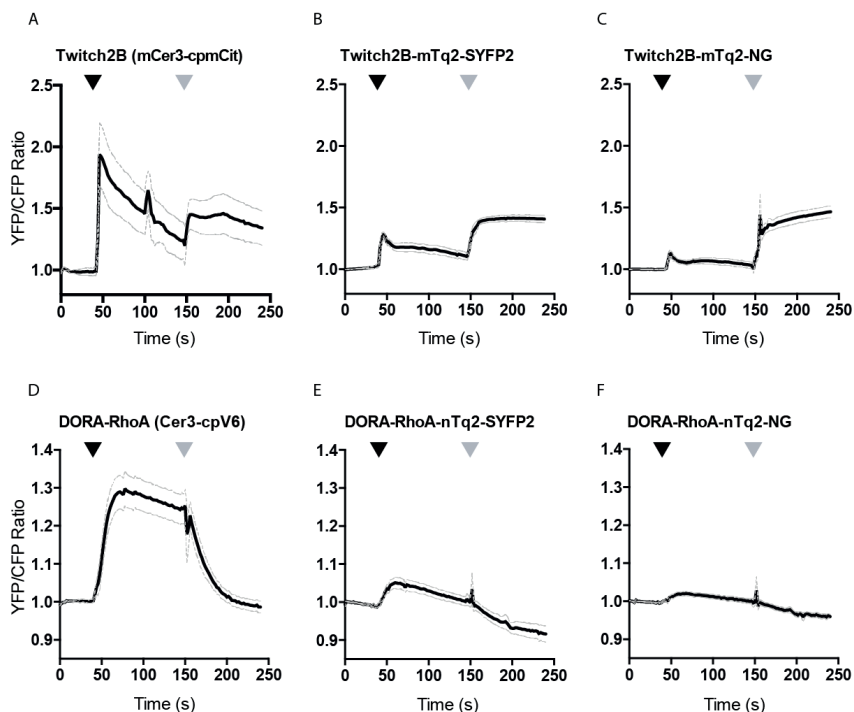
S10. Brightness and dimerization of mNeonGreen.

The left graph shows a brightness comparison of mNeonGreen and Clover relative to mTurquoise2 by employing a T2A construct with both FPs (mTurquoise2 and either Clover or mNeonGreen). Cells were imaged on a widefield fluorescence microscope (Axiovert 200 M; Carl Zeiss GmbH) equipped with a xenon arc lamp with monochromator (Cairn Research, Faversham, Kent, UK), using a 40x objective (oil-immersion Plan-Neo- fluor 40x/1.30; Carl Zeiss GmbH). Clover and mNeonGreen are excited with 500nm light and emission was detected with a BP535/30 filter. To prevent cross excitation, reference mTurquoise2 was excited with 405nm light and emission was detected with a BP470/30 filter. After subtraction of background signal, the mean fluorescence intensity of the cells was calculated. Each dot represents a cell. The lines show the fit with a linear regression, forced through the origin, the steeper the line the higher the brightness. The number of cells analyzed are: mNeonGreen-T2A-mTq2 $n=99$ and Clover-T2A-mTq2 $n=69$. The right picture shows cellular localization of mNeonGreen tagged cytERM, used in the OSER assay to determine dimerization tendency.



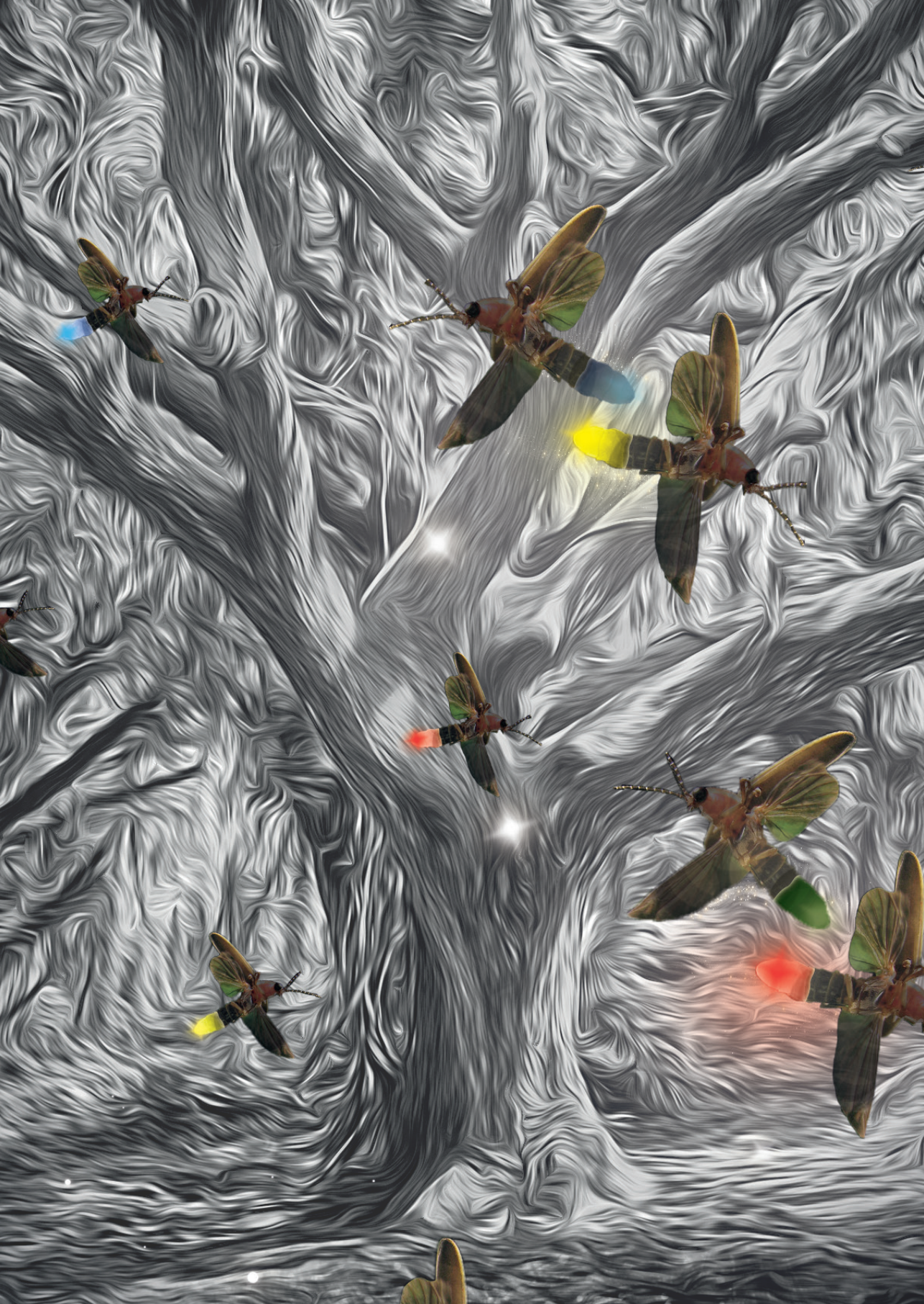
S11. Filtersets for FLIM and Ratiometric FRET imaging.

Graphs depicting emission spectra overlaid with emission bandpass filters. In the graphs of the filterset for FLIM the standard BP480-40 CFP filter (black intermittent line) is compared with the combination of this filter with a BP447-60 BFP filter (grey intermittent line). The figure shows that when using the combination of both filters hardly any emission of mNeonGreen is detected and this filterset is used to record the FLIM data. In the graph of the filterset for ratiometric imaging, the emission filters for CFP (BP470-30) (black intermittent line) and YFP (BP535-30) (grey intermittent line) are shown in combination with the emission spectra of FPs measured in this experiments.



S12. mNeonGreen as acceptor in unimolecular FRET sensors.

These graphs show data of unimolecular sensors for calcium (Twitch2B) (A-C) and RhoA activation (DORA-RHOA) (D-F), comparing the FRET pairs Tq2-SYFP2 (B, E) with Tq2-mNeonGreen (C, F). In the calcium sensor experiments a mTq2 is used, which is Tq2-206K, while in the RhoA activation experiments a nTq2 is used, which is Tq2-206A, because this sensor is believed to rely on stickiness interactions for its high dynamic range. The published, optimized sensors for calcium (A) and RhoA activation (D) are shown, containing respectively mCerulean3 and cpmCitrine, and Cerulean3 and cpVenus6 as FRET pair, showing the original dynamic range of the optimized sensors in which also circular permutations are applied. Cells were imaged with a wide-field fluorescence microscope (Axiovert 200 M; Carl Zeiss GmbH) (Adjobo-Hermans et al., 2011) equipped with a xenon arc lamp with monochromator (Cairn Research, Faversham, Kent, UK) using a 40x objective (oil-immersion Plan-Neo-fluor 40x/1.30; Carl Zeiss GmbH). Fluorophores were excited with 420nm light (slit width 30 nm), mTq2 emission was detected with the BP470/30 filter, GFP/YFP emission was detected with the BP535/30 filter. For the calcium sensor HeLa cells are stimulated with 100 μ M Histamine at $t=44$ s (black arrow) and at $t=150$ s with 10 μ g/ml Ionomycin (Cayman chemical #10004974) (gray arrow). For the RhoA sensor cells are stimulated with 100 μ M Histamine at $t=44$ s (black arrow) and antagonized at $t=150$ s with 10 μ M Pyrilamine (gray arrow). In these cells a GEFT-mCherry construct is overexpressed next to the FRET sensor. The error is indicated with grey lines and corresponds to 95% confidence interval. The number of cells imaged is: DORA-RHOA original $n=26$ (and 4 non responding cells were imaged), DORA-RHOA-nTq2-SYFP2 $n=22$, DORA-RHOA-nTq2-mNeonGreen $n=26$, Twitch2B original $n=19$ (and 2 non-responding cells were imaged), Twitch2B-mTq2-SYFP2 $n=23$ and Twitch2B-mTq2-mNeonGreen $n=26$.





3. Effects of fluorescent protein dimerization and permutation on the performance of a FRET based RhoA sensor

Marieke Mastop¹, Nikki van Bommel¹, Theodorus W.J. Gadella Jr.¹, and Joachim Goedhart¹

¹Swammerdam Institute for Life Sciences, Section of Molecular Cytology, van Leeuwenhoek Centre for Advanced Microscopy, University of Amsterdam, P.O. Box 94215, NL-1090 GE Amsterdam, The Netherlands.



Abstract

Genetically encoded, fluorescent proteins can be applied in FRET based biosensors enabling to measure changes in the chemical state of a cell. The performance of a FRET based biosensor depends on the properties of the fluorescent proteins.

The DORA-RhoA sensor, reporting on the activation of RhoA, would benefit from improved characteristics of novel FPs in terms of FRET efficiency, brightness or photostability. However, exchange of FPs for improved novel FPs often leads to a diminished dynamic range of the sensor, since in a unimolecular FRET sensor, factors as stickiness, distance between the FPs and relative orientation of the FPs become more important than in bimolecular sensors. This study was conducted to evaluate the effect of FP stickiness and the FPs relative orientation, on the dynamic range of the DORA-RhoA sensor.

To evaluate dimerization tendency, we performed an OSER assay and compared the dynamic range of DORA-RhoA sensor variants in static or dynamic FRET experiments. We focused on residue 206, comparing hydrophobic alanine with hydrophilic lysine.

To evaluate the effects of the relative FP orientation on the dynamic range of the DORA-RhoA sensor, circular permuted variants of mTurquoise2 and mNeonGreen, were constructed, characterized and applied in the DORA-RhoA biosensor. The dynamic range of DORA-RhoA sensor variants was compared in dynamic FRET experiments.

In our study no clear relation between dynamic range and 206A conferred stickiness was observed. Circular permutation of mTurquoise2 or mNeonGreen at residue 173, however, did result in an improved dynamic range of the sensor.

We conclude that circular permutation of fluorescent proteins is a viable strategy to improve the dynamic range of the DORA-RhoA FRET sensor variants. Altering the dimerization tendency or linker length may further improve the dynamic range of these sensor variants.

Introduction

Fluorescent proteins, derived from jelly fish and corals, are entirely genetically encoded and do not need a co-factor to become fluorescent. Fluorescent proteins can be fused to proteins of interest, enabling to track these proteins of interest in living cells (Chalfie et al., 1994). For these reasons, fluorescent proteins are frequently used to study biological processes in living cells (Chudakov et al., 2010; Tsien, 1998). Fluorescent proteins are also applied in biosensors enabling to measure concentrations of ions or small molecules, phosphorylation of peptides or the nucleotide loading state of a protein (Mehta and Zhang, 2011; Okumoto et al., 2012). These biosensors are based on Förster Resonance Energy Transfer (FRET), which is the radiationless transfer of energy from a donor to a nearby acceptor (Jares-Erijman and Jovin, 2003; Pietraszewska-Bogiel and Gadella Jr, 2011).

A typical unimolecular biosensor consists of a sensing domain and a FRET pair connected by a linker. The sensing domain recognizes a specific change in chemical state of the cell, causing a change in conformation of the sensor. The conformation change alters the distance between and/or orientation of the fluorescent proteins, thereby changing the FRET efficiency. As a consequence, the changes in the sensing domain are translated into a spectroscopic change that can be measured by fluorescence microscopy.

The performance of a biosensor is based on its selectivity, affinity and dynamic range. Selectivity entails the accuracy of reporting changes in the chemical state of a cell. The affinity defines the threshold of concentration changes that can be detected. Both selectivity and affinity are defined by properties of the sensing domain. The dynamic range, or FRET contrast, is the extent of the FRET change induced by the conformational change of the sensor. On the other hand, the dynamic range, or FRET contrast, is largely defined by the spectroscopic properties of the FRET pair (Goedhart et al., 2007; Mastop et al., 2017; van der Krogt et al., 2008). In addition, the length and composition of the linkers that connect the various modules and the relative orientation of the fluorescent proteins' dipoles may affect the dynamic range (Fritz et al., 2013).

The characteristics of the employed fluorescent proteins greatly influences the performance of a biosensor. The higher the Förster radius (R_0), determined by spectral overlap, quantum yield of the donor, extinction coefficient of the acceptor and relative dipole orientation of the FPs, the higher the FRET efficiency of a FRET pair (Hamers et al., 2014; Kremers et al., 2006; Wu and Brand, 1994). The brightness of the employed FPs affects the signal-to-noise ratio. Additionally, some FPs lack for example photostability or pH-stability. Another very important characteristic of fluorescent proteins is their tendency to dimerize. For many applications of fluorescent proteins,



tendency to form dimers is undesirable. However, in the case of unimolecular sensors a mild dimerization tendency, named “stickiness” throughout this manuscript, could lead to a higher dynamic range due to *hetero*-dimerization in the FRET “on”-state (Kotera et al., 2010; Lindenburg et al., 2014; Nguyen and Daugherty, 2005; Vinkenburg et al., 2007). The extent of stickiness can be tuned by introduction of hydrophobic or hydrophilic residues at the dimer interface (Kotera et al., 2010; Lindenburg et al., 2014; Vinkenburg et al., 2007; Zacharias et al., 2002).

The relative orientation of the FPs’ dipoles can be tuned by circular permutation of the FPs, connecting the N- and C-termini with a short linker and introducing new N- and C-termini in the loops between the β -strands (Baird et al., 1999; Nagai et al., 2004; Topell et al., 1999).

Several studies aimed to increase selectivity and/or dynamic range of FRET based unimolecular biosensors by either varying linker length (Komatsu et al., 2011; Peroza et al., 2015; Shimozono et al., 2006) or composition (Schifferer and Griesbeck, 2012), changing relative dipole orientation via circular permutation (Fritz et al., 2013; Nagai et al., 2004), changing sensor topology (Fritz et al., 2013; Ohta et al., 2016) or altering the FRET pair (Goedhart et al., 2007; Mastop et al., 2017; Nguyen and Daugherty, 2005).

We previously reported a tremendous decline in the dynamic range of the DORA-RhoA sensor upon exchange of the fluorescent proteins (Mastop et al., 2017).

The diminished performance cannot be explained by the FRET efficiency of the FRET pair since the R_0 and the *in vivo* determined FRET efficiency are higher and therefore should show an increase in the dynamic range of the sensor (Mastop et al., 2017). However, in a unimolecular FRET sensor, factors as stickiness, distance between the FPs and relative orientation of the FPs become more important (Kotera et al., 2010; Lindenburg et al., 2014; Nguyen and Daugherty, 2005). To obtain more insight in the factors that define the dynamic range of the DORA RhoA sensor we focused on the characteristics of the fluorescent proteins used as FRET pair and the relative orientation of the fluorescent proteins’ dipoles.

To evaluate stickiness we performed an OSER assay and compared the dynamic range of DORA-RhoA sensor variants in static or dynamic FRET experiments. We focused on residue 206 comparing hydrophobic alanine with hydrophilic lysine, for which an effect on dimerization tendency has been reported (Cranfill et al., 2016; Zacharias et al., 2002).

To evaluate the effects of the relative FP orientation on the dynamic range of the DORA-RhoA sensor, circular permuted variants of novel FPs, mTurquoise2 and mNeonGreen, were constructed, characterized and applied in the DORA-RhoA

biosensor. The dynamic range of DORA-RhoA sensor variants was compared in dynamic FRET experiments.

Results

In our hands the photostability of mTurquoise2 is superior to that of mCerulean3 (Goedhart et al., 2012). Next to that, mNeonGreen was shown to be an efficient and photostable FRET acceptor (Mastop et al., 2017). Since the DORA-RhoA uses Cerulean3 as the donor, we examined the photostability of a similar sensor in which the donor was exchanged for mTurquoise2.

Figure 1 shows the photostability of DORA-RhoA sensor variants, comparing the original nCerulean3-nVenus-cp173 FRET pair with the novel nTurquoise2-mNeonGreen FRET pair. Application of the latter FRET pair greatly improves the photostability of the sensor. Therefore, it would be advantageous if the decrease in dynamic range for the mTurquoise2-mNeonGreen based sensor could be resolved.

The aim of this study is to evaluate the effects of stickiness and relative FP orientation on the dynamic range of the DORA-RhoA sensor, with as ultimate goal the generation of allround DORA-RhoA sensor variants equipped with a bright and photostable FRET pair.

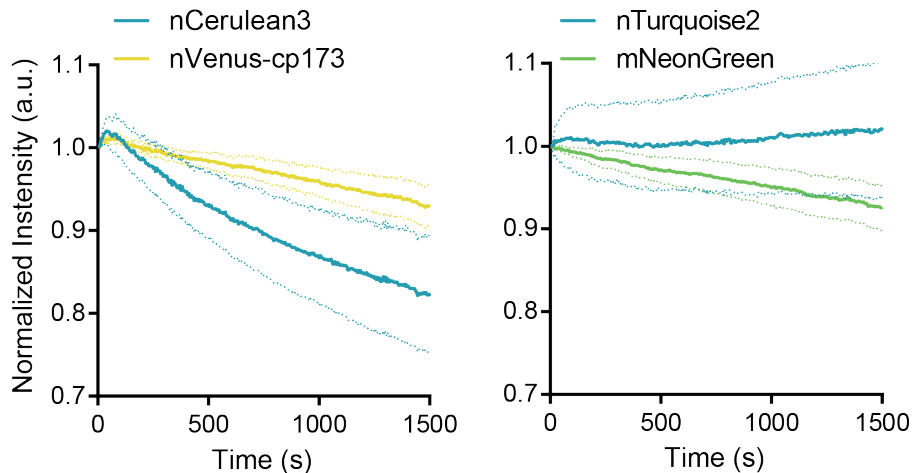


Figure 1. Photostability of RhoA sensor variants.

Donor and acceptor normalized, mean fluorescence intensity traces of HeLa cells, transiently expressing the DORA-RhoA sensor employed with either nCerulean3-nVenus-cp173 (left, $n=16$) or nTurquoise2-mNeonGreen (right, $n=24$) as FRET pair. The dotted lines represent the 95%CI. Photostability is shown under alternatingly imaging with 420nm (562 μ W) and 500nm (1.98mW) light, with an exposure time of 200ms and an interval of 5s for 25 minutes in total.



Quantifying the dimerization tendency of monomeric (206K) and native (206A) fluorescent proteins

We set out to evaluate stickiness with a focus on residue 206 located at the dimer interface of the FRET pair. This residue is natively a hydrophobic alanine, changing it into a hydrophilic lysine results in less hydrophobic FP interactions, e.g. a more monomeric behavior (Kotera et al., 2010; Zacharias et al., 2002).

As a first step in the evaluation of stickiness we performed an OSER assay to determine the difference in dimerization tendency between native and monomeric FPs, quantitatively (table 1) (Costantini et al., 2012). Of note, this assay evaluates *homo*-dimerization tendency, whereas *hetero*-dimerization may be more relevant to the dynamic range of a sensor. Still, the OSER assay will give insight in the properties of the fluorescent proteins.

From table 1 can be inferred that nVenus (206A) shows a higher dimerization tendency than mVenus (206K), which is as expected and reported before (Cranfill et al., 2016). Circular permutation of nVenus showed a dimerization tendency similar to mVenus, suggesting that circular permutation affects dimerization tendency. Overall, the dimerization tendency of the cyan fluorescent proteins is low. The dimerization tendency of native and monomeric Turquoise2 is more or less the same and for Cerulean3 the monomeric variant was even slightly more dimerizing (table 1). These data suggest that residue 206 does not have a pronounced effect on *homo*-dimerization tendency. These data are in line with structural information that shows that the CFP specific N164I or N146F mutation is sufficient to prevent dimerization (von Stetten et al., 2012).

We wanted to exclude FRET independent effects of the Venus barrel on the fluorescence intensity of nCerulean3. Therefore we used a nVenus-cp173 variant with a Y66C mutation, rendering it non-fluorescing and non-absorbing (Koushik et al., 2006). We determined if activation of the RhoA sensor variant, with native Cerulean3 and the mutated nVenus-cp173-66C led to donor quenching. We observed no donor quenching, supporting the notion that the change in CFP and YFP signals is due to FRET (figure 2).

Evaluating the effect of stickiness on the dynamic range of the DORA-RhoA sensor

Since effects of residue 206 on *hetero*-dimerization tendency in context of FRET sensors have been reported multiple times, we proceeded with an evaluation of changing residue 206 on the dynamic range of the DORA-RhoA sensor (Jost et al., 2008; Kotera et al., 2010; Zacharias et al., 2002). Figure 3 shows spectra of DORA-RhoA sensor variants in the GTP-locked state. The first peak shows the donor fluorescence intensity. The height of the donor intensity in this FRET "on"-state gives information on

the dynamic range, the lower the peak, the higher the dynamic range (Goedhart et al., 2014; Mastop et al., 2017; Piston and Kremers, 2007).

Table 1. Dimerization tendency of monomeric (206K) and native (206A) CFP and YFP variants.

The OSER assay is performed on HeLa cells, transiently expressing the CytERM sequence fused to a CFP or YFP variant and the percentage of cells containing OSER structures and the number of cells analyzed are shown in this table.

	Dimerization tendency (% cells with OSER structures)	Number of cells analyzed
mTurquoise2-206K	5	122
Turquoise2-206A	4	223
Venus-206K	3	122
Venus-206A	17	358
Venus-206A-cp173	4	135
Cerulean3-206K	12	170
Cerulean3-206A	9	240

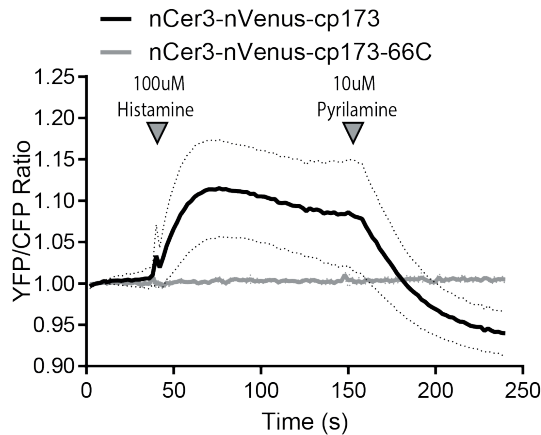


Figure 2. Barrel interactions, independent of FRET, are not responsible for the high dynamic range of the DORA-RhoA FRET sensor.

Ratiometric FRET traces of HeLa cells expressing a DORA-RhoA FRET sensor employed with either nCerulean3-nVenus-cp173 ($n=7$) or nCerulean3-nVenus-cp173-66C ($n=5$) as FRET pair and a Histamine1 receptor, tagged with mCherry (dotted lines represent 95% CI). Histamine and pyrilamine were added at $t=50s$ and $t=150s$ respectively, as indicated by the arrowheads.

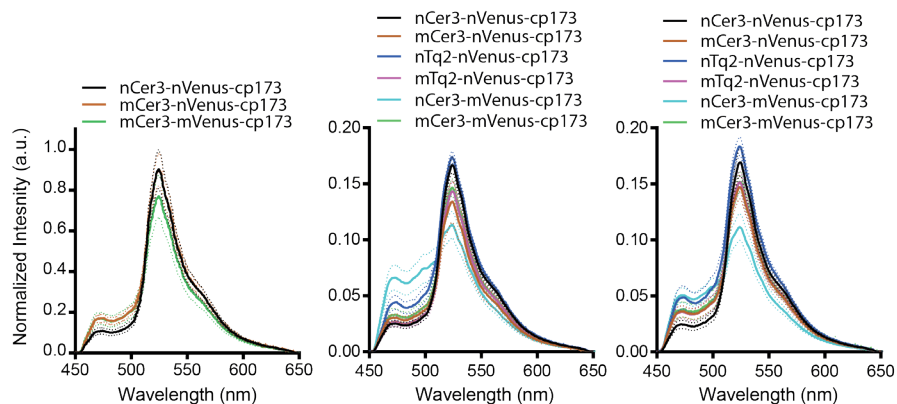


Figure 3. Spectral images of DORA-RhoA sensors in GTP-locked state expressing either monomeric or native FP variants as FRET pair.

The sensor emission spectra were recorded from single living HeLa cells. The lines show the average emission spectrum and the dotted lines represent the 95%CI. The spectra are normalized to acceptor level. The lower the first peak, the higher the donor quenching. The higher the second peak, the higher the sensitized emission. The three graphs show data from three independent experiments on different days. The number of cells analyzed is; left: $n=10$ per RhoA sensor; middle: nCerulean3-nVenus-cp173 $n=15$, mCerulean3-nVenus-cp173 $n=10$, nTurquoise2-nVenus-cp173 $n=11$, mTurquoise2-nVenus-cp173 $n=8$, nCerulean3-mVenus-cp173 $n=9$, mCerulean3-mVenus-cp173 $n=11$; right: nCerulean3-nVenus-cp173 $n=13$, mCerulean3-nVenus-cp173 $n=21$, nTurquoise2-nVenus-cp173 $n=16$, mTurquoise2-nVenus-cp173 $n=17$, nCerulean3-mVenus-cp173 $n=14$, mCerulean3-mVenus-cp173 $n=16$.

The original DORA-RhoA FRET pair, nCerulean3-nVenus-cp173 performed best in each experiment, however, no relation between dynamic range and 206A-based stickiness is observed (figure 3). Figure 4 shows dynamic activation of DORA-RhoA sensor variants. Again, no clear relation between dynamic range and 206A-based stickiness is observed. Surprisingly, the sensor equipped with two monomeric FPs shows the best performance (figure 4). In two of the three experiments the sensor equipped with nTurquoise2 instead of nCerulean3 shows a clearly decreased dynamic range independent of the nature of residue 206 (figure 4).

Stickiness could still be responsible for the differences in dynamic range in sensors equipped with either nCerulean3 or nTurquoise2. Since the sequence of these FPs differs by ten amino acid residues, one or more of these residues could be accountable for the differences in stickiness (Goedhart et al., 2012; Markwardt et al., 2011). It would be labor intensive to systematically test all different residues and combinations. We did assess a small subset of mutations, either from nCerulean3 towards nTurquoise2 or from nTurquoise2 towards nCerulean3, showing only minor effects on the dynamic range of the sensor (supplemental figure S1).

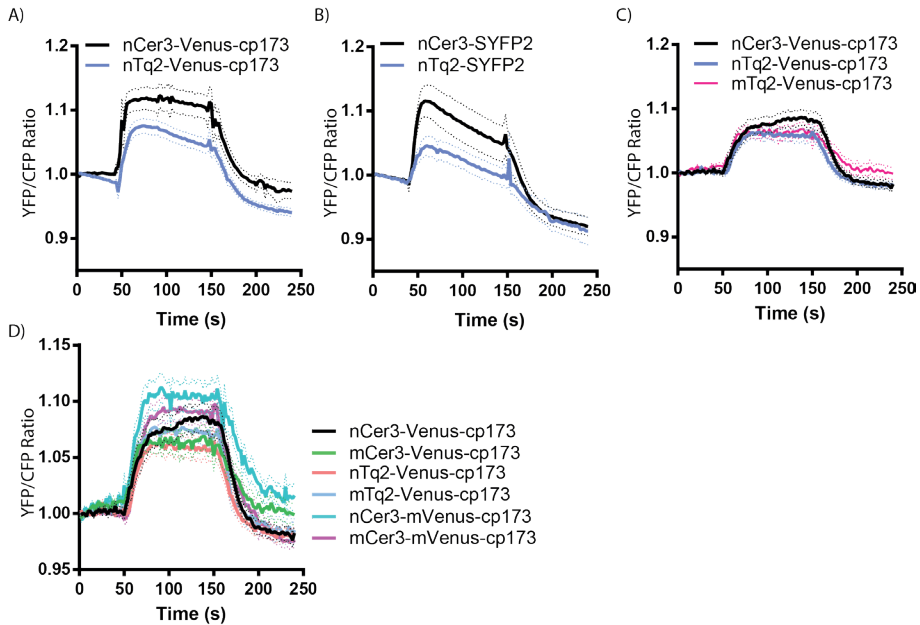


Figure 4. Dynamic FRET measurements of DORA-RhoA sensors employing either monomeric or native FP variants as FRET pair.

Ratiometric FRET traces of HeLa cells expressing a DORA-RhoA FRET sensor variant and guanine exchange factor, GEFT, tagged with mCherry (dotted lines represent 95% CI). Histamine and pyrillamine were added at $t=50$ s and $t=150$ s respectively, as indicated by the arrowheads. (A-C) show data from three independent experiments, performed on different days. The number of cells analyzed is for (A) nCerulean3-nVenus-cp173 $n=41$, for nTurquoise2-nVenus-cp173 $n=61$; for (B) nCerulean3-SYFP2 $n=20$, for nTurquoise2-SYFP2 $n=24$; for (C) nCerulean3-nVenus-cp173 $n=69$, for nTurquoise2-nVenus-cp173 $n=75$ and for mTurquoise2-nVenus-cp173 $n=63$. (D) The same data as shown in (C) including more different RhoA sensor variants. The number of cells analyzed is for mCerulean3-nVenus-cp173 $n=42$, for nCerulean3-mVenus-cp173 $n=56$ and mCerulean3-mVenus-cp173 $n=84$.

Circularly permuted mTurquoise2 and mNeonGreen variants

Since the decreased dynamic range of DORA-RhoA sensor variants could not be solved by altering FP stickiness, we turned to circular permutation of the FPs in the sensor (Fritz et al., 2013; Nagai et al., 2004; van der Krogt et al., 2008). In this section we focus on the mTurquoise2-mNeonGreen FRET pair since it outperformed CFP-YFP in a bimolecular Gq activation sensor (Mastop et al., 2017) and showed improved photostability (figure 1).

We designed circularly permuted (cp) variants of mTurquoise2 and mNeonGreen based on protein structure and previous publications (Clavel et al., 2016; Fritz et al., 2013; Goedhart et al., 2012; Nagai et al., 2004; Rekas et al., 2002; Shaner et al., 2013; Topell et al., 1999) (figure 5A and 6A). The cpFP variants were characterized in HeLa cells, focusing on the emission spectra, lifetime and brightness (figure 5B-D, figure 6B, C).

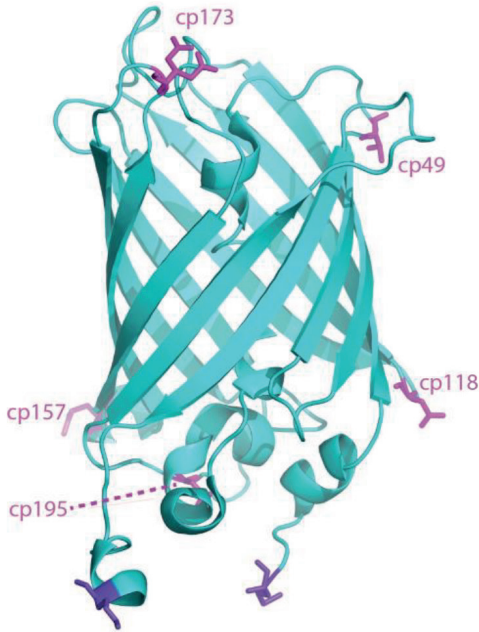


The lifetime and emission spectra of circularly permuted variants, visibly fluorescing, are similar to the emission spectra of regular mTurquoise2 and mNeonGreen, respectively (figure 5B, C and figure 6B, C). The circularly permuted variants mTurquoise2-cp157 and -cp173 are the brightest variants, though less bright than mTurquoise2. mTurquoise2-cp195 is less bright but still well visible (figure 5D). It was not possible to determine the brightness of mTurquoise2-cp40, using this assay, due to aberrant localization of this variant, to intracellular compartments (figure 5E). The circularly permuted variants mNeonGreen-cp173 and -cp118 are well visible, though less bright than mNeonGreen. The other circularly permuted mNeonGreen variants hardly showed fluorescence (figure 6D).

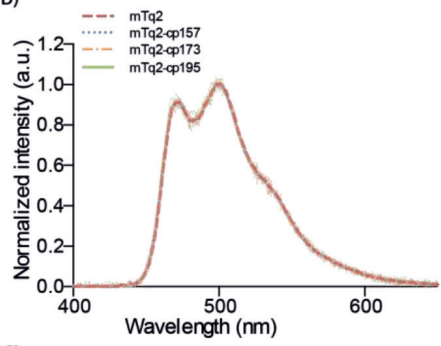
> Figure 5. Design and Characterization of circularly permuted mTurquoise2 variants.

- A) The protein structure of mTurquoise2 (PDB ID: 3ZTF), which is used, together with literature research, to determine interesting sites for circular permutation of mTurquoise2. The beginning and end of the protein are highlighted in purple and the circular permutation sites tested are highlighted in pink. The highlighted residue is the start of the protein in the respective circularly permuted variant.
- B) Emission spectra of mTurquoise2 and circularly permuted variants, in living HeLa cells, using spectral imaging, $n=3$ for mTurquoise2 and mTurquoise2-cp195; and $n=4$ for mTurquoise2-cp157 and mTurquoise2-cp173. Thinner dashed lines represent 95% CI.
- C) Phase lifetimes of mTurquoise2 and circularly permuted variants, in living HeLa cells. The number of cells analyzed is $n=50$ for mTurquoise2; $n=41$ for mTurquoise2-cp157; $n=48$ for mTurquoise2-cp173; $n=48$ for mTurquoise2-cp195. Shown is the average \pm the 95% CI.
- D) The *in vivo* brightness of the mTurquoise2 variants relative to mScarlet-I by employing P2A constructs, resulting in the separate expression of the fluorescent proteins in equal amounts. The experiment is performed in HeLa cells. Each dot represents a single cell. The number of cells analyzed is $n=62$ for mTurquoise2; $n=49$ for mTurquoise2-cp118; $n=73$ for mTurquoise2-cp157; $n=57$ for mTurquoise2-cp173; $n=79$ for mTurquoise2-cp195.
- E) Widefield microscopy images of HeLa cells expressing the dual expression construct used for the brightness assay mTurquoise2-cp49 (left) with as reference mScarlet-I (right). The left image shows that mTurquoise2-cp49 is localized to cellular structures, while it should be in the cytoplasm, as shown for the mScarlet-I reference. This made it impossible to determine the brightness of mTurquoise2-cp49 using this assay. The width of the images is 108 μm .

A)



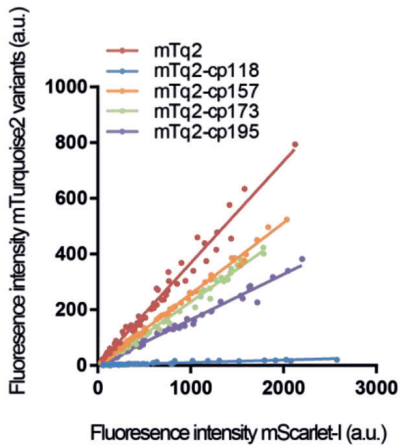
B)



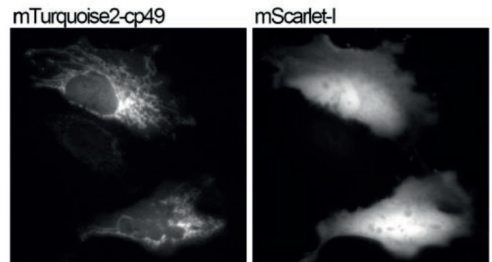
C)

Fluorescent protein variant	Average phase lifetime (ns)
<i>mTurquoise2</i>	3.86 ± 0.01
<i>mTurquoise2-cp157</i>	3.85 ± 0.01
<i>mTurquoise2-cp173</i>	3.84 ± 0.01
<i>mTurquoise2-cp195</i>	3.76 ± 0.07

D)



E)





Circular permuted FP variants applied in the DORA-RhoA FRET sensor

The promising circular permuted variants were applied in the DORA RhoA biosensor and the FRET contrast of the sensors was evaluated (figure 7). We see clear effects of circular permutation on the dynamic range of the sensor (figure 7 A, B), where mNeonGreen-cp118 lead to a decrease and -cp173 lead to an increase in the dynamic range. However, another experiment hardly shows an effect of mNeonGreen-cp173 compared to regular mNeonGreen, combined with nTurquoise2 (figure 7C). Figure 7D, shows the FRET contrast of the DORA-RhoA sensor employed with circular permuted nTurquoise2 variants combined with mNeonGreen or mNeonGreen-cp173. The combination of nTurquoise2-cp173 and mNeonGreen showed the highest FRET contrast. The improved FRET contrast obtained with the nTurquoise2-cp173-mNeonGreen FRET pair, still does not yield a dynamic range as high as the original sensor, employing the FRET pair nCerulean3-nVenus-cp173. However, we observed high day-to-day variation in sensor performance next to relatively broad confidence intervals in figure 7B and 7D.

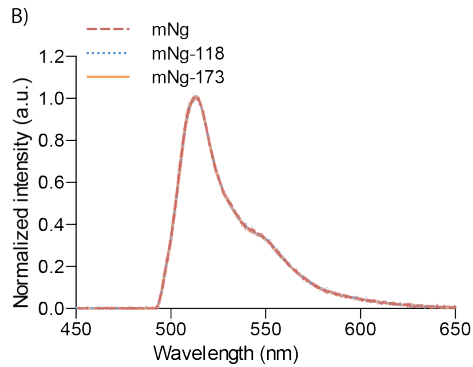
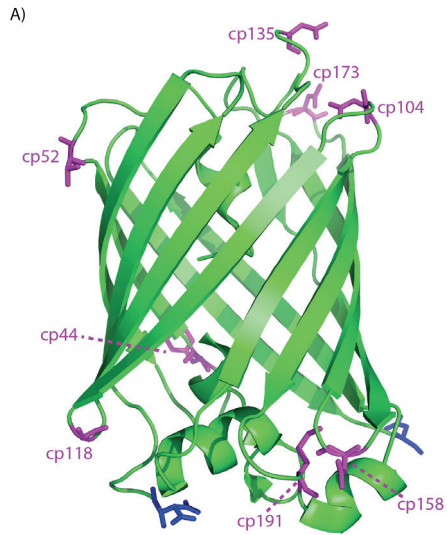
> Figure 6. Design and Characterization of circular permuted mNeonGreen variants.

A) The protein structure of mNeonGreen (PDB ID: 5LTR), which is used, together with literature research, to determine interesting sites for circular permutation of mNeonGreen. The beginning and end of the protein are highlighted in blue and the circular permutation sites tested are highlighted in pink. The highlighted residue is the start of the protein in the respective circular permuted variant.

B) Emission spectra of mNeonGreen and circular permuted variants, in living HeLa cells, using spectral imaging, $n=3$ for mNeonGreen-cp118 and $n=4$ for mNeonGreen and mNeonGreen-cp173, Thinner dashed lines represent 95% CI.

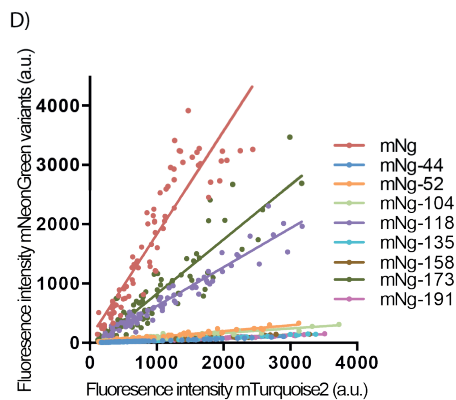
C) Phase lifetimes of mNeonGreen and circular permuted variants, in living HeLa cells. The number of cells analyzed is $n=41$ for mNeonGreen; $n=35$ for mNeonGreen -cp118; $n=58$ for mNeonGreen -cp173. Shown is the average \pm the 95%CI.

D) The in vivo brightness of the mNeonGreen variants relative to mTurquoise2 by employing P2A constructs, resulting in the separate expression of the fluorescent proteins in equal amounts. The experiment is performed in HeLa cells. Each dot represents a single cell. The number of cells analyzed is $n=81$ for mNeonGreen; $n=68$ for mNeonGreen-cp44; $n=73$ for mNeonGreen-cp52; $n=78$ for mNeonGreen-cp104; $n=79$ for mNeonGreen-cp118; $n=78$ for mNeonGreen-cp135; $n=83$ for mNeonGreen-cp158; $n=81$ for mNeonGreen-cp173; $n=81$ for mNeonGreen-cp191.



C)

Fluorescent protein variant	Average phase lifetime (ns)
<i>mNeonGreen</i>	2.85±0.03
<i>mNeonGreen-cp118</i>	2.85±0.02
<i>mNeonGreen-cp173</i>	2.81±0.01





Effects of fluorescent protein dimerization and permutation on the performance of a FRET based RhoA sensor

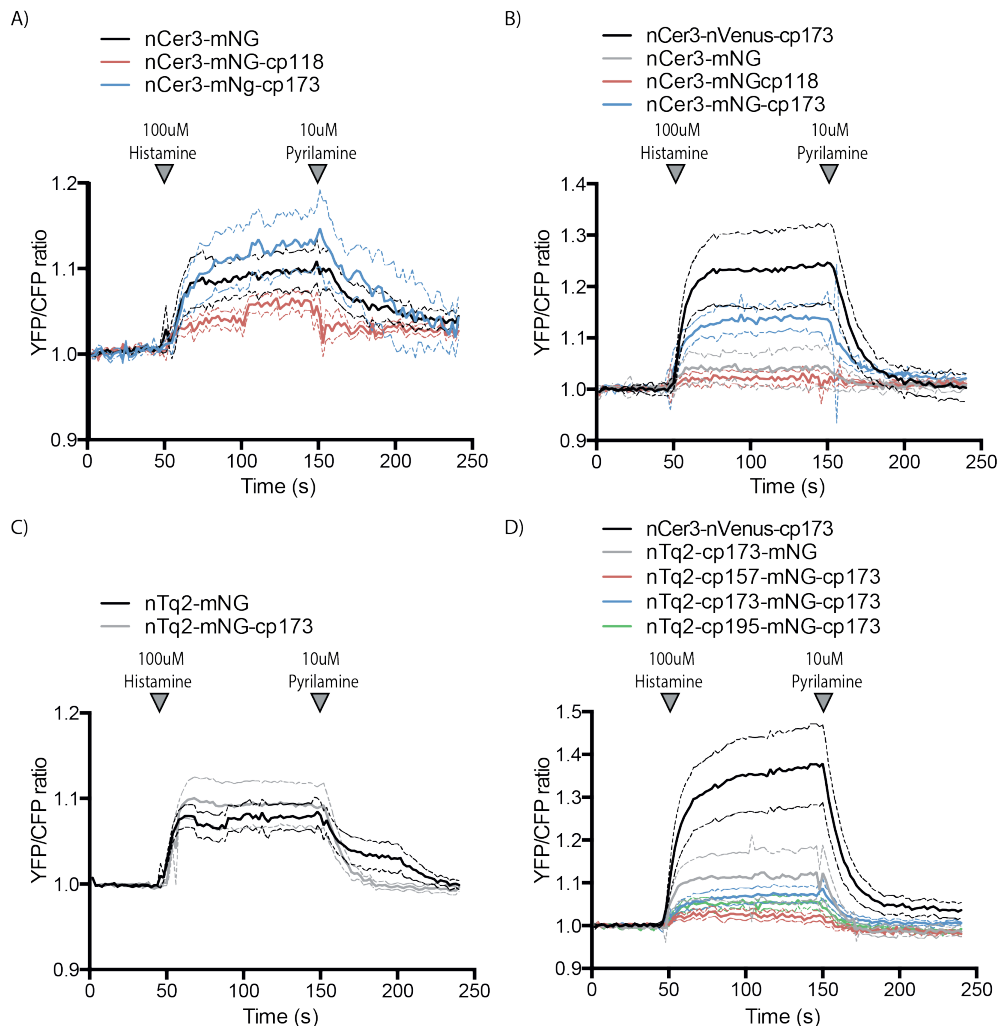


Figure 7. Dynamic FRET measurements of DORA-RhoA sensors, employing circular permuted fluorescent protein variants.

Ratiometric FRET traces of HeLa cells expressing a DORA-RhoA FRET sensor variant and a Histamine1 receptor, tagged with mCherry (dotted lines represent 95% CI). Histamine and pyrilamine were added at $t=50s$ and $t=150s$ respectively, as indicated by the arrowheads. (A-D) show data from four independent experiments, performed on different days. The number of cells analyzed is for (A) nCerulean3-mNeonGreen $n=8$, for nCerulean3-mNeonGreen-cp118 $n=20$ and for nCerulean3-mNeonGreen-cp173 $n=14$; for (B) nCerulean3-nVenus-cp173 $n=6$, for nCerulean3-mNeonGreen $n=4$, for nCerulean3-mNeonGreen-cp118 $n=8$ and for nCerulean3-mNeonGreen-cp173 $n=4$; for (C) nTurquoise2-mNeonGreen $n=32$ and for nTurquoise2-mNeonGreen-cp173 $n=16$; for (D) nCerulean3-nVenus-cp173 $n=8$, for nTurquoise2-cp173-mNeonGreen $n=7$, for nTurquoise2-cp157-mNeonGreen-cp173 $n=10$, for nTurquoise2-cp173-mNeonGreen-cp173 $n=10$ and for nTurquoise2-cp195-mNeonGreen-cp173 $n=11$.

Discussion

The DORA-RhoA sensor would benefit from improved characteristics of novel FPs in terms of, for example, FRET efficiency, brightness or photostability. However, exchange of the donor-acceptor pair with other FRET pairs frequently leads to a diminished dynamic range of the sensor. This study was conducted to evaluate the effect of FP stickiness and the relative orientation of the FPs employed, on the dynamic range of the DORA-RhoA sensor. Our results showed no clear relation between dynamic range of the DORA-RhoA sensor and residue 206A-based stickiness. Circular permutation of mTurquoise2 or mNeonGreen at residue 173, however, did result in an improved dynamic range of the sensor.

We conclude that circular permutation can be used to improve the dynamic range of the DORA-RhoA FRET sensor variants, which is in line with a previous study (Fritz et al., 2013). Further research into stickiness and possibly linker length and composition is required to further improve the dynamic range of these sensor variants.

The OSER assay results showed no clear effect of 206A or 206K, for Cerulean3 and Turquoise2, while effects of these residues on dimerization tendency have been reported several times (Cranfill et al., 2016; Jost et al., 2008; Kotera et al., 2010; Zacharias et al., 2002). Strikingly, circular permutation of nVenus resulted in a more monomeric character according to the OSER assay results, for which we have no explanation.

The original DORA-RhoA FRET pair, nCerulean3-nVenus-cp173, performed best in each static or dynamic FRET experiment, however, no clear relation between dynamic range and 206A-based stickiness is observed. The lack of a clear effect of 206A or 206K in Cerulean3 and Turquoise2 might be due to other residues exerting a stronger (anti-) stickiness effect. We did assess a small subset of mutations, either from nCerulean3 towards nTurquoise2 or from nTurquoise2 towards nCerulean3, showing only minor effects on the dynamic range of the sensor.

Our data suggests that stickiness is not of major influence on the dynamic range of this particular sensor. Still, stickiness might be under the influence of one or a combination of the ten residues that differ between nCerulean3 and nTurquoise2. To rule out any effects of stickiness, the different positions need to be evaluated systematically, starting with residues in or in close proximity to the dimer interface (Goedhart et al., 2012; Markwardt et al., 2011).

Another strategy to improve the dynamic range of DORA-RhoA sensors employed with novel FRET pairs could be, the introduction of other residues reported to increase stickiness, such as 221K, 223R, 208F and 224L (Lindenburg et al., 2014; Nguyen and Daugherty, 2005; Vinkenborg et al., 2007; Zacharias et al., 2002). Note that the extent



to which the 208F mutation stabilizes intramolecular FRET pair *hetero*-dimerization differs between FRET pairs, making it difficult to predict the effect of this mutation (Lindenburg et al., 2014). Moreover, Kotera et.al. reported that 208F and 224L do not improve the dynamic range of intramolecular FRET sensors, increasing the basal FRET level of these sensors (Kotera et al., 2010).

In conclusion, stickiness has been reported to improve the dynamic range of intramolecular sensors, but the appropriate level of stickiness varies with sensor design and FRET pair and it remains to be determined if and how stickiness can influence the dynamic range of the DORA-RhoA sensor.

Several bright circular permuted variants of mTurquoise2 and mNeonGreen were generated, exhibiting lifetimes and emission spectra similar to the published not circular permuted FPs (Goedhart et al., 2012; Shaner et al., 2013). However, reduction in brightness compared to non-circular permuted variants was observed. This reduced brightness could be due to slower or incomplete maturation of these variants, which remains to be established experimentally. The characterization of the circular permuted FP variants reported here is brief and it would be interesting to further characterize the variants in terms of quantum yield, extinction coefficient, pKa, maturation speed and efficiency and dimerization tendency.

For both mTurquoise2 and mNeonGreen circular permutation at residue 173 performed best when applied in the DORA-RhoA sensor, which is corresponding with previous studies on other circular permuted FP variants and sensors (Fritz et al., 2013; Kotera et al., 2010; Nagai et al., 2004). GFP dimerizes in an antiparallel configuration and dimerization in this configuration is facilitated by circular permutation at residue 173, possibly explaining the increased dynamic range when this FP variant is applied in the DORA-RhoA sensor (Kotera et al., 2010; Yang et al., 1996). For mNeonGreen three other circular permutation sites that would result in antiparallel configuration were tested, at residue 52, 104 and 135, but these variants were hardly fluorescent. It would be interesting to test more circular permutation sites, leading to an antiparallel configuration, to see if other circular permutation sites yield an even more optimal *hetero*-dimer configuration. Since maturation efficiency is an important factor that determines FRET efficiency, it is expected that improved maturation of circular permuted variants would increase the FRET efficiency and dynamic range.

Furthermore, it would be interesting to fine-tune *hetero*-dimerization between the Tq2-NeonGreen FRET pair. In close proximity of the *A. victorea* 206A/K, mNeonGreen displays two charged amino acids a glutamate (208E) and a lysine (210K) that could be mutated to alanine to potentially mimic the native FP effect of *A. victorea* derived FPs. Additionally, the 208E of mNeonGreen might strongly interact with the 206K of mTq2, making it worthwhile to look into basal FRET activity of this FRET pair in the DORA-RhoA sensor.

A general concern of the FRET experiments in which we compared variants of the DORA-RhoA FRET sensor is the high day-to-day variation in sensor performance. This limited us to comparing solely sensor variants measured on the same day. The high day-to-day variation in sensor performance could be due to the different batches and passage numbers of the used HeLa cells. Furthermore, the data presented in figure 4 were recorded using cells ectopically expressing GEFT, while the data presented in figure 7 were recorded using cells ectopically expressing histamine-1 receptor (H1R). In general, stimulation of the H1R seems to induce higher RhoA sensor responses. Additionally, the data presented in figure 7B, D is less firm due to the relatively low number of analyzed cells in these experiments. In order to obtain stronger data, the experiments should be repeated, analyzing a larger number of cells. For some of the investigated sensor variants the 95% confidence intervals are rather broad. This means that the actual population mean is not well-determined in these experiments, which could also be improved by imaging more cells per experiment.

In summary, the results of this study point out that circular permutation can be used to improve the dynamic range of the DORA-RhoA sensor, employed with novel FRET pairs, increasing sensor photostability. Further research into stickiness and possibly linker length and composition is required to improve the dynamic range of these sensor variants further in order to eventually match or even outcompete the original DORA-RhoA sensor FRET pair.

Methods

Cloning / plasmid construction

We used previously reported fluorescent proteins mCerulean3 (Goedhart et al., 2012; Markwardt et al., 2011), nCerulean3 and nVenus-cp173 from the DORA-RhoA sensor (Lin et al., 2015; van Unen et al., 2015b), mTurquoise2 (Goedhart et al., 2012), nTurquoise2 (Mastop et al., 2017) and mNeonGreen (Shaner et al., 2013). In order to mutagenize nVenus-cp173, its sequence and part of the linker were transferred from the DORA-RhoA sensor to a clontech style C1 vector using restriction enzymes *AgeI*/*Bam*HI. The A206K mutation for obtaining mVenus-cp173 was introduced by whole plasmid PCR on the clontech style C1 vector encoding nVenus-cp173 (Fw: 5'-CTGAGCTACCAGTCCaagCTGAGCAAAGACCCCA-3' and Rv: 5'-TGGGGTCTTTGCTCAGcttGGACTGGTAGCTCAG-3'). The Y66C mutation of nVenus-cp173 was introduced by whole plasmid PCR on the clontech style C1 vector encoding nVenus-cp173 (Fw: 5'-ACCCTCGTGACCACCCTCGGCTGCGGCCTGCAGTGCTTCGCCGC-3' and Rv: 5'-GCGGGCGAAGCACTGCAGGCCGAGCCGAGGGTGGTACGAGGGT-3'). After mutagenesis in the clontech style C1 vector, the Venus-cp173 mutants were transferred to the DORA-RhoA sensor using again restriction enzymes *AgeI*/*Bam*HI.



mCerulean, nTurquoise2 and mTurquoise2 were transferred from a clontech style C1 vector to the DORA-RhoA sensor via PCR (Fw: 5'-AACGGATCCGTGAGCAAGGGCGAGG-3' and Rv: 5'-AGCGCTAGCCCCGGCGGGTCAC-3') introducing flanking restriction sites BamHI and NheI, subsequently used for the FP exchange. To obtain the GTP-locked variants of the DORA-RhoA sensors, the RhoA sequence is exchanged for the RhoA sequence including a Q63L mutation, using HindIII/NheI restriction enzymes, as reported before (Bindels et al., 2017; Reinhard et al., 2016; van Unen et al., 2015b).

For the OSER vectors we used vector mEmerald-CytERM-N-17 (#54056) from addgene and exchanged the FP, except for nVenus-cp173, using AgeI/BsrGI restriction enzymes. In order to clone nVenus-cp173 in the OSER vector, we used a clontech style C1 vector previously reported as YFP-Gy2 (Adjobo-Hermans et al., 2011). First, a PCR (Fw: 5'-AGGTCTATATAAGCAGAGC-3' Rv: 5'-GCTGCGGCCGCTTACTCGATGTTGTGGCGGAT-3') was performed, followed by restriction digestion of both PCR product and OSER vector using AgeI/NotI restriction enzymes.

For the photostability measurements the DORA-RhoA sensor (Lin et al., 2015; van Unen et al., 2015b) was compared with a DORA-RhoA sensor variant containing nTurquoise2 and mNeonGreen as FRET pair (Mastop et al., 2017).

We created tandem FP constructs for mTurquoise2 and mNeonGreen by performing a PCR (Fw: 5'-AGCGGTACCAGGGTGGCAGCGGTGGCATGGTGGAGCAAGGGCGAG-3'; Rv: 5'-TCTACAAATGTGGTATGGC-3'), followed by digestion of the PCR product with Acc65I/BsrGI and digestion with BsrGI of the clontech style C1 vector containing the mTurquoise2 or mNeonGreen construct, respectively. The PCR product was ligated in the clontech style C1 vector and the orientation of the ligated inserted was checked.

These tandem FP constructs were used to make the circular permuted variants by PCR at different positions in the tandem FP flanking these novel circular permuted variants with AgeI and BsrGI restriction sites for cloning into clontech style C1 vectors or pDx vectors (modified TriEX vector, expressing a FP in both bacteria, under a rhamnose promoter, and in mammalian cells, under a CMV promoter). Primers used to create circular permuted variants from the tandem FP constructs are for mTurquoise2 circular permuted at residue 40 Fw: 5'-GCTACCGGTCGCCACCATGTACGGCAAGCTGACCCTG-3' and Rv: 5'-GCTTGTACAGGTGGCATGCCCTC-3'; for mTurquoise2 circular permuted at residue 49 Fw: 5'-GCTACCGGTCGCCACCATGACCACCGCAAGCTGC-3' and Rv: 5'-GCTTGTACAGCAGATGAACTTCAGGGTCAG-3'; for mTurquoise2 circular permuted at residue 118 Fw: 5'- GCTACCGGTCGCCACCATGGACACCCTGGTGAACCG

-3' and Rv: 5'-GCTTGTACAGCCCTCGAACTTCACCTC-3'; for mTurquoise2 circular permuted at residue 157 Fw: 5'-GCTACCGGTCGCCACCATGCAGAAGAACGG-

CATCAAGGC-3' and Rv: 5'- GCTTGACTACTTGTGCGCGGTGATATAGAC-3'; for mTurquoise2 circular permuted at residue 173 Fw: 5'-GCTACCGGTCGCCACCATGGACGCGCGTGCA-3' and Rv: 5'-GCTTGACTACTCGA-TGTTGTGGCGGATC-3'; for mTurquoise2 circular permuted at residue 195 Fw: 5'-GCTACCGGTCGCCACCATGCTGCTGCCGACAACC-3' and Rv: 5'-ACTGTACACACGGG-GCCGTCG-3'; for mNeonGreen circular permuted at residue 44 Fw: 5'-GCTACCGGT-CGCCACCATGTATGAGGAGTTAAACCTGAAGTCC-3' and Rv: 5'-GCTTGACAACCATCA-TTTGGATTGCC-3'; for mNeonGreen circular permuted at residue 52 Fw: 5'-GCTACCGGTCGCCACCATGACCAAGGGTGACCTCCA-3' and Rv: 5'-GCTTGACAGGACT-TCAGGTTAACTCCTCA-3'; for mNeonGreen circular permuted at residue 104 Fw: 5'-GCTACCGGTCGCCACCATGGATGGTGCCTCCCTTACTGTT-3' and Rv: 5'-GCTTGACATTCAAACCTGCATTGTGCGAT-3'; for mNeonGreen circular permuted at residue 118 Fw: 5'-GCTACCGGTCGCCACCATGGGAAGCCACATCAAAGGAG-3' and Rv: 5'-GCTTGACTACTCGTAGGTGTAGCGGTAGTTA-3'; for mNeonGreen circular permuted at residue 135 Fw: 5'-GCTACCGGTCGCCACCATGGACGGTCTGTGATGACC-3' and Rv: 5'-GCTTGACAAGCAGGGAAACCAGTCC-3'; for mNeonGreen circular permuted at residue 158 Fw: 5'-GCTACCGGTCGCCACCATGGACAAAACATCATCAGTACCTT-3' and Rv: 5'-GCTTGACAGTTGGGGTAAGTCTTCTTCG-3'; for mNeonGreen circular permuted at residue 173 Fw: 5'-GCTACCGGTCGCCACCATGAATGGCAAGCGCTACC-3' and Rv: 5'-GCTTGACATCCAGTGGTGAACCTCACT-3'; for mNeonGreen circular permuted at residue 191 Fw: 5'-GCTACCGGTCGCCACCATGATGGCGGCTAACTATCTGAA-3' and Rv: 5'-GCTTGACATGGCTTGGCAAAGGTGTA-3'.

The brightness of the circular permuted variants was analyzed using a dual expression vector including a P2A sequence, reported elsewhere (Bindels et al., 2017). The FP of interest could be exchanged using *AgeI*/*BsrGI* restriction enzymes and mTurquoise2 is used as reference. This construct is used to measure the relative brightness of mNeonGreen variants. In order to determine the brightness of circular permuted mTurquoise2 variants, mScarlet-I was used as reference FP. To exchange mTurquoise2 as reference for mScarlet-I, a silent mutation was introduced in the mScarlet-I sequence, changing a *BsrGI* restriction site into a *SacI* restriction site (Fw: 5'- CGGCGCATGGACGAGCTCTACAAGTAAGTGATTAAC-3' and Rv: 5'-GTTAATCACTTACTTGTAGAGCTCGTCCATGCCCGG-3'). The mutagenized mScarlet-I expressed in a pDx vector was digested with *EcoRI*/*SacI* and used to replace the mTurquoise2 reference in the dual expression vector used for the brightness analysis (Bindels et al., 2017), followed by a mutagenesis PCR, destroying an *AgeI* site in front of the mScarlet-I sequence (Fw: 5'-CAGCTCGCTAGCGTCCGGTCCACCATG -3' and Rv: 5'- CATGGTGGCGACCGGCAGCGCTAGCGAGCTG-3'), so the FP of interest, in this case circular permuted mTurquoise2 variants and their controls, can easily be exchanged using *AgeI*/*BsrGI* restriction enzymes while the reference FP, mScarlet-I, remains unaffected.



For cloning of the DORA-RhoA sensor with circularly permuted variants, a gBlock (Integrated DNA technologies (IDT)) was ordered to enable swift exchange of FPs. The gBlock contained part of the RhoA sensor sequence including mutations to introduce restriction sites flanking the FPs in the sensor. Additionally, the linker between the FPs was codon optimized to facilitate synthesis of the gBlock. The gBlock was cloned into the DORA-RhoA sensor sequence using PstI/Kpn2I restriction enzymes. The resulting gBlock sensor is not yet in frame. The donor FP in the sensor could be exchanged using SgaI/Acc65I restriction enzymes and the acceptor FP could be exchanged using AgeI/BsiwI restriction enzymes. Exchanging these FPs yields a RhoA sensor that is in frame, due to a frame shift. Circularly permuted donor or acceptor candidates could be transferred to a digested gBlock RhoA sensor using AgeI/BsrGI from a pDx or clontech style C1 vector. Not circularly permuted FPs expressed from a clontech style C1 vector could be transferred to the digested vector by performing a PCR, creating a truncation (excluding the last 10 amino acids) of the fluorescent protein (Fw: 5'-AGGTCTATATAAGCAGAGC-3' and either Rv: 5'-AGCTGTACACCCGGCGGCGGTAC-3' (mTurquoise2) or Rv: 5'-AGCTGTACAGGTAAAGGCCTTTTGCCACTC-3' (mNeonGreen)). The PCR product was digested with AgeI/BsrGI and ligated in the gBlock RhoA sensor.

Cell culture and transfection

HeLa cells (CCL-2, American Tissue Culture Collection; Manassas, VA, USA) were cultured in Dulbecco's modified Eagle's medium (DMEM) (Gibco, cat# 61965-059) supplemented with 10% fetal bovine serum (Invitrogen, cat# 10270-106), 100U/ml penicillin and 100µg/ml streptomycin at 37 °C in 7% CO₂, as previously mentioned (Mastop et al., 2017). For microscopy experiments cells were grown on 24mm Ø round coverslips, 0.13–0.16mm thick (Menzel, cat# 360208) to 50% confluency and transfected with 500ng plasmid DNA, 3µl PEI (1mg/ml) in water (pH 7.3) and 100µl OptiMEM (Gibco, cat# 31985-047) per 35mm Ø dish holding a 24mm Ø coverslip and 2ml DMEM. One or two days after transfection the coverslip was mounted in a cell chamber (Attofluor, Invitrogen). Microscopy medium (20mM HEPES (pH=7.4), 137mM NaCl, 5.4mM KCl, 1.8mM CaCl₂, 0.8mM MgCl₂ and 20mM glucose) was added to the coverslip in the cell chamber. The OSER assay, Ratiometric FRET, bleaching and brightness experiments were performed at 37 °C. Fluorescence lifetime microscopy (FLIM) and spectral imaging microscopy were performed at room temperature.

OSER assay

Confocal imaging for the OSER assay was performed on a Nikon A1 confocal microscope, equipped with a 60x oil immersion objective (Plan Apochromat VC, NA 1.4). We analyzed HeLa cells expressing the CytErm-FP fusion constructs and determined the percentage of cells that contained OSER structures (Costantini et al., 2012; Mastop et al., 2017). The Cerulean3 and Turquoise2 variants were excited with 457nm laser and a 482/35BP emission filter was used. The Venus variants were excited with a 514nm laser and a 540/30BP emission filter was used.

Photostability

Photostability of RhoA sensor variants was measured on a widefield fluorescence microscope (Axiovert 200 M; Carl Zeiss GmbH) equipped with a xenon arc lamp with monochromator (Cairn Research, Faversham, Kent, UK). Photostability is alternately imaged with 420nm (562 μ W) and 500nm (1.98mW) light, with an exposure time of 200ms and an interval of 5s for 25 minutes in total, using a 40x objective (oil-immersion Plan-Neo-fluor 40 \times /1.30; Carl Zeiss GmbH).

The power was measured at the 20x objective (Zeiss LD-A-plan 20x Air/0,30 ph1 ∞) using a coherent power meter (FM Fieldmaster Power Energy Meter, 0210-761-99).

CFP emission was detected with a 525/40BP filter and nVenus-cp173 or mNeonGreen emission was detected with a 535/30BP filter. Image analysis was done in ImageJ. After subtraction of background signal, the mean fluorescence intensity of the cells was calculated for each time point. The intensity was normalized to the first time frame.

Ratiometric FRET imaging

FRET ratio-imaging was performed on a widefield fluorescence microscope (Axiovert 200 M; Carl Zeiss GmbH) (Adjobo-Hermans et al., 2011) equipped with a xenon arc lamp with monochromator (Cairn Research, Faversham, Kent, UK) for 240 s and with a time interval of 2 s. The fluorescence intensity of the donor and acceptor were recorded with an exposure time of 200ms per image using a 40x objective (oil-immersion Plan-Neo-fluor 40 \times /1.30; Carl Zeiss GmbH). HeLa cells were used expressing a histamine-1 receptor-P2A-mCherry construct (Adjobo-Hermans et al., 2011; van Unen et al., 2016b) and a DORA-RhoA sensor.

Fluorophores were excited with 420nm light (slit width 30nm), CFP emission was detected with the 525/40BP filter, YFP or mNeonGreen emission was detected with the 535/30BP filter. At the first and last time frame an additional image is recorded with 600nm excitation light and a 620/60BP filter is used for the detection of mCherry emission. After 50s HeLa cells were stimulated with 100 μ M (final concentration) histamine (Sigma-Aldrich) and after 150s 10 μ M (final concentration) ppyramine (mepyramine) (Sigma-Aldrich) was added as antagonist. The curves were normalized to the average intensity of the first five frames that were recorded. ImageJ was used to perform a background correction and calculation of mean intensity of each cell for each time point.

Spectral imaging microscopy

Spectral imaging of living cells was performed with hardware as described (Vermeer et al., 2004), two days after transfection using an imaging spectrograph-CCD detector. For the spectral imaging of constitutively active RhoA sensor variants (Q63L), spectral images of single cells, were acquired using donor excitation at 436/20nm, an 80/20



(transmission/reflection) dichroic and a 460LP (long-pass) emission filter. Subsequently a spectral image was acquired using acceptor excitation without exciting the donor, excitation at 500/20nm and for detection a 534/20BP (band-pass) filter was used.

Each spectral image was normalized to directly excited FRET acceptor fluorescence intensity to correct for differences in protein expression (Goedhart et al., 2010). A custom matlab script was used to select cells and obtain spectra corrected for background signal.

Spectral imaging of circularly permuted mTurquoise2 and mNeonGreen variants expressed in HeLa cells, to obtain emission spectra of the FP variants, was performed using excitation with 436/20nm (mTurquoise2) or 470/40nm (mNeonGreen) light, attenuated 10 times by a neutral density filter, an 80/20 (transmission/reflection) dichroic and a 460LP (mTurquoise2) or 500LP (mNeonGreen). A custom matlab script was used to select cells and obtain spectra corrected for background signal.

Fluorescence lifetime imaging microscopy (FLIM) of circularly permuted variants

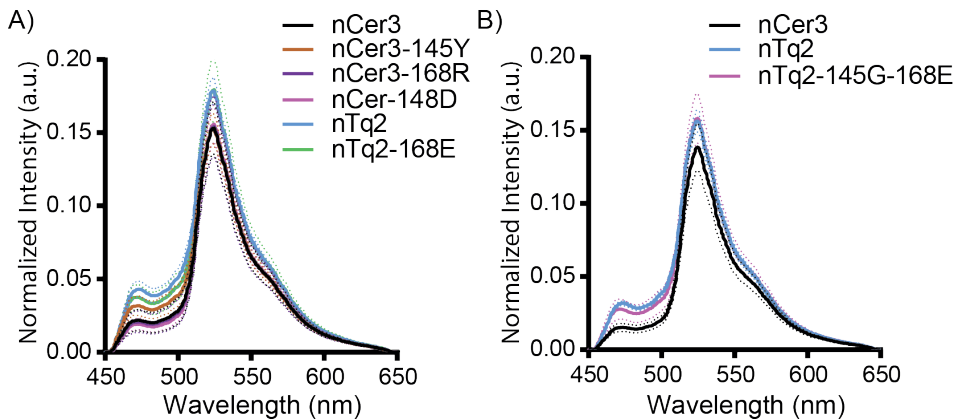
We performed the fluorescence lifetime measurements with a Nikon Eclipse Ti-E inverted microscope equipped with a LIFA system (Multi-Led illumination and LI2CAM; Lambert Instruments) (Bindels et al., 2017; Mastop et al., 2017). The modulated 446nm (mTurquoise2) or 470nm (mNeonGreen) LED excitation light passed through a 448/20BP (FF01-448/20, Semrock) (mTurquoise2) or a 470/30BP (FF02-472/30, Semrock) (mNeonGreen) excitation filter, reflected towards the sample by a 442nm (Di02-R442, Semrock) (mTurquoise2) or 488nm (Di02-R488, Semrock) (mNeonGreen) dichroic mirror and focused using a 40x objective (Plan Apo 40x NA 0.95 air, MDR01405). The emission was filtered by a 482/25BP (FF01-482/25, Semrock) (mTurquoise2) or a 520/35BP (FF01-520/35, Semrock) (mNeonGreen). The LI-FLIM software (LI-FLIM 1.223 Lambert Instruments) recorded 18 phase steps (with three times averaging) in pseudorandom order at a frequency of 40MHz. Erythrosine B (198269, Sigma-Aldrich) dissolved in ddH₂O was used as reference dye (fluorescence lifetime 0.086ns; ten times averaging for reference stack). After background subtraction and 3x3 blurring, the lifetimes were calculated by the LI-FLIM software.

In vivo brightness analysis

HeLa cells were transfected with tandem FP constructs encoding a protein of interest, P2A sequence and mTurquoise2 or mScarlet-I as reference (Bindels et al., 2017). The P2A sequence allows for separate expression of both FPs in equal amounts. Imaging was performed on a widefield fluorescence microscope (Axiovert 200M; Carl Zeiss GmbH) equipped with a xenon arc lamp with monochromator (Cairn Research, Faversham, Kent, UK), using a 40x objective (oil-immersion Plan-Neo- fluor 40x/1.30; Carl Zeiss GmbH).

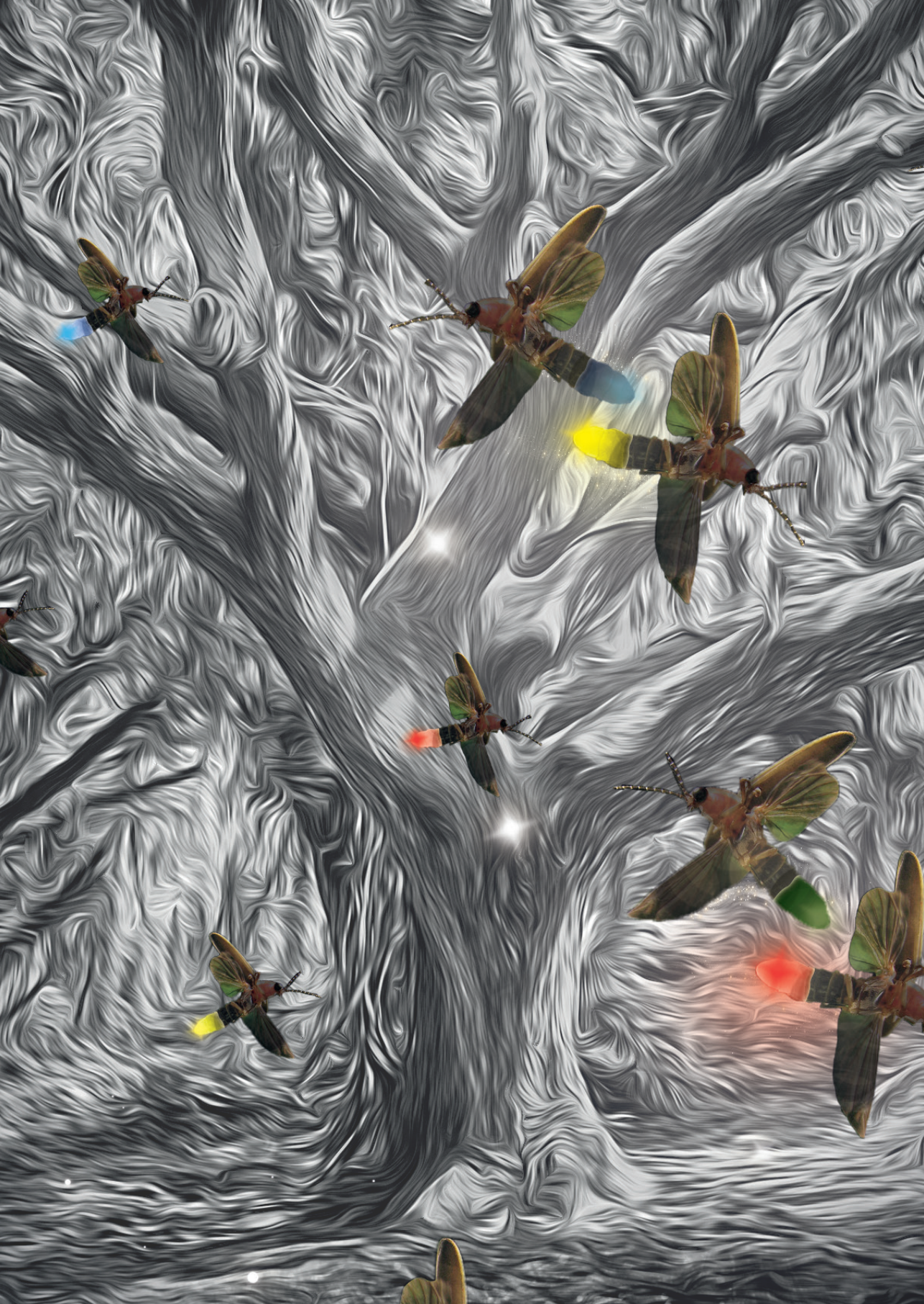
For figure 5, cells were excited with 420nm (mTurquoise2 variants) and 570nm (reference mScarlet-I) light and emission was detected with a 470/30BP (mTurquoise2 variants) and 620/60BP (reference mScarlet-I) filter. The images were corrected for background signal and the fluorescence intensity of the proteins of interest are plotted relative to the mScarlet-I fluorescence intensity, enabling comparison of brightness amongst these proteins of interest. For figure 6, cells were excited with 420nm (reference mTurquoise2) and 500nm (mNeonGreen) light and emission was detected with a 470/30BP (reference mTurquoise2) and 535/30BP (mNeonGreen variants) filter. The images were corrected for background signal and the fluorescence intensity of the proteins of interest are plotted relative to the mTurquoise2 fluorescence intensity, enabling comparison of brightness amongst these proteins of interest.

Supplemental Figures



Supplemental figure S1. FRET measurements of the DORA-RhoA FRET sensor, mutations potentially affecting stickiness.

(A-B) Spectral images of DORA-RhoA sensors in GTP-locked state expressing varying FRET donor FPs combined with nVenus-cp173. The sensor emission spectra were recorded from single living HeLa cells. The lines show the average emission spectrum and the dotted lines represent the 95%CI. The spectra are normalized to acceptor level. The lower the first peak, the higher the donor quenching. The higher the second peak, the higher the sensitized emission. The two graphs show data from two independent experiments on different days. The number of cells analyzed is $n=10$ per DORA-RhoA sensor variant.





4. A FRET based biosensor for measuring Gα13 activation in single cells

Marieke Mastop¹, Nathalie R. Reinhard¹, Cristiane R. Zuconelli², Fenna Terwey¹, Theodorus W.J. Gadella Jr.¹, Jakobus van Unen^{1,3}, Merel J.W. Adjobo-Hermans², and Joachim Goedhart¹

¹Swammerdam Institute for Life Sciences, Section of Molecular Cytology, van Leeuwenhoek Centre for Advanced Microscopy, University of Amsterdam, Amsterdam, The Netherlands.

²Department of Biochemistry, Radboud Institute for Molecular Life Sciences, Radboud University Medical Center, Nijmegen, The Netherlands.

³Current address: Department of Biology, Institute of Cell Biology, University of Bern, Bern, Switzerland.



Abstract

Förster Resonance Energy Transfer (FRET) provides a way to directly observe the activation of heterotrimeric G-proteins by G-protein coupled receptors (GPCRs). To this end, FRET based biosensors are made, employing heterotrimeric G-protein subunits tagged with fluorescent proteins. These FRET based biosensors complement existing, indirect, ways to observe GPCR activation. Here we report on the insertion of mTurquoise2 at several sites in the human G α 13 subunit, aiming to develop a FRET-based G α 13 activation biosensor. Three fluorescently tagged G α 13 variants were found to be functional based on i) plasma membrane localization and ii) ability to recruit p115-RhoGEF upon activation of the LPA2 receptor. The tagged G α 13 subunits were used as FRET donor and combined with cp173Venus fused to the Gy2 subunit, as the acceptor. We constructed G α 13 biosensors by generating a single plasmid that produces G α 13-mTurquoise2, G β 1 and cp173Venus-Gy2. The G α 13 activation biosensors showed a rapid and robust response when used in primary human endothelial cells that were exposed to thrombin, triggering endogenous protease activated receptors (PARs). This response was efficiently inhibited by the RGS domain of p115-RhoGEF and from the biosensor data we inferred that this is due to GAP activity. Finally, we demonstrated that the G α 13 sensor can be used to dissect heterotrimeric G-protein coupling efficiency in single living cells. We conclude that the G α 13 biosensor is a valuable tool for live-cell measurements that probe spatiotemporal aspects of G α 13 activation.

Introduction

G-protein coupled receptors (GPCRs) are members of a large family of membrane located receptors, with around 750 genes encoding a GPCR identified in the human genome (Vassilatis et al., 2003). These seven transmembrane containing proteins can perceive a wide variety of signals including light, hormones, ions and neurotransmitters (Wettschureck and Offermanns, 2005). GPCRs act as Guanine Exchange Factors (GEFs) (Rens-Domiano and Hamm, 1995) for heterotrimeric G-proteins. These protein complexes are comprised of a $G\alpha$, $G\beta$ and $G\gamma$ subunit. The heterotrimer is a peripheral membrane protein complex due to lipid modification of the $G\alpha$ and $G\gamma$ subunit (Wedegaertner et al., 1995).

The GEF activity is exerted on the $G\alpha$ subunit, which can be converted from an inactive GDP-bound state to an active GTP-bound state (Hepler and Gilman, 1992). The activation of the complex results in a conformational change and in some cases the dissociation of the $G\alpha$ subunit from the $G\beta\gamma$ dimer (Frank et al., 2005; Levitzki and Klein, 2002; Wettschureck and Offermanns, 2005). Both the activated GTP-bound $G\alpha$ subunit and $G\beta\gamma$ dimer are capable of activating downstream effectors (Wettschureck and Offermanns, 2005).

Almost twenty different $G\alpha$ subunits can be discerned and these are grouped in four classes; G_i/o , G_s , G_q and $G_{12/13}$ (Wettschureck and Offermanns, 2005). Throughout this manuscript we will use $G\alpha_{13}$ to indicate the subunit and G_{13} to indicate the heterotrimer, consisting of $G\alpha_{13}$, $G\beta$ and $G\gamma$, the same terminology will be used for $G_q/G\alpha_q$ and $G_i/G\alpha_i$, respectively. Each class of $G\alpha$ subunits activates different downstream effectors (Hepler and Gilman, 1992). The best characterized effectors of the $G\alpha_{12}/G\alpha_{13}$ subunits are RhoGEFs that activate RhoA, e.g. LARG, PDZ-RhoGEF and p115-RhoGEF (Aittaleb et al., 2010; Siehler, 2009). For quite some time, it was thought that GPCR activation of the $G\alpha_{12}/G\alpha_{13}$ subunits was the predominant way to activate RhoA. This view has changed over the last decade with the identification of RhoGEFs that can be activated by $G\alpha_q$ (Aittaleb et al., 2010; Rojas et al., 2007). Nowadays, it is clear that both $G\alpha_q$ and $G\alpha_{12}/G\alpha_{13}$ can rapidly activate RhoA signaling in cells (Reinhard et al., 2017; van Unen et al., 2016a), albeit by activating different effectors. Since the G_q class and $G_{12/13}$ class both efficiently activate RhoA, it has been difficult to distinguish which of these two heterotrimeric G-protein complexes is activated when only downstream effects are measured. To further complicate matters, GPCRs that activate $G_{12/13}$ often activate G_q as well (Riobo and Manning, 2005; Worzfeld et al., 2008). Yet, it is clear that signaling through either G_q or $G_{12/13}$ has different physiological effects (Takefuji et al., 2012; Wirth et al., 2008; Worzfeld et al., 2008). Therefore, it is necessary to have tools that can measure activation of the heterotrimeric G-protein itself.



Direct observation of heterotrimeric G-protein activation has classically been performed by quantifying the binding of radiolabeled nucleotides (Milligan, 2003). This approach is labor-intensive, uses disrupted cells and lacks temporal resolution. Moreover, this technique is generally less suitable for G_q , G_s and $G_{12/13}$, due to their low expression levels compared to G_i (Strange, 2010). On the other hand, optical read-outs, often based on FRET and Bioluminescence Resonance Energy Transfer (BRET) techniques are well suited to measure signaling activity with high temporal resolution in intact cells (Lohse et al., 2012; van Unen et al., 2015a). Several groups have generated BRET or FRET based biosensors for detecting events immediately downstream of activated GPCRs (Clister et al., 2015; Hébert et al., 2006; Lohse et al., 2012; Salahpour, 2012; van Unen et al., 2016c). Optical biosensors that are based on heterotrimeric G-proteins are particularly suited to report on GPCR activation (Janetopoulos and Devreotes, 2002). However, only a few optical biosensors for reporting activation of $G\alpha_{12}$ or $G\alpha_{13}$ have been reported.

Sauliere et al. reported a BRET based biosensor for detection of $G\alpha_{13}$ activation, enabling the detection of biased-agonism via the angiotensin II type 1 receptor (AT1R) (Saulière et al., 2012). The approach, however, lacks spatial resolution. Improved luciferases, such as Nanoluciferase, enabled single cell BRET measurements, but longer acquisition times are required, so temporal resolution is decreased (Goyet et al., 2016). In general, FRET-based sensors have higher emission intensities, requiring shorter acquisition times to obtain sufficient spatial and temporal resolution. Thus, development of a FRET based biosensor reporting on the activation of $G\alpha_{13}$ would be a real asset for GPCR signaling research. We have previously reported on single plasmid systems that enable the expression of a multimeric FRET based sensor for $G\alpha_q$ and $G\alpha_i$ (Goedhart et al., 2011; van Unen et al., 2016c). Here, we report on the development, characterization and application of a single plasmid, FRET based biosensor for the activation of $G\alpha_{13}$.

Results

Strategy for tagging $G\alpha_{13}$ with a fluorescent protein

To directly measure the activation of $G\alpha_{13}$ with high spatiotemporal resolution in living cells, we aimed at generating a functional, fluorescent protein (FP) tagged $G\alpha_{13}$ subunit. $G\alpha$ subunits cannot be tagged at the N- or C-terminus since these are required for interaction with the $G\beta\gamma$ subunit and the GPCR (Wall et al., 1995). To functionally tag $G\alpha_{13}$, the FP should be inserted in the $G\alpha_{13}$ sequence, as was previously done for other $G\alpha$ isoforms (Gibson and Gilman, 2006; Janetopoulos and Devreotes, 2002).

Initially, we used a sequence alignment of the four classes of $G\alpha$ -proteins and identified the residues of $G\alpha_q$ (Adjobo-Hermans et al., 2011) and $G\alpha_i$ (van Unen et al., 2016c) after which we had previously inserted mTurquoise2 (figure 1B and supplemental figure S1). Based on sequence homology, we chose to insert mTurquoise2 after

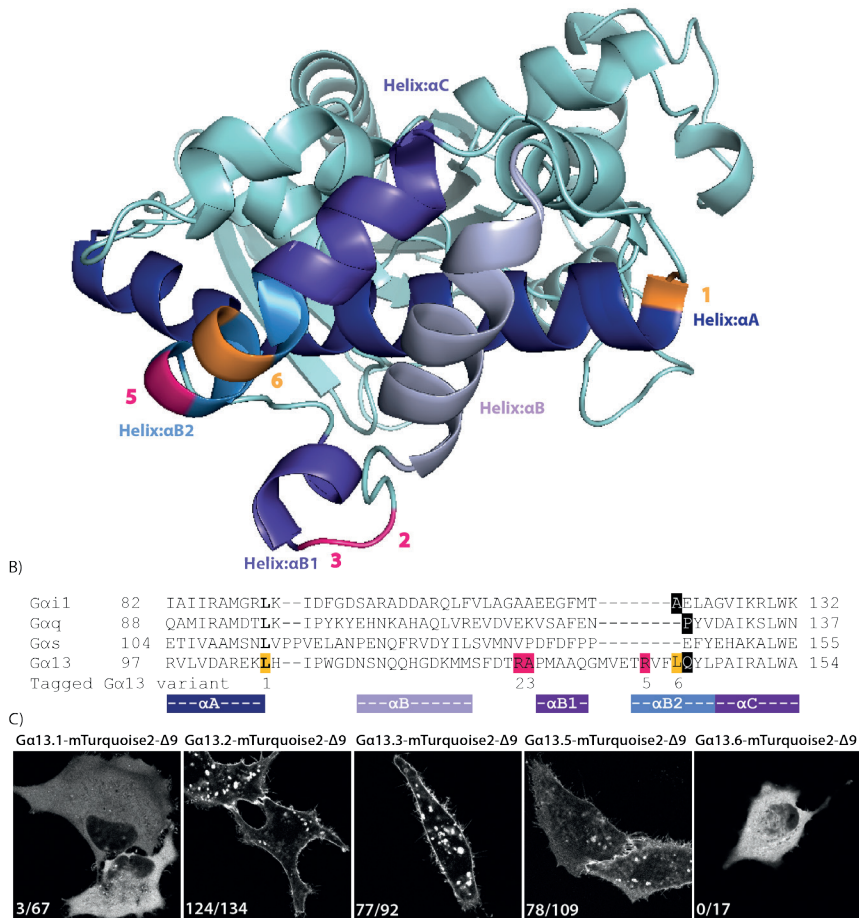


Figure 1. Insertion of a fluorescent protein at different positions in Ga13

(A) The protein structure of human Ga13 (PDB ID: 1ZCB). The highlighted residues indicate the amino acid preceding the inserted fluorescent protein. Successful sites for inserting mTurquoise2-Δ9 into Ga13 in pink and unsuccessful sites in orange.

(B) A partial protein sequence alignment (full alignment see S1 Fig) of different Ga classes. The highlighted residues indicate the amino acid preceding the inserted fluorescent protein (or luciferase). In bold, the sites that were previously used to insert Rluc (Saulière et al., 2012) pleiotropic and crosstalk signaling of GPCRs makes functional selectivity difficult to decode. To look from the initial active receptor point of view, we developed new, highly sensitive and direct bioluminescence resonance energy transfer-based G protein activation probes specific for all G protein isoforms, and we used them to evaluate the G protein-coupling activity of [(1. Insertion of mTurquoise2-Δ9 in Ga13 after residue Q144 (black) was based on homology with previous insertions in Gaq and Gai (black). Successful sites for inserting mTurquoise2-Δ9 (R128, A129 and R140) in pink and unsuccessful sites (L106 and L143) in orange. The numbers indicated below the alignment correspond with the Ga13 variant numbers, used throughout the manuscript. The colors under the alignment match with the colors of the αHelices shown in (A).

(C) Confocal images of the tagged Ga13 variants transiently expressed in HeLa cells. The numbers in the left bottom corner of each picture indicate the number of cells that showed plasma membrane localization out of the total number of cells analyzed. The tagged Ga13 variants also localize to structures inside the cell, which are presumably endomembranes. The width of the images is 76μm.



residue Q144 of human Gα13, indicated with a black rectangular box in the alignment. Upon transfection of the plasmid encoding this variant, we observed cytoplasmic fluorescence. This localization probably reflects incorrect folding or targeting of the Gα subunit, since well-folded and functionally tagged variants are located at the plasma membrane (Adjobo-Hermans et al., 2011; Gibson and Gilman, 2006). Inspection of the crystal structure (PDB ID: 1ZCB), revealed that Q144 is part of an α-helix (αB2), which is likely to be disrupted after modification or insertion (Kreutz et al., 2006).

Next, we used the protein structure to select a number of residues that were nearby previous insertion sites and next to or close to the end of an α-helix (αA, αB2 or αB1). We also took along an insertion site (L106) that was previously used to insert a luciferase into Gα13 (Saulière et al., 2012). We used a truncated mTurquoise2, deleting the last 9 amino acids, since this worked well in the Gi sensor (van Unen et al., 2016c). The insertion sites are highlighted on the protein structure and in the sequence alignment in figure 1A, B. The different variants are numbered as Gα13.1, Gα13.2, Gα13.3, Gα13.5 and Gα13.6 throughout the manuscript.

The plasmids encoding the different tagged variants were transfected into HeLa cells and we observed striking differences in localization. As shown in figure 1C, variant 1 and 6 showed cytoplasmic localization. In contrast, strong plasma membrane labeling was observed for variant Gα13.2, Gα13.3 and to a lesser extent for Gα13.5. Since native Gα13 is expected to localize at the plasma membrane by virtue of palmitoylation (Wedegaertner et al., 1995), we decided to continue with the optimization and characterization of variants 2, 3 and 5.

Functionality of the tagged Gα13 variants

The correct localization of the tagged Gα13 variants does not necessarily reflect functionality with respect to activity in signaling, i.e. the capacity to exchange GDP for GTP. To determine functionality, we turned to a dynamic cell-based assay. This assay is based on the observation that ectopic Gα13 expression is required for p115-RhoGEF relocation to the plasma membrane upon GPCR stimulation (Meyer et al., 2008). To evaluate the functionality of Gα13, we co-expressed the LPA2 receptor-P2A-mCherry (van Unen et al., 2016b), p115-RhoGEF, tagged with SYFP1, and different variants of Gα13, including an untagged, native variant (figure 2 and supplemental figure S2). Cells in which Gα13 was not over-expressed did not show p115-RhoGEF relocation after GPCR activation (figure 2B, C). However, in the presence of native Gα13, a relocation of p115-RhoGEF was noticed (figure 2B, C). These findings are in agreement with previous findings and show that a functional Gα13 is required for the recruitment of p115-RhoGEF to the plasma membrane. Next, similar experiments were performed in the presence of Gα13 variants 2, 3 and 5, tagged with mTurquoise2Δ9. In all three cases a robust relocation of p115-RhoGEF was observed (figure 2). In contrast, the relocation was not evident when a Gα13 variant (variant 1) was employed that did

not show efficient plasma membrane localization (figure 2B, C). Hence, we observed a correlation between membrane localization and functionality in the recruitment assay. Altogether, the results support the notion that the tagged variants 2, 3 and 5 of Gα13 can be activated by a GPCR and are capable of recruiting p115-RhoGEF.

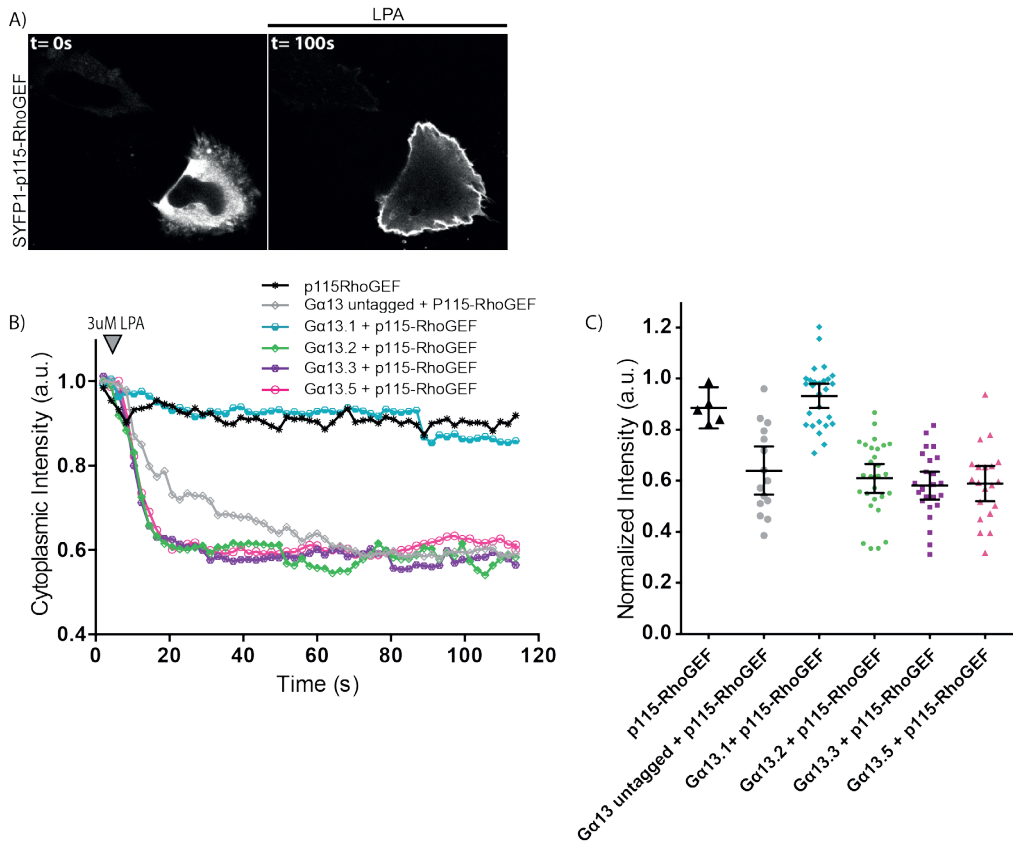


Figure 2. Capacity of the tagged Gα13 variants to recruit p115-RhoGEF.

(A) Confocal images of a representative HeLa cell expressing SYFP1-p115-RhoGEF, Ga13.2-mTurquoise2-Δ9 and LPA2-P2A-mCherry (here only SYFP1-p115-RhoGEF is shown, for the localization of the other constructs see S2 Fig) (before (t=0s) and after (t=100s) addition of 3μM LPA). The width of the pictures is 67μm.

(B) The mean cytoplasmic fluorescence intensity of SYFP1-p115-RhoGEF over time. After 8s, 3μM LPA was added. All cells transiently expressed LPA2 receptor-P2A-mCherry. The number of cells imaged is p115-RhoGEF $n=5$, Ga13 untagged + p115-RhoGEF $n=15$, Ga13.1 + p115-RhoGEF $n=27$, Ga13.2 + p115-RhoGEF $n=28$, Ga13.3 + p115-RhoGEF $n=24$, Ga13.5 + p115-RhoGEF $n=20$. Data have been derived from three independent experiments.

(C) Quantification of the fluorescence intensity at t=50s for each Ga13 variant, relative to t=0s. The dots indicate individual cells and the error bars show 95% confidence intervals. The numbers of cells analyzed is the same as in (B).



Evaluation of tagged Gα13 variants for measuring Gα13 activation

Having engineered several correctly localizing Gα13 variants capable of recruiting p115-RhoGEF, we examined whether these variants can be used to report on G13 activation. Using a FRET-based approach (as described for Gq (Adjobo-Hermans et al., 2011)), we monitored the interaction between the different generated mTurquoise2-tagged Gα13 constructs and a Gβγ dimer, consisting of untagged-Gβ and 173cpVenus-Gγ, on separate plasmids. These constructs allow acceptor (173cpVenus) – donor (mTurquoise2) FRET ratio measurements, where G13 activation results in a change in distance and/or orientation between the FRET pair, thereby inducing a FRET ratio decrease.

Here we co-expressed an untagged LPA2-receptor, with one of the three tagged Gα13 variants, untagged Gβ, and tagged Gγ. Upon LPA2-receptor activation, a FRET ratio change was observed for all three selected Gα13 variants (figure 3A). The Gα13.2 variant showed the largest FRET ratio change and the Gα13.5 variant the lowest (figure 3A). Some cells expressing the Gα13.3 variant showed a slower response (figure 3A).

Recently, a FRET sensor for Gα13 was reported that employed a tagged Ga and a Gβ subunit (Bodmann et al., 2017). Therefore, we also examined if tagging the Gβ subunit instead of the Gγ subunit yields a higher FRET ratio change for the best performing Gα13 variant. From figure 3B it can be inferred that tagging the Gγ subunit with the FRET acceptor results in the highest FRET ratio change upon activation of the Gα13 via the LPA2 receptor, which is consistent with our previous observations (Adjobo-Hermans et al., 2011).

Construction and characterization of FRET biosensors for Gα13 activity

We have previously shown for Gαq (Goedhart et al., 2011) and Gαi (van Unen et al., 2016c) activation biosensors that a single expression plasmid ensures robust co-expression of the sensor components and simplifies the transfection. Since all three tagged Gα13 variants are able to report on Gα13 activation using 173cpVenus-Gγ as FRET acceptor, we developed single plasmid sensors using each of the Gα13 variants. Figure 4A shows a schematic overview of the plasmid design for a Gα13 sensor. Analysis of CFP and YFP intensities from single cells show a better correlation for the single plasmid system as compared to cells transfected with separate plasmids (figure 4B).

As can be inferred from figure 4C, the subcellular localization of the different Gα13 sensors expressed in HeLa cells is similar. The Gα13 variants are mainly located at the plasma membrane and Gγ is located to the plasma membrane and endomembranes, as published (Goedhart et al., 2011). In Hek293T cells, however, transient expression of the Gα13.2 sensor lead to very round cells that easily detach (supplemental figure S3), suggesting that very high, transient expression of the sensor can result in enhanced basal Gα13 activity.

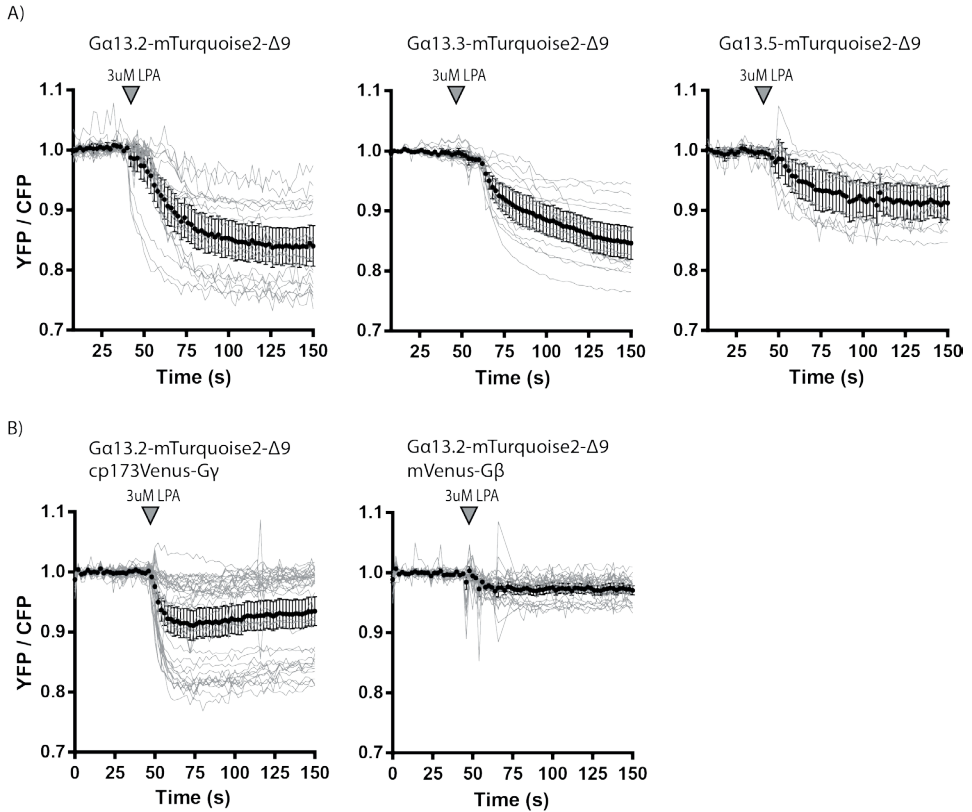


Figure 3. The ability of the tagged Ga13 variants to report on dynamic Ga13 activation via ratiometric FRET imaging.

(A) Ratiometric FRET traces of HeLa cells expressing the LPA2 Receptor (untagged), G β (untagged), one of the Ga13 variants (as indicated in the title of the graphs) tagged with mTurquoise2- Δ 9 and Gy tagged with cp173Venus. The grey lines represent individual cells and the black graph represents the average of which the error bars indicate the 95% confidence intervals. LPA was added at $t=42-50$ s, indicated by the arrowhead. The number of cells analyzed is: Ga13.2-mTurquoise2- Δ 9 $n=20$, Ga13.3-mTurquoise2- Δ 9 $n=16$ and Ga13.5-mTurquoise2- Δ 9 $n=11$. The data from panel A are acquired on multiple days.

(B) Ratiometric FRET traces of HeLa cells expressing the LPA2 Receptor (untagged), Ga13.2-mTurquoise2- Δ 9 and either G γ tagged with cp173Venus ($n=38$) (and untagged G β) or G β tagged with mVenus ($n=25$) (and untagged G γ). LPA was added at $t=50$ s, indicated by the arrowhead. The data from panel B are acquired on the same day.

Next, we evaluated the performance of the sensors in Human Umbilical Vein Endothelial cells (HUVEC). HUVECs are known to respond to thrombin, activating endogenous Protease Activated Receptors (PARs), which results in Ga13-RhoA signaling (Reinhard et al., 2016; Reinhard et al., 2017). We observed no effect of ectopic sensor expression in HUVEC. When thrombin was added to HUVECs, the Ga13.2 sensor showed the most

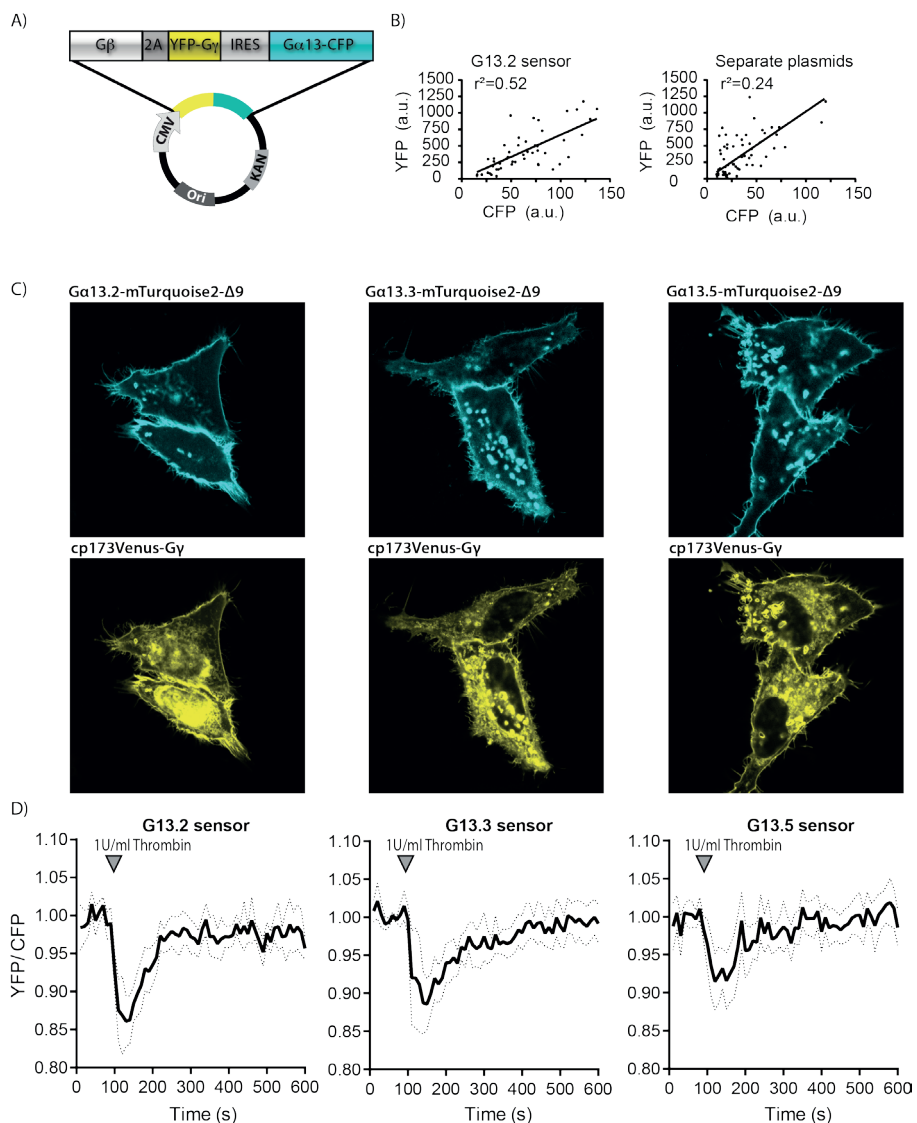


Figure 4. Development and characterization of Ga13 activation FRET based biosensors. (A) Architecture of the Ga13 biosensor construct, encoding Gβ₂-2A-cp173Venus-Gy₂-IRES-Ga13-mTurquoise2-Δ9, under control of the CMV promoter.

(B) CFP and YFP emission was measured from individual cells expressing the Ga13.2 sensor from a single plasmid or from cells transfected with separate plasmids that encoded Ga13.2 and cp173Venus-Gy₂. The r^2 is the correlation coefficient.

(C) Confocal images showing the localization of the Ga13 in the sensor variants (upper, cyan) and cp173Venus-Gy₂ (lower, yellow) in HeLa cells (for Ga13.2 sensor localization in Hek293T and HUVEC see S3 Fig). The width of the images is 75μm.

(D) FRET ratio traces of HUVECs expressing the different Ga13 biosensors, stimulated with Thrombin at t=100s (dotted lines depict 95% CI). For the corresponding YFP and CFP traces see S4 Fig. The number of cells analyzed is: Ga13.2 sensor $n=16$, Ga13.3 sensor $n=11$, Ga13.5 sensor $n=16$.

pronounced FRET change (figure 4D). This is in line with previously reported well-defined FRET change of the Ga13.2 sensor upon S1P stimulation in HUVECs (Reinhard et al., 2017). Based on the FRET ratio-imaging data in HUVECs and HeLa, we selected the Ga13.2 sensor as the Ga13 activation biosensor of choice due to its high sensitivity and robust FRET ratio change upon Ga13 activation.

Characterization of Ga13 inhibition by a GTPase Activating Protein

Our data show that the Ga13.2 sensor is sensitive enough to detect G13 signaling activated by endogenous thrombin receptors in HUVECs. We and others (Kelly et al., 2006; Martin et al., 2001; Reinhard et al., 2017) have used a Regulator of G-protein Signaling (RGS) domain of p115-RhoGEF as an inhibitor of G13 signaling. The RGS domain exhibits GTPase Activating Protein (GAP) activity (Kozasa et al., 1998). However, it is unclear whether the inhibition by the RGS domain in cells is due to GAP activity or due to competitive binding of the RGS domain and downstream effectors to Ga13. In the latter case, we would expect a change in FRET ratio in the presence of the RGS domain. To gain insight in the mechanism of action, we employed the Ga13.2 sensor and co-expressed a membrane bound RGS (Lck-mCherry-p115-RGS), which is shown to effectively inhibit RhoA activation (Reinhard et al., 2017).

In the presence of the RGS domain, we did not observe a FRET ratio change of the Ga13.2 sensor after adding thrombin to HUVECs (figure 5A, B and supplemental movie S1). In the control sample (Lck-mCherry) we did observe a ratio change of the Ga13.2 sensor induced by thrombin (figure 5A, B and supplemental movie S2), while resting state FRET ratios were similar for both conditions. The lack of a FRET response in presence of the RGS domain, reflecting suppression of active GTP-bound Ga13, provides evidence that GAP activity is involved in the inhibitory effect of the RGS domain. Additionally, we looked into thrombin-induced contraction of HUVECs and show that over-expression of the RGS domain prevents cell contraction, even leading to an overall increase in cell area (figure 5C and supplemental movie S3). Together, these data show that the RGS domain inhibits the activation of Ga13 and the consequent activation of RhoA which effectively blocks cell contraction.

Application of the Ga13.2 biosensor in GPCR activation assays

Published data on GPCRs coupling to Ga13 is often based on indirect measures and since downstream signaling effects overlap with the downstream signaling effects of Gq, it is difficult to draw solid conclusions about the involvement of either subunit (Riobo and Manning, 2005). Our novel FRET sensor enables direct observation of Ga13 activation. Therefore, we evaluated the Gaq and Ga13 responses to the stimulation of a selection of GPCRs published as coupling to Ga13 (Inoue et al., 2012; Meyer et al., 2008; Navenot et al., 2009; Saulière et al., 2012). These experiments were performed in HeLa cells transiently expressing the corresponding GPCR. As a control, cells only expressing the Ga13 or Gaq sensor were stimulated, which did not elicit a noticeable

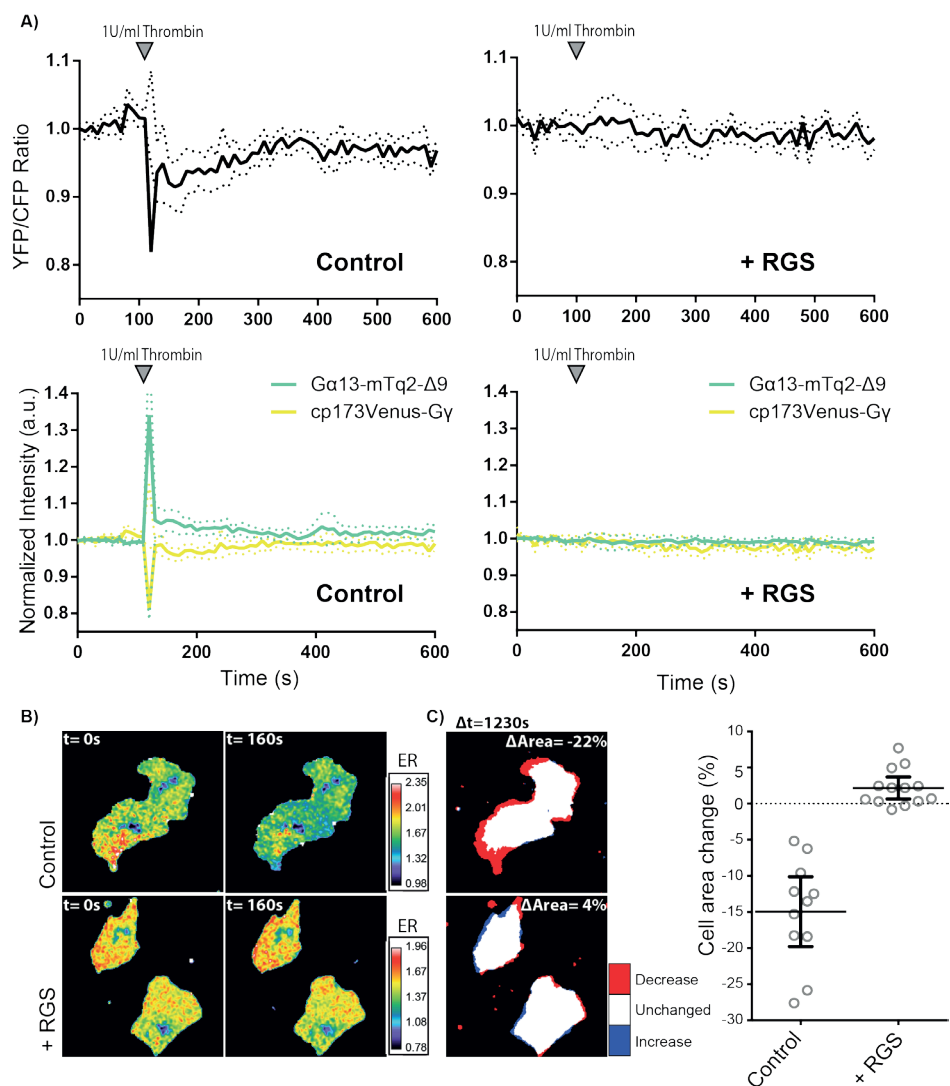


Figure 5. Effects of the p115-RhoGEF RGS domain on Ga13.2 activity and cell morphology.

(A) Normalized ratiometric traces (upper graphs) and corresponding YFP and CFP traces (lower graphs) (dotted lines depict 95% CI) of HUVECs that were transfected with either the Ga13.2 FRET sensor and Lck-mCherry (Control, $n=11$) or the Ga13.2 FRET sensor and Lck-mCherry-RGS (+ RGS, $n=13$). Cells were stimulated at $t = 110$ s.

(B) Ratiometric images of representative cells measured in (A). Cool colors represent low YFP/CFP ratios, corresponding to emission ratios (ERs) on the right.

(C) Cell area change of the cells measured in (B), visualized according to the LUT panel on the right. Dotplots on the right represent individual measurements (\pm 95% CI) of corresponding cells measured in (A). Image width = $54\mu\text{m}$.

sensor response (figure 6A). Upon LPA2 receptor (LPA2R) stimulation, Gαq and Gα13 were both activated, which corresponds to published data. Of note is that a number of cells (47 out of 60 for Gαq and 23 out of 37 for Gα13), transiently expressing the LPA2 receptor, failed to show a Gα13 or Gαq response (figure 6B). Upon Angiotensin II type 1 receptor (AT1R) stimulation a notable response of the Gαq sensor is observed as compared to a minimal response of the Gα13 sensor, which is similar to the control (compare figure 6C and 6A). The Kisspeptin receptor (KissR or GPR54) showed a clear Gαq and no Gα13 sensor response upon stimulation (figure 6D). Together, these results indicate that the LPA2R couples to both Gαq and Gα13, while the AT1R and KissR are coupled to Gαq and hardly or not to Gα13. Moreover, it shows that our novel Gα13 sensor can indeed be used to distinguish between Gα13- and Gαq-coupled GPCR signaling.

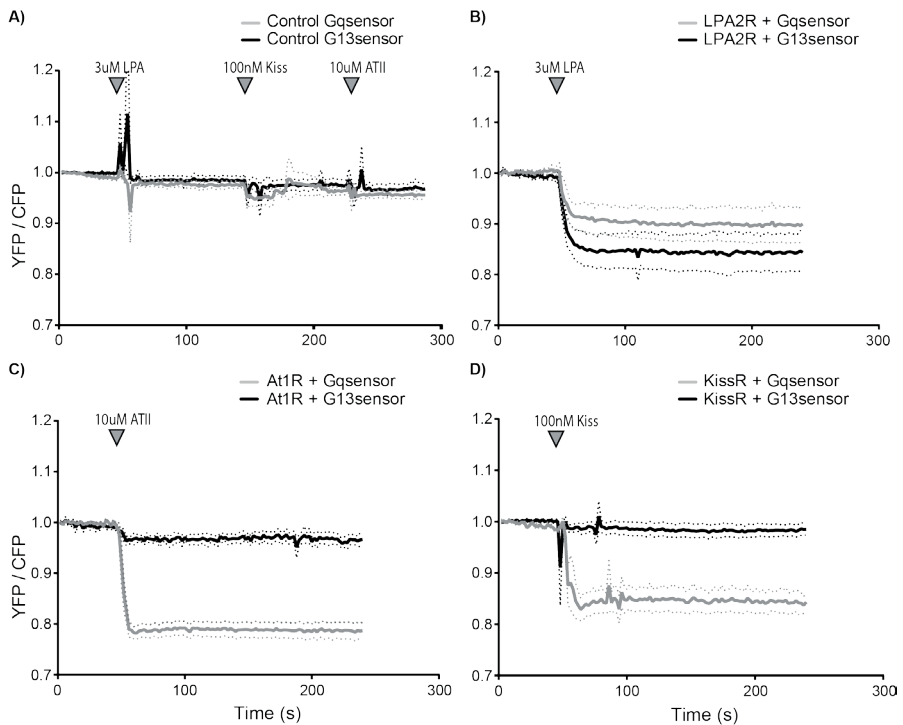


Figure 6. Direct observation of Gα13 and Gαq activation by different GPCRs.

Normalized ratio-metric FRET traces of HeLa cells transfected with the Gq sensor (grey line) or the G13.2 sensor (black line) (dotted lines depict 95% CI).

(A) As a control, cells expressing only the Gq ($n=37$) or G13.2 ($n=20$) sensor were measured. Agonists were sequentially added after 50s, 150s and 230s of imaging.

(B) Ratio traces of cells transfected with an untagged LPA2 receptor next to the Gαq ($n=13$ (out of 60 in total)) or the Gα13.2 ($n=14$ (out of 37 in total)), stimulated at $t=50$ s.

(C) Ratio traces of cells transfected with AngiotensinII type 1 receptor-P2A-mCherry next to the Gαq ($n=22$) or the Gα13.2 ($n=9$) sensor, stimulated at $t=50$ s.

(D) Ratio traces of cells transfected with an untagged kiss-receptor next to the Gαq ($n=13$) or the Gα13.2 ($n=30$) sensor, stimulated at $t=50$ s (indicated with the arrowhead).



Discussion

The combined activation of different heterotrimeric G-protein classes by a GPCR defines which signaling networks will be activated. For one of the classes of G-proteins, G12/13, it has been notoriously difficult to measure its activation. Here, we report on the development, characterization and application of a FRET based biosensor for Gα13 activation. This novel tool can be used to study the activation of Gα13 by GPCRs in single living cells. We furthermore show that the G13 sensor is sensitive enough to report on the activation of an endogenous receptor in human primary cells (HUVECs).

Thus far, the tools available to study the activation of Gα13 in single living cells have been limited. BRET-based strategies have been used to study activation of the G12 class. To this end, *Renilla reniformis* luciferase (Rluc) was inserted in Gα13 after residue Ile 108 (Ayoub et al., 2010) or Leu 106 (Saulière et al., 2012). However, we find that insertion of mTurquoise2 after residue Leu 106 (Gα13.1) does not result in a functionally tagged subunit, possibly because Leu106 is part of an α -helix.

Three of the five evaluated mTurquoise2 insertion sites resulted in plasma membrane localized, tagged Gα13, which were able to recruit p115-RhoGEF to the plasma membrane. The cytoplasmic-localized, tagged Gα13.1 variant was not able to recruit p115-RhoGEF, indicating that plasma membrane localization is required for functionality. Since all functional Gα13 variants could report on G13 activation as determined by FRET ratio-imaging, we developed single plasmid sensors for these three variants. In HeLa cells the localization is as expected, Gα13 at the plasma membrane and Gγ at the plasma membrane and endomembranes. The Gα13 activation biosensors were expressed in HUVECs and could report on G13 activation via endogenous Protease Activated Receptors (PARs). The Gα13.2 sensor is the best performing Gα13 biosensor, based on its sensitivity and magnitude of the FRET ratio change upon activation. Further improvement of the sensors might be achieved by varying FRET pairs (Mastop et al., 2017) or changing their relative orientation by circular permutation (Fritz et al., 2013).

While our manuscript was in preparation, another mTurquoise2 tagged Gα13 variant was reported (Bodmann et al., 2017). In that study, the fluorescent protein was inserted after residue 127 of Gα13, closely resembling our Gα13.2 variant, and it showed plasma membrane localization. Moreover, Bodmann et al. observed a FRET change when an YFP tagged Gα13 variant was used in combination with a CFP tagged Gβ subunit to report on the activation of the thromboxane A2 receptor (Bodmann et al., 2017). The independent observation of a FRET change using a similar tagged Gα13 variant, supports our notion that the G13.2 FRET based biosensor is a valuable tool for studying the activation of Gα13.

An advantage of our FRET sensor is that a higher ratio change is detected than for the sensor reported by Bodmann et al. 2017. While they detected a maximal FRET ratio change of 10%, we could reach a FRET ratio change of up to 25% (figure 3). This might be due to using a tagged G β instead of G γ subunit, since we also observe a lower FRET ratio change when a tagged G β is employed (figure 3B). It is remarkable that Bodmann et al. detect a FRET increase upon Ga13 stimulation (increased YFP, decreased CFP intensity) whereas we detect a FRET decrease upon Ga13 stimulation (figure 3B). All of the G-protein sensors reported by us (Gaq, Gai1,2,3 and Ga13) show a FRET decrease upon activation under all conditions tested thus far (Adjobo-Hermans et al., 2011; Reinhard et al., 2017; van Unen et al., 2016c), consistent with a dissociation of Ga and G $\beta\gamma$ subunits. Moreover, Ga13 subunits, tagged at different sites (Ga13.2, Ga13.3 and Ga13.5) all show a FRET decrease (figure 3). One notable difference is that we use a donor tagged G α 13 and Bodmann et al. use an acceptor (YFP) tagged G α 13. However, it is unclear how this difference would lead to opposite changes in FRET upon activation and as such, we do not have a solid explanation for the differences in FRET change observed by Bodmann et al. (Bodmann et al., 2017) and in this study.

An advantage of the sensor that we constructed, is that it enables the simultaneous production of the three proteins that comprise the heterotrimer from a single plasmid and that the donor and acceptor are present at a well-defined stoichiometry (Goedhart et al., 2011). This is evident from the better correlation between CFP and YFP emission intensities as compared to transfection of separate plasmids (figure 4B). Moreover, the single plasmid system simplifies the distribution and application of the sensor. Especially in primary cells, such as HUVECs, it is more complicated to obtain simultaneous protein expression from multiple plasmids, whereas transient expression of the single sensor plasmid in HUVECs was efficient.

The RGS domain of p115-RhoGEF effectively inhibits GPCR-Ga12/13 mediated RhoA activation in endothelial cells (Reinhard et al., 2017) and cell contraction as shown in figure 5C. Under these conditions, the Ga13.2 sensor did not display a FRET ratio change, reflecting a lack of activation. The absence of a FRET change is consistent with the idea that the GAP activity of the RGS domain shuts down Ga13 activity (Kozasa et al., 1998).

Applying the Ga13.2 sensor in HeLa cells, we showed that both Ga13 and Gaq are activated via the LPA2 receptor. In contrast, the Kiss receptor and the AT1 receptor elicited predominantly a Gaq sensor response. From our data it is not possible to judge whether the minor response of Ga13 upon AT1 receptor activation is biologically relevant. The GPCRs analyzed in this study, were reported as coupling to Ga13 and/or Gaq in other studies (Inoue et al., 2012; Meyer et al., 2008; Navenot et al., 2009; Saulière et al., 2012). Of note, transient expression of the LPA2 receptor shows several non-responders in terms of Gaq or Ga13 activity. This could be explained by insufficient levels of receptor to achieve detectable activation.



Strikingly, the Kiss receptor did not activate the Ga13 biosensor, indicating that a specific, promiscuous coupling of a GPCR to an ectopically expressed G-protein biosensor is not detected. Conversely, we previously observed that HUVECs treated with S1P do show Ga13 activation, but no Gαq activation (Reinhard et al., 2017). Together, these observations suggest that our FRET based biosensor toolkit provides a way to determine GPCR coupling selectivity towards heterotrimeric G-proteins in living cells. It would be advisable to complement such studies with more downstream read-outs to verify the possible perturbation by the ectopically expressed G-protein sensors.

In summary, the results obtained in this study point out that the Ga13.2 biosensor is a sensitive Ga13 activation sensor for live cell imaging, that is suitable for application in primary cells and able to detect endogenous GPCR activation.

Methods

Cloning/plasmid construction

mTurquoise2-Δ9 was inserted in the Ga13 sequence using a previously reported strategy (van Unen et al., 2016c). A PCR was performed on the mTurquoise2 sequence to truncate it and flank it with Agel sites using primers Fw 5'-ATACCGGTTCTATGGTGAGCAAGGGCG-3' and Rv 5'-TAACCGGTGATCCCGGCGGC-3'. To determine at which positions we wanted to insert mTurquoise2 in Ga13, we used Pymol to look at the structure of Ga13 and we used ClustalW to make an alignment of multiple Ga classes. A whole-vector PCR was performed on a pcDNA vector encoding human Ga13 (ordered from cDNA.org) to introduce an Agel restriction site at the spot where we wanted to insert mTurquoise2, using primers Fw 5'-ATACCGGTCATATTCCTGGGGAGACAAC-3' and Rv 5'-ATACCGTAAGCTTCTCTCGAGCATCAAC-3' for Ga13.1, primers Fw 5'-ATACCGGTGCCCCATGGCAGCCC-3' and Rv 5'-ATACCGGTCCGGGTATCAAACGACATCATCTTATC-3' for Ga13.2, primers Fw 5'-ATACCGGTCCCATGGCAGCCCAAGG-3' and Rv 5'-ATACCGGTGGCCGGGTATCAAACGAC-3' for Ga13.3, primers Fw 5'-ATACCGG-TGTTTTCTTACAATATCTTCTGCTATAAGA-3' and Rv 5'-ATACCGGTCTTGTTCACCATTCTTG-3' for Ga13.5 and primers Fw 5'-ATCCGGTCAATATCTTCTGCTATAAGAGCA-3' and Rv 5'-ATACCGGTTAAGAAAACCCTTGTTCACC-3' for Ga13.6. The Ga13 pcDNA vector including Agel site and the mTq2 PCR product were cut with Agel and ligated, resulting in mTurquoise2 tagged Ga13. Of note, the cloning of variant Ga13.4, with an insertion of mTurquoise2-Δ9 after T139, failed.

We used GFP-p115-RhoGEF (a kind gift of Keith Burridge, UNC, Chapel Hill, USA) as a template to amplify p115-RhoGEF with the primers Fw 5'-AACAGATCTCTTGGTACCGAGCTCGGATC-3' and Rv 5'-AGCGTCTGACTCAGTGCAGCCAGGCTG-3'. The PCR product, flanked with the restriction sites BglIII and Sall, was used to clone p115-RhoGEF into a clontech-style C1 vector, generating mVenus-p115-RhoGEF.

The untagged LPA2 receptor was ordered from cDNA.org. To create the clontech-style N1 LPA2 receptor-P2A-mCherry construct, a PCR was performed using primers Fw 5'-AGGTCTATATAAGCAGAGC-3' and Rv 5'-TATGTCGACTTGGGTGGAGTCATCAGTG-3'. The N1-P2A-mCherry construct, described previously (van Unen et al., 2016b) and the LPA2 receptor PCR product were digested with EcoRI and Sall and ligation resulted in the LPA2 receptor-P2A-mCherry construct.

The G13 single plasmid sensor variants were constructed as described previously by overlap-extension PCR (Heckman and Pease, 2007; van Unen et al., 2016c). The first PCRs were performed on the previously published Gaq sensor (Goedhart et al., 2011) using primerA Fw 5'-GAAGTTTTTCTGTGCCATCC-3' and primerB Rv 5'-GTCCGCCATATTATCATCGTGTTCCTCAAAG-3' and on the mTurquoise2 tagged Ga13 variants using primerC Fw 5'-ACGATGATAATATGGCGGACTTCCTGC-3' and primerD Rv 5'-ATCAGCGGGTTAAACG-3'. The second PCR was performed on a mix of both PCR products using primerA and primerD. This second PCR product and the Gaq sensor were digested with SacI and XbaI and the PCR product was ligated into the sensor, resulting in a G13 single plasmid sensor.

Lck-mCherry-p115-RhoGEF-RGS was constructed as described before (Reinhard et al., 2017). The p115-RhoGEF-RGS domain (amino acid 1-252) was PCR amplified using Fw 5'-GAGATCAGATCTATGGAAGACTTCGCCCCGAG-3' and Rv 5'-GAGATCGAATTCTTAGTTCCCCATCACCTTTTTC-3'. The PCR product and clontech-style C1 Lck-mCherry vector were digested with BglII and EcoRI and ligation resulted in a clontech-style C1 vector encoding Lck-mCherry-p115-RhoGEF-RGS.

The untagged Kiss receptor was purchased from www.cDNA.org.

The rAT1aR-mVenus was a kind gift from Peter Várnai (Semmelweis University, Hungary). The coding sequence of AT1R was inserted into mCherry-N1 with a P2A peptide to obtain AT1R-P2A-mCherry.

Cell culture and sample preparation

HeLa cells (CCL-2, American Tissue Culture Collection; Manassas, VA, USA) were cultured in Dulbecco's modified Eagle's medium (DMEM) (Gibco, cat# 61965-059) supplemented with 10% fetal bovine serum (Invitrogen, cat# 10270-106), 100U/ml penicillin and 100 µg/ml streptomycin at 37 °C in 7% CO₂. For microscopy experiments, cells were grown on 24mm Ø round coverslips, 0.13–0.16 mm thick (Menzel, cat# 360208) to 50% confluency and transfected with 500ng plasmid DNA, 1 µL Lipofectamin 2000 (Invitrogen, cat# 11668-019) or 4.5 µl PEI (1 mg/ml) in water (pH 7.3) and 100 µl OptiMEM (Gibco, cat# 31985-047) per 35mm Ø dish holding a 24mm Ø coverslip. One day after transfection the coverslip was mounted in a cell chamber (Attofluor, Invitrogen). Microscopy medium (20 mM HEPES (pH=7.4), 137 mM NaCl, 5.4 mM KCl,



1.8 mM CaCl₂, 0.8 mM MgCl₂ and 20 mM glucose) was added to the coverslip in the cell chamber. The ratiometric FRET experiments were performed at 37 °C.

Primary HUVECs, acquired from Lonza (Verviers, Belgium) were seeded on fibronectin (FN)-coated culture flasks. HUVECs, grown in EGM-2 medium, supplemented with singlequots (Lonza) at 37 °C in 5% CO₂. For microscopy experiments HUVECs were transfected at passage #4 or #5 with a Neon transfection system (MPK5000, Invitrogen) and Neon transfection kit (Invitrogen) and grown on FN-coated 24mm Ø round coverslips, 0.13–0.16 mm thick (Menzel, cat# 360208). Per transfection, 2 µg plasmid DNA was used and a single pulse was generated at 1300 Volt for 30 ms. (Reinhard et al., 2017). The ratiometric FRET experiments were performed at 37 °C in EGM-2 medium and in 5% CO₂.

Confocal microscopy

To obtain confocal images of live HeLa cells transiently expressing either a tagged Ga13 variant or G13 single plasmid sensor, a Nikon A1 confocal microscope, equipped with a 60x oil immersion objective (Plan Apochromat VC, NA 1.4), was used. The pinhole size was set to 1 Airy unit. To check the localization of tagged Ga13 variants, samples were excited with a 457nm laser line, a 457/514 dichroic mirror was used and the emission was filtered through a 482/35BP filter. To check the localization of the G13 single plasmid sensor constructs, samples were excited with a 440nm (CFP) and a 514nm (YFP) laser line, a 457/514 dichroic mirror was used and the emission was filtered through a 482/35BP (CFP) or 540/30BP (YFP), respectively. Images were acquired with sequential line scanning modus, to avoid bleedthrough.

p115-RhoGEF recruitment assay

For the p115-RhoGEF recruitment assay, HeLa cells were cultivated in RPMI medium supplemented with 10% fetal calf serum and L-Glutamine (2 mM) (PAN Biotech GmbH, Aidenbach, Germany) and kept at 37 °C in a 5% CO₂ atmosphere. Cells were harvested, and 50.000 cells/well were seeded in eight-well µ-slides (Ibidi). After 24 hours, cells were transiently transfected with 0.25 µg of the LPA2receptor-P2A-mCherry, the SYFP1-p115-RhoGEF and the Ga13 variants tagged with mTurquoise2 (Ga13.1, Ga13.2, Ga13.3, Ga13.5). Transfection of HeLa cells was performed using Lipofectamine 3000 and Plus Reagent, according to the manufacturer's instructions (Invitrogen). Twenty-four hours after transfection, the growth medium was replaced by RPMI phenol red-free medium and measurements were performed after a total incubation time of 48h. Throughout the measurements, cells were kept at 37 °C. Cells were stimulated with Oleoyl-L-α-lysophosphatidic acid (10 µM, Sigma) at the indicated time point. Confocal images were taken with a Leica TCS SP5 laser scanning confocal microscope (Leica Microsystems, Mannheim, Germany) equipped with an HCX PL APO 63x, N.A. 1.2, water immersion lens. mTurquoise2 was excited at 458 nm and emission was detected between 465-500 nm; SYFP1 was excited at 514 nm and emission was detected

between 520-550 nm; mCherry was excited at 561 nm and emission was detected between 600-670 nm. To avoid bleedthrough, images were acquired in the sequential line scanning modus. Image analysis was performed with Fiji.

Widefield microscopy

Ratiometric FRET imaging HeLa cells

Ratiometric FRET experiments were performed on a wide-field fluorescence microscope (Axiovert 200 M; Carl Zeiss GmbH)(Adjobo-Hermans et al., 2011) equipped with a xenon arc lamp with monochromator (Cairn Research, Faversham, Kent, UK) and Metamorph 6.1 software, for 240s or 288s (controls in figure 6A) and with a time interval of 2s. The fluorescence intensity of the donor and acceptor were recorded with an exposure time of 200ms per image using a 40x objective (oil-immersion Plan-Neo- fluor 40x/1.30; Carl Zeiss GmbH). HeLa cells were used, expressing cp173Venus-Gy (or untagged Gy in figure 3B), untagged G β (or mVenus tagged G β in figure 3B) and one of the mTurquoise2 tagged G α 13 variants from multiple plasmids or expressing the single plasmid Gq-sensor or one of the G13 sensor variants. A GPCR is expressed from a separate plasmid, which was either untagged LPA2 receptor, untagged Kiss receptor or AngiotensinII type 1 receptor-P2A-mCherry. Fluorophores were excited with 420 nm light (slit width 30 nm), mTq2 emission was detected with the BP470/30 filter, YFP emission was detected with the BP535/30 filter and RFP emission was detected with a BP620/60 filter by turning the filter wheel. After 50s HeLa cells (unless stated otherwise) were stimulated with either a final concentration of 3 μ M LPA (Sigma), 100nM Kiss-1 (112-121) Amide (Phoenix pharmaceuticals) or 10 μ M angiotensin (Sigma). The curves were normalized to the average intensity of the first 5 frames that were recorded. ImageJ was used to perform a background correction and calculation of mean intensity of each cell for each time point. Cells that did not show a visible response were not used for the analysis. The total number of cells imaged and the number of cells analyzed ("the responders") are indicated in the figure legends.

Ratiometric FRET imaging HUVECs

To perform ratiometric FRET experiments on HUVECs we used the same microscopy equipment and filter settings as were used to perform ratiometric FRET imaging of HeLa cells, however there are some differences in the way the data is recorded. The HUVECs are imaged for 1230s with a time interval of 10s and the imaging is performed at 37 °C in EGM-2 medium and in 5% CO₂. After 110s, HUVECs were stimulated with a final concentration of 1U/ml thrombin (Haematologic Technologies). The image processing procedure that was used to display the change in cell area during live cell microscopy of HUVECs is described elsewhere (Reinhard et al., 2017). In order to show the FRET ratio in images of cells, imageJ was used. We first converted the CFP and the YFP stack to 32-bit type and corrected for background signal. Then the stacks were divided to obtain a YFP/CFP stack. We used the CFP stack to make a binary mask and multiplied this mask with the YFP/CFP stack. Finally, we applied a smooth filter to reduce noise and used the lookup table (LUT) to visualize changes in FRET ratio.

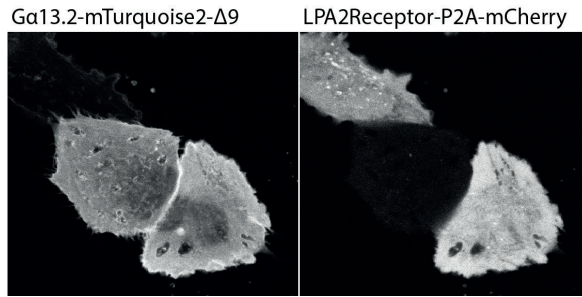


Supplemental Figures

Gai1	MGCTLS-----AEDKAAVERSKMIDRNLRDGEDGEKAAAREVK	36
Gaq	MTLESIMACCLS-----EEAKEARRINDEIERQLRRDKRDARRELKL	42
Gas	MGCLGNSKTEDQ--RNEEKAQREANKKIEKQLQKDKQVYRATHRL	43
Ga13	MADFLPSRSVLSVCFPGCLLTSGEAEQQRKSKEIDKCLSREKTYVKRLVKI	51
Gai1	LLLGAGESGKSTIVKQMKI IHEAGYSEEECKQYKAVVYSN-----TIQSI	81
Gaq	LLLGGTGESGKSTFIKQMRI IHGSGYSDEDKRGFTKLVYQN-----IFTAM	87
Gas	LLLGAGESGKSTIVKQMRI LHVNGFNNGEGEEDPQAARSNSDGEKATKVQDIKNNLKEAI	103
Ga13	LLLGAGESGKSTFLKQMRI IHGQDFDQRAREEFRPTIYSN-----VIKGM	96
Gai1	IAIIRAMGR LK --IDFGDSARADDARQLFVLAGAAEE-----GFMT A ELAGVIKRLWK	132
Gaq	QAMIRAMDT LK --IPYKYEHNKAAQLVREVDVEKVS A -----FEN PY VDAIKSLWN	137
Gas	ETIVAAMS NL VPPVELANPENQFRVDYILSVMNVPDFD-----FPPEFYEHAKALWE	155
Ga13	RVLVDAREK LH --IPWGDNSNQQHGDKMMSFD T R APMAAQGMVET R V F L O YLPAIRALWA	154
Gai1	DSGVQACFNRSREYQLNDSAAYYLNDLDRIAQPNYIPTQQDVLTRVKTGTGIVETHFTFK	192
Gaq	DPGIQECYDRRREYQLSDSTKYLLNDLDRVADPAYLPTQQDVLRVVPTTGIIEYPFDFLQ	197
Gas	DEGVRACYERSNEYQLIDCAQYFLDKIDVIKQADYVPSDQDLLRCRVLTSGIFETKFQVD	215
Ga13	DSGIQNAVDRRREFQLGESVKYFLDNLDKLGEPTYIPSQDILLARRPTKGIHEYDFEIK	214
Gai1	DLHFKMFDVGGQRSEKRWIHCPEGVTAIIFCVALSDDYDLVLAEDEEMNRMHESMKLFDS	252
Gaq	SVIFRMVDVGGQRSEKRWIHCFENVTSIMFLValseyDQVLVESDNENRMEESKALFRT	257
Gas	KVNFHMF'DVGGQRDERRKWIQCFNDVTAIIIFVASSSYNMVIREDNQTNRLQEALNLFKS	275
Ga13	NVPFKMVDVGGQRSEKRWFEFCFDSVTSILFLVSSSEFDQVLMEDRLTNRLTESLNIFET	274
Gai1	ICNNKWFTDTSIILFLNKKDLFEEKIKK--SPLTICYPEYA-----G-SNTYE	297
Gaq	IITYPWFQNSSVILFLNKKDLLEEKIMY--SHLVDYFPEYD-----GPQRDAQ	303
Gas	IWNRRWLRTISVILFLNKQDLAEKVLGKSKIEDYFPEFARYTTPEDATPEPGEDPRVT	335
Ga13	IVNNRVFSNVSIIILFLNKTDLLEEKVQI--VSIKDYFLEFE-----GDPHCLR	320
Gai1	EAAAYIQCFEDLNKRKDT--KEIYTHFTCATDTKNVQFVFDVAVTDVVIKNNLKDCLF	354
Gaq	AAREFILKMFVDLNPDS---KIIYSHFTCATDTENIRFVFAVKDTILQLNLKEYNLV	359
Gas	RAKYFIRDEFRLISTASGDGRHYCPHFCAVDTENIRRVFNDCRDI IQRMHLRQYELL	394
Ga13	DVQKFLVECFRNKRDRDQQ--KPLYHHFTTAINTENIRLVRFDVKDTILHDNLKQMLQ	377

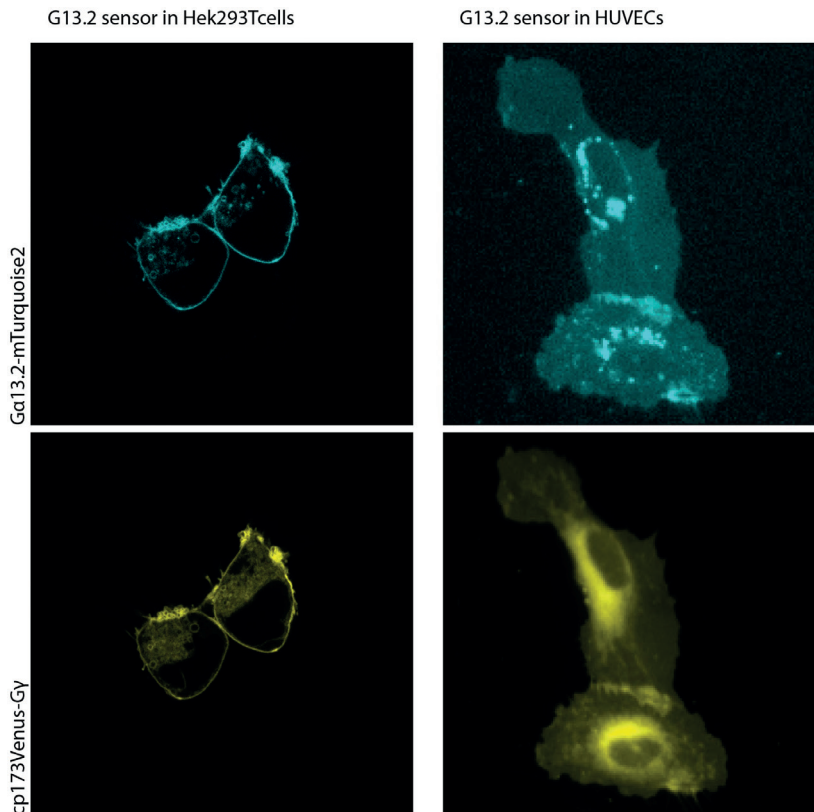
S1. Full amino acid alignment of four classes of human Ga subunits of heterotrimeric G-proteins.

Note that the amino acid sequence of Gas is that of the short isoform. The highlighted residues indicate the amino acid preceding the inserted fluorescent protein (or luciferase). In bold, the sites that were previously used to insert Rluc (Saulière et al., 2012). Insertion of mTurquoise2-Δ9 in Ga13 after residue Q144 (black) was based on homology with previous insertions in Gaq and Gai (black). Successful sites for inserting mTurquoise2-Δ9 (R128, A129 and R140) in pink and unsuccessful sites (L106 and L143) in orange.



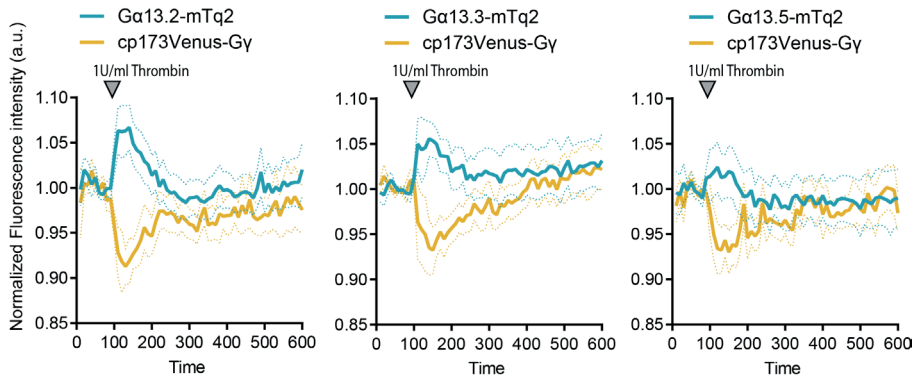
S2. Confocal images of HeLa cells expressing both the G α 13.2-mTurquoise2 (left) and LPA2-p2A-mCherry (right) used in p115-RhoGEF recruitment assay (figure 2).

The width of the images is 67 μ m.



S3. Confocal microscopy images of Hek293T cells (left) or widefield microscopy images of HUVECs, both expressing the G13.2 sensor.

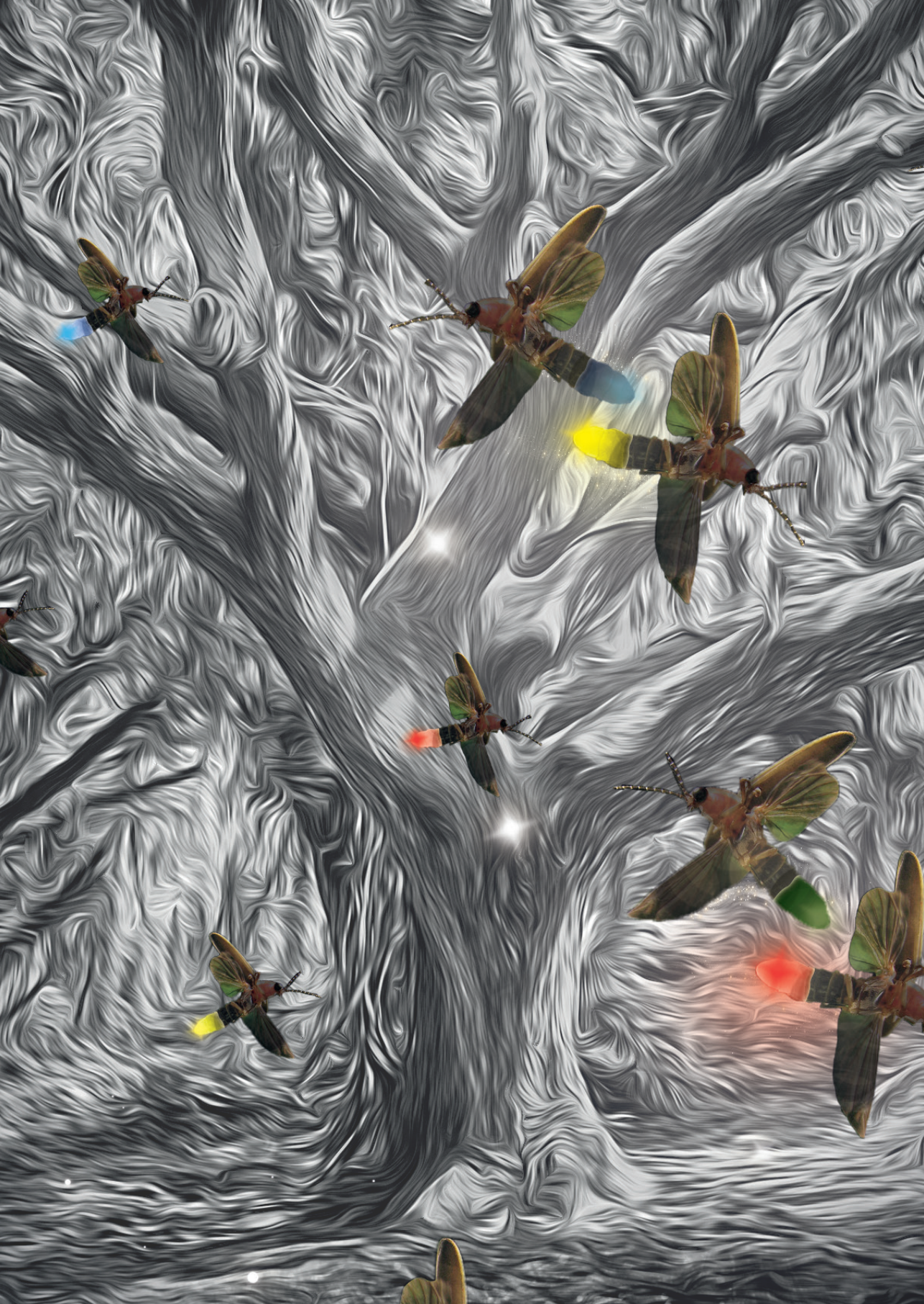
The upper images show G α 13.2 localization and the lower images show Gy localization. Hek293T cells were excited with 457nm (CFP) and 514nm (YFP) light and respectively, a 482/35BP and 540/30BP were used for detection of emission light. The width of the images is 70 μ m. HUVEC cells were excited with 420nm (CFP) and 490nm (YFP) light and respectively, a 470/30BP and 535/30BP were used for detection of emission light.



S4. The CFP and YFP traces of HUVECs expressing the different G13 biosensors, stimulated with 1 U/ml Thrombin at t=100s (dotted lines depict 95% CI).

The number of cells analyzed is: G13.2 sensor $n=16$, G13.3 sensor $n=11$, G13.5 sensor $n=16$.








5. Optimization of FRET pairs based on large Stokes-shift fluorescent proteins (LSS-FPs) for application in multiplex FRET imaging

Marieke Mastop¹, Nikki van Bommel¹, Sanne van der Niet¹, Emma Linssen¹, Marten Postma¹, Mark A. Hink¹, Theodorus W.J. Gadella Jr.¹, and Joachim Goedhart¹

¹Swammerdam Institute for Life Sciences, Section of Molecular Cytology, van Leeuwenhoek Centre for Advanced Microscopy, University of Amsterdam, Amsterdam, The Netherlands.





Abstract

In order to obtain novel insights in signaling pathways it is highly desirable to monitor several signaling events simultaneously with high temporal and spatial resolution. This can be achieved by the simultaneous use of multiple FRET-based biosensors in a multiplex FRET imaging experiment.

The aim of this study was to develop a FRET biosensor that can be combined with a CFP-YFP based sensor for the simultaneous detection of two processes in GPCR signaling. The sensor is designed such that it is excitable with the same wavelength of light as CFP-YFP based sensors, while providing orthogonal detection. A single excitation wavelength for exciting both FRET donors will increase the temporal resolution. Therefore, we chose to use mTurquoise2 and a large Stokes-shift (LSS) FP as FRET donors. After characterizing existing LSS-FPs, we selected mT-Sapphire for further optimization. Rational design resulted in a 2-fold brighter variant, LSS-SGFP2. We demonstrate that LSS-SGFP2 can be used as a FRET donor together with mScarlet-I or mCherry as FRET acceptor in living cells. The LSS-SGFP2-RFP FRET pairs could report on the activation of RhoA, Gq and G13. To further improve the performance of the LSS-SGFP2-mScarlet-I based unimolecular RhoA activation biosensors, circular permuted variants were generated. We report bright circular permuted LSS-SGFP2 and mScarlet-I variants that could be successfully applied in a unimolecular sensor. However, the assessed circular permuted variants did not confer improved sensor performance of the LSS-SGFP2-mScarlet-I RhoA activation sensor.

As a proof of principle, LSS-SGFP2 and mTurquoise2 were used as FRET donors in a multiplex FRET experiment, where both donors transferred energy to a common FRET acceptor, mScarlet-I. The emission signals of these three FPs are disentangled using spectral imaging and linear unmixing. The multiplex experiment enabled to simultaneously monitor the activation of Gq and G13.

Introduction

Fluorescent proteins derived from corals and jellyfish are valuable tools for visualizing proteins of interest in living mammalian cells, since they are entirely genetically encoded and do not require a co-factor (Chudakov et al., 2010; Tsien, 1998). Importantly, fluorescent proteins are widely employed in biosensors, for instance relying on Förster resonance energy transfer (FRET) between fluorescent proteins, to report on changes in the chemical state of the cell. These biosensors enable monitoring of cellular signaling events in single, living cells (Gadella Jr et al., 1999; Miyawaki, 2011; Piston and Kremers, 2007; Pollok and Heim, 1999). FRET is the radiationless transfer of energy from an excited donor to a nearby acceptor and it depends on several parameters. These parameters include, on one side, characteristics of the employed fluorescent proteins, such as brightness, oligomeric state, photostability, maturation efficiency and spectral overlap of the FRET pair; and on the other side, characteristics of the sensor design, such as linker length, linker composition, properties of the used sensing domains, and the relative dipole orientation of the fluorescent proteins in the sensor (Fritz et al., 2013; Mastop et al., 2017; Nagai et al., 2004; Shimozono et al., 2006; Vinkenborg et al., 2007). Biosensors are optimized to obtain the highest possible contrast in FRET efficiency between the “on” and “off” state of the sensor.

FRET-based biosensors are widely used to study many different aspects of cellular dynamics and their combined use is desirable to achieve temporal and spatial resolution of several events, simultaneously, in the same cell. One approach for multiplex FRET imaging uses a single excitation wavelength for two FRET donors with resolvable emission spectra. In this approach, large Stokes-shift FPs (LSS-FPs) are used (Laviv et al., 2016; Shcherbakova et al., 2012).

LSS-FPs are fluorescent protein variants with a Stokes-shift, the spectral distance between excitation and emission maxima, of more than 100nm. FPs exist as a mixture, containing protonated or deprotonated chromophores in the ground state. This was discovered already for wtGFP from *A. victoria*, which also partially exists as a large Stokes-shift variant (Tsien, 1998). The chromophore of non-LSS-FPs that contain a phenolate (tyrosine), is mostly deprotonated in the ground state caused by a strong proton network around the chromophore. Mutations in residues around the chromophore that alter this proton network may lead to an LSS-FP phenotype, where the chromophore is mostly protonated in the ground state. Protonated chromophores show a blue-shifted absorption spectrum, thereby increasing the Stokes shift. Excitation of a protonated chromophore highly increases its acidity, leading to a process called excited state proton transfer (ESPT). ESPT converts the chromophore into an intermediate state, via proton transfer over the hydrogen bonding network around the chromophore. The emission spectrum is similar to that of a non-LSS-FP from the same spectral class, because the chromophore becomes deprotonated in



the excited state. This explanation of the large Stokes-shift phenomenon shows how targeted mutagenesis can be used to introduce and optimize this feature in a FP of interest (Ai et al., 2007; Ai et al., 2008; Jung et al., 2005; Piatkevich et al., 2010; Shcherbakova et al., 2012; Tsien, 1998; Zapata-Hommer and Griesbeck, 2003).

FRET imaging with large Stokes-shift proteins excited at a single excitation wavelength offers several advantages, such as speed, no occurrence of donor-to-donor FRET, no need for very narrow bandpass filters, as would be the case when combining CFP-YFP with OFP-RFP based sensors, and reduced photochromism.

Imaging speed is important when dealing with fast-moving objects or when studying fast processes, such as GPCR signaling. When a single excitation wavelength is used for FRET imaging, in combination with a multisplit device that projects four emission channels on a camera, the intensities of four components can be acquired at once with no time delays (Niino et al., 2009). As a consequence, movement artifacts are avoided, and the imaging rate is determined by the time that is needed to acquire a single measurement.

Photochromism and photoconversion complicate quantitative microscopy methods. It has been shown that red fluorescent proteins (Bindels et al., 2017; De Keersmaecker et al., 2016; Kremers et al., 2009), or red-shifted FRET pairs (Goedhart et al., 2007; Mastop et al., 2017) are prone to photochromism or photoconversion when excited off-peak, e.g. with blue light. When a single excitation wavelength is used, both donors are excited near their absorbance peak. Still, acceptors should be chosen in such a way that photochromism is minimized. Furthermore, exciting two FRET donor FPs with the same wavelength of light, avoids FRET between the donor FPs.

Nowadays, several spectral variants of LSS-FPs are available, including mT-Sapphire (green) (Zapata-Hommer and Griesbeck, 2003), mAmetrine (yellow) (Ai et al., 2008) (Ding et al., 2011), LSSmOrange (orange) (Shcherbakova et al., 2012) and CyRFP (red) (Laviv et al., 2016). Of note, all these variants are used for multiplex FRET studies (Ai et al., 2008; Ding et al., 2011; Laviv et al., 2016; Niino et al., 2009; Shcherbakova et al., 2012).

The purpose of this research was to develop a sensor that can be used for multiplex FRET ratio-imaging, together with a popular CFP-YFP based sensor, in order to study simultaneous events in GPCR signaling.

First, we evaluated the characteristics of reported LSS-FPs. mT-Sapphire was selected for further optimization of FP characteristics to obtain a photostable, bright, monomeric, large Stokes-shift FP (LSS-FP) as FRET donor to combine with the bright monomeric mScarlet-I as FRET acceptor. Then, LSS-SGFP2-RFP FRET pairs were used

to measure the activation of RhoA, Gq and G13. In order to further optimize the FRET pair in the unimolecular RhoA sensor, the relative FP dipoles were varied by means of circular permutation. Several bright circular permuted variants of LSS-SGFP2 and mScarlet-I were constructed and successfully applied in the RhoA sensor. However, the assessed circular permuted FPs did not confer an improved performance of the LSS-SGFP2-mScarlet-I employed RhoA sensor. Finally, a multiplex FRET experiment was performed, where LSS-SGFP2 and mTurquoise2 were used as FRET donors, transferring energy to a common FRET acceptor, mScarlet-I. The emission signals of these three FPs are disentangled using spectral imaging and linear unmixing. The multiplex experiment enabled to simultaneously monitor the activation of Gq and G13. Further optimization of filter settings and sensor co-expression is required to enable simultaneous, ratiometric FRET measurements of CFP-YFP and LSS-SGFP2-mScarlet-I based sensors.

Results

Characterization of existing LSS-FPs

This study aimed to develop FRET based biosensors for simultaneous imaging, together with the abundantly available CFP-YFP equipped FRET sensors (Fritz et al., 2013; Goedhart et al., 2011; Nagai et al., 2004; Ponsioen et al., 2004; van Unen et al., 2016c). LSS-FPs are appealing, as FRET donor, since they can be excited with the same wavelength of light as CFP, while their emission signals remain distinguishable. Furthermore, donor-to-donor FRET does not occur between CFP and LSS-FPs, enabling less complicated data analysis compared to triple-color FRET experiments (Galperin et al., 2004; Pauker et al., 2012; Scott and Hoppe, 2015). Therefore, we set out to evaluate the characteristics of published LSS-FPs. We determined the brightness, photostability and dimerization tendency of green (mT-Sapphire), yellow (mAmetrine and mAmetrine1.2) and orange (LssmOrange) large Stokes-shift FP variants (Ai et al., 2007; Ai et al., 2008; Shcherbakova et al., 2012; Zapata-Hommer and Griesbeck, 2003). As can be inferred from figure 1, LssmOrange is least bright, not very photostable and tends to form dimers, therefore we chose not to continue with this fluorescent protein. mAmetrine1.2 is the brightest and despite low photostability and high tendency to dimerize, we tagged G_{aq} with mAmetrine1.2 to use in FRET experiments with a tagged G_γ, reporting G_q activation (Adjobo-Hermans et al., 2011). Figure 2A shows localization of G_{aq}-mAmetrine1.2 in the cytoplasm and as aggregates, suggesting loss of functionality since G_{aq} should be localized at the plasma membrane (Wall et al., 1995). The aberrant localization of mAmetrine1.2-tagged G_{aq} could be related to its high dimerization tendency (Snapp, 2009; Snapp et al., 2003). mAmetrine has a similar brightness to mAmetrine1.2 (figure 2B), next to lower photostability (figure 1B) and considerably lower tendency to form dimers (figure 1C). The lower dimerization tendency might make it a better tag for G_{aq}. Tagging G_{aq} with mAmetrine,



however, resulted in cytoplasmic localization (figure 2A). We introduced a mutation in mAmetrine (F208S) resulting in increased plasma membrane localization when used to tag Gαq (figure 2A). Gαq-mAmetrine (F208S) was used in a FRET experiment together with mCherry tagged Gγ (and untagged Gβ) to report on Gq activation upon histamine-1 receptor stimulation, which resulted in a very small FRET ratio change and clear photobleaching (figure 2C, D). These results led us to discard mAmetrine (F208S) as FRET donor candidate.

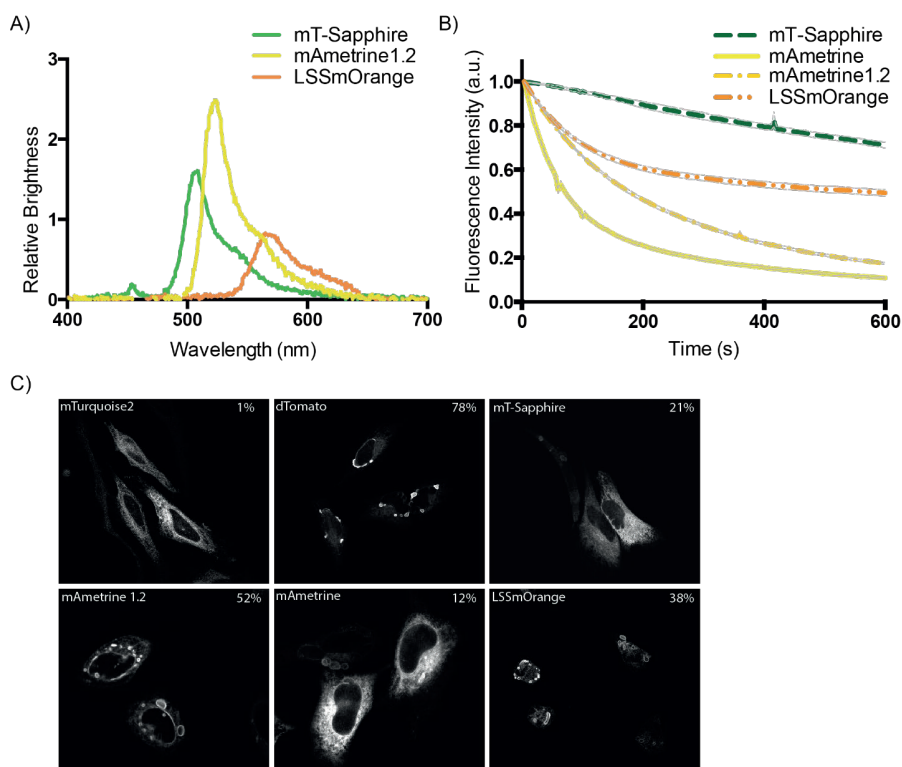


Figure 1. Characteristics of published LSS-FPs.

A) Spectral images showing the brightness of LSS-FPs relative to mTq2, employing a tandem FP construct with a T2A linker, resulting in separate and equal expression of the FPs. The number of cells analyzed is for mT-Sapphire $n=8$, mAmetrine1.2 $n=2$ and LSSmOrange $n=3$.

B) The graph shows the photostability of mT-Sapphire $n=36$, mAmetrine $n=20$, mAmetrine1.2 $n=27$ and LSSmOrange $n=25$, expressed in HeLa cells, imaged under continuous illumination for 600s. mT-Sapphire is excited with 400nm light at a power of 4.91mW, mAmetrine and mAmetrine1.2 are excited with 405nm light at a power of 4.91mW and LSSmOrange is excited with 440nm light at a power of 5.06mW. The initial fluorescence intensity was set on 100%. The dashed grey lines display the 95%CI.

C) Confocal images of HeLa cells expressing CytErm-FP fusion constructs that are used in the OSER assay to determine the dimerization tendency of FPs. The percentage of cells containing OSER structures is indicated in the right upper corner of the images. The number of cells analyzed is for mTurquoise2 $n=91$, dTomato $n=96$, mT-Sapphire $n=92$, mAmetrine1.2 $n=110$, mAmetrine $n=129$ and LssmO $n=58$. The width of the images is 188.29 μ m.

In summary, mT-Sapphire shows intermediate brightness, high photostability and a low tendency to dimerize. Therefore, we decided to continue with LSS-GFP variants.

The *in vitro* characterization of LSS-GFP variants

The mT-Sapphire exhibits moderate brightness in cells. We attempted to improve the brightness by targeted mutagenesis of different GFP variants. The LSS-GFP variants discussed in this paper were constructed by introducing mutations T65S and T203I in several GFP variants that were optimized for expression in mammalian cells, i.e. mEGFP, SGFP2 and msfGFP (superfolder GFP) (Kremers et al., 2007; Pédelacq et al., 2006; Tsien, 1998). We purified these LSS-GFP variants and determined the absorbance and emission spectra (figure 3A). Furthermore, molar extinction coefficient, quantum yield, *in vitro* brightness and pKa were determined (figure 3B and table 1). The spectra, molar extinction coefficient, quantum yield and pKa were similar to what was found for mT-Sapphire. *In vitro* evaluation with FCS showed that LSS-mEGFP and LSS-SGFP2 were 18% and 19% brighter than mT-Sapphire (table 1), respectively.

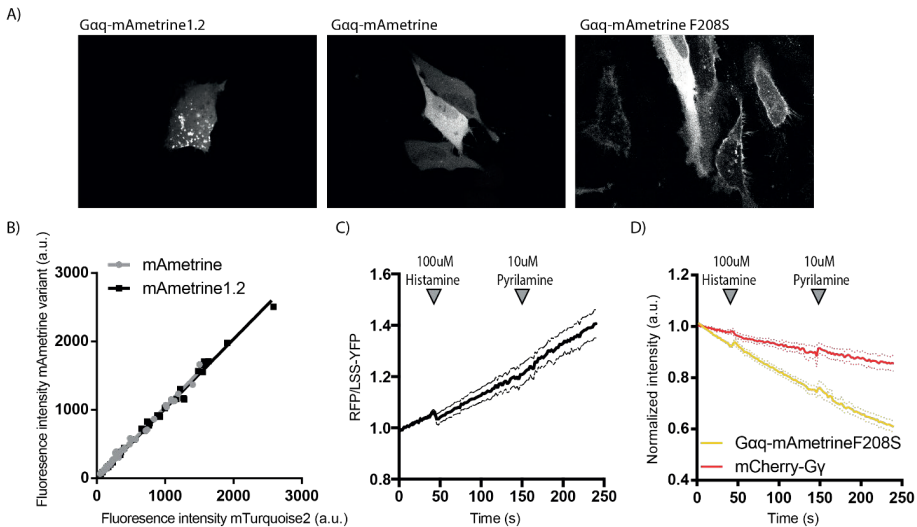


Figure 2. FRET using mAmetrine as Donor.

A) Confocal images of HeLa cells expressing Gaq tagged with mAmetrine1.2 (left), mAmetrine (middle) or mAmetrine mutated on residue 208 from phenylalanine to serine. The width of the images is 158 μ m.

B) The *in vivo* brightness of mAmetrine variants relative to mTurquoise2 by employing T2A constructs, resulting in the separate expression of the fluorescent proteins in equal amounts. The experiment is performed in HeLa cells. Each dot represents a single cell. The number of cells analyzed is $n=50$ for mAmetrine and $n=36$ for mAmetrine1.2.

C) Ratiometric FRET traces of HeLa cells expressing Gaq-mAmetrine F208S, untagged G β , mCherry-Gy and an untagged Histamine1 receptor ($n=15$) (dotted lines depict 95% CI). Histamine and pyrilamine were added at $t=50$ s and $t=150$ s respectively, as indicated by the arrowheads.

D) Normalized donor and acceptor traces of HeLa cells expressing Gaq-mAmetrine F208S, untagged G β , mCherry-Gy and an untagged Histamine1 receptor ($n=15$) (dotted lines depict 95% CI). Histamine and pyrilamine were added at $t=50$ s and $t=150$ s respectively, as indicated by the arrowheads.



Optimization of FRET pairs based on large Stokes-shift fluorescent proteins (LSS-FPs) for application in multiplex FRET imaging

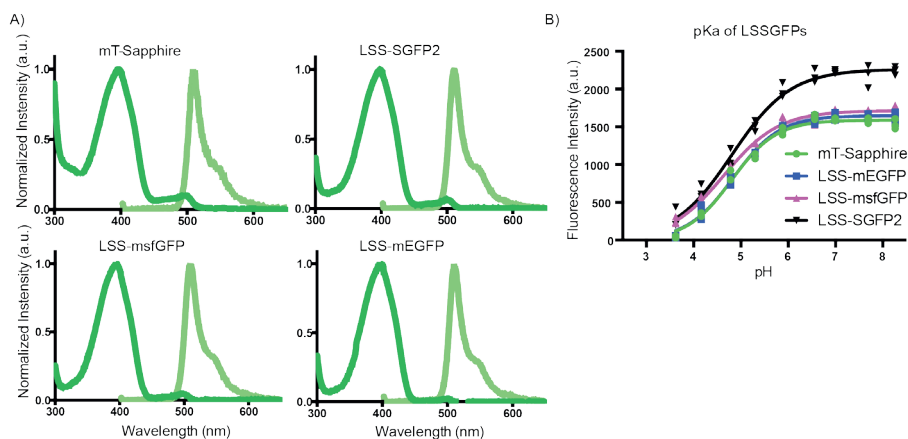


Figure 3. The *in vitro* characterization of LSS-GFPs.

A) Absorption and emission spectra of mT-Sapphire, LSS-SGFP2, LSS-mEGFP and LSS-msfGFP. The spectra were recorded from purified proteins and were normalized to their peak values. Dark green lines indicate absorption spectra and pale green lines indicate emission spectra.

B) The graphs show pH titrations versus fluorescence intensity of LSS-GFP variants, measured three times. The fitted curves are used to determine the pKa values of the fluorescent proteins (see table 1).

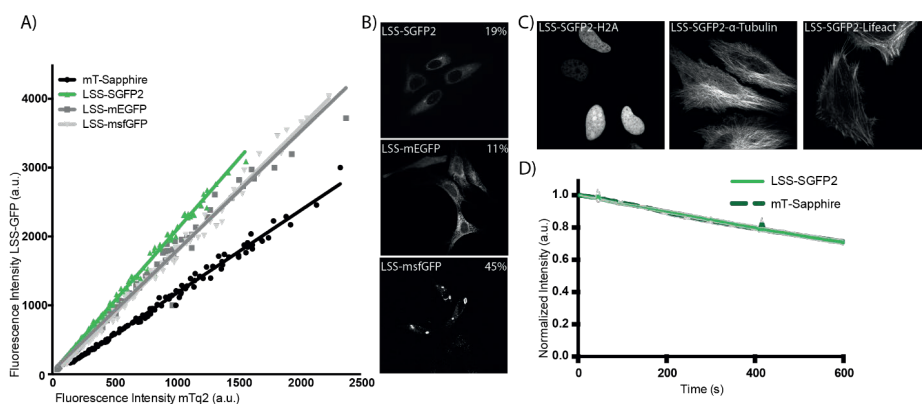


Figure 4. The *in vivo* characterization of LSS-GFPs.

A) The *in vivo* brightness of the LSS-GFPs relative to mTurquoise2 by employing T2A constructs, resulting in the separate expression of the fluorescent proteins in equal amounts. The experiment is performed in HeLa cells. Each dot represents a single cell. The number of cells analyzed is $n=126$ for mT-Sapphire, $n=125$ for LSS-mEGFP, $n=118$ for LSS-SGFP2 and $n=135$ for LSS-msfGFP.

B) Representative confocal images from the OSER assay to assess the dimerization tendency of FPs. mTurquoise2 is used as monomeric control and dTomato as dimeric control. The percentage of cells containing OSER structures is indicated in the right upper corner of the images. The width of the images is $188.3\mu\text{m}$.

C) Confocal images of HeLa cells expressing LSS-SGFP2 fused to either histone 2A, α -tubulin or Lifeact. The width of the images is $93.5\mu\text{m}$.

D) Photostability of mT-Sapphire ($n=36$) and LSS-SGFP2 ($n=30$), expressed in HeLa cells, imaged under continuous illumination for 600s. The FPs are excited with 400nm light at a power of 4.91mW. The initial fluorescence intensity was normalized to 100%. The dashed grey lines display the 95%CI.

The *in vivo* characterization of LSS-GFP variants

Since we aimed for applications in biosensors in living mammalian cells, all LSS-GFP variants were further characterized in living HeLa cells. The brightness was compared to mTurquoise2, which was co-expressed using a 2A peptide (Goedhart et al., 2010; Szymczak et al., 2004). As can be inferred from figure 4A and table 1, all new LSS-GFP variants are brighter than mT-Sapphire. Strikingly, the LSS-SGFP2 variant was 2-fold brighter than mT-Sapphire in cells.

The OSER assay is used to determine the dimerization tendency of the novel LSS-GFP variants (Costantini et al., 2012). The dimerization tendency is rather low and similar for mT-Sapphire, LSS-mEGFP and LSS-SGFP2, while LSS-msfGFP has a much higher dimerization tendency (figure 4B and table 1).

The chromophore of regular GFP predominantly exists in the deprotonated, anionic form, which has an excitation maximum around 488 nm. On the other hand, the chromophore in LSS-GFPs is protonated, giving rise to an excitation maximum at 400 nm. To examine to which extent the new variants have a neutral chromophore, we determined the 400/488 excitation ratio (Tsien, 1998). All new LSS-GFP variants have a higher 400/488 excitation ratio than mT-Sapphire (table 1), showing that the deprotonated chromophore dominates. The highest 400/488 excitation ratio is found for LSS-mEGFP. LSS-SGFP2 and LSS-msfGFP show similar excitation ratios (table 1).

We selected LSS-SGFP2 for the remainder of this study since it was the brightest variant in cells. Furthermore, the dimerization tendency and the 400/488 excitation ratio were respectively, similar and improved compared to mT-Sapphire (table 1). Additionally, we compared the photostability of LSS-SGFP2 with mT-Sapphire, showing a similar photostability under continuous illumination with 400nm light (figure 4D). Subsequently, we evaluated the ability of LSS-SGFP2 to functionally tag a protein of interest. LSS-SGFP2-tagged histon 2A (H2A), α -tubulin and lifeact, localizes to respectively, the nucleus, the microtubule network and the actin cytoskeleton, suggesting that the tagged proteins are functional (figure 4C). LSS-SGFP2 is the preferred LSS-GFP variant since it shows several improved characteristics compared to mT-Sapphire.

LSS-SGFP2 as FRET donor

In order to examine whether LSS-SGFP2 is a suitable FRET donor, we made tandem FP constructs either with a small linker resulting in high FRET or with a linker containing a viral T2A sequence resulting in equal amounts of separate proteins (Kim et al., 2011). In these constructs we compared LSS-SGFP2 with mT-Sapphire and as FRET acceptor, we tested mCherry and mScarlet-I. We observed a similar FRET efficiency for the tested FRET pairs (figure 5A). Figure 5A shows the increased brightness of LSS-SGFP2 compared to mT-Sapphire, and mScarlet-I as FRET acceptor shows a higher sensitized



Table 1. Characteristics of Large Stokes Shift fluorescent proteins (LSS-FPs).

The LSS-FPs reported in this paper are indicated with green shading and compared to previously published LSS-FPs. The molar extinction coefficient is measured two times (except for LssmsGFP), shown is the average and the 95%CI. The quantum yield is measured three times, shown is the average and the 95% confidence interval. The *in vitro* brightness of purified proteins is determined using FCS and is given relative to the brightness of mT-Sapphire, with the 98%CI. The *in vivo* brightness is determined relative to the brightness of mTq2, using tandem constructs with a T2A linker. The number of cells analyzed is $n=126$ for mT-Sapphire, is $n=125$ for LSS-mEGFP, is $n=118$ for LSS-SGFP2 and is $n=135$ for LSS-msfGFP, shown is the average *in vivo* brightness. The number of analyzed cells for determining the 400/488 excitation ratio is $n=117$ for mT-Sapphire, is $n=87$ for LSS-mEGFP, is $n=119$ for LSS-SGFP2 and is $n=108$ for LSS-msfGFP, shown is the average 400/488 excitation ratio and the 95%CI. The number of cells analyzed for the OSER assay is $n=92$ for mT-Sapphire, $n=131$ for LSS-mEGFP, $n=100$ for LSS-SGFP2, $n=116$ for LSS-msfGFP, $n=129$ for mAmetrine, $n=110$ for mAmetrine1.2 and $n=58$ for LSSmOrange. The average pKa value ($n=3$) is shown and the 95%CI.

Protein	Molar extinction QY coefficient ($10^3 \text{ M}^{-1} \text{ cm}^{-1}$)	Brightness		400/488 excitation ratio	Dimerization tendency (% cells with OSER structures)	pKa
		<i>in vitro</i> (FCS)	<i>in vivo</i>			
mT-Sapphire	33.7 ± 19.4	100 (79-109)	1.15	6 ± 0.2	21	4.8 ± 0.08
LSS-mEGFP	32.8 ± 6.7	118 (89-123)	1.86	15 ± 0.3	11	4.8 ± 0.07
LSS-SGFP2	35.2 ± 14.4	119 (110-126)	2.13	10 ± 0.2	19	4.8 ± 0.1
LSS-msfGFP	33.6	92 (65-114)	1.74	9 ± 0.1	45	4.6 ± 0.07
mAmetrine	$45^2 / 35^3$	-	-	-	12	6.0(Ai et al., 2008)
mAmetrine1.2	31^3	-	-	-	52	-
LSSmOrange	52^2	-	-	-	38	5.7(Shcherbakova et al., 2012)

emission than mCherry, which might result in a better contrast in ratiometric FRET imaging.

Based on these results, we selected the FRET pairs LSS-SGFP2 – mCherry and LSS-SGFP2 – mScarlet-I for our FRET biosensors. We made two DORA RhoA FRET sensors that report on RhoA activation (Bindels et al., 2017; Reinhard et al., 2016). As seen in figure 5B, both biosensors show FRET contrast and report on RhoA activation. As expected based on the increased sensitized emission, usage of mScarlet-I instead of mCherry as FRET acceptor leads to an increased FRET contrast, in agreement with other reported FRET sensors (Bindels et al., 2017; Mastop et al., 2017) (figure 5B).

In addition to the Rho sensors, we used both FRET pairs to construct FRET based Gq sensors. In contrast to the Gq sensor with mAmetrine(F208S) as FRET donor (figure 2B), Gaq-LSS-SGFP2 localized predominantly at the plasma membrane (figure 5C). By fusing the mCherry or mScarlet-I to G γ , two functional bimolecular Gq FRET sensors can be made with the same Gaq-LSS-SGFP2 donor. Both sensors could report on Gq activation, showing a similar FRET contrast (figure 5D).

Together, these results show that LSS-SGFP2 is an effective FRET donor in combination with mCherry or mScarlet-I in both bimolecular and unimolecular FRET-based biosensors. We chose LSS-SGFP2-mScarlet-I as FRET pair for further experiments, due to the improved characteristics of mScarlet-I and its superior performance in the unimolecular RhoA sensor.

Circular permuted LSS-SGFP2 and mScarlet-I variants

We set out to further improve the FRET contrast of the unimolecular DORA RhoA sensor employed with LSS-SGFP2 and mScarlet-I by varying the relative orientation of the fluorophores within this sensor, using circular permuted FP variants.

Promising sites for circular permutation of either LSS-SGFP2 or mScarlet-I were determined by comparing the protein structure of EGFP or mScarlet to the structures of FPs for which successful circular permutations were reported (Fritz et al., 2013; Nagai et al., 2004; Topell et al., 1999). We selected sites for circular permutation based on the successful circular permutation sites in Venus (49, 157, 173, 195, 229) (Nagai et al., 2004), GFPuv (38, 49, 102, 116, 157, 173, 204) (Topell et al., 1999) and mTFP (105, 159, 175, 227) (Fritz et al., 2013). Furthermore, the loops showing less conserved shapes were deemed interesting sites for circular permutation, since their variation in shape apparently does not affect the functionality of the FP. We selected positions 40, 118 and 135 due to their location in loops with a less conserved shape (figure 6A and figure 7A).

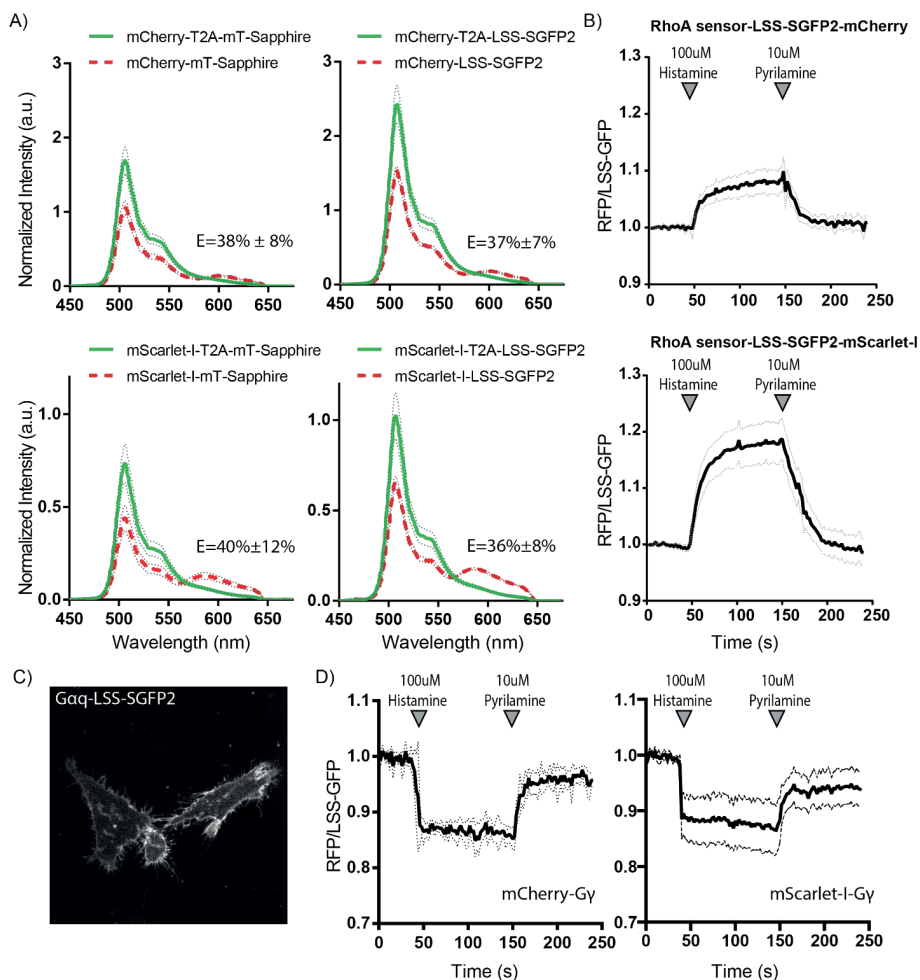


Figure 5. LSS-SGFP2 as FRET donor using RFPs as FRET acceptor.

A) Characterization of FRET pairs using either mT-Sapphire or LSS-SGFP2 as donor and either mCherry or mScarlet-I as acceptor. Emission spectra are recorded in living HeLa cells. Spectral images of fused donor and acceptor (red, dashed, thick lines) and constructs expressing both donor and acceptor separately in equal amounts due to a T2A linker, as a control (green, solid, thick lines). The 95% confidence interval is indicated with red (fusion) or green (control) thinner dotted lines. The fluorescence intensity is normalized to directly excited FRET acceptor FP fluorescence. The drop in donor fluorescence intensity in the fusion construct versus the control (T2A) construct enables calculation of the FRET efficiency (E) (shown in the graphs). The number of cells analyzed is $n=10$ for each construct.

B) C) Confocal image of HeLa cells expressing Gaq tagged with LSS-SGFP2. The width of the image is $95\mu\text{m}$.

D) Ratiometric FRET traces of HeLa cells expressing Gaq-LSS-SGFP2, untagged $G\beta$, mCherry-Gy (left, $n=6$) or mScarlet-I-Gy (right, $n=15$) and an untagged Histamine1 receptor (dotted lines depict 95% CI). Histamine and pyrilamine were added at $t=50\text{s}$ and $t=150\text{s}$ respectively, as indicated by the arrowheads.

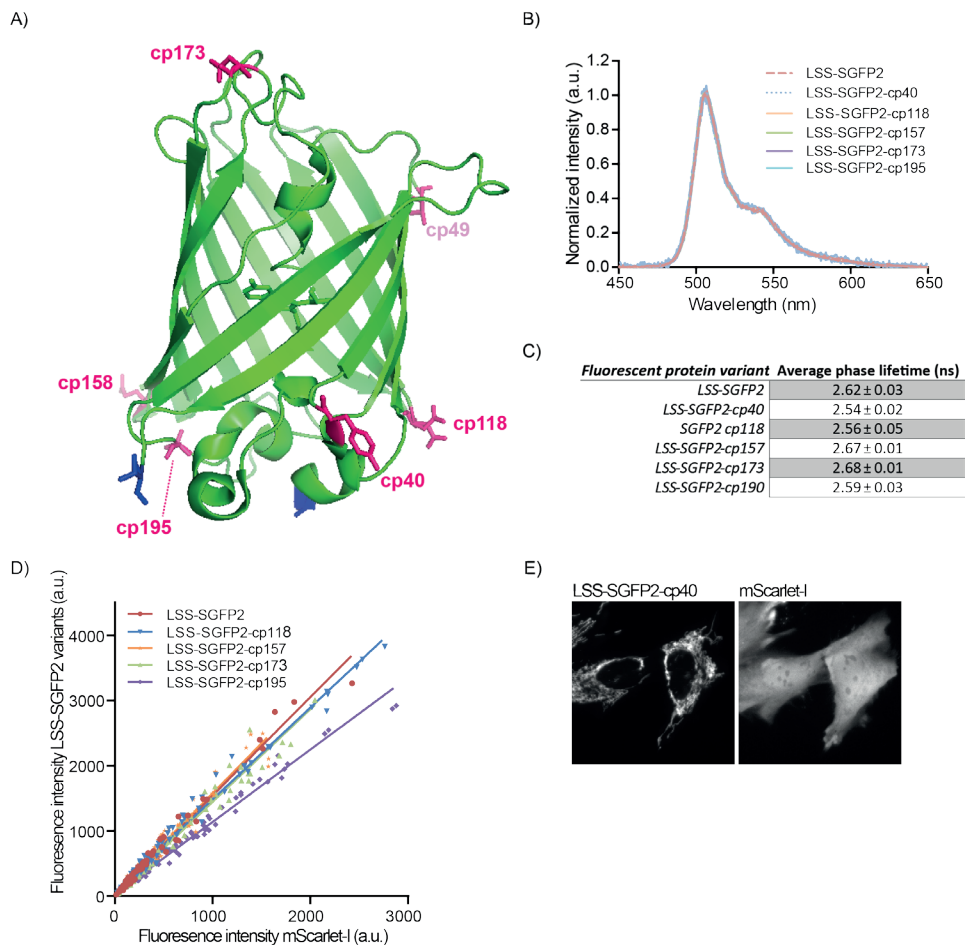


Figure 6. Design and characterization of LSS-SGFP2 circularly permuted variants.

A) The protein structure of EGFP (PDB ID: 2Y0G), which is used, together with literature research, to determine interesting sites for circular permutation of LSS-SGFP2. The beginning and end of the protein are highlighted in blue and the circular permutation sites tested are highlighted in pink. The highlighted residue is the start of the protein in the respective circularly permuted variant.

B) Emission spectra of LSS-SGFP2 and circularly permuted variants, in living HeLa cells, using spectral imaging, $n=3$ for LSS-SGFP2-cp40 and LSS-SGFP2-cp195; and $n=4$ for LSS-SGFP2, LSS-SGFP2-cp118, LSS-SGFP2-cp157 and LSS-SGFP2-cp173. Thinner dashed lines represent 95% CI.

C) Phase lifetimes of LSS-SGFP2 and circularly permuted variants, in living HeLa cells. The number of cells analyzed is $n=48$ for LSS-SGFP2; $n=41$ for LSS-SGFP2-cp40; $n=45$ for LSS-SGFP2-cp118; $n=48$ for LSS-SGFP2-cp157; $n=52$ for LSS-SGFP2-cp173; $n=47$ for LSS-SGFP2-cp195. Shown is the average \pm the 95% CI

D) The *in vivo* brightness of the LSS-SGFP2 variants relative to mScarlet-I by employing P2A constructs, resulting in the separate expression of the fluorescent proteins in equal amounts. The experiment is performed in HeLa cells. Each dot represents a single cell. The number of cells analyzed is $n=72$ for LSS-SGFP2; $n=81$ for LSS-SGFP2-cp118; $n=70$ for LSS-SGFP2-cp157; $n=98$ for LSS-SGFP2-cp173; $n=77$ for LSS-SGFP2-cp195.

E) Widefield microscopy images of HeLa cells expressing the dual expression construct used for the brightness assay for LSS-SGFP2-cp40 (left) with as reference mScarlet-I (right). The left image shows that LSS-SGFP2-cp40 is localized to cellular structures, while it should be in the cytoplasm, as shown for the mScarlet-I reference. This made it impossible to determine the brightness of LSS-SGFP2-cp40 using this assay. The width of the images is 96.11 μm .

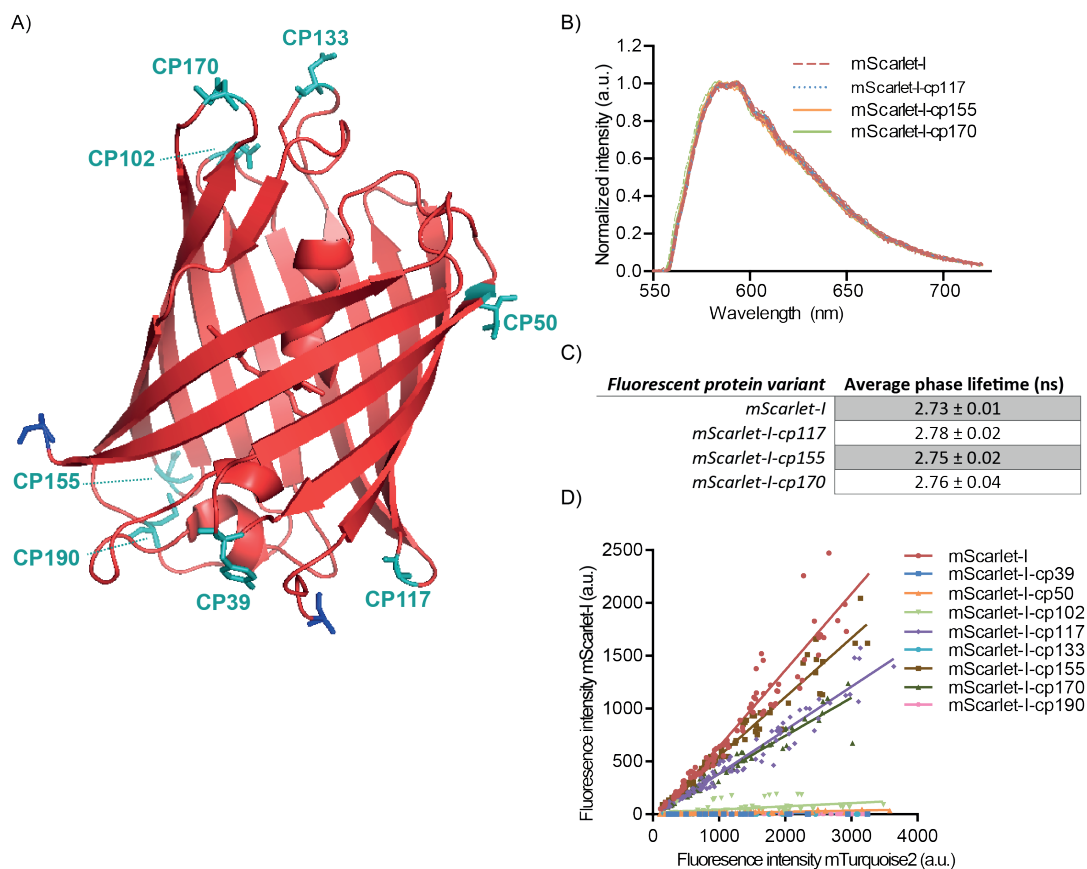


Figure 7. Design and characterization of mScarlet-I circular permuted variants.

A) The protein structure of mScarlet (PDB ID: 5LK4), which is used, together with literature research, to determine interesting sites for circular permutation of mScarlet-I. The beginning and end of the protein are highlighted in blue and the circular permutation sites tested are highlighted in cyan. The highlighted residue is the start of the protein in the respective circular permuted variant.

B) Emission spectra of mScarlet-I and circular permuted variants, in living HeLa cells, using spectral imaging, $n=5$ for mScarlet-I and mScarlet-I-cp117; $n=4$ for mScarlet-I-cp170; $n=3$ for mScarlet-I-cp155. Thinner dashed lines represent 95% CI.

C) Phase lifetimes of mScarlet-I and circular permuted variants, in living HeLa cells. The number of cells analyzed is $n=46$ for mScarlet-I; $n=53$ for mScarlet-I-cp117; $n=64$ for mScarlet-I-cp155; $n=30$ for mScarlet-I-cp170. Shown is the average \pm the 95% CI

D) The *in vivo* brightness of the mScarlet-I variants relative to mTurquoise2 by employing P2A constructs, resulting in the separate expression of the fluorescent proteins in equal amounts. The experiment is performed in HeLa cells. Each dot represents a single cell. The number of cells analyzed is $n=93$ for mScarlet-I; $n=73$ for mScarlet-I-cp39; $n=86$ for mScarlet-I-cp50; $n=82$ for mScarlet-I-cp102; $n=93$ for mScarlet-I-cp117; $n=90$ for mScarlet-I-cp133; $n=89$ for mScarlet-I-cp155; $n=71$ for mScarlet-I-cp170; $n=89$ for mScarlet-I-cp190.

To determine if the novel circular permuted variants of LSS-SGFP2 and mScarlet-I are still functional, a brief *in vivo* characterization was performed. First, the shape of the emission spectra was compared to the spectra of the regular LSS-SGFP2 or mScarlet-I. From figure 6B and figure 7B can be inferred that no shifts in emission spectra occurred with circular permutation. Similarly, the lifetime remains virtually unchanged with circular permutation (figure 6C and figure 7C). Furthermore, the brightness was evaluated with either mScarlet-I (LSS-SGFP2 variants) or mTurquoise2 (mScarlet-I variants) as reference.

For LSS-SGFP2 the variants permuted at residue 118, 157 or 173 show virtually the same brightness as regular LSS-SGFP2, while the variant permuted at residue 195 is slightly less bright (figure 6D). The brightness of the variant permuted at residue 40 was not determined due to aberrant localization of the construct (figure 6E).

For mScarlet-I, the variant permuted at residue 155 was the brightest, followed by the variants permuted at residues 117 and 170, while the other circular permutations (residue 39, 50, 102, 133 and 190) hardly showed fluorescence and were excluded from further research (figure 7D). All circular permuted variants were less bright than regular mScarlet-I. However, the three fluorescent circular permuted mScarlet-I variants display a much higher relative brightness than the reported circular permuted mCherry variants (Carlson et al., 2010; Li et al.; Shui et al., 2011).

Circular permuted FP variants applied in the DORA RhoA FRET sensor

The brief characterization of the novel circular permuted LSS-SGFP2 and mScarlet-I variants was followed by the application of promising variants in the unimolecular DORA RhoA FRET sensor, to evaluate if the FRET contrast could be further improved by varying the relative orientation of the donor and acceptor FP (Fritz et al., 2013; Nagai et al., 2004; van der Krogt et al., 2008).

Figure 8A shows preliminary data where Cerulean3 (206A) is used as FRET donor and mScarlet-I or a permuted variant as FRET acceptor. Employing mScarlet-I variants, permuted at residue 117 or 155 as FRET acceptor did not affect the FRET contrast of the DORA RhoA sensor. The mScarlet-I variant permuted at residue 170, however, showed a clear increase in FRET contrast (figure 8A). Therefore, this variant was compared to regular mScarlet-I as FRET acceptor in combination with LSS-SGFP2 as FRET donor, since this is the FRET pair of interest for multiplex FRET imaging. In figure 8B a minimal increase in FRET contrast is shown when the mScarlet-I variant, permuted at residue 170, is used as acceptor.

In figure 8C we show the FRET contrast for mScarlet-I with either LSS-SGFP2 or circular permuted variants of LSS-SGFP2 as FRET donor. The highest FRET contrast was obtained with the regular LSS-SGFP2 as FRET donor (figure 8C). Additionally,



comparing the permuted variants of LSS-SGFP2 shows significant differences in FRET contrast of the DORA RhoA sensor, with the highest contrast when using the variant permuted at residue 173 and the lowest FRET contrast when using the variant, permuted at residue 118, meaning that the FRET contrast of the sensor is affected by circular permutation of the FPs employed, as reported before for other FRET pairs (figure 8C) (Fritz et al., 2013; Nagai et al., 2004; van der Krogt et al., 2008).

Multiplex FRET imaging

After having obtained well performing FRET-based biosensors, the next step would be to apply these sensors in a multiplex FRET experiment. The aim is eventually to combine the LSS-SGFP2-mScarlet-I based FRET sensor with the frequently used CFP-YFP based sensors. First, however, a less complicated multiplex strategy is examined with three FPs. This approach involves two FRET donors (mTurquoise2 and LSS-SGFP2), transferring energy to a common FRET acceptor (mScarlet-I or mCherry) (figure 9). In order to perform linear unmixing, the shape of the spectra, i.e. the spectral signature, of each FP, is determined (figure 9A). The spectral signatures were used to make an unmixing matrix required for linear unmixing.

The functionality of Ga13-LSS-SGFP2 was evaluated by performing a FRET experiment with mCherry-Gy as FRET acceptor upon stimulation of an untagged, ectopically expressed LPA2 receptor (figure 9B). This stimulation of the LPA2 receptor resulted in a clear FRET ratio change, suggesting that the Ga13-LSS-SGFP2 is functional and can report on GPCR activation. Next, we transfected Gaq-mTurquoise2 and Ga13-LSS-SGFP2 together with Gy-mScarlet-I, and stimulated an ectopically expressed histamine-1 receptor.

The unmixed donor and acceptor traces are shown in figure 9C. These multiplex data show activation of Gq but not G13 upon stimulation of an ectopically expressed histamine-1 receptor. A disadvantage of the used multiplex setup and single excitation wavelength is that no ratiometric imaging can be performed since it is not known which of the Gy-mScarlet-I molecules interact with the Gaq or Ga13. The next step would be to perform a multiplex FRET experiment where the sensors both contain a distinguishable FRET pair, enabling ratiometric FRET imaging. The RhoA activation biosensor equipped with LSS-SGFP2 and mScarlet-I is presumably applicable in multiplex FRET imaging combined with a CFP-YFP based sensor. However, further optimization of the sensor, sensor co-expression and/or filter settings might facilitate robust FRET measurements and correct unmixing.

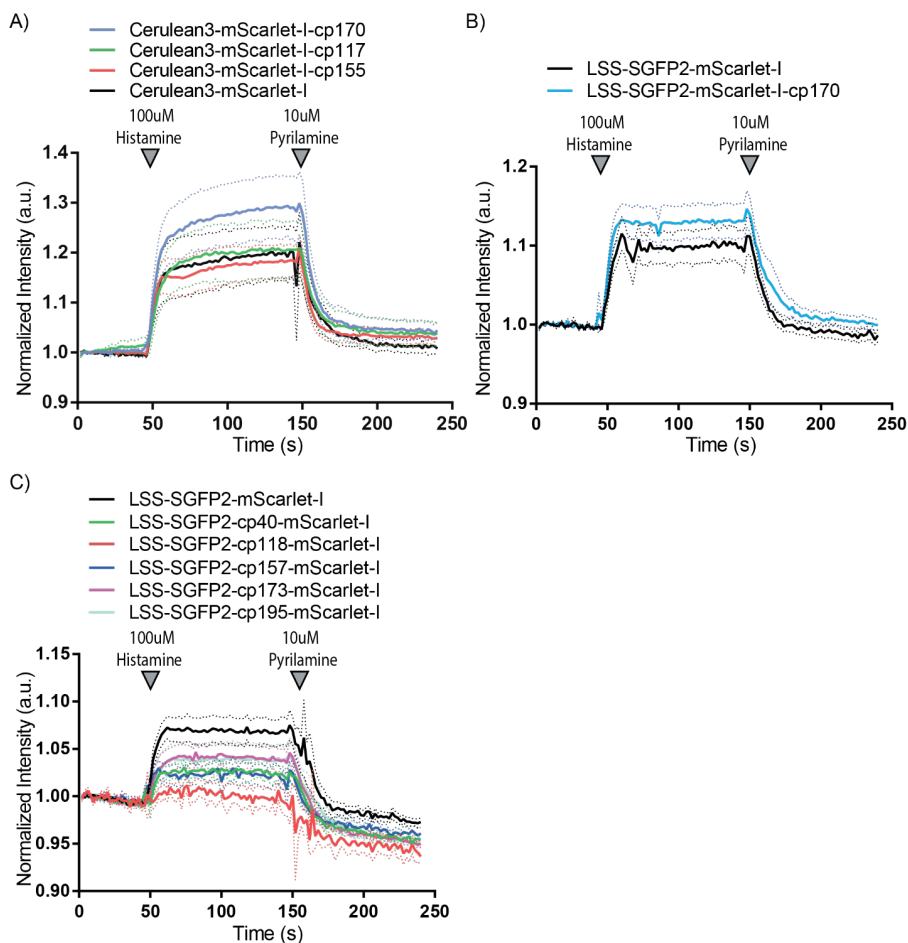


Figure 8. Circular permuted variants of mScarlet-I and LSS-SGFP2 applied in the DORA-RhoA FRET sensor.

A) Ratiometric FRET traces of HeLa cells expressing the DORA-RhoA FRET sensor employed with Cerulean3(206A) as FRET donor and either mScarlet-I ($n=11$), mScarlet-I-cp117 ($n=8$), mScarlet-I-cp155 ($n=8$) or mScarlet-I-cp170 ($n=10$) as acceptor and an untagged Histamine1 receptor (dotted lines depict 95% CI). Histamine and pyrilamine were added at $t=50s$ and $t=150s$ respectively, as indicated by the arrowheads.

B) Ratiometric FRET traces of HeLa cells expressing the DORA-RhoA FRET sensor employed with LSS-SGFP2 as FRET donor and either mScarlet-I ($n=31$) or mScarlet-I-cp170 ($n=24$), as acceptor and an untagged Histamine1 receptor (dotted lines depict 95% CI). Histamine and pyrilamine were added at $t=50s$ and $t=150s$ respectively, as indicated by the arrowheads.

C) Ratiometric FRET traces of HeLa cells expressing the DORA-RhoA FRET sensor employed with either LSS-SGFP2 ($n=27$), LSS-SGFP2-cp40 ($n=19$), LSS-SGFP2-cp118 ($n=12$), LSS-SGFP2-cp157 ($n=21$), LSS-SGFP2-cp173 ($n=16$) or LSS-SGFP2-cp195 ($n=18$) as FRET donor and mScarlet-I as acceptor and an untagged Histamine1 receptor (dotted lines depict 95% CI). Histamine and pyrilamine were added at $t=50s$ and $t=150s$ respectively, as indicated by the arrowheads.

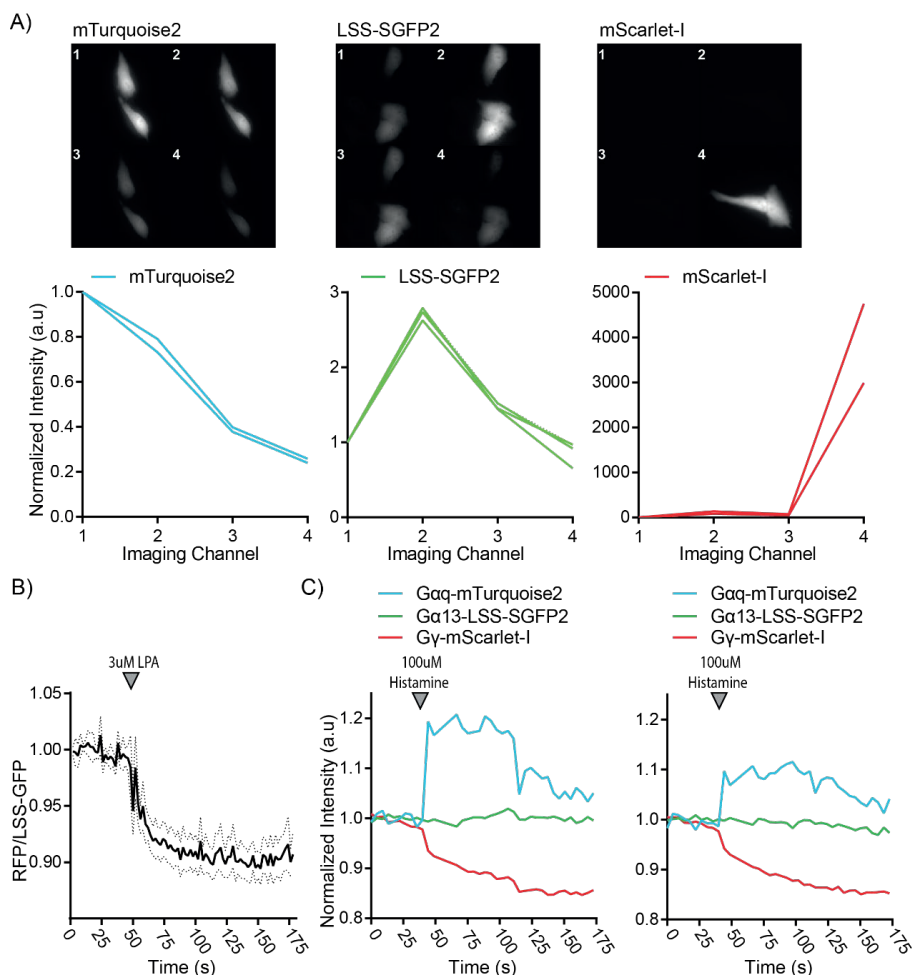


Figure 9. Multiplex FRET imaging of Gq and G13 activation.

A) The spectral 'signatures' of mTurquoise2 (ex390/20BP), LSS-SGFP2 (ex390/20BP) and mScarlet-I (ex556/20BP) used to construct an unmixing matrix enabling linear unmixing. At the top, the images show cells expressing one of the FPs in the four emission channels of the quadsplit module. Below, the normalized fluorescence intensity for each emission channel of the quadsplit module is shown, 1= 460-495nm; 2= 495-525nm; 3=525-560nm; 4= >560nm. The emission is recorded in combination with a HQ460LP filter. Each line represents an individual cell.

B) Single FRET pair, ratiometric FRET traces of HeLa cells expressing Ga13-LSS-SGFP2, untagged Gβ, mCherry-Gγ and an untagged LPA2 receptor (n=13)(dotted lines depict 95% CI). LPA was added at t=50s, indicated by the arrowhead.

C) The unmixed normalized intensity of Gq-mTurquoise2, Ga13-LSS-SGFP2 and Gy-mScarlet-I is shown upon stimulation of an ectopically expressed, untagged, histamine1 receptor. Histamine was added at t=44s, indicated by an arrowhead. The linear unmixing is performed using the unmixing matrix for which the spectral 'signatures' shown in figure 9A were recorded. Each graph shows the response of an individual cell, imaged from the same coverslip.

Discussion

To gain more insight in crosstalk between signaling pathways in GPCR signaling, it is essential to monitor multiple signaling events simultaneously in living cells. In this study we assessed and optimized characteristics of LSS-FPs in order to develop FRET sensors that are compatible with the CFP-YFP based sensors for application in multiplex FRET imaging.

We report LSS-SGFP2 as an improved LSS-FP, based on increased brightness and increased 400/488 excitation ratio relative to mT-Sapphire (Zapata-Hommer and Griesbeck, 2003).

Next to LSS-SGFP2, we characterized two other novel LSS-GFP variants. LSS-msfGFP was excluded due to its high dimerization tendency. LSS-mEGFP is a substantially improved LSS-GFP as well, however, we chose to continue with the brightest LSS-FP variant, LSS-SGFP2. LSS-mEGFP does show a higher 400/488 excitation ratio. This means that less cross excitation of LSS-GFP occurs when combined with the excitation of a GFP, which might facilitate correct linear unmixing of these FPs. The added value of this characteristic will become more evident in future experiments, when an increasing number of FPs will be imaged simultaneously.

In this study we constructed and characterized novel LSS-FPs for application in multiplex FRET imaging, even though others have reported successful multiplex FRET experiments using the LSS-FPs that were already available. However, these reports often used 1) methods limited in image acquisition speed (Shcherbakova et al., 2012), 2) limited image acquisitions to avoid photobleaching (Ai et al., 2008; Ding et al., 2011) or 3) straightforward sensors that do not pose strict requirements on the FPs, such as protease sensors (Ai et al., 2008; Ding et al., 2011; Elliott et al., 2017; Niino et al., 2009; Shcherbakova et al., 2012). mAmetrine, for example, was successfully applied in multiplex FRET experiments monitoring caspase activity (Ai et al., 2008). However, our attempt to use mAmetrine variants to monitor Gq activation reveals the suboptimal characteristics of this LSS-FP. Therefore, we opted to optimize LSS-FP characteristics in order to be less restricted in which methods or sensors are used.

The assessment of the optimized LSS-SGFP2 in FRET pair tandem FP fusion constructs clearly shows the increased brightness of LSS-SGFP2 and mScarlet-I, resulting in an increased SNR. Furthermore, the RhoA activation biosensor equipped with LSS-SGFP2 and mScarlet-I showed an increased FRET contrast compared to the sensor equipped with LSS-SGFP2 and mCherry. This could be explained by the higher extinction coefficient of mScarlet-I and the larger spectral overlap of mScarlet-I excitation with LSS-SGFP2 emission. In contrast, when comparing these FRET pairs, in bimolecular Gq sensors, no clear differences in FRET contrast are observed. Perhaps this is caused



by variation in the relative expression levels of the heterotrimeric G-protein subunits, since G α , G β and G γ are expressed from separate plasmids. This highlights again the importance of a set stoichiometry between sensor components (Goedhart et al., 2011).

To further improve the FRET contrast of the LSS-SGFP2-mScarlet-I based RhoA activation sensor, circular permutation of the novel FPs, LSS-SGFP2 and mScarlet-I, was performed. For both FPs, bright circular permuted FP variants were obtained that could be successfully applied in the RhoA biosensor. Obtaining proper circular permuted variants was expected to be less challenging for LSS-SGFP2 than for mScarlet-I. This because FPs, highly homologous to LSS-SGFP2, were already successfully permuted (Nagai et al., 2004; Topell et al., 1999). mScarlet-I, on the other hand, was synthetically designed and lacks highly homologous FPs that were already successfully permuted. Additionally, the results of circular permutation of other RFPs were moderate. The circular permuted variants reported for mCherry are much dimmer than mCherry and/or show reduced maturation (Carlson et al., 2010; Shui et al., 2011). All permuted LSS-SGFP2 variants were clearly fluorescent, while some mScarlet-I variants were hardly fluorescent. However, we selected more circular permutation sites for mScarlet-I than for LSS-SGFP2 to increase the chance on obtaining a proper permuted mScarlet-I variant. Five bright permuted LSS-SGFP2 variants and three bright permuted mScarlet-I variants were obtained.

We observed that a few circular permutation sites, such as 157 and 173, often yield proper permuted FP variants, apparently unaffected by the origin of the FP. This suggests that the overall structural homology between FPs is such that these sites, selected based on protein structure alignments with successfully permuted FPs, will work for any FP. On the other hand, between FPs, large differences exist in circular permutation sites that yield a proper permuted FP variant. For example circular permutation site 105 yields the brightest mTFP variant (Fritz et al., 2013), while corresponding circular permutation site 102 yields a hardly fluorescent mScarlet-I variant. Small differences in FP structure and the underlying interactions between amino acids may determine if circular permutation at a certain site will be successful. Limited knowledge in this area makes it difficult to predict the outcome. The study on circular permutation of mTFP, includes a comparison of several circular permutation sites for each loop in the FP (Fritz et al., 2013). Performing likewise comparisons for the circular permutation of other FPs derived from varying origins, presumably contributes tremendously to the overall knowledge in this area. Additionally, the study on circular permutation of mTFP shows that within one loop it matters greatly which site is selected for circular permutation, e.g. mTFP-cp105 is much brighter than mTFP-cp106 or mTFP-cp107 and similarly mTFP-cp175 is much brighter than mTFP-cp174 (Fritz et al., 2013). Therefore, it might be interesting to look at multiple circular permutation sites per loop.

The characterization of the circular permuted variants performed in this study is incomplete. Especially for promising permuted FP variants, further characterization should be performed, since theoretically all characteristics could be altered upon circular permutation. Changes in quantum yield, extinction coefficient, maturation speed and the shape of the excitation spectrum, were reported upon circular permutation (Baird et al., 1999; Shui et al., 2011; Topell et al., 1999). The reduced brightness observed for several permuted FP variants might be caused by inefficient folding, which is detrimental for their application in biosensors.

Dynamic FRET experiments indicate that circular permutation does affect the dynamic range of the sensor but the dynamic range of the RhoA activation biosensor employed with FRET pair LSS-SGFP2-mScarlet-I does not benefit from the circular permutations that were assessed in this study. It could be that with circular permutation, characteristics of the FPs are modified that make the FRET pair less efficient, negating the positive effect of the altered relative orientation. Furthermore, the combined performance of permuted FP variants or even a new selection of circular permutations could be assessed. This might result in the optimal relative orientation of this FRET pair in this sensor.

A pronounced effect of circular permutation of mScarlet-I was, however, observed when nCerulean3-mScarlet-I was applied in the RhoA activation biosensor. Here, mScarlet-I-cp170 clearly improves the FRET contrast of the sensor. This suggests that for nCerulean3 and mScarlet-I as FRET pair, circular permutation of mScarlet-I at residue 170 positively affects the relative dipole orientation, increasing the FRET efficiency at the FRET "on" state of the sensor. Furthermore, for *A. victorea* derived FPs, this circular permutation site, corresponding to Venus-cp173, introduces the novel N- and C-termini at the other side of the barrel, turning the barrel upside down relative to the other FP of the FRET pair. Thus, an antiparallel configuration of the FRET pair is facilitated, which is reported to be a favored configuration for FP dimerization for *A. victorea* derived FPs (Palm et al., 1997). Kotera et al. suggested that the positive effect of this circular permutation site on the FRET contrast of sensors might be partially caused by *hetero*-dimerization in the FRET "on" state of the sensor (Kotera et al., 2010). The FRET pair nCerulean3-mScarlet-I, however, lacks a common dimerization interface. Therefore, it is unlikely that the improved performance of this FRET pair upon circular permutation of mScarlet-I is due to increased tendency to heterodimerize in the FRET "on" state of the sensor, although the possibility cannot be excluded entirely. It would be interesting to assess more circular permutation sites resulting in an antiparallel configuration of the FRET pair. The other evaluated circular permutation sites leading to an antiparallel configuration of the FRET pair, either failed in the cloning phase (LSS-SGFP2-cp49) or produced hardly fluorescent variants (mScarlet-I-cp50, mScarlet-I-cp102, mScarlet-I-cp133).



Finally, we performed a multiplex FRET experiment where the LSS-SGFP2-mScarlet-I FRET pair was applied, showing that stimulation of an ectopically expressed histamine-1 receptor activates Gq but not G13. The coupling of the histamine-1 receptor to Gq but not to G13 was reported several times by others and therefore we used this experiment as a proof of principle for the multiplex FRET imaging and image analysis (Chikumi et al., 2002; Fitzsimons et al., 2004; Mikelis et al., 2015; Wettschureck and Offermanns, 2005). A few difficulties were experienced while performing multiplex FRET imaging. It was challenging to obtain balanced co-expression of multiple sensors and a GPCR. The correct amount of DNA for transfection has to be determined for each construct and this must be adjusted in case the combination of co-expressed constructs is altered. In the future it might be worthwhile to make constructs that express multiple sensors at a fixed stoichiometry. Furthermore, the filter settings of the multiplex FRET imaging setup require optimization. We performed FRET experiments on two different imaging setups. The multiplex FRET imaging setup (Nikon Eclipse Ti-E) shows less FRET contrast for the LSS-SGFP2-RFP based sensors than the imaging setup (Carl Zeiss GmbH Axiovert 200M) without a multisplit device that is well established for ratiometric FRET imaging (data not shown). Figure 8B shows the FRET ratio for a LSS-SGFP2-mScarlet-I FRET pair applied to monitor G13 activation measured on the setup that is well established for ratiometric FRET imaging. We did not determine the FRET contrast of this G13 sensor on the multiplex FRET imaging setup. The ability of this sensor, imaged on the multiplex FRET imaging setup, to show a robust FRET response upon G13 activation remains to be determined. The multiplex FRET imaging setup should be modified to allow detection of a FRET contrast similar to the other imaging setup, while retaining its ability to perform single excitation, four emission channel imaging. After optimizing the multiplex FRET imaging setup to show robust FRET responses, different neutral density filters should be examined to improve the degree of photobleaching.

Eventually, when more and more signaling events are imaged simultaneously and the unmixing of more than four FPs is required, a snapshot image mapping spectrometer (IMS) for hyperspectral imaging could be of interest. This IMS can achieve spectral information using 60 imaging channels (Gao et al., 2010), thereby being theoretically able to separate 60 FPs imaged simultaneously. At this point, it has been used for the simultaneous FRET imaging of two sensors (Elliott et al., 2012; Elliott et al., 2017).

In summary, we developed and characterized LSS-GFPs, optimized to LSS-SGFP2. Bright circularly permuted variants of LSS-SGFP2 and mScarlet-I were constructed to aid further improvement of unimolecular sensors. LSS-SGFP2 could be successfully used in several FRET sensors. LSS-SGFP2 was applied in a multiplex FRET experiment, showing that it can be combined with CFP, using a single excitation wavelength to excite both FPs, while providing orthogonal detection.

Methods

Cloning / plasmid construction

We obtained mAmetrine (#54660) and mT-Sapphire (#54545) in a clontech-style C1 mammalian expression vector and mAmetrine1.2 (#42171) in a pBad-HisB vector, from addgene (Ai et al., 2007; Ai et al., 2008; Zapata-Hommer and Griesbeck, 2003). In order to transfer the mAmetrine1.2 sequence to a clontech-style C1 vector, a PCR was performed on the pBad-HisB- mAmetrine1.2 vector (Fw: 5'-GATCCACCGGTCGCCACCATGGTGAGCAAGGGCGAGGAG-3' and Rv: 5'-TCTACAAATGTGGTATGGC-3'), the PCR product and the clontech-style C1 vector were digested with AgeI/BsrGI, subsequent ligation yielded a clontech-style C1-mAmetrine1.2.

LSSmOrange in a clontech-style C1 vector was previously reported (Shcherbakova et al., 2012). LSS-SGFP2 and LSS-mEGFP were obtained by introducing mutations T65S (Fw: 5'-CTCGTGACCACCCTGAGCTACGGCGTGTCAGTG-3'; Rv: 5'-CACTGCACGCCGTAGCTCAGGGTGGTCACGAG-3') and T203I (Fw: 5'-AACCACTACCTGAGCATCCAGTCCAAGCTGAGC-3'; Rv: 5'-GCTCAGCTTGACTGGATGCTCAGGTAGTGGTT-3') into respectively SGFP2 (Kremers et al., 2007) and mEGFP (Tsien, 1998). LSS-msfGFP, based on the msfGFP sequence with mutations 65S and 203I including flanking AgeI and BsrGI restriction sites, was ordered from Eurofins in a pEX-A2 vector. The LSS-msfGFP sequence was transferred to a clontech-style C1 vector using AgeI and BsrGI restriction enzymes (Pédélec et al., 2006).

In order to construct circular permuted variants of LSS-SGFP2 and mScarlet-I, first, tandem FP constructs were designed. We used a forward primer encoding an Acc65I restriction site, a GGSGG linker and the first five amino acids of a FP and a reverse primer that anneals to SV40 polyA (Fw: 5'-AGCGGTACCAGGGTGGCAGCGGTGGCATGGTGAGCAAGGGCGAG-3'; Rv: 5'-TCTACAAATGTGGTATGGC-3'). The PCR was performed on LSS-SGFP2 or mScarlet-I expressed from a clontech style C1 vector. The product could be digested with Acc65I and BsrGI and ligated into the clontech style C1 vector expressing the same FP, digested with BsrGI, resulting in a tandem FP clontech style C1 vector. These tandem FP constructs were used to make the circular permuted variants by PCR at different positions in the tandem FP flanking these novel circular permuted variants with AgeI and BsrGI restriction sites for cloning into clontech style C1 vectors or pDx vectors (modified TriEX vector, expressing a FP in both bacteria, under a rhamnose promoter, and in mammalian cells, under a CMV promoter). Primers used to create circular permuted variants from the tandem FP constructs are for LSS-SGFP2 circular permuted at residue 40 Fw: 5'-GCTACCGGTCGCCACCATGTACGGCAAGCTGACCCTG-3' and Rv: 5'-GCTTGACAGGTGGCATCGCCCTC-3'; for LSS-SGFP2 circular permuted at residue 49 (cloning not succeeded) Fw: 5'-GCTACCGGTCGCCACCATGACCACCGCAAGCTGC-3'



and Rv: 5'-GCTTGTACAGCAGATGAACTTCAGGGTCAG-3'; for LSS-SGFP2 circular permuted at residue 118 Fw: 5'-GCTACCGGTCGCCACCATGGACACCTGGTGAACCG-3' and Rv: 5'-GCTTGTACAGCCCTCGAACTTCACCTC-3'; for LSS-SGFP2 circular permuted at residue 158 Fw: 5'-GCTACCGGTCGCCACCATGCAGAAGAACGGCATCAAGGC-3' and Rv: 5'-GCTTGTACACTTGTGCGCGGTGATATAGAC-3'; for LSS-SGFP2 circular permuted at residue 173 Fw: 5'-GCTACCGGTCGCCACCATGGACGGCGGCGTGCA-3' and Rv: 5'-GCTTGTACACTCGATGTTGTGGCGGATC-3'; for LSS-SGFP2 circular permuted at residue 195 Fw: 5'-GCTACCGGTCGCCACCATGCTGCTGCCCCACAACC-3' and Rv: 5'-ACTTGTACACACGGGGCCGTCG-3'; for mScarlet-I circular permuted at residue 39 Fw: 5'-GCTACCGGTCGCCACCATGTACGAGGGCACCCAGACCGCC-3' and Rv: 5'-GCTTGTACAGGGGCGGCCCTCGCCC-3'; for mScarlet-I circular permuted at residue 50 Fw: 5'-GCTACCGGTCGCCACCATGACCAAGGGTGGCCCCCT-3' and Rv: 5'-GCTTGTACACACCTTACGCTTGGCGGTCT-3'; for mScarlet-I circular permuted at residue 102 Fw: 5'-GCTACCGGTCGCCACCATGGACGGCGGCGCCGTGA-3' and Rv: 5'-GCTTGTACTCTCGAAGTTCATCACGCGCTCCC-3'; for mScarlet-I circular permuted at residue 117 Fw: 5'-GCTACCGGTCGCCACCATGGGCACCTGATCTACAAGG-3' and Rv: 5'-GCTTGTACAGTCTCCAGGGAGGTGTC-3'; for mScarlet-I circular permuted at residue 133 Fw: 5'-GCTACCGGTCGCCACCATGGACGGCCCCGTAATGC-3' and Rv: 5'-GCTTGTACAAGGAGGGAAGTTGGTGCC-3'; for mScarlet-I circular permuted at residue 155 Fw: 5'-GCTACCGGTCGCCACCATGGACGGCGGTGCTGAAGG-3' and Rv: 5'-GCTTGTACTCTCGGGGTACAACCGCT-3'; for mScarlet-I circular permuted at residue 170 Fw: 5'-GCTACCGGTCGCCACCATGGACGGCGGCGCTACCT-3' and Rv: 5'-GCTTGTACACTTCAGGCGCAGGGCCAT-3' and for mScarlet-I circular permuted at residue 190 Fw: 5'-GCTACCGGTCGCCACCATGATGCCCGGCGCCTACAA-3' and Rv: 5'-GCTTGTACTCTGCACGGGCTTCTTGCC-3'.

The clontech-style C1 vectors containing LSS-FPs are used for the photostability experiments and for cloning the tandem FP constructs for the brightness assay and the spectral imaging experiments. The brightness of LSS-FP variants was analyzed using tandem FP constructs with a T2A linker resulting in equal expression of two fluorescent proteins, originally reported as SYFP2-T2A-mTurquoise2 (Goedhart and Gadella Jr, 2005; Kim et al., 2011; Mastop et al., 2017), where the SYFP2 can be replaced with a FP from a clontech-style C1 using NdeI/Kpn2I restriction enzymes and mTurquoise2 is used as reference. For the spectral imaging we use this T2A tandem FP construct to create the non-FRET control vectors. We use SYFP2-mTurquoise2, reported previously (Goedhart et al., 2012; Mastop et al., 2017), to clone the high FRET tandem FP constructs used in the spectral imaging experiments. The SYFP2 was replaced using NdeI/Kpn2I restriction enzymes as mentioned for the T2A tandem FP constructs. The mTurquoise2 is replaced with a FP from a clontech-style N1 vector, using BamHI/NotI restriction enzymes. First, the FP was transferred from a C1 to a N1 vector, using AgeI/BsrGI restriction enzymes.

The brightness of the circularly permuted variants was analyzed using a similar construct as used for the brightness analysis of LSS-FPs, a tandem FP construct including a P2A sequence, reported elsewhere (Bindels et al., 2017). The FP of interest could be exchanged using AgeI/BsrGI restriction enzymes and mTurquoise2 is used as reference. In order to determine the brightness of circularly permuted LSS-SGFP2 variants mScarlet-I was used as reference FP. To exchange mTurquoise2 for mScarlet-I, a silent mutation was introduced in the mScarlet-I sequence, changing a BsrGI restriction site into a SacI restriction site (Fw: 5'-CGGCGCATGGACGAGCTCTACAAGTAAGTGATTAAC-3' and Rv: 5'-GTTAATCACTTACTTGTAGAGCTCGTCCATGCCGCCG-3'). The mutagenized mScarlet-I expressed in a pDx vector was digested with EcoRI and SacI and used to replace the mTurquoise2 reference in the dual expression system used for the brightness analysis (Bindels et al., 2017), followed by a mutagenesis PCR, destroying an AgeI site in front of the mScarlet-I sequence (Fw: 5'-CAGCTCGCTAGCGCTGCCGTGCCACCATG-3' and Rv: 5'-CATGGTGGCGACCGCAGCGCTAGCGAGCTG-3'), so the FP of interest, in this case circularly permuted FP variants and their controls, can easily be exchanged using AgeI/BsrGI restriction enzymes while the reference FP, mScarlet-I, remains unaffected.

RSET bacterial expression vectors were used for protein production and isolation. FPs could be transferred from clontech-style C1 or N1 vectors to the RSET vector using AgeI/BsrGI restriction enzymes.

To show LSS-SGFP2 localized to subcellular structures, the following constructs from addgene: pLifeAct-mTurquoise2 (#36201); pmTurquoise2-H2A (#36207) and pmTurquoise2-Tubulin (#36202), were digested with AgeI/BsrGI (histone 2A and lifeact) or SnaBI/BsrGI (α -tubulin) to exchange mTurquoise2 for LSS-SGFP2.

For the OSER vectors we used vector mEmerald-CytERM-N-17 (#54056) from addgene and replaced the FP using AgeI/BsrGI restriction enzymes.

The DORA-RhoA FRET sensor (a kind gift from Y. Wu (van Unen et al., 2015b) (Center for Cell Analysis and Modeling, University of Connecticut Health Center, Farmington, USA), with an introduced BglII restriction site, described elsewhere (Bindels et al., 2017; Mastop et al., 2017) was used to construct different sensor variants. In order to replace the donor FP by LSS-SGFP2, a PCR was performed on a clontech-style C1-LSS-SGFP2 vector (Fw: 5'-AACGGATCCGTGAGCAAGGGCGAGG-3' and Rv: 5'-AGCGCTAGCCCCGCGCGGTCAC-3') and subsequently the restriction enzymes BamHI/NheI were used to digest both the PCR product and the DORA-RhoA sensor. To replace the acceptor FP by either mCherry or mScarlet-I, a PCR was performed on a clontech-style C1-mCherry/mScarlet-I vector (Fw: 5'-CTACCGGTGCCACCATG-3' and Rv: 5'-TCTACAAATGTGGTATGGC-3') and subsequently the restriction enzymes AgeI/BglII were used to digest both the PCR product and the DORA-RhoA sensor, containing LSS-SGFP2 as donor. For cloning of the DORA-RhoA sensor with circularly permuted



variants, a gBlock (Integrated DNA technologies (IDT)) was ordered to enable swift exchange of FPs. The gBlock contained part of the RhoA sensor sequence including mutations to introduce restriction sites flanking the FPs in the sensor. Additionally, the linker between the FPs was codon optimized to facilitate synthesis of the gBlock. The gBlock was cloned into the DORA-RhoA sensor sequence using PstI/Kpn2I restriction enzymes. The resulting gBlock sensor is not yet in frame. The donor FP in the sensor could be exchanged using SgaI/Acc65I restriction enzymes and the acceptor FP could be exchanged using AgeI/BsiwI restriction enzymes. Circular permuted donor or acceptor candidates could be transferred to the digested sensor using AgeI/BsrGI from a pDx or clontech style C1 vector. Not circular permuted FPs expressed from a clontech style C1 vector could be transferred to the digested vector by performing a PCR, creating a truncation (excluding the last 10 amino acids) of the fluorescent protein (Fw: 5'-AGGTCTATATAAGCAGAGC-3' and either Rv: 5'-AGCTGTACACCCGGCGGCGGTAC-3' (Cerulean or LSS-SGFP2) or Rv: 5'-AGCTGTACAGTGGCGGCCCTCGGA-3' (mScarlet-I)). The PCR product was digested with AgeI/BsrGI and ligated in the DORA-RhoA sensor.

To replace the FP in previously reported tagged Gaq (Adjobo-Hermans et al., 2011; Mastop et al., 2017) a PCR was performed on a clontech-style C1 vector containing the LSS-FP sequence using primers Fw: 5'-TTGAGGATCCAAGCGGAGCGGAGGCAGCATGGTGAGCAAGGGCG-3' and Rv: 5'-GATATGCCGAGAGTGATCCCGGC-3' (LSS-SGFP2), Rv: 5'-gtatatgccgggagtgatcccggc-3' (mAmetrine(208F/S)) or Rv: 5'-gtatatgccgggagttatcccggc-3' (mAmetrine1.2). The PCR product and the pcDNA3.1 vector containing tagged Gαq were both digested with BamHI and SnaBI (PCR product digested with only BamHI since half the SnaBI site is present in the reverse primer, which can be directly ligated in the SnaBI cut vector) and the digested PCR product was ligated in the Gaq pcDNA3.1 vector. To replace the FP in previously reported Ga13 (Mastop et al., 2018), a PCR was performed on a clontech-style C1 vector containing the LSS-SGFP2 sequence using primers Fw: 5'-ATACCGTTCTATGGTGAGCAAGGGCG-3' and Rv: 5'-TAACCGTGATCCCGGCGGC-3'. The PCR product and the pcDNA3.1 vector encoding mTurquoise2 tagged Ga13 were both digested with AgeI and the digested PCR product was ligated in the Ga13 pcDNA3.1 vector. The orientation of the insert is tested via a colony PCR using Fw: 5'-AGGTCTATATAAGCAGAGC-3' and Rv: 5'-TAACCGTGATCCCGGCGGC-3' that will only result in a band of 700bp if the FP is correctly oriented.

The used constructs containing untagged Gβ, mCherry-Gy and mScarlet-I-Gy were reported previously (Adjobo-Hermans et al., 2011; Mastop et al., 2017).

Spectroscopy of purified fluorescent proteins

His6-tagged proteins were produced in *E.coli* (BL21) and purified as reported previously (Bindels et al., 2014; Mastop et al., 2017). Absorption spectra were recorded on a Libra S70 double-beam spectrophotometer (Biochrom) (Goedhart et al., 2012).

Emission spectra were recorded on a Perkin Elmer LS55 fluorimeter. Emission spectra were recorded with following settings: ex400nm, slit 2.5nm; em405–650nm slit 2.5nm; scan speed 150 nm/min; pmt 800V.

Emission spectra were corrected for instrument response factors after calibration with emission spectra of established fluorophores.

In order to determine the relative quantum yield of the LSS-GFP variants compared to mT-Sapphire, we used 400nm light to excite the sample and determined the integrated emission. We divided the integrated emission by the absorbance of the sample at 400nm. We multiplied these values by a constant to set the quantum yield value for mT-Sapphire to 0.6 and to obtain the relative quantum yield values for the other LSS-GFP variants.

To determine the extinction coefficient, absorption spectra of LSS-GFP variants were recorded in PB buffer (43.5ml 0.2M Na₂HPO₄; 6.5ml 0.2M NaH₂PO₄) or 0.2M NaOH. The extinction coefficient of denatured GFP (in 0.2 NaOH) is $44 \times 10^3 \text{ M}^{-1} \text{ cm}^{-1}$ and this value is used to determine the extinction coefficient in PB buffer based on the OD values of the peak absorption (Patterson et al., 1997).

The pK_a values for each LSS-GFP variant was determined by measuring their fluorescence in buffers differing in pH (for pH 3-5.4: 0.1M Citric Acid – Sodium Citrate Buffer; for pH5.9-8: 0.1M Na₂HPO₄ – NaH₂PO₄ Buffer; 180µl of buffer and 20µl of purified protein was used for each measurement). Plates were analyzed using an FL600 fluorescence microplate reader (Bio-Tek Instruments), using custom ordered filters, ex380/20nm and 530/25BP emission filter (Chroma Technology Corp., Rockingham, VT) (Kremers et al., 2006) and GraphPad Prism software was used to determine the pK_a.

***In vitro* brightness determination with FCS**

Purified LSS-GFP protein samples were diluted in PBS and stored in glass-bottomed 96 well plates (Whatman). Fluorescence fluctuation spectroscopy was performed on an inverted Fluoview 1000 laser scanning microscope (Olympus). The excitation light of a 405nm 20MHz pulsing laser diode (Picoquant), as controlled by a Sepiall laser driver unit (Picoquant), was attenuated 10 times by a neutral density filter. The light was guided via a D405/480-488/560/635 primary dichroic mirror (Olympus) through a water immersed 60x UPlanSApo objective lens (NA1.2) into the sample. The emission light was guided via a size-adjustable pinhole, set at 130µm, through the Olympus detection box to the fibre output channel. The optical fibre was coupled to a custom-made detection box (Picoquant) containing four PDM avalanche photodiodes. The light was guided into two of the PDM avalanche photodiodes using a 50/50 splitter. In front of the detectors, the light was filtered by 525/45 emission filters (Chroma). The photon arrival times were recorded by a PicoHarp 300 time-correlated single-photon



counting system (Picoquant) during 180 seconds, controlled via the SymPhoTime 64 (Picoquant) software. The microscope was optimized by measuring the calibration dye Alexa488, as outlined in (Maeder et al., 2007). The molecular brightness of the LSS-GFP variants was analysed by photon-counting distribution analysis in FFS Data Processor 2.3 software (SSTC), essentially as described before (Goedhart et al., 2010). The data was binned in time windows of 0.1, 0.5, 1 and 5ms and analysed using an one-component three dimensional diffusion model (Chen et al., 1999). The obtained molecular brightness values and their 98% confidence intervals are expressed in photons per second.

Cell culture and transfection

HeLa cells (CCL-2, American Tissue Culture Collection; Manassas,VA, USA) were cultured in Dulbecco's modified Eagle's medium (DMEM) (Gibco, cat# 61965-059) supplemented with 10% fetal bovine serum (Invitrogen, cat# 10270-106), 100U/ml penicillin and 100µg/ml streptomycin at 37 °C in 7% CO₂, as previously mentioned (Mastop et al., 2017). For microscopy experiments cells were grown on 24mm Ø round coverslips, 0.13–0.16mm thick (Menzel, cat# 360208) to 50% confluency and transfected with 500ng plasmid DNA, 3µl PEI (1mg/ml) in water (pH 7.3) and 100µl OptiMEM (Gibco, cat# 31985-047) per 35mm Ø dish holding a 24mm Ø coverslip. Two days after transfection the coverslip was mounted in a cell chamber (Attofluor, Invitrogen). Microscopy medium (20mM HEPES (pH=7.4), 137mM NaCl, 5.4mM KCl, 1.8mM CaCl₂, 0.8mM MgCl₂ and 20mM glucose) was added to the coverslip in the cell chamber. The OSER assay, Ratiometric FRET, bleaching and brightness experiments are performed at 37 °C.

In vivo brightness analysis

HeLa cells were transfected with tandem FP constructs encoding a protein of interest, T2A (or P2A) sequence and mTurquoise2 or mScarlet-I as reference (Mastop et al., 2017). The T2A sequence allows for separate expression of both FPs in equal amounts. Imaging was performed in two different ways. For 1 we used hardware as described (Vermeer et al., 2004) using an imaging spectrograph detector. Cells were excited with 405/10nm light, an 80/20 (transmission/reflection) dichroic and a 435LP (long-pass) emission filter were used. The images were corrected for background signal. The spectra were normalized to mTurquoise2 fluorescence intensity and then the spectrum of mTurquoise2 was subtracted, yielding a normalized spectrum of the protein of interest. For figure 2, 4, 6 and 7 imaging was performed on a widefield fluorescence microscope (Axiovert 200 M; Carl Zeiss GmbH) equipped with a xenon arc lamp with monochromator (Cairn Research, Faversham, Kent, UK), using a 40x objective (oil-immersion Plan-Neo- fluor 40x/1.30; Carl Zeiss GmbH). For figure 2, cells were excited with 420nm (reference mTurquoise2) or 405nm (mAmetrine) light and emission was detected with a 470/30BP (reference mTurquoise2) and 535/30BP (mAmetrine) filter. For figure 4, cells were excited with 400nm light and emission was detected with a

470/30BP (reference mTurquoise2) and 535/30BP (LSS-GFP) filter. For figure 6, cells were excited with 400nm (LSS-SGFP2 variants) and 570nm (reference mScarlet-I) light and emission was detected with a 535/30BP (LSS-SGFP2 variants) and 620/60BP (reference mScarlet-I) filter. For figure 7, cells were excited with 420nm (reference mTurquoise2) and 570nm (mScarlet-I variants) light and emission was detected with a 470/30BP (reference mTurquoise2) and 620/60BP (mScarlet-I variants) filter. The images were corrected for background signal and the fluorescence intensity of the proteins of interest are plotted relative to the mTurquoise2 fluorescence intensity, enabling comparison of brightness amongst these proteins of interest.

Confocal microscopy

To obtain confocal images of live HeLa cells transiently expressing different LSS-FP variants tagged to Gaq or subcellular localization markers, a Nikon A1 confocal microscope, equipped with a 60x oil immersion objective (Plan Apochromat VC, NA 1.4), was used. The pinhole size was set to 1 Airy unit. To check the localization of LSS-GFP-tagged structures, cells were excited with a 405nm laser line, a 405/488/561 dichroic mirror was used and the emission was filtered through a 535/70BP emission filter. Images were averaged 16 times.

OSER assay

Confocal imaging for the OSER assay was performed on a Nikon A1 confocal microscope, equipped with a 60x oil immersion objective (Plan Apochromat VC, NA 1.4). We analyzed HeLa cells expressing the CytErm-FP fusion constructs and determined the percentage of cells that contained OSER structures (Costantini et al., 2012; Mastop et al., 2017). The LSS-GFPs/mAmetrines were excited with a 405nm laser and a 535/70BP emission filter was used. The LSS-mOrange was excited with a 457nm laser and a 595/50BP emission filter was used. The monomeric control mTurquoise2 was excited with a 457nm laser and a 482/35BP emission filter was used. The dimeric control dTomato was excited with a 561nm laser and a 595/50BP emission filter was used.

Photostability

Photostability of LSS-FPs was measured on a widefield fluorescence microscope (Axiovert 200 M; Carl Zeiss GmbH) equipped with a xenon arc lamp with monochromator (Cairn Research, Faversham, Kent, UK). Measurements were performed under continuous illumination for 600s with light of 400nm (LSS-GFP), 405nm (mAmetrine) or 440nm (LSS-mOrange) (slit width 30 nm).

The power was measured at the 20x objective (Zeiss LD-A-plan 20x Air/0,30 ph1 ∞) using a coherent power meter (FM Fieldmaster Power Energy Meter, 0210-761-99). Each 4s, fluorescence intensity was recorded with an exposure time of 200ms using a 40x objective (oil-immersion Plan-Neo- fluor 40x/1.30; Carl Zeiss GmbH).



LSS-GFP emission was detected with a 525/40BP filter, mAmetrine emission was detected with a 535/30BP filter and LSS-mOrange emission was detected with a 600/37BP filter. Image analysis was done in ImageJ. After subtraction of background signal, the mean fluorescence intensity of the cells was calculated for each time point. The intensity was normalized to the first time point.

Spectral imaging microscopy

Spectral imaging of living cells was performed with hardware as described (Vermeer et al., 2004), two days after transfection using an imaging spectrograph-CCD detector. For the spectral imaging of FRET pairs, spectral images of single cells, expressing tandem FP constructs with or without T2A sequence, were acquired using donor excitation at 405/10nm, an 80/20 (transmission/reflection) dichroic and a 435LP (long-pass) emission filter. Subsequently a spectral image was acquired using acceptor excitation without exciting the donor, excitation at 546/10nm and for detection a 590LP filter was used.

Each spectral image was normalized to directly excited FRET acceptor FP fluorescence intensity to correct for differences in protein expression (Goedhart et al., 2010). The tandem FP constructs containing a T2A sequence were used as non-FRET controls. A custom matlab script was used to select cells and extract spectra corrected for background signal. The difference in the donor intensity peak between the tandem FP construct with and without T2A is used to calculate the FRET efficiency of that FRET pair.

Spectral imaging of circularly permuted LSS-SGFP2 and mScarlet-I variants expressed in HeLa cells, to obtain emission spectra of the FP variants, was performed using excitation with 405/10nm (LSS-SFGFP2) or 546/10nm (mScarlet-I) light, attenuated 10 times by a neutral density filter, an 80/20 (transmission/reflection) dichroic and a 435LP (LSS-SGFP2) or 570LP (mScarlet-I). A custom matlab script was used to select cells and extract spectra corrected for background signal.

Ratiometric FRET imaging

FRET ratio-imaging was performed on a widefield fluorescence microscope (Axiovert 200 M; Carl Zeiss GmbH) (Adjobo-Hermans et al., 2011) equipped with a xenon arc lamp with monochromator (Cairn Research, Faversham, Kent, UK) for 240s (178s for Ga13-LSS-SGFP2 experiments) and with a time interval of 2s. The fluorescence intensity of the donor and acceptor were recorded with an exposure time of 200ms (300ms for Gaq-LSS-SGFP2 experiments) per image using a 40x objective (oil-immersion Plan-Neo-fluor 40x/1.30; Carl Zeiss GmbH). HeLa cells were used expressing an untagged histamine-1 receptor (Adjobo-Hermans et al., 2011) and either tagged Gaq, untagged G β and tagged G γ or a DORA-RhoA sensor.

Fluorophores were excited with 400nm (405nm for Gαq-mAmetrine experiments) light (slit width 30nm), LSS-GFP emission was detected with the 525/40BP filter, mAmetrine emission was detected with the 535/30BP filter and mCherry/mScarlet-I emission was detected with 620/60BP filter. In experiments where the activation of Gq or RhoA is monitored, HeLa cells were stimulated with 100μM (final concentration) histamine (Sigma-Aldrich) after 50s and with 10μM (final concentration) pyrilamine (mepyramine) (Sigma-Aldrich), as antagonist, after 150s. In experiments where the activation of G13 is monitored, HeLa cells were stimulated with 3μM LPA (Sigma-Aldrich) after 44s. The curves were normalized to the average intensity of the first 5 frames that were recorded. ImageJ was used to perform a background correction and calculation of mean intensity of each cell for each time point.

Fluorescence lifetime imaging microscopy (FLIM) of circular permuted variants

We performed the fluorescence lifetime measurements with a Nikon Eclipse Ti-E inverted microscope equipped with a LIFA system (Multi-Led illumination and LI2CAM; Lambert Instruments) (Bindels et al., 2017; Mastop et al., 2017). The modulated 446nm (LSS-SGFP2) or 532nm (mScarlet-I) LED excitation light passed through a 448/20BP (FF01-448/20, Semrock) (LSS-SGFP2) or a 556/20BP (FF01-556/20, Semrock) (mScarlet-I) excitation filter, reflected towards the sample by a 442nm (Di02-R442, Semrock) (LSS-SGFP2) or 561nm (Di02-R561, Semrock) (mScarlet-I) dichroic mirror and focused using a 40x objective (Plan Apo 40x NA 0.95 air, MDR01405). The emission was filtered by a 482/20BP (FF01-482/25, Semrock) (LSS-SGFP2) or a 609/54BP (FF01-609/54, Semrock) (mScarlet-I). The LI-FLIM software (LI-FLIM 1.223 Lambert Instruments) recorded 18 phase steps (with three times averaging) in pseudorandom order at a frequency of 40MHz. Erythrosine B (198269, Sigma-Aldrich) dissolved in ddH₂O was used as reference dye (fluorescence lifetime 0.086 ns; ten times averaging for reference stack). After background subtraction and 3x3 blurring, the lifetimes were calculated by the LI-FLIM software.

Multiplex FRET imaging

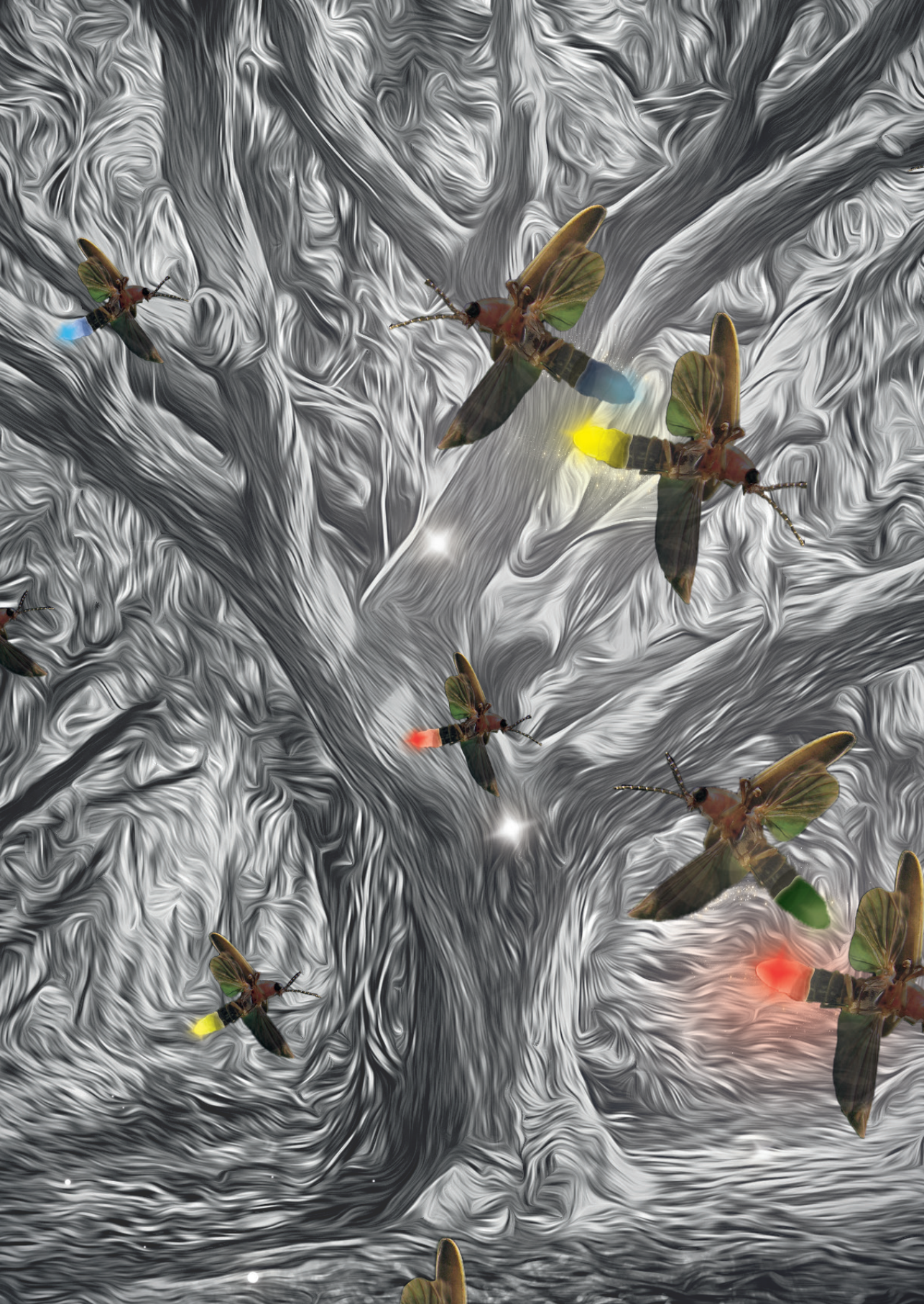
Multiplex FRET imaging was performed on a Nikon Eclipse Ti-E inverted microscope (Nikon) equipped with an Intensilight Epi-fluorescence Illuminator (Nikon) and a 40x objective (Plan Apo 40x NA 0.95 air, MDR01405). Filter wheels and microscope stage were controlled by a ProScan III unit (ProScan H31, Prior Scientific). Emission light was passed through a HQ460LP filter and subsequently through a multisplit device (Cairn Research, UK) that projects four emission channels on a camera. The unit holds three dichroics, a primary dichroic of 525nm, and two secondary dichroics of 495nm and 560nm. The 25.5x36x2mm ultraflat (UF) dichroics were purchased from Chroma (Chroma Technology Corporation, USA). Images were recorded by an ORCA-Flash4.0 V2 Digital CMOS camera (C11440-22CU, Hamamatsu Photonics).



Clontech-style C1 vectors expressing one of the FPs in HeLa cells were excited using an ex390/20BP filter (mTurquoise2 and LSS-SGFP2) or an ex556/20BP filter (mScarlet-I). The emission was recorded in the four emission channels of the multisplit device: 460-495nm; 495-525nm; 525-560nm; >560nm. The intensity of the signals in the four emission channels was used to determine the spectral signature of each FP. The spectral signature of each FP was determined for two or three individual cells and the average spectral signature was used to construct an unmixing matrix, using a custom made Matlab script.

HeLa cells expressing Gαq-mTurquoise2, Gα13-LSS-SGFP2, Gγ-mScarlet-I, an untagged Gβ and an untagged histamine-1 receptor were used to conduct a preliminary multiplex FRET experiment. An ex390/20BP filter was used for excitation with an exposure time of 250ms, imaged for 172.77s in total, with 4.43s intervals between the images. Subsequently, the emission was recorded in all four channels. A custom made Matlab script is used to automatically split and align channels, conduct a background subtraction and perform the linear unmixing using the unmixing matrix obtained from the spectral signatures of the FPs.







6. Connecting S1P signaling to endothelial barrier regulation: a possible link between pRex1 and Cdc42

Nathalie R. Reinhard¹, Marieke Mastop¹, Jos van Rijssel², Amber Thijsse¹, Jaap D. van Buul², Theodorus W.J. Gadella Jr.¹, Peter L. Hordijk^{1,3}, and Joachim Goedhart¹.

¹ University of Amsterdam, Molecular Cytology, Swammerdam Institute for Life Sciences, van Leeuwenhoek Centre for Advanced Microscopy, Amsterdam, the Netherlands

² Department of Plasma Proteins and Department of Molecular Cell Biology, Sanquin Research and Landsteiner Laboratory, Academic Medical Center, University of Amsterdam, Amsterdam, the Netherlands

³ Department of Physiology, Free University Medical Center, Amsterdam, The Netherlands





Abstract

Sphingosine-1-phosphate (S1P) is present in high concentrations in the circulation and controls the endothelial barrier function. Exogenous S1P stimulates G-protein coupled receptors (S1PR1-S1PR3 in endothelial cells), activating various downstream signaling cascades. This study focusses on the S1P-mediated endothelial barrier-promoting effect, induced by the relatively unexplored S1PR1–Gi-Cdc42 signaling axis. We elucidate the role of the Gi-protein complex, showing that not the $G\alpha_i$ subunit but the $G\beta\gamma$ subunit is required for signaling towards Cdc42. We subsequently screened for RhoGEFs, acting downstream of this $G\beta\gamma$, in a HeLa cell-based model system. Among the analyzed RhoGEFs; FGD5, ITSN1, PLEKHG2 and pRex1, only pRex1 was able to activate Cdc42 through GPCRs. In summary, this study reveals a S1PR1- $G\beta\gamma$ -pRex1-Cdc42 signaling module that may positively regulate endothelial barrier function.

Introduction

The endothelium consists of a single cell layer of endothelial cells (ECs) that line all blood and lymphatic vessels, and regulate vascular homeostasis (Aird, 2007a; Aird, 2007b). While ECs prevent vascular leakage, they also provide selective permeability, allowing transport of oxygen, nutrients and waste (Del Vecchio et al., 1987; Pappenheimer et al., 1951; Siflinger-Birnboim et al., 1987). ECs furthermore mediate several cellular processes, related to physiological functions in the human body. This includes regulation of vascular tone, blood clotting, immune responses, and the formation of new blood vessels (Korn and Augustin, 2015; Nourshargh et al., 2010; Schaefer and Hordijk, 2015; van Hinsbergh et al., 2015).

A central theme in EC-mediated functions comprises endothelial barrier regulation. This process depends on various networks, controlling intra- as well as intercellular signaling (Mehta and Malik, 2006). One of the main barrier-controlling endothelial signaling cascades is activated by sphingosine-1-phosphate (S1P), a bioactive sphingolipid present in high concentrations in our circulatory system (Berdyshev et al., 2005; Caligan et al., 2000; Xiong and Hla, 2014; Yatomi et al., 1997). S1P mediates EC spreading (Reinhard et al., 2017), and stabilizes the VE-cadherin complex (Lee et al., 1999), the main endothelial cell-cell junction protein. These are fundamental processes, directly linked to endothelial barrier promotion.

Exogenous S1P can activate three different G-protein-coupled receptors (GPCRs) in ECs (S1PR1-S1PR3) (Waeber et al., 2004). GPCRs contain 7 transmembrane-spanning domains and couple to heterotrimeric G-proteins in the cytoplasm. S1PRs couple to Gi and G12/13 protein complexes (Reinhard et al., 2017). The heterotrimeric G-protein complex consists of a G α subunit and a G $\beta\gamma$ dimer. The G α subunit is a G-protein that exists in a GDP bound, inactive state or a GTP-bound active state. Both components, i.e. G α and G $\beta\gamma$, can interact with downstream effectors (Wettschreck and Offermanns, 2005).

Activation of GPCRs results in downstream, activity of Rho GTPases that mediate EC morphology changes. We have previously shown that the net effect of GPCR activation on EC cell shape depends on a balance between RhoA and Rac1/Cdc42 signaling. Two antagonistic signaling modules can be activated in parallel, a S1PR1-Gi-Rac1/Cdc42 signaling axis that results in cell spreading and S1PR2-G12/13-RhoA signaling axis that results in cell contraction. The barrier promoting effect of S1P exists, since the S1PR1-Gi-Rac1/Cdc42 axis dominates (Reinhard et al., 2017).

While Rac1 has already been linked to lamellipodia-driven migration and expansion, Cdc42 has been mainly identified as the Rho GTPase involved in filopodia formation (Ridley, 2003; Ridley, 2015). So far, evidence for a role for Cdc42 in EC cell spreading



is lacking. This study set out to explore the molecular basis of Cdc42-mediated endothelial cell spreading and barrier regulation and we identified previously unrecognized components of the S1PR1Gi-Cdc42 signaling axis. To this end, we characterize and use a set of synthetic tools to perturb Gi/Cdc42 signaling, including DREADDS, chemical induced dimerization and protein-based inhibitors. As read-out we employed single cells imaging of FRET based sensors that report on Gi or Cdc42. Finally, we over-expressed a set of RhoGEFs, to explore RhoGEF-mediated Cdc42 activation in the S1PR1-Gi-Cdc42 signaling axis. Together, these experiments reveal new insights in S1P-mediated Cdc42 activation and endothelial barrier regulation.

Results

Synthetic Cdc42 activation induces EC spreading

While Cdc42 activation has classically been associated to filopodia formation (Ridley, 2003; Ridley, 2015), our previous study has demonstrated that S1P-mediated EC spreading and barrier regulation is accompanied by Rac1 and Cdc42 activation (Reinhard et al., 2017). In order to investigate whether Cdc42 plays a role in EC spreading, we employed a synthetic Cdc42 activation system (figure 1A). This rapamycin-based *hetero*-dimerization system, allows spatiotemporal control over a Cdc42 GEF that can activate endogenous Cdc42 following recruitment to the plasma membrane (Goedhart and van Unen, 2017). Here, the catalytic domain of ITSN1 is linked to a F12 component, tagged with a yellow fluorescent protein (YFP) (kind gift from T. Kortemme, (Kapp et al., 2012)). Upon rapamycin addition, F12-ITSN1 is recruited to plasma membrane-linked FRB, labeled with cyan fluorescent protein (CFP). Combining rapamycin-based ITSN1 recruitment with endogenous F-actin and VE-cadherin labeling demonstrated the induction of a specific phenotype in ECs (figure 1B and supplemental figure S1A, B). While control cells (no rapamycin addition) showed VE-cadherin labeling at the cell border, a marked induction of protrusion was observed after ITSN1 recruitment induced by rapamycin. In line with this protruding phenotype, single EC analysis revealed clear cell spreading after rapamycin-induced ITSN1 recruitment (figure 1C, D). In addition, ITSN1-induced cell spreading was also observed in HeLa cells (supplemental figure S1B, C). Together, these data demonstrate that Cdc42 activation via ITSN1 induces protrusion, which supports the notion that Cdc42 activation is sufficient for induction of cell spreading.

Synthetic activation of Gi demonstrates G $\beta\gamma$ -dependent activation of Cdc42

The rapamycin-based recruitment assay directly linked Cdc42 activity to EC spreading. It is unclear however, to what extent GPCR activation can trigger Cdc42 activity. Our previous study has shown robust Gi-mediated Cdc42 activation upon S1P addition (Reinhard et al., 2017). However, in that study we did not address whether Gi signaling in general can activate Cdc42 or whether it is specific to S1PR1 signaling.

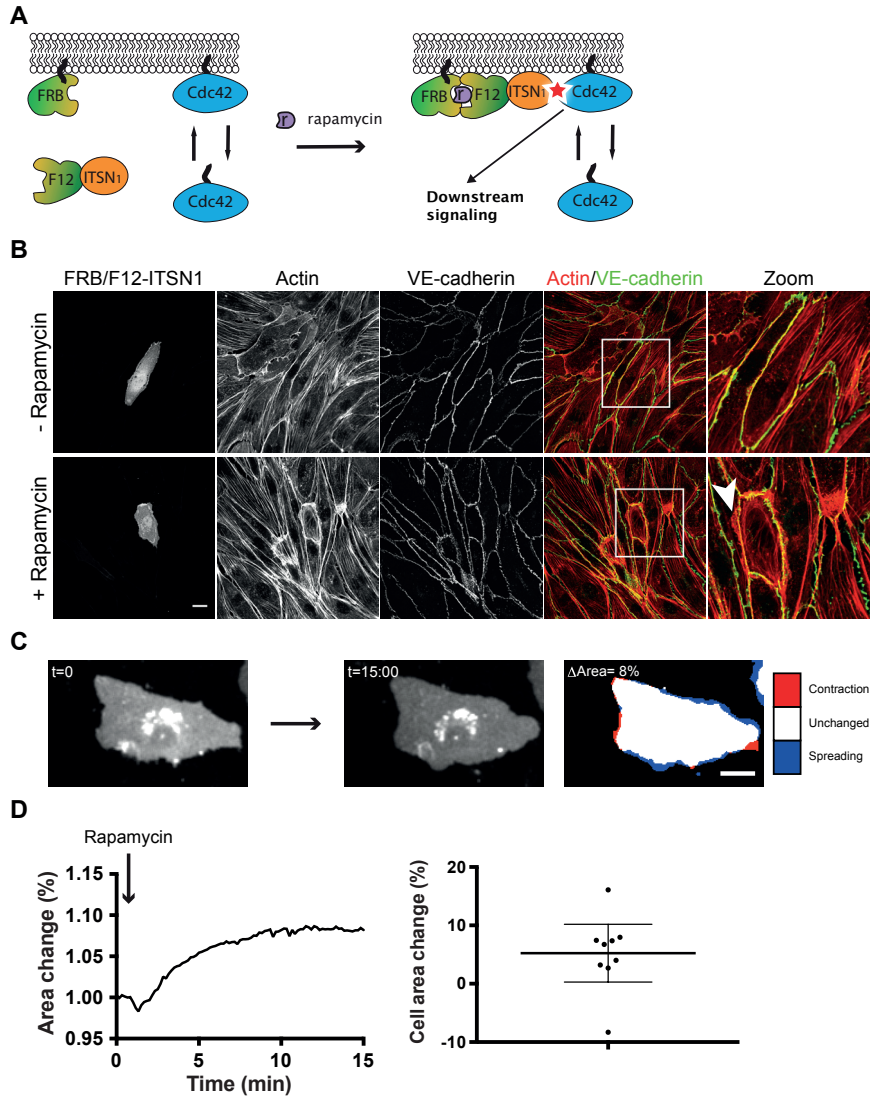


Figure 1. ITSN1-based Cdc42 activation induces cell protrusions and EC spreading.

A) A rapamycin-based recruitment system activates Cdc42 at the PM. FRB= Lck-FRB-ECFP; F12= mCherry-FKBP12-ITSN1. B) ECs were co-transfected with Lck-FRB-ECFP (FRB) and mCherry-FKBP12-ITSN1 (F12-ITSN1), grown to a monolayer, stimulated with rapamycin when indicated, and stained for F-actin and VE-cadherin. FRB/F12-ITSN1 represents merged image of these two constructs, individual expression is illustrated in Supplemental Figure S1A. Arrowhead indicates protruding phenotype. Scale bar = 20 μ m. C) ECs were co-transfected with Lck-FRB-ECFP (represented by fluorescent image) and mCherry-FKBP12-ITSN1, grown to a monolayer and stimulated with rapamycin (100 nM at t = 1:10 min) to measure single cell area changes. Colors on the right image represent area changes according to legend on the right. Scale bar = 20 μ m. D) Corresponding cell area change graph of the EC represented in C). E) EC area change (\pm 95% CI) for n = 9, analyzed as described for C).



To address this question, we turned to a synthetic DREADD receptor (Designer Receptors Exclusively Activated by Designer Drugs) approach in HeLa cells. DREADDs are mutagenized muscarinic receptors that can activate Gq-, Gi-, or Gs-signaling pathways with a synthetic compound that does not have any other biological effect (Armbruster et al., 2007; Zhu and Roth, 2014).

To explore the DREADD-based system in live cells, we used a Gi-specific DREADD (hM4Di) together with validated Gi- or Cdc42 FRET sensors (Kedziora et al., 2016; van Unen et al., 2016c). These sensors allow single cell-based imaging of responses to cell stimulation. The Gi FRET sensor is a loss-of-FRET sensor, and as a result activation is reflected by a loss of the YFP/CFP ratio. In contrast, the Cdc42 sensor is a gain-of-FRET sensor and an increase in Cdc42 activation corresponds to an increase in the YFP/CFP ratio of the Cdc42 sensor.

In order to validate the system, hM4Di was co-expressed with either the Gi- or Cdc42 FRET sensor in HeLa cells. Robust Gi and Cdc42 activation was observed after clozapine-Noxide (CNO, a synthetic DREADD agonist) stimulation, while no response was detected in control cells (Gi or Cdc42 FRET sensor positive cells without hM4Di expression), which fits with the notion that the synthetic activator has no biological effect by itself (figure 2A). These results demonstrate that synthetic activation of Gi results in a Cdc42 response and that Cdc42 signaling is possibly a general response to activation of Gi-coupled receptors.

Next, to explore the differential function of the $G\alpha_i$ subunit and $G\beta\gamma$ dimer in the Gi protein complex, two different inhibitory approaches were used: pertussis toxin (PTX) and the C-terminal domain of G-protein coupled receptor kinase (GRKct), respectively. While PTX abolishes $G\alpha_i$ activation via ADP-ribosylation of the α_i subunit, GRKct selectively inhibits $G\beta\gamma$ signaling without affecting $G\alpha$ -mediated signaling (Koch et al., 1994; O'Neill and Gautam, 2014). PTX pre-treatment completely inhibited CNO-DREADD-mediated Gi activation, as monitored by the Gi-FRET sensor (figure 2B, left graph), indicating that PTX prevents $G\alpha_i$ - $G\beta\gamma$ dissociation. Moreover, there was also no Cdc42 activation after PTX pre-treatment and CNO-DREADD stimulation (figure 2B, right graph).

While PTX inhibits Gi, the GRKct domain selectively inhibits $G\beta\gamma$ by binding to it. To improve the potency of this inhibitor, we made a new, membrane bound variant. The membrane targeting motif from Lck was used to generate Lck-mCherry-GRKct. Co-expressing the Gi FRET sensor with either Lck-mCherry or Lck-mCherry-GRKct, showed robust activation of Gi, under both conditions, after CNO-DREADD stimulation (figure 2C, left graph). The same strategy using Cdc42 FRET sensor, however, showed complete inhibition in the Lck-mCherryGRKct condition after CNO-DREADD stimulation (figure 2C, right graph).

In summary, synthetic stimulation of a DREADD induces robust Gi and Cdc42 activation, which was abolished by selective inhibition of G $\beta\gamma$, suggesting that G $\beta\gamma$ signaling is responsible for Cdc42 activation.

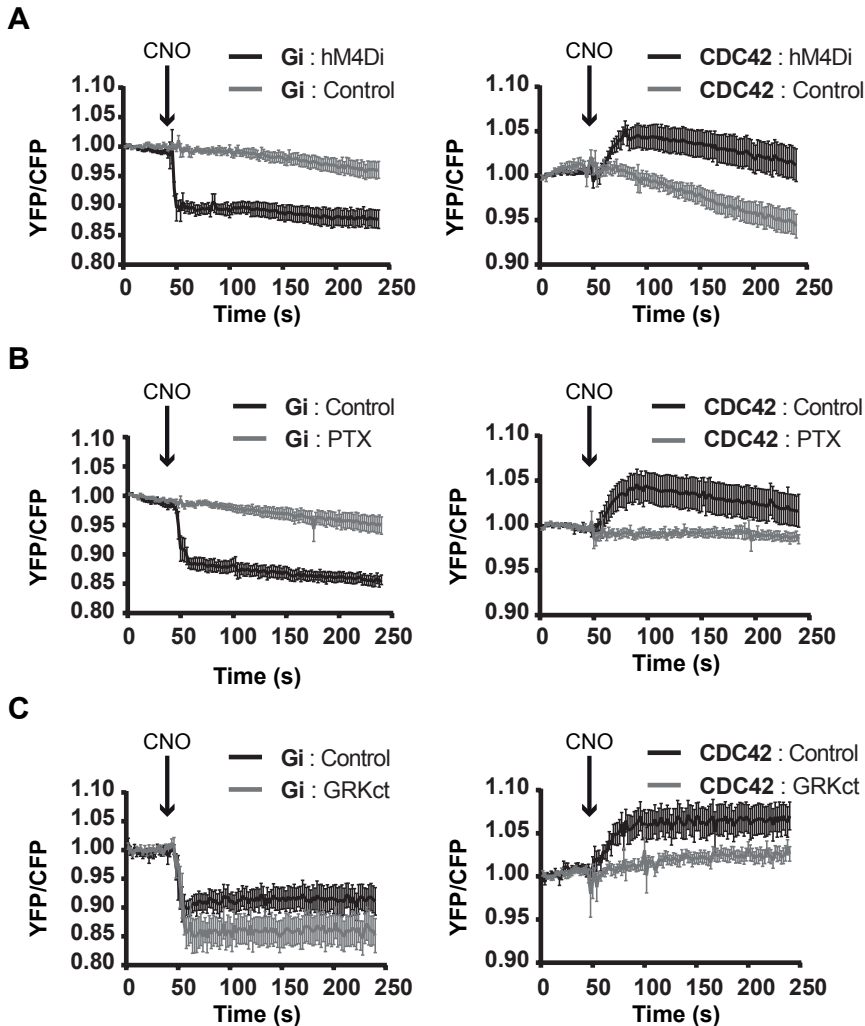


Figure 2. The DREADD-G $\beta\gamma$ system reveals G $\beta\gamma$ -dependent Cdc42 activation in HeLa cells.

A) Normalized average YFP/CFP ratios ($\pm 95\%$ CI) of HeLa cells transfected with either the Gi FRET sensor (Control, n=19), the Gi FRET sensor and hM4Di (n=15) (left graph), or either the Cdc42 FRET sensor (Control, n=32), or Cdc42 FRET sensor and hM4Di (n=32) (right graph). Cells were stimulated with 5 μ M CNO at t = 50 s. B) Normalized YFP/CFP ratios ($\pm 95\%$ CI) of HeLa cells transfected with the Gi FRET sensor and hM4Di (left graph, Control n=15, PTX n=14), or the Cdc42 FRET sensor and hM4Di (right graph, Control n=19, PTX n=11). Cells were stimulated with 5 μ M CNO at t = 50 s, PTX cells were pre-treated with 100 ng/ml PTX for at least 18 hours. C) Normalized average YFP/CFP ratios ($\pm 95\%$ CI) of HeLa cells transfected with either the Gi FRET sensor, hM4Di and Lck-mCherry (Control, n=14), the Gi FRET sensor, hM4Di and Lck-mCherry-GRKct (n=15) (left graph), or either the Cdc42 FRET sensor, hM4Di and Lck-mCherry (Control, n=20), or Cdc42 FRET sensor, hM4Di and Lck-mCherry-GRKct (n=20) (right graph). Cells were stimulated with 5 μ M CNO at t = 50 s.



Gβγ inhibition diminishes S1P-mediated Cdc42 activation and EC spreading

Our data showed that Cdc42 responses induced by activating the Gi-coupled DREADD can be inhibited by a protein-based inhibitor of the Gβγ complex. The same tool to inhibit Gβγ was used to test the function of Gβγ in S1P-mediated Cdc42 activation and endothelial barrier regulation.

ECs were transfected with the Cdc42 FRET sensor and with either Lck-mCherry (Control) or Lck-mCherry-GRKct (figure 3A). Control cells showed fast and transient Cdc42 activation after S1P stimulation paralleled by an increase in cell area in 7 out of 10 cells (figure 3B, C). However, in ECs overexpressing Lck-mCherry-GRKct, the Cdc42 activation was absent. Strikingly, majority of these cells (5 out of 7) showed a reduction of area due to cell contraction (figure 3B, C). Collectively, the GRKct inhibitory approach demonstrates that Gβγ signaling is required for S1P-mediated Cdc42 activation and the correspondent EC spreading

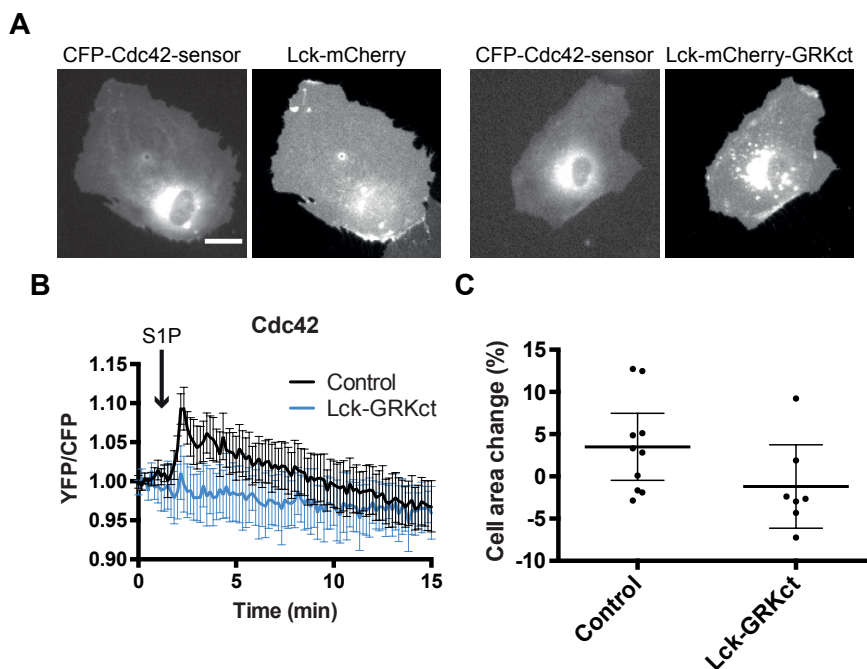


Figure 3. Gβγ inhibition by GRKct, blocks S1P-mediated Cdc42 activation in ECs.

A) Images representing ECs that were co-transfected with the Cdc42 FRET sensor and Lck-mCherry (Control, Left) or the Cdc42 and Lck-mCherry-GRKct (Right). Scale bar = 20 μm. B) Normalized average YFP/CFP ratios (±95% CI) of ECs that were transfected as described in A) (Control, n=10, Lck-GRKct n=7), grown to a monolayer and stimulated with S1P (500 nM). C) Corresponding cell area changes (±95% CI) of ECs measured in B).

SEW-mediated Cdc42 activation as a screening method in HeLa cells

Our results point to a role for $G\beta\gamma$ in the activation of Cdc42 activation, revealing new details regarding S1P-mediated signaling in ECs. However, the identity of the GEFs in this signaling cascade is still unknown. Before we focused on this missing link, we first turned to a cell model that was easier to grow and transfect and can be used to delineate signaling with FRET sensors. HeLa cells fit this profile (van Unen et al., 2016b), and we first analyzed whether G_i and Cdc42 responses could be detected in this cell system under endogenous conditions, i.e. without GPCR overexpression. To this end, we examined the response of HeLa cells to SEW2871 (SEW), which activates G_i signaling through the S1P receptor 1 (S1PR1) (Reinhard et al., 2017). As can be inferred from figure 4A and B, both G_i and Cdc42 are activated by SEW stimulation. Additionally, an increase in cell area was detected for Cdc42 (increase in 7 out of 10 cells), but not for G_i (increase in 1 out of 7 cells).

Overall, these data show that G_i and Cdc42 activation can be monitored in HeLa cells upon stimulation of endogenous S1PR1 via SEW. These observations furthermore suggest that GEFs are present in HeLa cells that can connect G_i activation with Cdc42 activation.

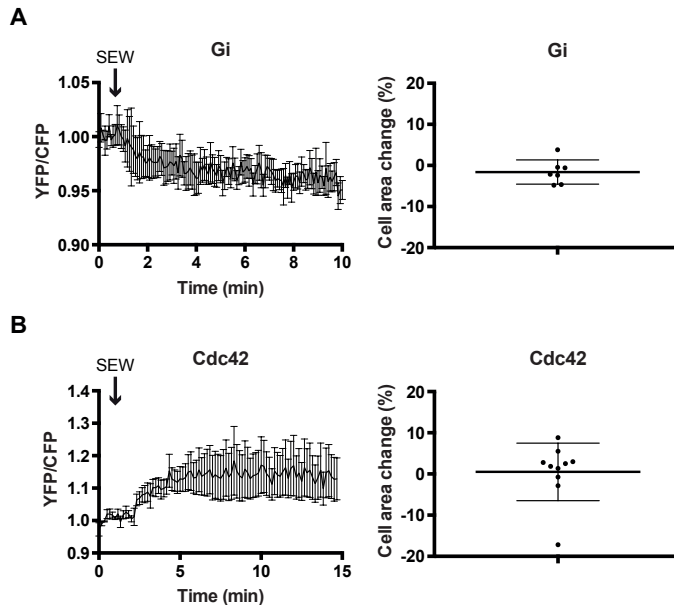


Figure 4. G_i and Cdc42 FRET sensor stimulation in HeLa cells, upon activation of the S1PR1 with SEW.

A) Normalized YFP/CFP ratios ($\pm 95\%$ CI) of HeLa cells transfected with the G_i FRET sensor ($n=7$) and stimulated with $5 \mu\text{M}$ SEW at $t=0:55$ (left graph) and corresponding cell area changes (right graph). B) Normalized YFP/CFP ratios ($\pm 95\%$ CI) of HeLa cells transfected with the Cdc42 FRET sensor ($n=10$) and stimulated with $5 \mu\text{M}$ SEW at $t=0:55$ (left graph) and corresponding cell area changes (right graph).



pRex1 overexpression enhances SEW-mediated Cdc42 activation

HeLa cells showed SEW-mediated Cdc42 activation via endogenous S1PR1, suggesting that this system could be used to screen for GEFs involved in this pathway. Since combined FRET and RhoGEF knockdown studies are time-consuming and technically challenging, we turned to a RhoGEF overexpression-based approach. Four RhoGEFs of interest were selected, including FGD5, ITSN1, PLEKHG2, and pRex1. While FGD5 and ITSN1 have already been linked to Cdc42 activation in the endothelium (Ando et al., 2013; Hernández-Vásquez et al., 2017; Pannekoek et al., 2018), PLEKHG2 and pRex1 are stimulated by G $\beta\gamma$ signaling (reviewed in (Vázquez-Prado et al., 2016)), making them interesting candidates for SEW-mediated Cdc42 activation.

Cdc42 FRET sensor-expressing cells were co-transfected with mCherry (Control) or one of the selected RhoGEFs, fused to mCherry. Similar Cdc42 activation kinetics were observed in the Control, ITSN1, FGD5 and PLEKHG2 condition, while cells overexpressing pRex1 demonstrated a large increase in Cdc42 activation, mediated by the SEW compound (figure 5A). Cell area analysis showed increased cell areas in all conditions, with the largest change observed for the pRex1 condition (figure 5B). In the pRex1 overexpression cells, we observed extensive ruffling induced by SEW (compare Control and pRex1 panel in figure 5C). Together, these data suggest that pRex1 can be activated by S1PR1 and induce Cdc42 activation.

Discussion

Previously, we studied S1P-mediated endothelial barrier regulation (Reinhard et al., 2017) using biochemical approaches and a series of FRET based sensors for heterotrimeric G-proteins and Rho GTPase activity. Although we identified a novel barrier-promoting, Gi mediated Cdc42 signaling axis in ECs, specific molecular details were lacking. We were unable to link Cdc42 activation with changes in cell area, we could not conclude which part of the Gi heterotrimer (G α i subunit or G $\beta\gamma$ dimer) signals towards Cdc42 and the identity of the relevant Cdc42-GEF(s) was unknown.

This study aimed to better define the activation and function of the Rho GTPase Cdc42 in ECs. Uncovering the mechanism by which Cdc42 is controlled under physiologically relevant conditions, reveals new molecular insights in S1P-mediated barrier protection. Our principal findings are that (i) Cdc42 activation is sufficient to induce EC spreading, (ii) G $\beta\gamma$ activity is required for Cdc42 activation in ECs and (iii) G $\beta\gamma$ derived from Gi activation can activate Cdc42 via pRex1. Together, our data suggest that S1P-mediated positive barrier regulation in ECs can be the consequence of a G $\beta\gamma$ -pRex1-Cdc42 signaling axis.

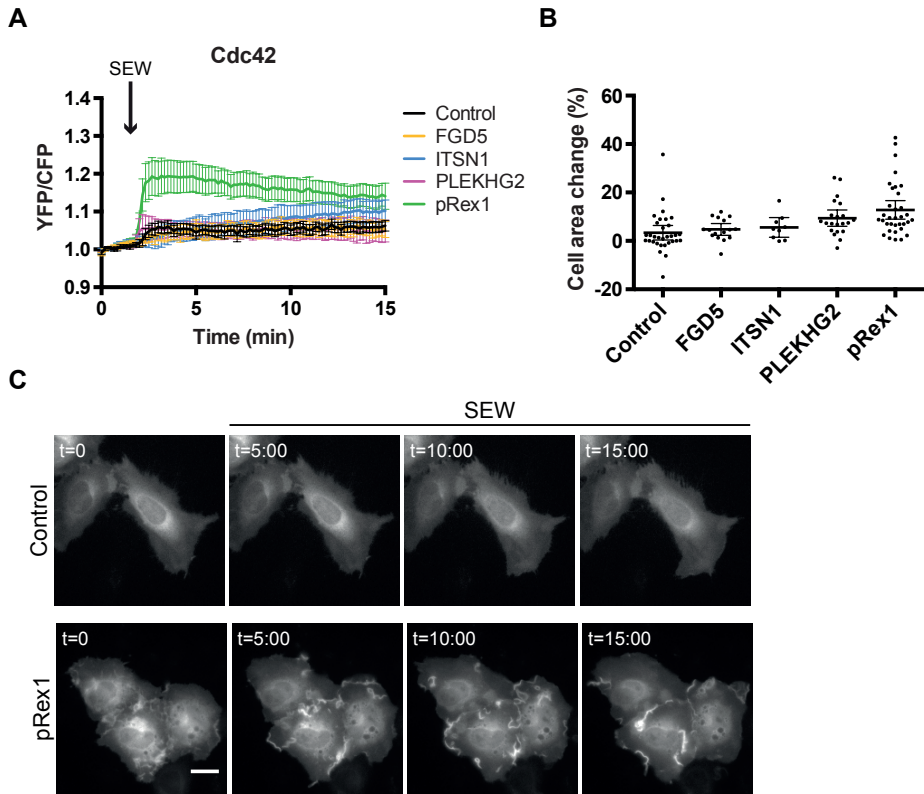


Figure 5. Ectopic expression of pRex1 enhances SEW-mediated Cdc42 activation.

A) HeLa cells were transfected with the Cdc42 FRET sensor and either C1-mCherry (Control, n=32), mCherry-FGD5 (n=16), mCherry-ITSN1 (n=9), mCherry-PLEKHG2 (n=22) or mCherry-pRex1 (n=33), grown to a monolayer and stimulated with 5 μ M SEW at t=0:55. B) Corresponding cell area changes (\pm 95% CI) of cells measured in A). Images of cells measured in C), representing cells from the Control and pRex1 condition. Scale bar = 20 μ m.



Before we could study Gi protein signaling in ECs, the validation of tools to activate and inhibit Gi-based signaling was required. We employed an engineered GPCR (DREADD, (Armbruster et al., 2007; Zhu and Roth, 2014)) and demonstrated that the synthetic ligand induces strong, robust activation of Gi in HeLa cells. The stimulation of the DREADD shows also activation of the Cdc42 FRET sensor. Using the DREADD, we analyzed the molecular and cellular consequences of PTX-and GRKct-mediated inhibition. PTX-treated cells fail to show a Gi-FRET sensor response after DREADD stimulation, indicating that this toxin prevents dissociation of the $G\alpha_i$ subunit and $G\beta\gamma$ dimer, in line with published studies (Burns, 1988). In addition to Gi inhibition, PTX also inhibits signaling towards Cdc42, corresponding to our previous observations for S1P-mediated signaling in ECs (Reinhard et al., 2017) and (Kedziora et al., 2016).

In contrast to PTX, subunit specific inhibition can be accomplished via the $G\beta\gamma$ inhibitor GRKct (Koch et al., 1994; O'Neill and Gautam, 2014). To increase the potency of the inhibiting domain, we targeted it to the plasma membrane by using a lipid-modifying motif from Lck. Employing this new $G\beta\gamma$ inhibitor with DREADD and the Gi FRET sensor, still results in activation of the Gi-complex which can be interpreted as dissociation of the respective subunits. Interestingly, Cdc42 activation is completely blocked by GRKct, suggesting $G\beta\gamma$ -dependent Cdc42 activation. It also reveals the power of the membrane bound GRKct-based inhibitor.

After validation of the $G\beta\gamma$ -specific GRKct-mediated inhibition, we were now able to use this selective tool in ECs. We demonstrate that $G\beta\gamma$ is required for S1P-mediated signaling towards Cdc42, as monitored by the Cdc42 FRET sensor. In line with the lack of Cdc42 activation, $G\beta\gamma$ inhibition predominantly results in a negative EC area change following agonist stimulation, corresponding to cell contraction. This corresponds to our previous finding that in absence of S1PR1-Gi-Rac1-Cdc42 signaling, S1P mediates EC contraction via S1PR2-G12/13- RhoA activation (Reinhard et al., 2017).

Next to unraveling the involvement of G-protein subunits in S1P-mediated Cdc42 activation, we searched for potential RhoGEF proteins in this pathway. Since HeLa cells show moderate Cdc42 activation in response to S1PR1 stimulation, this cell type was used to perform a RhoGEF-screening method based on ectopic expression of a selection of candidate Cdc42 GEFs. Based on FRET measurements, we identify pRex1 as a potential RhoGEF in S1P-mediated Cdc42 signaling. Although we demonstrated the $G\beta\gamma$ -dependent and pRex1-mediated Cdc42 activation, a direct functional $G\beta\gamma$ -pRex1 link could not be deduced from these data. Besides the effect on Cdc42 activation, we also observe effects on cellular morphology since we detected increased spreading in S1PR1-stimulated, pRex1 overexpressing cells. However, additional studies are required to determine the sole effect of pRex1 overexpression.

The observation that pRex1 overexpression results in robust activation of Cdc42 is somewhat surprising, given the fact that pRex1 is characterized as a Rac specific GEF. Moreover, the activation of Cdc42 by pRex1 *in vivo* is qualified as unlikely (Welch, 2015). Still, *in vitro* analysis with purified proteins shows a robust activation of Cdc42 by pRex1 (Jaiswal et al., 2013). The reason for this discrepancy may be the lack of tools for *in vivo* measurements of Cdc42. Of note, the biochemical detection of Cdc42 activation by pull-down strategies is notoriously difficult (Reinhard, not shown). In addition, Cdc42 activation is indirectly inferred from morphological changes, i.e. filopodia formation. As we demonstrate, the Cdc42 activation may result in cell spreading which is a phenotype that is exclusively (and mistakenly) linked with Rac activity.

The Cdc42 sensor reports Cdc42 GEF activity after stimulation of endogenous receptors in HeLa cells or primary ECs, demonstrating its sensitivity. As for selectivity, we have previously shown that the Cdc42 sensor is specifically activated by Cdc42 GEFs and not by Rac GEFs (Reinhard et al, unpublished). In summary, we think that G $\beta\gamma$ induced pRex1 activity in cells results in active, Cdc42-GTP, which is a hitherto largely ignored consequence of Gi signaling.

In TNF α -treated endothelium, pRex1 has been implicated in the loss of barrier, in marked contrast to our results (Naikawadi et al., 2012). These authors showed that pRex1 mediates Rac1 activation, albeit that Cdc42 was not analyzed, and that this leads to production of reactive oxygen species which are known to reduce barrier function (Hordijk, 2006). It cannot be excluded that in ECs, activation of Rac1/Cdc42 may have a different outcome in the context of TNF-induced barrier loss, which takes several hours, as compared to S1P-induced barrier stabilization which takes place within minutes (Reinhard et al., 2017).

Now that we proposed pRex1 as RhoGEF regulator in S1P-mediated Cdc42 activation, future experiments should focus on its specific function in the vasculature. First of all, either knockdown or knockout experiments are required to investigate the direct link between pRex1 and Cdc42 activation. These strategies can also be applied *in vitro* to Electrical Cell-sensing Impedance System (ECIS) measurements, a validated approach to quantitatively study endothelial barrier regulation. Additionally, since pRex1 has been linked to Rac1 signaling (Naikawadi et al., 2012; van Hooren et al., 2014; Welch, 2015), we also need to include this Rho GTPase in our study to define Rac1 vs Cdc42-specific signaling outcomes.

In summary, this study reports novel molecular insights in Cdc42-mediated signaling. We show that Cdc42 activation can be directly linked to EC spreading and furthermore demonstrate that Cdc42 can be controlled by S1P-mediated G $\beta\gamma$ and pRex1 activation. This signaling axis is of great relevance in the vasculature, where it will positively



regulate the endothelial barrier, protecting against unwanted edema and tissue damage.

Methods

Plasmids

Cry-2-mCherry-GRKct (Addgene plasmid #64212) and Lck-mCherry were digested with BsrGI and EcoRI. In turn, digested fragments were ligated to generate Lck-mCherry-GRKct.

The translocatable, catalytic ITSN1 construct was a kind gift from T. Kortemme (Kapp et al., 2012). DREADD-hM4Di was obtained from Addgene (plasmid # 45548). mCherryFGD5, mCherry-ITSN1, mCherry-PLEKHG2 and mCherry-pRex1 originate from our Cdc42 GEF screen study (Reinhard et al., unpublished). Gi (van Unen et al., 2016c) and Cdc42 (Kedziora et al., 2016; Reinhard et al., 2017) FRET sensors were as described in their cited references.

Direct antibody labeling

Actin-stain 555 Phalloidin was from Cytoskeleton. mAb Mouse anti-VE-cadherin/CD144 AF647 was obtained from BD Pharmingen.

Reagents

The following reagents were used in this study; Rapamycin from LC Laboratories (Woburn, MA), S1P from Avanti Polar Lipids, CNO was from Enzo life Sciences, PTX (PHZ1174) was from Thermo Fisher, and SEW2871 (10006440) from Cayman Chemical. These compounds were prepared, following the manufacturers' instructions.

HUVEC culture and transfection

Primary HUVECS, acquired from Lonza (Verviers, Belgium), were cultured on fibronectin (FN)-coated culture dishes. HUVECs were grown in EGM-2 medium supplied with singlequots (Lonza) and transfected at passage #4 or #5. Transfections were performed with a Neon transfection system (MPK500) and corresponding transfection kit (both from Invitrogen), using 2 μ g plasmid DNA. A single pulse was generated at 1300V for 30ms, and cells were seeded on fibronectin-coated glass coverslips (Menzel-Gläser, Braunschweig, Germany) and grown to a monolayer.

HeLa cell culture and transfection

HeLa cells were acquired from American Tissue Culture Collection (Manassas, VA, USA) and cultured in Dulbecco's Modified Eagle Medium (DMEM, (Invitrogen)), supplemented with Glutamax, 10% FBS, Penicillin (100U/ml) and Streptomycin (100 μ g/ml). HeLa cells were seeded on glass coverslips (Menzel-Gläser, Braunschweig,

Germany) and transfected with 3 μ l PEI (1 mg/ml), 100 μ l OptiMeM (Life Technologies, Bleiswijk, NL) and in total 1 μ g plasmid DNA.

Confocal imaging

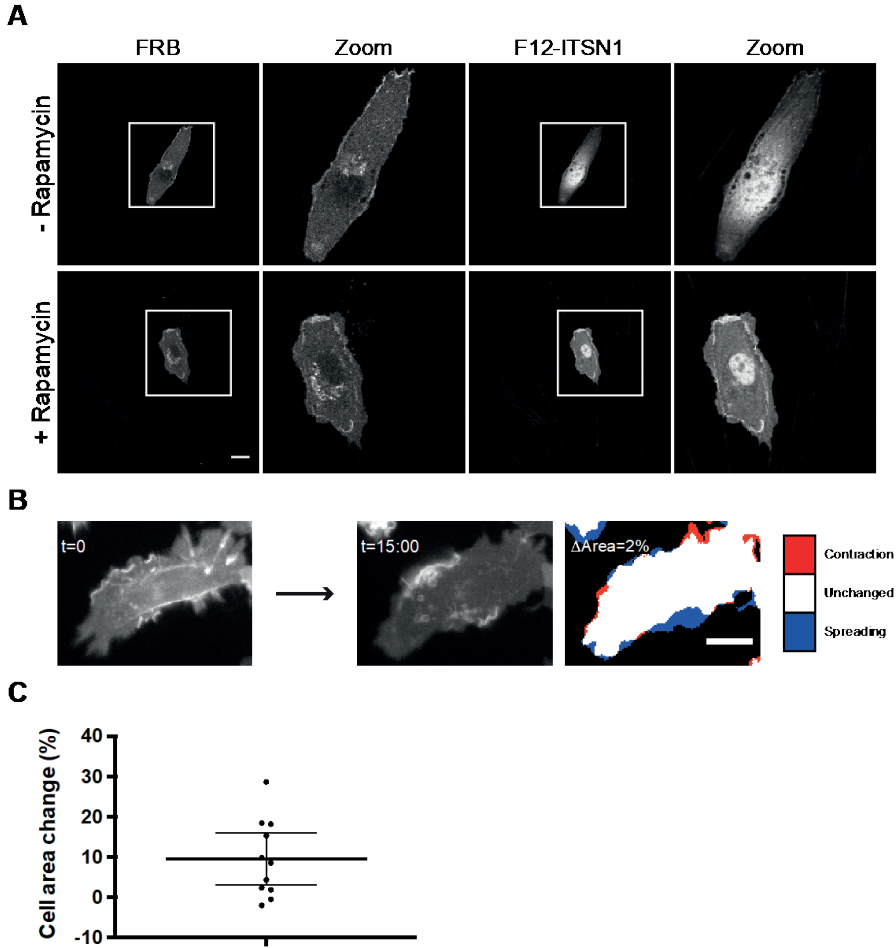
HUVECs were transfected and stimulated as indicated. Cells were washed in PBS (1mM CaCl₂ and 0.5 mM MgCl₂) and fixed for 5 minutes in PBS (1mM CaCl₂ and 0.5mM MgCl₂) with 4% formaldehyde. Next cells were permeabilized for 5 minutes in PBS, supplied with 0.5% Triton X100 and blocked for 20 minutes in PBS-BSA (0.5%). Eventually, cells were incubated for at least 45 minutes with directly-labeled antibodies in PBS-BSA (0.5%). Image acquisition was performed on Nikon A1 Confocal microscope equipped with a 60x oil immersion objective (NA 1.40, Plan Aplanachromat VC) and corresponding Nikon NIS elements software.

Live HUVEC ITSN1 recruitment experiments and cell area change measurements

HUVECs were transfected and stimulated as indicated. Widefield images were obtained on a Zeiss Observer Z1 microscope, equipped with a 40x oil immersion objective (NA 1.3), a HXP 120V excitation light source Metamorph 6.1 software. Next, cell area change analysis was performed according to the method described in Reinhard et al., 2017.

Live HUVEC and HeLa cell FRET measurements

Both HUVECs and HeLa cells on glass coverslips were transfected as described and placed in Metal Attofluor cell chambers at least 16 hours after transfection. In turn, live-cell images were collected on a widefield Zeiss Axiovert 200 M microscope (Carl Zeiss GmbH), equipped with an Plan- Neofluor 40x oil-immersion objective (NA 1.30), xenon arc lamp with monochromator (Cairn Research, Faversham, Kent, UK), cooled charged-coupled device camera (Coolsnap HQ, Roper Scientific, Tucson, AZ, USA), and Metamorph 6.1 software. Images were recorded, applying 420nm excitation light (slit width 30nm) and 455 DCLP dichroic long-pass mirror. Next, light was directed to CFP and YFP bandpass emission filters of 470/30nm and 535/30nm, respectively. mCherry was excited with 570nm light (slit width 10nm), and a 585 DCXR mirror directed mCherry emission to a 620/60nm emission filter. Images were all background subtracted and YFP images were bleed-through corrected (55%) for leakage of the CFP into the YFP channel.



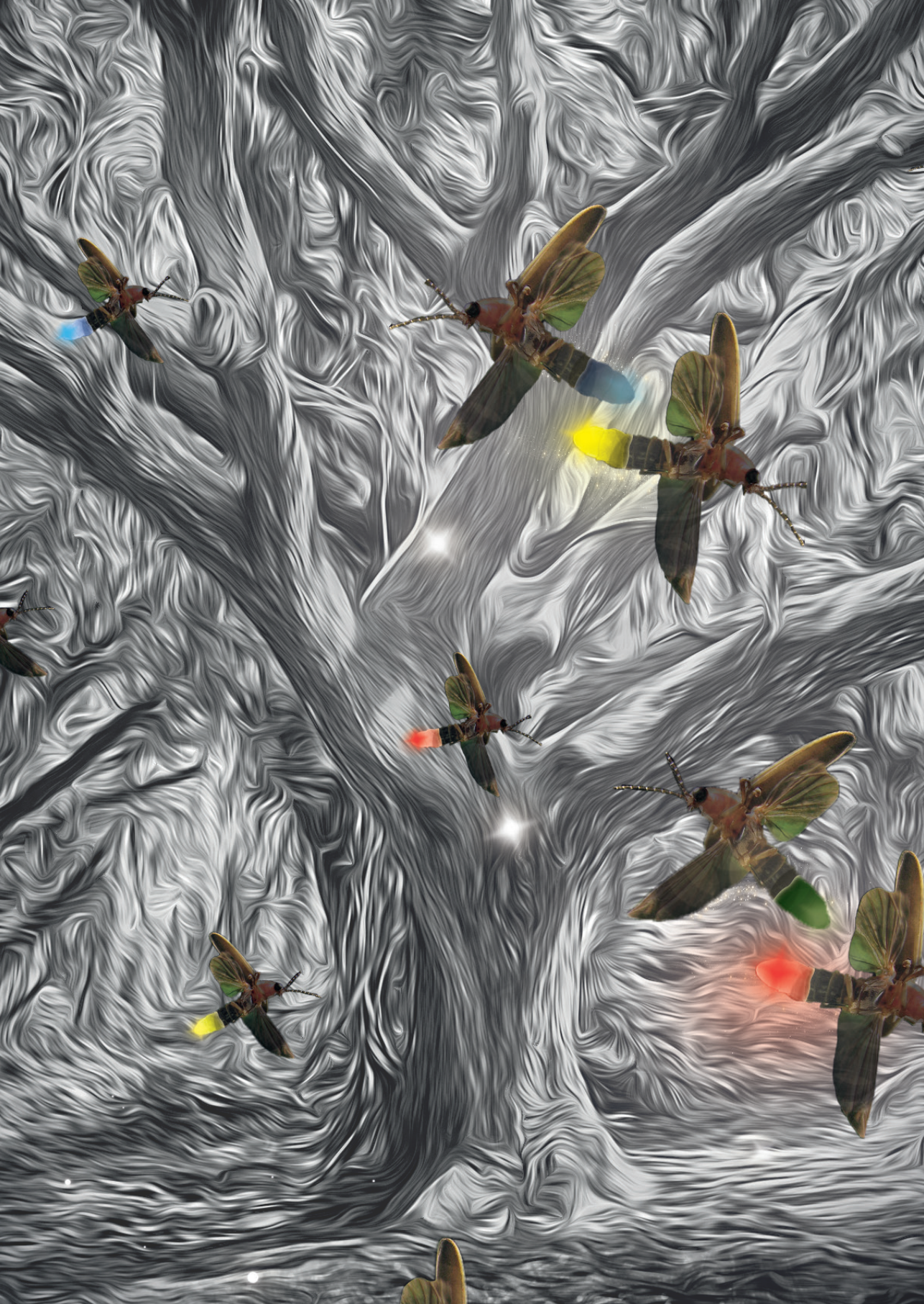
Supplemental Figure S1. ITSN1-based Cdc42 activation induces cell spreading in ECs and HeLa cells.

A) Additional examples of protruding phenotype illustrated in Figure 1A. Asterisks indicate Lck-FRB-ECFP/YFP-FKBP12-ITSN1 positive cells. Arrowheads indicate protruding phenotype.

B) Individual CFP and YFP channels representing Lck-FRB-ECFP (FRB) and YFP-FKBP12-ITSN1 (F12-ITSN1) positive ECs corresponding to ECs in Figure 1B. Translocation of F12-ITSN1 in the “+ rapamycin condition” is recognized by homogeneous localization of the construct. B) HeLa cells were co-transfected with Lck-FRB-ECFP (represented by fluorescent image) and mCherry-FKBP12-ITSN1, and stimulated with rapamycin (100 nM at t = 1:05 min) to measure single cell area changes. Colors on the right image represent area changes according to legend on the right.

C) HeLa cell area change (\pm 95% CI) for n = 11, analyzed as described for B). Scale bars depict 20 μ m.





7. General Discussion

The research presented in this thesis aimed at gaining a better understanding of intracellular signaling by generating and applying FRET based biosensors. To this end fluorescent proteins (FPs) were characterized and the resulting knowledge is used to develop and optimize FRET based biosensors. The biosensors delivered new insights into the regulation of GPCR signaling via dynamic FRET imaging of living cells.

7.1 Optimizing FRET based biosensors

The accuracy and quality of the data obtained with FRET imaging relies heavily on the performance of the biosensors that are employed. If a biosensor is not functioning as intended, the observed changes in FRET efficiency might not correlate with the occurrence of the specific events in cellular signaling for which the biosensor was designed. Therefore, it is extremely important that biosensors and the FPs constituting the FRET pair are thoroughly characterized. The selectivity, affinity and dynamic range of a sensor determine its performance, as was already touched upon in the general introduction of this thesis. The selectivity and affinity are primarily defined by the sensing domain. On the other hand, the dynamic range (or contrast) heavily depends on the properties of the donor and acceptor fluorophore. Below we focus on various aspects by which probes affect the FRET biosensor performance, i.e. FRET pair, the FP characteristics, or the overall sensor design.

First, the selection of an optimal FRET pair should be based on careful evaluation of existing FPs and selecting an efficient donor FP and an efficient acceptor FP to constitute the FRET pair (**chapter 2 and 3**). Ideally, all FP characteristics should be optimal. Nonetheless, in reality, no FP is flawless and several important FP characteristics are dependent on the experimental conditions of the sensor application. However, some general guidelines apply to choosing an efficient FRET pair. An important property for choosing a donor FP, is the quantum yield, for efficient energy transfer towards the acceptor. Furthermore, the brightness is important since it affects the signal-to-noise ratio. Thereby, increased brightness facilitates discrimination between the FRET "on" and "off" state of the sensor. An important feature for choosing an acceptor FP is the extinction coefficient, since it determines the efficiency for energy transfer via FRET. When the sensor will be used for ratiometric FRET imaging, the brightness, influenced by the extinction coefficient, quantum yield and maturation efficiency, is important to obtain a high signal-to-noise ratio. However, when the sensor will be used for FLIM-FRET imaging, the quantum yield of the acceptor is not important because only the fluorescence signal of the donor FP is monitored in this application.



Next to these important characteristics to consider for the donor and the acceptor FP separately, it is of importance to consider efficient donor and acceptor FP combinations. The FRET efficiency between a donor and acceptor FP is determined by the orientation of the FP dipoles, the distance between the FPs and spectral overlap between the emission spectrum of donor and the absorption spectrum of acceptor. The distance and orientation are optimized when focusing on the overall sensor design as will be discussed later. The larger the spectral overlap, the higher the FRET efficiency in the FRET “on” state. The larger the difference between the FRET “on” and “off” states, the higher the dynamic range of the sensor will be. However, the emission spectra of the donor and acceptor FPs should be clearly distinguishable and direct excitation of the acceptor with the donor excitation wavelength should be avoided. Therefore, FPs exhibiting narrow excitation and emission peaks are preferred. Additionally, it is important that the donor and acceptor FPs do not show a high tendency to dimerize. This can disrupt the functional localization of the sensor construct, lead to sensor aggregates, or in case of high *hetero*-dimerization, to a sensor that is locked in the FRET “on” state. However, some sensors are more affected by a high dimerization tendency than others. Additionally, false FRET readouts could be due to different maturation rates of the donor and the acceptor, when one of the FPs is still maturing during the experiment, or due to a different photostability of the FPs affecting the dynamics of the sensor. Furthermore, the importance of certain FP characteristics are dependent on the experimental conditions. For example, a low pKa of the FPs constituting the FRET pair is important when a sensor is applied in an acidic environment, and long experiments with short imaging intervals require FPs with a high photostability and fast maturation. Finally, control experiments should be performed to determine the qualities and limitations of the sensor.

Second, the characteristics of the individual FPs constituting the FRET pair can be optimized via mutagenesis (**chapter 5**). This approach is necessary when existing FPs do not exhibit the correct characteristics for the purpose of the sensor. Although several FPs have been successfully used in biosensors, there is often room for improvement. The characteristics of an FP are determined by the amino acid sequence, the resulting non-covalent interactions between amino acids that compose the β -barrel and the autocatalytic reaction that is needed for chromophore formation (Cubitt et al., 1999; Patterson et al., 1997; Siemering et al., 1996; Tsien, 1998). In the past decades ample knowledge was obtained about which amino acid residues affect which FP characteristics and this can be used to optimize FPs for specific applications. Optimizing FP characteristics involves a combination of studying the literature, i.e. what effects are reported for certain amino acid residues at certain positions within the FP structure, and studying crystal structures of FPs. Existing knowledge is used to predict what effects of certain residues could be or to explain the effects observed when empirically testing residues at a certain position within the FP structure. Note that, when optimizing one characteristic, this might affect another characteristic as well. Thus, optimizing FP characteristics mainly involves mutagenesis and characterization.

The third approach towards sensor optimization focusses on the overall sensor design. Optimizing the overall sensor design involves the relative orientation of the FP dipoles, weak FP *hetero*-dimerization, the sensor domains, the linker properties, and the order of the sensor components, such that the sensor response is specific, sensitive and shows a clear FRET contrast. Unimolecular sensors exist of one polypeptide containing sensor domains and a FRET pair separated by a linker that restricts the FRET pair in relative orientations and distance, which require substantial optimization next to selecting the right FPs as FRET pair. The bimolecular sensor design involves two separate FP-fused sensor domains. This sensor design requires less optimization focused on the overall sensor design since it does not contain a linker separating both FPs of the FRET pair, restricting the distance and relative orientation of the FPs dipoles. Furthermore, there are less possibilities for the order of the sensor components than in unimolecular sensors. An advantage of a bimolecular sensor construction is that the effect of alterations is rather predictable, due to the less restricted FP orientation and distance, which also makes that this sensor type is less affected by small conformational changes in sensor design. A disadvantage of this sensor design is that the labeled domains might interact with unlabeled endogenous proteins in the cell, meaning that part of the interactions will not result in a FRET readout. Furthermore, there is no set stoichiometry between both FP-labeled domains if they are expressed from different constructs or controlled by different promoters. This can be solved by using an IRES (3:1) or 2A (1:1) sequence between the domains, expressed from the same construct, controlled by the same promoter. Advantages of unimolecular sensors are that there is a set stoichiometry between the FPs and the FPs in the sensor are always in close proximity making interaction with endogenous proteins unlikely. Furthermore, more extensive optimization of FRET contrast between the FRET “on” and “off” states is possible due to the structurally more confined conformations of the sensor. The more confined conformations, however, also make it harder to predict the effects of small alterations due to the more confined structure of a unimolecular sensor in the FRET “on” and “off” states.

In summary, the contributions this thesis contains to the field of FRET sensor optimization starts with the evaluation of the FRET efficiency, brightness and photostability of several FRET pairs, with mTurquoise2 as FRET donor (**chapter 2**). The FRET pair mTurquoise2-mNeonGreen excelled in all characterization experiments as well as in FRET contrast when applied in a bimolecular FRET based sensor, reporting Gq activation. Additionally, the FRET pair mTurquoise2-sREACH stood out in the FLIM-FRET measurements. This because broader donor emission filter settings could be used, due to the negligible emission of sREACH, a dark acceptor. Moreover, mCherry and mScarlet-I surpassed the other red FRET acceptors, presumably due to their fast and complete maturation. This approach of selecting an efficient FRET pair, conceivably leads towards development of efficient bimolecular sensors. Selecting efficient FRET pairs is, however, often not sufficient for the optimization of unimolecular sensors. We demonstrated this by application of the efficient mTurquoise2-mNeonGreen FRET pair

in multiple unimolecular FRET based biosensors, all resulting in a decreased dynamic range (**chapter 2** and **chapter 3**). In chapter 3 and 5 we evaluated the effects of the relative orientation of the FP dipoles on the dynamic range of a unimolecular sensor, reporting RhoA activation. We observed an evident effect of the relative FP orientation on the dynamic range, as was also reported by others (Fritz et al., 2013; Nagai et al., 2004). It was, however hard to predict the effect of a certain circular permutation, but in general circular permutation around residue 173 led to a positive effect on the dynamic range. Additionally, we investigated the weak FP *hetero*-dimerization, i.e. stickiness, between the FPs constituting the FRET pair (**chapter 3**). Stickiness is believed to increase the dynamic range of unimolecular sensors, by yielding higher FRET efficiency in the FRET “on” state of the sensor. Certain amino acid residues, positioned at the dimer interface, are reported, or suggested to affect the level of stickiness (Kotera et al., 2010; Lindenburg et al., 2014; Vinkenburg et al., 2007; Zacharias et al., 2002). However, reported data are sometimes conflicting, suggesting a strong relation between level of desired stickiness and the structure of the sensor, i.e. one sensor benefits from a high level of stickiness between the FRET pair, while another sensor does not. We studied CFP variants Cerulean3 and mTurquoise2 at the FRET donor position in a unimolecular sensor, reporting RhoA activation. Application of novel, more optimized mTurquoise2 resulted in a decreased dynamic range of the sensor, though unexpected based on the FRET pair characteristics. 206A/K is a residue for which an effect on stickiness was previously reported (Cranfill et al., 2016; Kotera et al., 2010; Zacharias et al., 2002). Contradictory, we did not find a clear effect of 206A/K on the dynamic range of the RhoA activation biosensor (**chapter 3**). This shows again that the effects of small alterations in unimolecular sensors are hard to predict.

In order to decipher the crosstalk between signaling pathways via multiplex FRET imaging, CFP and LSS-FPs could be applied together as simultaneously excitable donor FPs. We evaluated the characteristics of existing LSS-FPs. We succeeded in improving the monomeric behavior of mAmetrine and successfully used it to tag Gαq. However, the photostability remained low. Therefore, we continued with GFP variants. Several variants were developed by mutagenesis to alter GFP variants into LSS-GFP variants (**chapter 5**).

For future FP optimization it might be fruitful to develop an algorithm that aligns multiple sequences, and compares the alignments with phenotypic scores for the FPs, to identify which parts of the genetic code influence certain characteristics (Orgogozo et al., 2015). The correctness of the phenotypic scoring is pivotal for the reliability of this algorithm and therefore the phenotypic scoring should be standardized for all characteristics. This implies that this will be a labor intense project, though feasible using the high throughput screening methods introduced previously (Bindels et al., 2017; Goedhart et al., 2010; Goedhart et al., 2012). Several FP categories exist that are interesting for applications in multiplex FRET studies, but could still benefit substantially from optimizations. Therefore, I would suggest to focus on dark acceptors, OFPs, LSS-FPs

and far-red FPs in future FP optimization studies. Additionally, the algorithm might be used to capture obtained information on dimer interface interactions that influence, amongst others, stickiness into a FP-FP interlinked phenotypic score, facilitating unimolecular sensor optimizations. A recent report uses machine learning to include synergistic and antagonistic effects of residues in mutagenesis of GFP towards YFP (Saito et al., 2018). First the model was trained with one round of mutagenesis. Then the model was used, directing the second round of mutagenesis. This already yielded more successful mutagenized variants. However, this model was only focused on two characteristics, brightness and red-shift of the emission spectrum, and only four residues were altered to create the mutagenized variants (Saito et al., 2018). Ultimately it would be interesting if a model could direct a mutagenesis that would consider the effects of each residue on all FP characteristics. Perhaps the standardized phenotypic scoring for all characteristics of existing FPs could be used to train such a machine learning model.

Another approach that might facilitate further unimolecular FRET sensor optimization involves solving and studying the crystal structures of different unimolecular sensors employed with different FRET pairs in the “on” and the “off” state of the sensor. This might yield novel insights on the interactions between the sensor components and how these can be optimized by mutagenesis, circular permutation or alterations of the overall sensor design.

An alternative to gaining more knowledge on unimolecular sensors would be to develop bimolecular sensors instead. The application of novel, improved FRET pairs in the unimolecular RhoA activation biosensor, is hampered by sensor interactions that are not yet completely understood. A bimolecular RhoA-RhoGDI dissociation sensor could be constructed. This sensor would report on the dissociation of activated RhoA from RhoGDI, which occurs subsequent to RhoA activation. In this sensor, there would be a less complicated relation between characteristics of the FRET pair and the performance of the sensor. Note that the dynamic range of this bimolecular sensor can never be fully optimized due to the less restricted orientations and distance between the FRET pair in this sensor design.

Thus, when performing sensor optimization keep in mind that in general bimolecular sensors are easier to optimize, since the effects of alterations are easier to predict. Additionally, the best characteristics of FP and FRET pair, do not always yield the best performing sensor, especially in unimolecular sensors. However, maximum dynamic range often demands the application of a unimolecular sensor, though this will probably involve profuse empirical testing. Furthermore, consider that it is often easier to optimize the thoroughly studied *A. victorea* derived FPs, than the recently reported FPs derived from other species or the synthetically designed FPs. However, the recently discovered/constructed FPs might benefit most from the optimization.

At the onset of sensor optimization, it is good to know that the candidate FRET pair(s) of your choosing are efficient, with the general qualities as optimal as possible. This might involve initial FP optimization via mutagenesis. In case of bimolecular sensors there is a fair chance that the optimized general qualities of the FPs will correspond rather well with improved sensor performance. In case of unimolecular sensors, the application of optimized FPs might affect the overall sensor design, requiring additional optimization of the sensor. A high throughput screen can be performed where multiple sensor design and FP characteristics (as in multiple, efficient candidate FRET pairs) are assessed in a parallel fashion (Fritz et al., 2013). Ultimately, such a screen yields the most optimal combination of sensor design and FP characteristics for that specific sensor.

7.2 Developing novel FRET based biosensors

Even now that an enormous variety in FRET based biosensors is available, there are still processes that are important in GPCR signaling for which sensors are missing. One of these important processes was the activation of the G α 13 heterotrimeric G-protein. The Gq class and G12/13 class both activate RhoA (Aittaleb et al., 2010; Rojas et al., 2007; Siehler, 2009). Furthermore, GPCRs that activate G12/13 often activate Gq as well (Riobo and Manning, 2005; Worzfeld et al., 2008). This hampers the separate study of these signaling pathways using sensors for downstream effectors. Further elucidation of GPCR signaling, therefore, required the development of a G α 13 activation FRET sensor. To fluorescently tag the G α subunit, the FP was inserted in the G α sequence, since G α subunits require their N- and C-termini for interactions with the G $\beta\gamma$ subunit and the GPCR. The FP insertion site, used for fluorescently tagging G α q, was unsuccessful in G α 13. This made the development of the G α 13 sensor challenging, since multiple FP insertion sites had to be examined. Nevertheless, we developed and characterized a FRET-based G α 13 activation biosensor. The resulting sensor is a multimeric, bimolecular sensor, expressed from a single plasmid, in a set stoichiometry, showing a rapid and robust response when used in primary human endothelial cells (**chapter 4**). We demonstrated that the G α 13 sensor can be used to dissect heterotrimeric G-protein coupling efficiency in single living cells.

Another process important in GPCR signaling for which a robust FRET based biosensor is still missing, is the activation of the G α s heterotrimeric G-protein. Attempts to develop this sensor were discontinued after none of the six evaluated FP insertion sites yielded a fluorescently tagged G α s with robust plasma membrane localization (figure 1). The best tagged G α s variant with a FP insertion at residue 122N, showed plasma membrane localization in 47% of the analyzed cells (data not shown). Perhaps inserting the FP at sites preceding 122N in the same loop, either 121M, 120V or 119S, will yield a more consistent plasma membrane localization (123V and 124P were

unsuccessful). It is important that the research towards a robust Gas activation biosensor will be continued. A Gas biosensor is desired for multiplex experiments, measuring the activation dynamics of multiple Ga classes simultaneously, to further elucidate how GPCR signaling is regulated. Eventually, when multiplex FRET imaging is implemented, it would be an asset to have FRET based biosensors for all the 16 different Ga subunits. These biosensors could be used to study the crosstalk between all the signaling induced via the different heterotrimeric G-proteins.

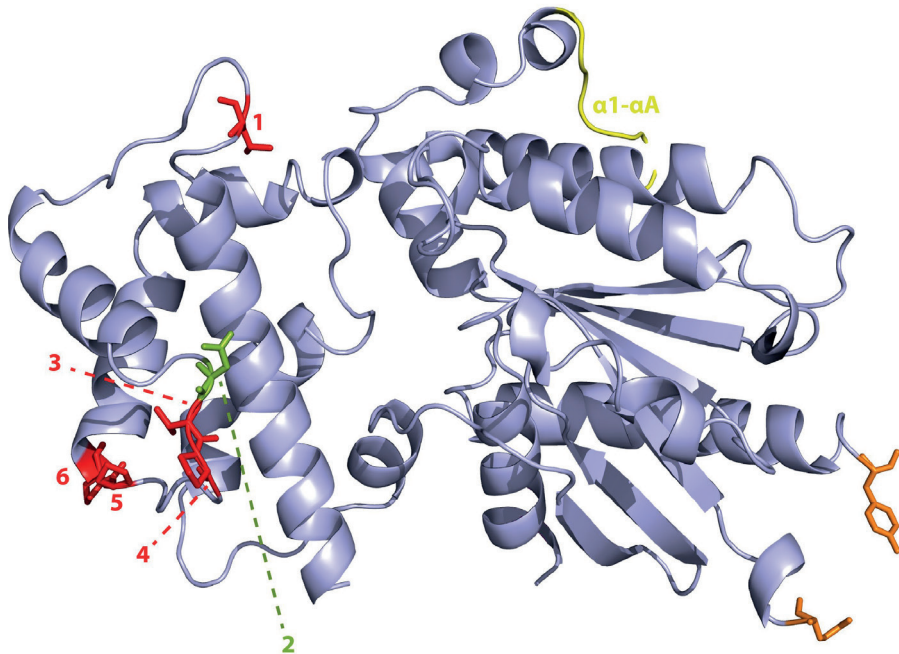


Figure 1. Insertion of a fluorescent protein at different positions in GaS.

The protein structure of bovine GaS (PDB: 1AZT). The highlighted residues indicate the amino acid preceding the inserted fluorescent protein. Unsuccessful sites for inserting mTurquoise2-Δ9 into GaS in red (1= L99, 3= V123, 4= P124, 5= P129, 6= P130) and the moderately successful site in green (2= N122). The N- and C-termini are indicated in orange. Hynes et.al. states that inserting GFP in the α1-αA loop (yellow), the site of alternative splicing in Gas, leaves its function intact. Hynes creates a CFP tagged GaS using a SGGGGS-linker on both sites of the FP insert (Hynes et al., 2004) we produced functional fluorescent fusion proteins and imaged them in HEK-293 cells. alphas-CFP, with cyan fluorescent protein (CFP. Hein et.al. uses the in Hynes et.al. reported GaS-CFP, replaces the CFP for a YFP and uses it for FRET measurements between Gas and Gy. Therefore, it might be interesting to assess this insertion site (Hein et al., 2006).

Furthermore, the previously mentioned development of a robust RhoA-RhoGDI dissociation sensor would be an asset for gaining knowledge on RhoA-RhoGDI dissociation in time and space. This sensor could be combined with the RhoA activation sensor variant developed for multiplex FRET experiments (**chapter 5**), to relate the moment and location of dissociation to the moment and location of activation of RhoA. While interesting sensors remain to be developed, the sensors that are already available are still being used to obtain new knowledge on the regulation of GPCR signaling.

7.3 Elucidating the regulation of GPCR signaling using FRET based biosensors

A substantial part of this research was devoted to the development and further optimization of FPs and FRET sensors. This was, however, all directed towards monitoring proteins and events important in GPCR signaling. FRET sensors and other molecular biology tools were applied to gain more insights in the regulation of GPCR signaling. The next paragraphs contain a brief summary of the, during this project, obtained novel insights in the regulation of GPCR signaling.

A major result is the newly developed Ga13 activation biosensor (**chapter 4**). The sensor reports inhibited G13 activation in presence of p115 RGS domain in HUVECs. This observation supports the previously reported role of p115 RGS domain as inhibitor of G13 signaling, while showing that the newly developed sensor can functionally interact with its inhibitor (Kelly et al., 2006; Martin et al., 2001; Reinhard et al., 2017). In addition, the sensor was used to evaluate which GPCRs activated the class of Ga13 heterotrimeric G-proteins. The ability to distinguish between Gaq and Ga13 induced signaling contributes novel insights on GPCR signaling. GPCRs can now be systematically assessed on G-protein coupling to Gaq, Ga13 and Gai in living cells. Moreover, the prospect of performing multiplex FRET imaging to determine balances between the early signaling events, seems very promising in terms of elucidating the pathways involved in GPCR signaling. **Chapter 5** showed preliminary multiplex FRET data, confirming that the histamine-1 receptor activates Gq but not G13 (Wettschureck and Offermanns, 2005).

Chapter 6 examines the details of the S1PR1-Gi-Cdc42 signaling axis leading to barrier protection in endothelial cells (EC). The study reveals that G $\beta\gamma$ signaling is required for Cdc42 activation and pRex1 is suggested as Cdc42 activating GEF. The direct link between pRex1 and Cdc42 should be further investigated via knockdown or knockout experiments. Furthermore, a link between pRex1 and the Rho GTPase Rac1 has been reported. Therefore, it is necessary to include Rac1 in this study and to compare Rac1- and Cdc42- specific signaling outcomes (Naikawadi et al., 2012; van Hooren et al., 2014; Welch, 2015).

The aforementioned novel insights into GPCR signaling leave several gaps in understanding the regulation of GPCR signaling. Further research in this topic is thus necessary. The research required, entails at least two sorts of microscopically acquired data: 1) data acquired using synthetic tools to manipulate or isolate certain signaling pathways, evading crosstalk between pathways. This part of the research will address the basics of GPCR signaling; 2) data acquired using multiparameter imaging, including multiplex FRET imaging, to analyze crosstalk between different signaling pathways. This part of the research will address the more physiological conditions, where signals have to be integrated to produce specific signaling outcomes. Ideally, these studies should be performed under (close to) physiological conditions, i.e. without overexpressed components of the signaling pathway.

The power of synthetic tools lies in the ability to specifically activate a single process, whereas signaling usually activates multiple events. In **chapter 6** the results were obtained using synthetic tools, including a rapamycin induced *hetero*-dimerization system, protein-based inhibitors and a Gi specific DREADD. A DREADD is a mutagenized muscarinic receptor that can activate Gi using a synthetic compound that is biologically inert (Conklin et al., 2008). Another synthetic tool that would greatly contribute in this type of research is optogenetics, providing means to spatiotemporally control GPCR signaling, using light-sensitive proteins. Optogenetics includes opto-XRs, which are modified opsins containing the intracellular loops and C-terminal tail of a specific GPCR. Opto-XRs are activated by light, enabling to spatially confine GPCR activation and to isolate the signaling induced by a specific GPCR (Spangler and Bruchas, 2017). Optogenetics also includes photoactivatable proteins, where light sensitive domains (LOV, CRY2-CIB1, phytochromes), tagged to proteins of interest, either induce dimerization or a change of conformation upon illumination. This leads to spatially confined dimerization or activation of the tagged proteins of interest (Spangler and Bruchas, 2017). Additionally, caged ligands and photoswitches exist. These are ligands, containing an attached photosensitive component that renders the ligand inactive. Spatially controlled illumination, with a certain wavelength of light, causes photolysis and activates the ligand (Spangler and Bruchas, 2017).

To elucidate the details in GPCR signaling that involve crosstalk between signaling pathways, multiplex FRET imaging could be applied. Multiplex FRET imaging enables the simultaneous monitoring of proteins of interest and/or specific signaling events. In **chapter 5** we optimized a RhoA activation biosensor for application in multiplex FRET imaging, employing the LSS-SGFP2-mScarlet-1 FRET pair. In addition, this FRET pair is used to show Gq activation in living cells. Furthermore, we showed the preliminary data of a multiplex FRET experiment, where the activation of both Gq and G13 were monitored simultaneously upon stimulation of an ectopically expressed histamine-1 receptor. Additional multiplex experiments should be performed to validate the imaging and subsequent unmixing methods, preferably using one sensor together

with one or more inert FPs, so that if FRET changes are observed for the inert FPs, this can certainly be attributed to an artifact. In the multiplex experiment we performed, a FRET response for G13 could indicate an unknown signaling pathway activated in this situation. In our attempts to implement multiplex FRET imaging and multiparameter imaging we experienced some challenges. It is important to limit the amount of imaging channels since the image acquisition time and the extent of photobleaching increase with increasing number of imaging channels. Adding a multisplit device to the detection system of the microscope enables to record four imaging channels at once. Furthermore, the quality of linear unmixing is affected by a reduction of the signal to noise ratio (SNR). The SNR declines with an increasing number of detection channels, with an increase in spectral overlap between FRET pairs and with lower FP brightness (Niino et al., 2009; Woehler, 2013; Zimmermann, 2005; Zimmermann et al., 2003). Another challenge comprises the balanced co-transfection and subsequent co-expression of multiple sensor constructs. For every new combination of constructs the expression levels should be assessed and the amount of DNA required of each construct should be adjusted. Additionally, the construction of one plasmid encoding multiple biosensors in a set stoichiometry could be considered. Furthermore, bystander FRET can occur if multiple FRET pairs are targeted to the same subcellular localization (Clayton and Chattopadhyay, 2014; King et al., 2014). The occurrence of bystander FRET should be excluded by performing appropriate control experiments. Then, after tackling above mentioned challenges that interfere with reliable multiplex FRET imaging, it would be very valuable to use this technique to study endothelial barrier function in ECs. In endothelial barrier regulation one agonist, S1P, can lead to the activation of different G α classes, Gi or G13 (Reinhard et al., 2017). The final signaling outcome, either cell spreading or cell contraction, might be the result of balances between the activation of both G-proteins. It would be very interesting to monitor Gi and G13 activation simultaneously upon stimulating endogenous receptors with S1P. Furthermore, it would be of interest to monitor the activation of G-proteins and /or arrestins simultaneous with proteins involved in vesicular transport, such as Rab GTPases and EB3 (Miaczynska et al., 2004; Seachrist and Ferguson, 2003). This because the transport of GPCRs through distinct intracellular membrane compartments influences GPCR signaling. Thus, in order to fully elucidate the regulation of GPCR signaling, more knowledge on the roles of vesicular transport in GPCR signaling should be obtained. Another idea for multiplex FRET imaging or multiparameter imaging is to use FLIM-FRET instead of ratiometric FRET imaging. The recently reported novel technique, siFLIM, enables reliable recording of the fluorescence lifetime with only one image (Raspe et al., 2016). Advantages of using FLIM-FRET is that dark acceptors can be applied and that fluorescence signals can be separated based on fluorescence lifetime instead of spectral properties.

In general, the research described in this thesis often turned to ectopic expression of fluorescently tagged proteins of interest. CRISPR/Cas facilitates the tagging of endogenous proteins, thus enabling to monitor proteins of interest in a more

physiologically relevant cellular environment (Jinek et al., 2012; Jinek et al., 2013). Furthermore, we often used immortal cell lines while using primary cells, organoids or whole organisms would be of higher physiological relevance. Signaling results obtained using immortal cell lines might not translate directly to the physiology of intact organisms. It is possible that the signaling outcome is different for different cell types, thus using cell lines of different origins might yield opposite results. For basic studies investigating, for example, which interactions can occur, looking into immortal cell lines will be an acceptable strategy. When the question, however, becomes which interactions do occur, more physiologically relevant cell systems should be considered.

Altogether, advances in techniques involving molecular biology, biochemistry, microscopy and image analysis facilitate the ongoing buildup of knowledge on how GPCR signaling is regulated. The work described in this thesis contributes to the ongoing buildup of knowledge. Moreover, the developed and optimized FPs, FRET based biosensors and other synthetic tools for unraveling signaling interactions could be applied in various future studies in GPCR signaling or related research fields.



References

A

- Adjobo-Hermans, M. J. W., Goedhart, J., van Weeren, L., Nijmeijer, S., Manders, E. M. M., Offermanns, S. and Gadella Jr, T. W. J.** (2011). Real-time visualization of heterotrimeric G protein Gq activation in living cells. *BMC Biol.* **9**, 32.
- Ai, H., Shaner, N. C., Cheng, Z., Tsien, R. Y. and Campbell, R. E.** (2007). Exploration of New Chromophore Structures Leads to the Identification of Improved Blue Fluorescent Proteins †. *Biochemistry* **46**, 5904–5910.
- Ai, H., Hazelwood, K. L., Davidson, M. W. and Campbell, R. E.** (2008). Fluorescent protein FRET pairs for ratiometric imaging of dual biosensors. *Nat. Methods* **5**, 401–3.
- Aird, W. C.** (2007a). Phenotypic heterogeneity of the endothelium: I. Structure, function, and mechanisms. *Circ. Res.* **100**, 158–73.
- Aird, W. C.** (2007b). Phenotypic heterogeneity of the endothelium: II. Representative vascular beds. *Circ. Res.* **100**, 174–190.
- Aittaleb, M., Boguth, C. A. and Tesmer, J. J. G.** (2010). Structure and function of heterotrimeric G protein-regulated Rho guanine nucleotide exchange factors. *Mol. Pharmacol.* **77**, 111–25.
- Allen, W., Zicha, D., Ridley, A. and Jones, G.** (1998). A role for Cdc42 in macrophage chemotaxis. *J. Cell Biol.* **141**, 1147–57.
- Ando, K., Fukuhara, S., Moriya, T., Obara, Y., Nakahata, N. and Mochizuki, N.** (2013). Rap1 potentiates endothelial cell junctions by spatially controlling myosin II activity and actin organization. *J. Cell Biol.* **202**, 901–16.
- Armbruster, B. N., Li, X., Pausch, M. H., Herlitze, S. and Roth, B. L.** (2007). Evolving the lock to fit the key to create a family of G protein-coupled receptors potently activated by an inert ligand. *Proc. Natl. Acad. Sci.* **104**, 5163–5168.
- Ayoub, M. A., Trinquet, E., Pflieger, K. D. G. and Pin, J.-P.** (2010). Differential association modes of the thrombin receptor PAR 1 with Gai1, Ga12, and β -arrestin 1. *FASEB J.* **24**, 3522–3535.

B

- Baird, G. S., Zacharias, D. A. and Tsien, R. Y.** (1999). Circular permutation and receptor insertion within green fluorescent proteins. *Proc. Natl. Acad. Sci. U. S. A.* **96**, 11241–6.
- Baird, G. S., Zacharias, D. A. and Tsien, R. Y.** (2000). Biochemistry, mutagenesis, and oligomerization of DsRed, a red fluorescent protein from coral. *Proc. Natl. Acad. Sci. U. S. A.* **97**, 11984–9.
- Bajar, B. T., Wang, E. S., Lam, A. J., Kim, B. B., Jacobs, C. L., Howe, E. S., Davidson, M. W., Lin, M. Z. and Chu, J.** (2016). Improving brightness and photostability of green and red fluorescent proteins for live cell imaging and FRET reporting. *Sci. Rep.* **6**, 20889.
- Baltoumas, F. A., Theodoropoulou, M. C. and Hamodrakas, S. J.** (2013). Interactions of the α -subunits of heterotrimeric G-proteins with GPCRs, effectors and RGS proteins: a critical review and analysis of interacting surfaces, conformational shifts, structural diversity and electrostatic potentials. *J. Struct. Biol.* **182**, 209–18.

- Bauer, M., Macdonald, J., Henri, J., Duan, W. and Shigdar, S.** (2016). The Application of Aptamers for Immunohistochemistry. *Nucleic Acid Ther.* **26**, 120–6.
- Becker, W.** (2012). Fluorescence lifetime imaging—techniques and applications. *J. Microsc.* **247**, 119–36.
- Becker, W., Bergmann, A., Hink, M. A., König, K., Benndorf, K. and Biskup, C.** (2004). Fluorescence lifetime imaging by time-correlated single-photon counting. *Microsc. Res. Tech.* **63**, 58–66.
- Belcher, S. M., Le, H. H., Spurling, L. and Wong, J. K.** (2005). Rapid estrogenic regulation of extracellular signal-regulated kinase 1/2 signaling in cerebellar granule cells involves a G protein- and protein kinase A-dependent mechanism and intracellular activation of protein phosphatase 2A. *Endocrinology* **146**, 5397–406.
- Berdyshev, E. V, Gorshkova, I. A., N. Garcia, J. G., Natarajan, V. and Hubbard, W. C.** (2005). Quantitative analysis of sphingoid base-1-phosphates as bisacetylated derivatives by liquid chromatography–tandem mass spectrometry. *Anal. Biochem.* **339**, 129–136.
- Berman, H. M., Westbrook, J., Feng, Z., Gilliland, G., Bhat, T. N., Weissig, H., Shindyalov, I. N. and Bourne, P. E.** (2000). The Protein Data Bank. *Nucleic Acids Res.* **28**, 235–242.
- Bindels, D. S., Goedhart, J., Hink, M. A., van Weeren, L., Joosen, L. and Gadella, T. W. J.** (2014). Optimization of Fluorescent Proteins. pp. 371–417.
- Bindels, D. S., Haarbosch, L., van Weeren, L., Postma, M., Wiese, K. E., Mastop, M., Aumonier, S., Gotthard, G., Royant, A., Hink, M. A., et al.** (2017). mScarlet: a bright monomeric red fluorescent protein for cellular imaging. *Nat. Methods* **14**, 53–56.
- Bodmann, E.-L., Krett, A.-L. and Bünemann, M.** (2017). Potentiation of receptor responses induced by prolonged binding of Ga 13 and leukemia-associated RhoGEF. *FASEB J.* **31**, 3663–3676.
- Bogdanov, A. M., Acharya, A., Titelmayer, A. V, Mamontova, A. V, Bravaya, K. B., Kolomeisky, A. B., Lukyanov, K. A. and Krylov, A. I.** (2016). Turning On and Off Photoinduced Electron Transfer in Fluorescent Proteins by π -Stacking, Halide Binding, and Tyr145 Mutations. *J. Am. Chem. Soc.* **138**, 4807–17.
- Boureux, A., Vignal, E., Faure, S. and Fort, P.** (2007). Evolution of the Rho family of ras-like GTPases in eukaryotes. *Mol. Biol. Evol.* **24**, 203–16.
- Broussard, J. A., Rappaz, B., Webb, D. J. and Brown, C. M.** (2013). Fluorescence resonance energy transfer microscopy as demonstrated by measuring the activation of the serine/threonine kinase Akt. *Nat. Protoc.* **8**, 265–81.
- Burns, D. L.** (1988). Subunit structure and enzymic activity of pertussis toxin. *Microbiol. Sci.* **5**, 285–7.

C

- Caligan, T. B., Peters, K., Ou, J., Wang, E., Saba, J. and Merrill, A. H.** (2000). A High-Performance Liquid Chromatographic Method to Measure Sphingosine 1-Phosphate and Related Compounds from Sphingosine Kinase Assays and Other Biological Samples. *Anal. Biochem.* **281**, 36–44.
- Campbell, R. E., Tour, O., Palmer, A. E., Steinbach, P. A., Baird, G. S., Zacharias, D. A. and Tsien, R. Y.** (2002). A monomeric red fluorescent protein. *Proc. Natl. Acad. Sci. U. S. A.* **99**, 7877–82.
- Carlson, H. J. and Campbell, R. E.** (2009). Genetically encoded FRET-based biosensors for multiparameter fluorescence imaging. *Curr. Opin. Biotechnol.* **20**, 19–27.

- Carlson, H. J., Cotton, D. W. and Campbell, R. E.** (2010). Circularly permuted monomeric red fluorescent proteins with new termini in the β -sheet. *Protein Sci.* **19**, 1490–1499.
- Chalfie, M., Tu, Y., Euskirchen, G., Ward, W. W. and Prasher, D. C.** (1994). Green fluorescent protein as a marker for gene expression. *Science* **263**, 802–5.
- Chandrasekera, P. C., Wan, T. C., Gizewski, E. T., Auchampach, J. A. and Lasley, R. D.** (2013). Adenosine A1 receptors heterodimerize with β 1- and β 2-adrenergic receptors creating novel receptor complexes with altered G protein coupling and signaling. *Cell. Signal.* **25**, 736–42.
- Chang, Y.-C., Yang, C.-Y., Sun, R.-L., Cheng, Y.-F., Kao, W.-C. and Yang, P.-C.** (2013). Rapid single cell detection of *Staphylococcus aureus* by aptamer-conjugated gold nanoparticles. *Sci. Rep.* **3**, 1863.
- Chen, Y., Müller, J. D., So, P. T. C. and Gratton, E.** (1999). The Photon Counting Histogram in Fluorescence Fluctuation Spectroscopy. *Biophys. J.* **77**, 553–567.
- Chen, S., Spiegelberg, B. D., Lin, F., Dell, E. J. and Hamm, H. E.** (2004). Interaction of Gbetagamma with RACK1 and other WD40 repeat proteins. *J. Mol. Cell. Cardiol.* **37**, 399–406.
- Chikumi, H., Vázquez-Prado, J., Servitja, J.-M., Miyazaki, H. and Gutkind, J. S.** (2002). Potent Activation of RhoA by Ga q and G q -coupled Receptors. *J. Biol. Chem.* **277**, 27130–27134.
- Chudakov, D. M., Lukyanov, S. and Lukyanov, K. A.** (2005). Fluorescent proteins as a toolkit for in vivo imaging. *Trends Biotechnol.* **23**, 605–13.
- Chudakov, D. M., Matz, M. V, Lukyanov, S. and Lukyanov, K. A.** (2010). Fluorescent proteins and their applications in imaging living cells and tissues. *Physiol. Rev.* **90**, 1103–63.
- Clavel, D., Gotthard, G., von Stetten, D., De Sanctis, D., Pasquier, H., Lambert, G. G., Shaner, N. C. and Royant, A.** (2016). Structural analysis of the bright monomeric yellow-green fluorescent protein mNeonGreen obtained by directed evolution. *Acta Crystallogr. Sect. D Struct. Biol.* **72**, 1298–1307.
- Clayton, A. H. A. and Chattopadhyay, A.** (2014). Taking care of bystander FRET in a crowded cell membrane environment. *Biophys. J.* **106**, 1227–8.
- Clistner, T., Mehta, S. and Zhang, J.** (2015). Single-cell Analysis of G-protein Signal Transduction. *J. Biol. Chem.* **290**, 6681–6688.
- Cody, C. W., Prasher, D. C., Westler, W. M., Prendergast, F. G. and Ward, W. W.** (1993). Chemical structure of the hexapeptide chromophore of the *Aequorea* green-fluorescent protein. *Biochemistry* **32**, 1212–8.
- Conklin, B. R., Hsiao, E. C., Claeyson, S., Dumuis, A., Srinivasan, S., Forsayeth, J. R., Guettier, J.-M., Chang, W. C., Pei, Y., McCarthy, K. D., et al.** (2008). Engineering GPCR signaling pathways with RASSLs. *Nat. Methods* **5**, 673–8.
- Cormack, B. P., Valdivia, R. H. and Falkow, S.** (1996). FACS-optimized mutants of the green fluorescent protein (GFP). *Gene* **173**, 33–8.
- Costantini, L. M., Fossati, M., Francolini, M. and Snapp, E. L.** (2012). Assessing the tendency of fluorescent proteins to oligomerize under physiologic conditions. *Traffic* **13**, 643–9.
- Costantini, L. M., Baloban, M., Markwardt, M. L., Rizzo, M., Guo, F., Verkhusha, V. V and Snapp, E. L.** (2015). A palette of fluorescent proteins optimized for diverse cellular environments. *Nat. Commun.* **6**, 7670.

- Cranfill, P. J., Sell, B. R., Baird, M. A., Allen, J. R., Lavagnino, Z., de Gruiter, H. M., Kremers, G.-J., Davidson, M. W., Ustione, A. and Piston, D. W.** (2016). Quantitative assessment of fluorescent proteins. *Nat. Methods* **13**, 557–62.
- Crosby, K. C., Postma, M., Hink, M. A., Zeelenberg, C. H. C., Adjobo-Hermans, M. J. W. and Gadella Jr, T. W. J.** (2013). Quantitative analysis of self-association and mobility of annexin A4 at the plasma membrane. *Biophys. J.* **104**, 1875–85.
- Cubitt, A. B., Heim, R., Adams, S. R., Boyd, A. E., Gross, L. A. and Tsien, R. Y.** (1995). Understanding, improving and using green fluorescent proteins. *Trends Biochem. Sci.* **20**, 448–55.
- Cubitt, A. B., Woollenweber, L. A. and Heim, R.** (1999). Understanding structure-function relationships in the *Aequorea victoria* green fluorescent protein. *Methods Cell Biol.* **58**, 19–30.

D

- De Keersmaecker, H., Fron, E., Rocha, S., Kogure, T., Miyawaki, A., Hofkens, J. and Mizuno, H.** (2016). Photoconvertible Behavior of LSSmOrange Applicable for Single Emission Band Optical Highlighting. *Biophys. J.* **111**, 1014–25.
- De Meyer, T., Muyldermans, S. and Depicker, A.** (2014). Nanobody-based products as research and diagnostic tools. *Trends Biotechnol.* **32**, 263–70.
- Del Vecchio, P. J., Siflinger-Birnboim, A., Shepard, J. M., Bizios, R., Cooper, J. A. and Malik, A. B.** (1987). Endothelial monolayer permeability to macromolecules. *Fed. Proc.* **46**, 2511–5.
- Dickson, R. M., Cubitt, A. B., Tsien, R. Y. and Moerner, W. E.** (1997). On/off blinking and switching behaviour of single molecules of green fluorescent protein. *Nature* **388**, 355–8.
- Ding, Y., Ai, H., Hoi, H. and Campbell, R. E.** (2011). Förster resonance energy transfer-based biosensors for multiparameter ratiometric imaging of Ca²⁺ dynamics and caspase-3 activity in single cells. *Anal. Chem.* **83**, 9687–93.
- DiPilato, L. M., Cheng, X. and Zhang, J.** (2004). Fluorescent indicators of cAMP and Epac activation reveal differential dynamics of cAMP signaling within discrete subcellular compartments. *Proc. Natl. Acad. Sci. U. S. A.* **101**, 16513–8.
- Dorsam, R. T. and Gutkind, J. S.** (2007). G-protein-coupled receptors and cancer. *Nat. Rev. Cancer* **7**, 79–94.
- Dror, R. O., Mildorf, T. J., Hilger, D., Manglik, A., Borhani, D. W., Arlow, D. H., Philippsen, A., Villanueva, N., Yang, Z., Lerch, M. T., et al.** (2015). SIGNAL TRANSDUCTION. Structural basis for nucleotide exchange in heterotrimeric G proteins. *Science* **348**, 1361–5.

E

- Elliott, A. D., Gao, L., Ustione, A., Bedard, N., Kester, R., Piston, D. W. and Tkaczyk, T. S.** (2012). Real-time hyperspectral fluorescence imaging of pancreatic -cell dynamics with the image mapping spectrometer. *J. Cell Sci.* **125**, 4833–4840.
- Elliott, A. D., Bedard, N., Ustione, A., Baird, M. A., Davidson, M. W., Tkaczyk, T. and Piston, D. W.** (2017). Hyperspectral imaging for simultaneous measurements of two FRET biosensors in pancreatic β -cells. *PLoS One* **12**, e0188789.
- Etienne-Manneville, S. and Hall, A.** (2002). Rho GTPases in cell biology. *Nature* **420**, 629–35.

F

- Festy, F., Ameer-Beg, S. M., Ng, T. and Suhling, K.** (2007). Imaging proteins in vivo using fluorescence lifetime microscopy. *Mol. Biosyst.* **3**, 381.
- Fitzsimons, C. P., Monczor, F., Fernández, N., Shayo, C. and Davio, C.** (2004). Mepyramine, a Histamine H 1 Receptor Inverse Agonist, Binds Preferentially to a G Protein-coupled Form of the Receptor and Sequesters G Protein. *J. Biol. Chem.* **279**, 34431–34439.
- Fölling, J., Bossi, M., Bock, H., Medda, R., Wurm, C. A., Hein, B., Jakobs, S., Eggeling, C. and Hell, S. W.** (2008). Fluorescence nanoscopy by ground-state depletion and single-molecule return. *Nat. Methods* **5**, 943–5.
- Frank, M., Thümer, L., Lohse, M. J. and Bünemann, M.** (2005). G Protein Activation without Subunit Dissociation Depends on a $G\alpha_i$ -specific Region. *J. Biol. Chem.* **280**, 24584–24590.
- Fredriksson, R., Lagerström, M. C., Lundin, L.-G. and Schiöth, H. B.** (2003). The G-protein-coupled receptors in the human genome form five main families. Phylogenetic analysis, paralogon groups, and fingerprints. *Mol. Pharmacol.* **63**, 1256–72.
- Fritz, R. D., Letzelter, M., Reimann, A., Martin, K., Fusco, L., Ritsma, L., Ponsoien, B., Fluri, E., Schulte-Merker, S., van Rheenen, J., et al.** (2013). A versatile toolkit to produce sensitive FRET biosensors to visualize signaling in time and space. *Sci. Signal.* **6**, rs12.
- Fukuda, H., Arai, M. and Kuwajima, K.** (2000). Folding of green fluorescent protein and the cycle3 mutant. *Biochemistry* **39**, 12025–32.

G

- Gadella Jr, T. W. J., Van der Krogt, G. N. and Bisseling, T.** (1999). GFP-based FRET microscopy in living plant cells. *Trends Plant Sci.* **4**, 287–291.
- Galperin, E., Verkhusha, V. V and Sorkin, A.** (2004). Three-chromophore FRET microscopy to analyze multiprotein interactions in living cells. *Nat. Methods* **1**, 209–17.
- Ganesan, S., Ameer-Beg, S. M., Ng, T. T. C., Vojnovic, B. and Wouters, F. S.** (2006). A dark yellow fluorescent protein (YFP)-based Resonance Energy-Accepting Chromoprotein (REACH) for Förster resonance energy transfer with GFP. *Proc. Natl. Acad. Sci. U. S. A.* **103**, 4089–94.
- Gao, L., Kester, R. T., Hagen, N. and Tkaczyk, T. S.** (2010). Snapshot Image Mapping Spectrometer (IMS) with high sampling density for hyperspectral microscopy. *Opt. Express* **18**, 14330.
- Gardiner, E. M., Pestonjamas, K. N., Bohl, B. P., Chamberlain, C., Hahn, K. M. and Bokoch, G. M.** (2002). Spatial and temporal analysis of Rac activation during live neutrophil chemotaxis. *Curr. Biol.* **12**, 2029–34.
- Gautier, A., Juillerat, A., Heinis, C., Corrêa, I. R., Kindermann, M., Beauflis, F. and Johnsson, K.** (2008). An engineered protein tag for multiprotein labeling in living cells. *Chem. Biol.* **15**, 128–36.
- Gibson, S. K. and Gilman, A. G.** (2006). G_i and G_o subunits both define selectivity of G protein activation by 2-adrenergic receptors. *Proc. Natl. Acad. Sci.* **103**, 212–217.
- Goedhart, J. and Gadella Jr, T. W. J.** (2005). Analysis of oligonucleotide annealing by electrophoresis in agarose gels using sodium borate conductive medium. *Anal. Biochem.* **343**, 186–187.

- Goedhart, J. and van Unen, J.** (2017). Molecular perturbation strategies to examine spatiotemporal features of Rho GEF and Rho GTPase activity in living cells. *Small GTPases* 1–9.
- Goedhart, J., Vermeer, J. E. M., Adjobo-Hermans, M. J. W., van Weeren, L. and Gadella Jr, T. W. J.** (2007). Sensitive detection of p65 homodimers using red-shifted and fluorescent protein-based FRET couples. *PLoS One* 2, e1011.
- Goedhart, J., van Weeren, L., Hink, M. A., Vischer, N. O. E., Jalink, K. and Gadella Jr, T. W. J.** (2010). Bright cyan fluorescent protein variants identified by fluorescence lifetime screening. *Nat. Methods* 7, 137–9.
- Goedhart, J., van Weeren, L., Adjobo-Hermans, M. J. W., Elzenaar, I., Hink, M. A. and Gadella Jr, T. W. J.** (2011). Quantitative co-expression of proteins at the single cell level--application to a multimeric FRET sensor. *PLoS One* 6, e27321.
- Goedhart, J., von Stetten, D., Noirclerc-Savoye, M., Lelimosin, M., Joosen, L., Hink, M. A., van Weeren, L., Gadella Jr, T. W. J. and Royant, A.** (2012). Structure-guided evolution of cyan fluorescent proteins towards a quantum yield of 93%. *Nat. Commun.* 3, 751.
- Goedhart, J., Hink, M. A. and Jalink, K.** (2014). An introduction to fluorescence imaging techniques geared towards biosensor applications. *Methods Mol. Biol.* 1071, 17–28.
- Goyet, E., Bouquier, N., Ollendorff, V. and Perroy, J.** (2016). Fast and high resolution single-cell BRET imaging. *Sci. Rep.* 6, 28231.
- Grant, D. M., Zhang, W., McGhee, E. J., Bunney, T. D., Talbot, C. B., Kumar, S., Munro, I., Dunsby, C., Neil, M. A. A., Katan, M., et al.** (2008). Multiplexed FRET to image multiple signaling events in live cells. *Biophys. J.* 95, L69-71.
- Grashoff, C., Hoffman, B. D., Brenner, M. D., Zhou, R., Parsons, M., Yang, M. T., McLean, M. A., Sligar, S. G., Chen, C. S., Ha, T., et al.** (2010). Measuring mechanical tension across vinculin reveals regulation of focal adhesion dynamics. *Nature* 466, 263–6.
- Greenbaum, L., Rothmann, C., Lavie, R. and Malik, Z.** (2000). Green fluorescent protein photobleaching: a model for protein damage by endogenous and exogenous singlet oxygen. *Biol. Chem.* 381, 1251–8.
- Griesbeck, O., Baird, G. S., Campbell, R. E., Zacharias, D. A. and Tsien, R. Y.** (2001). Reducing the environmental sensitivity of yellow fluorescent protein. Mechanism and applications. *J. Biol. Chem.* 276, 29188–94.
- Griffin, B. A., Adams, S. R. and Tsien, R. Y.** (1998). Specific covalent labeling of recombinant protein molecules inside live cells. *Science* 281, 269–72.
- Gurevich, V. V and Gurevich, E. V** (2017). Molecular Mechanisms of GPCR Signaling: A Structural Perspective. *Int. J. Mol. Sci.* 18,.

H

- Hall, A.** (1998). Rho GTPases and the actin cytoskeleton. *Science* 279, 509–14.
- Hamers, D., van Voorst Vader, L., Borst, J. W. and Goedhart, J.** (2014). Development of FRET biosensors for mammalian and plant systems. *Protoplasma* 251, 333–47.
- Hébert, T. E., Galés, C. and Rebois, R. V.** (2006). Detecting and Imaging Protein-Protein Interactions During G Protein-Mediated Signal Transduction In Vivo and In Situ by Using Fluorescence-Based Techniques. *Cell Biochem. Biophys.* 45, 85–110.

- Heckman, K. L. and Pease, L. R.** (2007). Gene splicing and mutagenesis by PCR-driven overlap extension. *Nat. Protoc.* **2**, 924–32.
- Hein, P., Rochais, F., Hoffmann, C., Dorsch, S., Nikolaev, V. O., Engelhardt, S., Berlot, C. H., Lohse, M. J. and Bünemann, M.** (2006). Gs activation is time-limiting in initiating receptor-mediated signaling. *J. Biol. Chem.* **281**, 33345–51.
- Heppler, J. R. and Gilman, A. G.** (1992). G proteins. *Trends Biochem. Sci.* **17**, 383–7.
- Herce, H. D., Schumacher, D., Schneider, A. F. L., Ludwig, A. K., Mann, F. A., Fillies, M., Kasper, M.-A., Reinke, S., Krause, E., Leonhardt, H., et al.** (2017). Cell-permeable nanobodies for targeted immunolabelling and antigen manipulation in living cells. *Nat. Chem.* **9**, 762–771.
- Hernández-Vásquez, M. N., Adame-García, S. R., Hamoud, N., Chidiac, R., Reyes-Cruz, G., Gratton, J. P., Côté, J.-F. and Vázquez-Prado, J.** (2017). Cell adhesion controlled by adhesion G protein-coupled receptor GPR124/ADGRA2 is mediated by a protein complex comprising intersectins and Elmo–Dock. *J. Biol. Chem.* **292**, 12178–12191.
- Hiller, C., Kühhorn, J. and Gmeiner, P.** (2013). Class A G-protein-coupled receptor (GPCR) dimers and bivalent ligands. *J. Med. Chem.* **56**, 6542–59.
- Hochreiter, B., Garcia, A. P. and Schmid, J. A.** (2015). Fluorescent proteins as genetically encoded FRET biosensors in life sciences. *Sensors (Basel)*. **15**, 26281–314.
- Hordijk, P. L.** (2006). Regulation of NADPH Oxidases. *Circ. Res.* **98**, 453–462.
- Horton, R. M., Hunt, H. D., Ho, S. N., Pullen, J. K. and Pease, L. R.** (1989). Engineering hybrid genes without the use of restriction enzymes: gene splicing by overlap extension. *Gene* **77**, 61–68.
- Huang, C., Rajfur, Z., Borchers, C., Schaller, M. D. and Jacobson, K.** (2003). JNK phosphorylates paxillin and regulates cell migration. *Nature* **424**, 219–23.
- Hynes, T. R., Mervine, S. M., Yost, E. A., Sabo, J. L. and Berlot, C. H.** (2004). Live cell imaging of Gs and the beta2-adrenergic receptor demonstrates that both alphas and beta1gamma7 internalize upon stimulation and exhibit similar trafficking patterns that differ from that of the beta2-adrenergic receptor. *J. Biol. Chem.* **279**, 44101–12.

I

- Inoue, A., Ishiguro, J., Kitamura, H., Arima, N., Okutani, M., Shuto, A., Higashiyama, S., Ohwada, T., Arai, H., Makide, K., et al.** (2012). TGF α shedding assay: an accurate and versatile method for detecting GPCR activation. *Nat. Methods* **9**, 1021–1029.
- Isberg, V., de Graaf, C., Bortolato, A., Cherezov, V., Katritch, V., Marshall, F. H., Mordalski, S., Pin, J.-P., Stevens, R. C., Vriend, G., et al.** (2015). Generic GPCR residue numbers - aligning topology maps while minding the gaps. *Trends Pharmacol. Sci.* **36**, 22–31.
- Itoh, R. E., Kurokawa, K., Ohba, Y., Yoshizaki, H., Mochizuki, N. and Matsuda, M.** (2002). Activation of rac and cdc42 video imaged by fluorescent resonance energy transfer-based single-molecule probes in the membrane of living cells. *Mol. Cell. Biol.* **22**, 6582–91.

J

- Jaffe, A. B. and Hall, A.** (2005). Rho GTPases: biochemistry and biology. *Annu. Rev. Cell Dev. Biol.* **21**, 247–69.

- Jaiswal, M., Dvorsky, R. and Ahmadian, M. R.** (2013). Deciphering the Molecular and Functional Basis of Dbl Family Proteins. *J. Biol. Chem.* **288**, 4486–4500.
- Janetopoulos, C. and Devreotes, P.** (2002). Monitoring receptor-mediated activation of heterotrimeric G-proteins by fluorescence resonance energy transfer. *Methods* **27**, 366–73.
- Jares-Erijman, E. A. and Jovin, T. M.** (2003). FRET imaging. *Nat. Biotechnol.* **21**, 1387–95.
- Jastrzebska, B.** (2013). GPCR: G protein complexes—the fundamental signaling assembly. *Amino Acids* **45**, 1303–14.
- Jinek, M., Chylinski, K., Fonfara, I., Hauer, M., Doudna, J. A. and Charpentier, E.** (2012). A programmable dual-RNA-guided DNA endonuclease in adaptive bacterial immunity. *Science* **337**, 816–21.
- Jinek, M., East, A., Cheng, A., Lin, S., Ma, E. and Doudna, J.** (2013). RNA-programmed genome editing in human cells. *Elife* **2**, e00471.
- Jost, C. A., Reither, G., Hoffmann, C. and Schultz, C.** (2008). Contribution of Fluorophores to Protein Kinase C FRET Probe Performance. *ChemBioChem* **9**, 1379–1384.
- Jung, G., Wiehler, J. and Zumbusch, A.** (2005). The photophysics of green fluorescent protein: influence of the key amino acids at positions 65, 203, and 222. *Biophys. J.* **88**, 1932–47.

K

- Kamato, D., Thach, L., Bernard, R., Chan, V., Zheng, W., Kaur, H., Brimble, M., Osman, N. and Little, P. J.** (2015). Structure, Function, Pharmacology, and Therapeutic Potential of the G Protein, Ga_q/11. *Front. Cardiovasc. Med.* **2**, 14.
- Kapp, G. T., Liu, S., Stein, A., Wong, D. T., Remenyi, A., Yeh, B. J., Fraser, J. S., Taunton, J., Lim, W. A. and Kortemme, T.** (2012). Control of protein signaling using a computationally designed GTPase/GEF orthogonal pair. *Proc. Natl. Acad. Sci.* **109**, 5277–5282.
- Kasai, R. S. and Kusumi, A.** (2014). Single-molecule imaging revealed dynamic GPCR dimerization. *Curr. Opin. Cell Biol.* **27**, 78–86.
- Kedziora, K. M., Leyton-Puig, D., Argenzio, E., Boumeester, A. J., van Butselar, B., Yin, T., Wu, Y. I., van Leeuwen, F. N., Innocenti, M., Jalink, K., et al.** (2016). Rapid Remodeling of Invadosomes by G_i-coupled Receptors. *J. Biol. Chem.* **291**, 4323–4333.
- Kelly, P., Stemmler, L. N., Madden, J. F., Fields, T. A., Daaka, Y. and Casey, P. J.** (2006). A Role for the G₁₂ Family of Heterotrimeric G Proteins in Prostate Cancer Invasion. *J. Biol. Chem.* **281**, 26483–26490.
- Kim, J. H., Lee, S.-R., Li, L.-H., Park, H.-J., Park, J.-H., Lee, K. Y., Kim, M.-K., Shin, B. A. and Choi, S.-Y.** (2011). High cleavage efficiency of a 2A peptide derived from porcine teschovirus-1 in human cell lines, zebrafish and mice. *PLoS One* **6**, e18556.
- King, C., Sarabipour, S., Byrne, P., Leahy, D. J. and Hristova, K.** (2014). The FRET signatures of noninteracting proteins in membranes: simulations and experiments. *Biophys. J.* **106**, 1309–17.
- Klarenbeek, J., Goedhart, J., van Batenburg, A., Groenewald, D. and Jalink, K.** (2015). Fourth-generation epac-based FRET sensors for cAMP feature exceptional brightness, photostability and dynamic range: characterization of dedicated sensors for FLIM, for ratiometry and with high affinity. *PLoS One* **10**, e0122513.

- Koch, W. J., Hawes, B. E., Inglese, J., Luttrell, L. M. and Lefkowitz, R. J.** (1994). Cellular expression of the carboxyl terminus of a G protein-coupled receptor kinase attenuates G beta gamma-mediated signaling. *J. Biol. Chem.* **269**, 6193–7.
- Komatsu, N., Aoki, K., Yamada, M., Yukinaga, H., Fujita, Y., Kamioka, Y. and Matsuda, M.** (2011). Development of an optimized backbone of FRET biosensors for kinases and GTPases. *Mol. Biol. Cell* **22**, 4647–56.
- Korn, C. and Augustin, H. G.** (2015). Mechanisms of Vessel Pruning and Regression. *Dev. Cell* **34**, 5–17.
- Kotera, I., Iwasaki, T., Imamura, H., Noji, H. and Nagai, T.** (2010). Reversible Dimerization of *Aequorea victoria* Fluorescent Proteins Increases the Dynamic Range of FRET-Based Indicators. *ACS Chem. Biol.* **5**, 215–222.
- Koushik, S. V., Chen, H., Thaler, C., Puhl, H. L. and Vogel, S. S.** (2006). Cerulean, Venus, and VenusY67C FRET Reference Standards. *Biophys. J.* **91**, L99–L101.
- Kozasa, T., Jiang, X., Hart, M. J., Sternweis, P. M., Singer, W. D., Gilman, A. G., Bollag, G. and Sternweis, P. C.** (1998). p115 RhoGEF, a GTPase activating protein for Galpha12 and Galpha13. *Science* **280**, 2109–11.
- Kraynov, V. S., Chamberlain, C., Bokoch, G. M., Schwartz, M. A., Slabaugh, S. and Hahn, K. M.** (2000). Localized Rac activation dynamics visualized in living cells. *Science* **290**, 333–7.
- Kremers, G.-J., Goedhart, J., van Munster, E. B. and Gadella Jr, T. W. J.** (2006). Cyan and yellow super fluorescent proteins with improved brightness, protein folding, and FRET Förster radius. *Biochemistry* **45**, 6570–80.
- Kremers, G.-J., Goedhart, J., van den Heuvel, D. J., Gerritsen, H. C. and Gadella, T. W. J.** (2007). Improved Green and Blue Fluorescent Proteins for Expression in Bacteria and Mammalian Cells †, ‡. *Biochemistry* **46**, 3775–3783.
- Kremers, G.-J., van Munster, E. B., Goedhart, J. and Gadella Jr, T. W. J.** (2008). Quantitative lifetime unmixing of multiexponentially decaying fluorophores using single-frequency fluorescence lifetime imaging microscopy. *Biophys. J.* **95**, 378–89.
- Kremers, G.-J., Hazelwood, K. L., Murphy, C. S., Davidson, M. W. and Piston, D. W.** (2009). Photoconversion in orange and red fluorescent proteins. *Nat. Methods* **6**, 355–8.
- Kreutz, B., Yau, D. M., Nance, M. R., Tanabe, S., Tesmer, J. J. G. and Kozasa, T.** (2006). A New Approach to Producing Functional Ga Subunits Yields the Activated and Deactivated Structures of Ga 12/13 Proteins †. *Biochemistry* **45**, 167–174.
- Kuner, T. and Augustine, G. J.** (2000). A genetically encoded ratiometric indicator for chloride: capturing chloride transients in cultured hippocampal neurons. *Neuron* **27**, 447–59.

L

- Lagerström, M. C. and Schiöth, H. B.** (2008). Structural diversity of G protein-coupled receptors and significance for drug discovery. *Nat. Rev. Drug Discov.* **7**, 339–57.
- Lam, A. J., St-Pierre, F., Gong, Y., Marshall, J. D., Cranfill, P. J., Baird, M. A., McKeown, M. R., Wiedenmann, J., Davidson, M. W., Schnitzer, M. J., et al.** (2012). Improving FRET dynamic range with bright green and red fluorescent proteins. *Nat. Methods* **9**, 1005–1012.
- Lambert, N. A.** (2008). Dissociation of heterotrimeric g proteins in cells. *Sci. Signal.* **1**, re5.

- Lambright, D. G., Noel, J. P., Hamm, H. E. and Sigler, P. B.** (1994). Structural determinants for activation of the alpha-subunit of a heterotrimeric G protein. *Nature* **369**, 621–8.
- Lappano, R. and Maggiolini, M.** (2011). G protein-coupled receptors: novel targets for drug discovery in cancer. *Nat. Rev. Drug Discov.* **10**, 47–60.
- Laviv, T., Kim, B. B., Chu, J., Lam, A. J., Lin, M. Z. and Yasuda, R.** (2016). Simultaneous dual-color fluorescence lifetime imaging with novel red-shifted fluorescent proteins. *Nat. Methods* **13**, 989–992.
- Lee, M. J., Thangada, S., Claffey, K. P., Ancellin, N., Liu, C. H., Kluk, M., Volpi, M., Sha'afi, R. I. and Hla, T.** (1999). Vascular endothelial cell adherens junction assembly and morphogenesis induced by sphingosine-1-phosphate. *Cell* **99**, 301–12.
- Levitzki, A. and Klein, S.** (2002). G-Protein Subunit Dissociation Is not an Integral Part of G-Protein Action. *ChemBioChem* **3**, 815–818.
- Li, Y., Sierra, A. M., Ai, H.-W. and Campbell, R. E.** Identification of sites within a monomeric red fluorescent protein that tolerate peptide insertion and testing of corresponding circular permutations. *Photochem. Photobiol.* **84**, 111–9.
- Li, Z., Hannigan, M., Mo, Z., Liu, B., Lu, W., Wu, Y., Smrcka, A. V, Wu, G., Li, L., Liu, M., et al.** (2003). Directional sensing requires G beta gamma-mediated PAK1 and PIX alpha-dependent activation of Cdc42. *Cell* **114**, 215–27.
- Li, H., Yang, L., Fu, H., Yan, J., Wang, Y., Guo, H., Hao, X., Xu, X., Jin, T. and Zhang, N.** (2013). Association between Gai2 and ELMO1/Dock180 connects chemokine signalling with Rac activation and metastasis. *Nat. Commun.* **4**, 1706.
- Lichtman, J. W. and Conchello, J.-A.** (2005). Fluorescence microscopy. *Nat. Methods* **2**, 910–9.
- Lin, B., Yin, T., Wu, Y. I., Inoue, T. and Levchenko, A.** (2015). Interplay between chemotaxis and contact inhibition of locomotion determines exploratory cell migration. *Nat. Commun.* **6**, 6619.
- Lindenburg, L. H., Malisauskas, M., Sips, T., van Oppen, L., Wijnands, S. P. W., van de Graaf, S. F. J. and Merkx, M.** (2014). Quantifying stickiness: thermodynamic characterization of intramolecular domain interactions to guide the design of Förster resonance energy transfer sensors. *Biochemistry* **53**, 6370–81.
- Liu, Y., An, S., Ward, R., Yang, Y., Guo, X.-X., Li, W. and Xu, T.-R.** (2016). G protein-coupled receptors as promising cancer targets. *Cancer Lett.* **376**, 226–39.
- Lodish, H., Berk, A., Kaiser, C. A., Krieger, M., Scott, M. P., Bretscher, Anthony Ploegh, H. and Matsudaira, P. T.** (2007). *Molecular Cell Biology*. 6th ed. New York: W.H. Freeman & Co.
- Lohse, M. J., Nuber, S. and Hoffmann, C.** (2012). Fluorescence/bioluminescence resonance energy transfer techniques to study G-protein-coupled receptor activation and signaling. *Pharmacol. Rev.* **64**, 299–336.
- Lukyanov, K. A., Fradkov, A. F., Gurskaya, N. G., Matz, M. V, Labas, Y. A., Savitsky, A. P., Markelov, M. L., Zaraisky, A. G., Zhao, X., Fang, Y., et al.** (2000). Natural animal coloration can be determined by a nonfluorescent green fluorescent protein homolog. *J. Biol. Chem.* **275**, 25879–82.
- Lutz, S., Freichel-Blomquist, A., Yang, Y., Rumenapp, U., Jakobs, K. H., Schmidt, M. and Wieland, T.** (2005). The guanine nucleotide exchange factor p63RhoGEF, a specific link between Gq/11-coupled receptor signaling and RhoA. *J. Biol. Chem.* **280**, 11134–9.

M

- Maeder, C. I., Hink, M. A., Kinkhabwala, A., Mayr, R., Bastiaens, P. I. H. and Knop, M.** (2007). Spatial regulation of Fus3 MAP kinase activity through a reaction-diffusion mechanism in yeast pheromone signalling. *Nat. Cell Biol.* **9**, 1319–1326.
- Markwardt, M. L., Kremers, G.-J., Kraft, C. A., Ray, K., Cranfill, P. J. C., Wilson, K. A., Day, R. N., Wachter, R. M., Davidson, M. W. and Rizzo, M. A.** (2011). An Improved Cerulean Fluorescent Protein with Enhanced Brightness and Reduced Reversible Photoswitching. *PLoS One* **6**, e17896.
- Martin, C. B., Mahon, G. M., Klinger, M. B., Kay, R. J., Symons, M., Der, C. J. and Whitehead, I. P.** (2001). The thrombin receptor, PAR-1, causes transformation by activation of Rho-mediated signaling pathways. *Oncogene* **20**, 1953–1963.
- Martin, P., Albagli, O., Poggi, M. C., Boulukos, K. E. and Pognonec, P.** (2006). Development of a new bicistronic retroviral vector with strong IRES activity. *BMC Biotechnol.* **6**, 4.
- Mastop, M., Bindels, D. S., Shaner, N. C., Postma, M., Gadella, T. W. J. and Goedhart, J.** (2017). Characterization of a spectrally diverse set of fluorescent proteins as FRET acceptors for mTurquoise2. *Sci. Rep.* **7**, 11999.
- Mastop, M., Reinhard, N. R., Zuconelli, C. R., Terwey, F., Gadella, T. W. J., van Unen, J., Adjobo-Hermans, M. J. W. and Goedhart, J.** (2018). A FRET-based biosensor for measuring Gα13 activation in single cells. *PLoS One* **13**, e0193705.
- Mehta, D. and Malik, A. B.** (2006). Signaling Mechanisms Regulating Endothelial Permeability. *Physiol. Rev.* **86**, 279–367.
- Mehta, S. and Zhang, J.** (2011). Reporting from the field: genetically encoded fluorescent reporters uncover signaling dynamics in living biological systems. *Annu. Rev. Biochem.* **80**, 375–401.
- Merzlyak, E. M., Goedhart, J., Shcherbo, D., Bulina, M. E., Shcheglov, A. S., Fradkov, A. F., Gaintzeva, A., Lukyanov, K. A., Lukyanov, S., Gadella Jr, T. W. J., et al.** (2007). Bright monomeric red fluorescent protein with an extended fluorescence lifetime. *Nat. Methods* **4**, 555–7.
- Meyer, B. H., Freuler, F., Guerini, D. and Siehler, S.** (2008). Reversible translocation of p115-RhoGEF by G(12/13)-coupled receptors. *J. Cell. Biochem.* **104**, 1660–70.
- Miaczynska, M., Pelkmans, L. and Zerial, M.** (2004). Not just a sink: endosomes in control of signal transduction. *Curr. Opin. Cell Biol.* **16**, 400–6.
- Mikelis, C. M., Simaan, M., Ando, K., Fukuhara, S., Sakurai, A., Amornphimoltham, P., Masedunskas, A., Weigert, R., Chavakis, T., Adams, R. H., et al.** (2015). RhoA and ROCK mediate histamine-induced vascular leakage and anaphylactic shock. *Nat. Commun.* **6**, 6725.
- Miller, K. E., Kim, Y., Huh, W.-K. and Park, H.-O.** (2015). Bimolecular Fluorescence Complementation (BiFC) Analysis: Advances and Recent Applications for Genome-Wide Interaction Studies. *J. Mol. Biol.* **427**, 2039–2055.
- Milligan, G.** (2003). Principles: extending the utility of [35S]GTP gamma S binding assays. *Trends Pharmacol. Sci.* **24**, 87–90.
- Milligan, G. and Kostenis, E.** (2006). Heterotrimeric G-proteins: a short history. *Br. J. Pharmacol.* **147 Suppl**, S46-55.

- Miyawaki, A.** (2011). Development of probes for cellular functions using fluorescent proteins and fluorescence resonance energy transfer. *Annu. Rev. Biochem.* **80**, 357–73.
- Miyawaki, A. and Niino, Y.** (2015). Molecular spies for bioimaging—fluorescent protein-based probes. *Mol. Cell* **58**, 632–43.
- Miyawaki, A., Shcherbakova, D. M. and Verkhusha, V. V.** (2012). Red fluorescent proteins: chromophore formation and cellular applications. *Curr. Opin. Struct. Biol.* **22**, 679–88.
- Mizuno, H., Mal, T. K., Wälchli, M., Kikuchi, A., Fukano, T., Ando, R., Jeyakanthan, J., Taka, J., Shiro, Y., Ikura, M., et al.** (2008). Light-dependent regulation of structural flexibility in a photochromic fluorescent protein. *Proc. Natl. Acad. Sci. U. S. A.* **105**, 9227–32.
- Murakoshi, H., Lee, S.-J. and Yasuda, R.** (2008). Highly sensitive and quantitative FRET-FLIM imaging in single dendritic spines using improved non-radiative YFP. *Brain Cell Biol.* **36**, 31–42.
- Murali, A. and Rajalingam, K.** (2014). Small Rho GTPases in the control of cell shape and mobility. *Cell. Mol. Life Sci.* **71**, 1703–21.

N

- Nagai, T., Ibata, K., Park, E. S., Kubota, M., Mikoshiba, K. and Miyawaki, A.** (2002). A variant of yellow fluorescent protein with fast and efficient maturation for cell-biological applications. *Nat. Biotechnol.* **20**, 87–90.
- Nagai, T., Yamada, S., Tominaga, T., Ichikawa, M. and Miyawaki, A.** (2004). Expanded dynamic range of fluorescent indicators for Ca(2+) by circularly permuted yellow fluorescent proteins. *Proc. Natl. Acad. Sci. U. S. A.* **101**, 10554–9.
- Naikawadi, R. P., Cheng, N., Vogel, S. M., Qian, F., Wu, D., Malik, A. B. and Ye, R. D.** (2012). A Critical Role for Phosphatidylinositol (3,4,5)-Trisphosphate-Dependent Rac Exchanger 1 in Endothelial Junction Disruption and Vascular Hyperpermeability. *Circ. Res.* **111**, 1517–1527.
- Navenot, J.-M., Fujii, N. and Peiper, S. C.** (2009). Activation of Rho and Rho-Associated Kinase by GPR54 and KiSS1 Metastasis Suppressor Gene Product Induces Changes of Cell Morphology and Contributes to Apoptosis. *Mol. Pharmacol.* **75**, 1300–1306.
- Nguyen, A. W. and Daugherty, P. S.** (2005). Evolutionary optimization of fluorescent proteins for intracellular FRET. *Nat. Biotechnol.* **23**, 355–60.
- Niino, Y., Hotta, K. and Oka, K.** (2009). Simultaneous live cell imaging using dual FRET sensors with a single excitation light. *PLoS One* **4**, e6036.
- Nobes, C. D. and Hall, A.** (1995). Rho, rac, and cdc42 GTPases regulate the assembly of multimolecular focal complexes associated with actin stress fibers, lamellipodia, and filopodia. *Cell* **81**, 53–62.
- Nourshargh, S., Hordijk, P. L. and Sixt, M.** (2010). Breaching multiple barriers: leukocyte motility through venular walls and the interstitium. *Nat. Rev. Mol. Cell Biol.* **11**, 366–378.

O

- O’Hayre, M., Degese, M. S. and Gutkind, J. S.** (2014). Novel insights into G protein and G protein-coupled receptor signaling in cancer. *Curr. Opin. Cell Biol.* **27**, 126–35.
- O’Neill, P. R. and Gautam, N.** (2014). Subcellular optogenetic inhibition of G proteins generates signaling gradients and cell migration. *Mol. Biol. Cell* **25**, 2305–2314.

- Ohta, Y., Kamagata, T., Mukai, A., Takada, S., Nagai, T. and Horikawa, K.** (2016). Nontrivial Effect of the Color-Exchange of a Donor/Acceptor Pair in the Engineering of Förster Resonance Energy Transfer (FRET)-Based Indicators. *ACS Chem. Biol.* **11**, 1816–22.
- Okumoto, S., Jones, A. and Frommer, W. B.** (2012). Quantitative imaging with fluorescent biosensors. *Annu. Rev. Plant Biol.* **63**, 663–706.
- Olofsson, B.** (1999). Rho guanine dissociation inhibitors: pivotal molecules in cellular signalling. *Cell. Signal.* **11**, 545–54.
- Orgogozo, V., Morizot, B. and Martin, A.** (2015). The differential view of genotype-phenotype relationships. *Front. Genet.* **6**, 179.
- Ostermaier, M. K., Schertler, G. F. X. and Standfuss, J.** (2014). Molecular mechanism of phosphorylation-dependent arrestin activation. *Curr. Opin. Struct. Biol.* **29**, 143–51.
- Ouyang, M., Huang, H., Shaner, N. C., Remacle, A. G., Shiryayev, S. A., Strongin, A. Y., Tsien, R. Y. and Wang, Y.** (2010). Simultaneous visualization of protumorigenic Src and MT1-MMP activities with fluorescence resonance energy transfer. *Cancer Res.* **70**, 2204–12.
- ## P
- Palczewski, K., Kumasaka, T., Hori, T., Behnke, C. A., Motoshima, H., Fox, B. A., Le Trong, I., Teller, D. C., Okada, T., Stenkamp, R. E., et al.** (2000). Crystal structure of rhodopsin: A G protein-coupled receptor. *Science* **289**, 739–45.
- Palm, G. J., Zdanov, A., Gaitanaris, G. A., Stauber, R., Pavlakis, G. N. and Wlodawer, A.** (1997). The structural basis for spectral variations in green fluorescent protein. *Nat. Struct. Biol.* **4**, 361–5.
- Pannekoek, W.-J., Vliem, M. J. and Bos, J. L.** (2018). Multiple Rap1 effectors control Epac1-mediated tightening of endothelial junctions. *Small GTPases* 1–8.
- Pappenheimer, J. R., Renkin, E. M. and Borrero, L. M.** (1951). Filtration, Diffusion and Molecular Sieving Through Peripheral Capillary Membranes. *Am. J. Physiol. Content* **167**, 13–46.
- Patowary, S.** (2013). Protein Association in Living Cells Using Fret Spectrometry: Application to G-Protein Coupled Receptor.
- Patterson, G. H., Knobel, S. M., Sharif, W. D., Kain, S. R. and Piston, D. W.** (1997). Use of the green fluorescent protein and its mutants in quantitative fluorescence microscopy. *Biophys. J.* **73**, 2782–90.
- Pauker, M. H., Hassan, N., Noy, E., Reicher, B. and Barda-Saad, M.** (2012). Studying the dynamics of SLP-76, Nck, and Vav1 multimolecular complex formation in live human cells with triple-color FRET. *Sci. Signal.* **5**, rs3.
- Pédelacq, J.-D., Cabantous, S., Tran, T., Terwilliger, T. C. and Waldo, G. S.** (2006). Engineering and characterization of a superfolder green fluorescent protein. *Nat. Biotechnol.* **24**, 79–88.
- Peroza, E. A., Boumezbeur, A.-H. and Zamboni, N.** (2015). Rapid, randomized development of genetically encoded FRET sensors for small molecules. *Analyst* **140**, 4540–8.
- Pertz, O., Hodgson, L., Klemke, R. L. and Hahn, K. M.** (2006). Spatiotemporal dynamics of RhoA activity in migrating cells. *Nature* **440**, 1069–1072.
- Peyker, A., Rocks, O. and Bastiaens, P. I. H.** (2005). Imaging activation of two Ras isoforms simultaneously in a single cell. *ChemBiochem* **6**, 78–85.

- Piatkevich, K. D., Malashkevich, V. N., Almo, S. C. and Verkhusha, V. V.** (2010). Engineering ESPT pathways based on structural analysis of LSSmKate red fluorescent proteins with large Stokes shift. *J. Am. Chem. Soc.* **132**, 10762–70.
- Pietraszewska-Bogiel, A. and Gadella Jr, T. W. J.** (2011). FRET microscopy: from principle to routine technology in cell biology. *J. Microsc.* **241**, 111–8.
- Piljic, A. and Schultz, C.** (2008). Simultaneous recording of multiple cellular events by FRET. *ACS Chem. Biol.* **3**, 156–60.
- Piston, D. W. and Kremers, G.-J.** (2007). Fluorescent protein FRET: the good, the bad and the ugly. *Trends Biochem. Sci.* **32**, 407–14.
- Piston, D. W. and Rizzo, M. A.** (2008). FRET by fluorescence polarization microscopy. *Methods Cell Biol.* **85**, 415–30.
- Pollok, B. A. and Heim, R.** (1999). Using GFP in FRET-based applications. *Trends Cell Biol.* **9**, 57–60.
- Ponsoen, B., Zhao, J., Riedl, J., Zwartkuis, F., van der Krogt, G., Zaccolo, M., Moolenaar, W. H., Bos, J. L. and Jalink, K.** (2004). Detecting cAMP-induced Epac activation by fluorescence resonance energy transfer: Epac as a novel cAMP indicator. *EMBO Rep.* **5**, 1176–80.
- Preininger, A. M., Meiler, J. and Hamm, H. E.** (2013). Conformational flexibility and structural dynamics in GPCR-mediated G protein activation: a perspective. *J. Mol. Biol.* **425**, 2288–98.

R

- Raspe, M., Kedziora, K. M., van den Broek, B., Zhao, Q., de Jong, S., Herz, J., Mastop, M., Goedhart, J., Gadella, T. W. J., Young, I. T., et al.** (2016). siFLIM: single-image frequency-domain FLIM provides fast and photon-efficient lifetime data. *Nat. Methods* **13**, 501–4.
- Reinhard, N. R., van Helden, S. F., Anthony, E. C., Yin, T., Wu, Y. I., Goedhart, J., Gadella, T. W. J. and Hordijk, P. L.** (2016). Spatiotemporal analysis of RhoA/B/C activation in primary human endothelial cells. *Sci. Rep.* **6**, 25502.
- Reinhard, N. R., Mastop, M., Yin, T., Wu, Y., Bosma, E. K., Gadella, T. W. J., Goedhart, J. and Hordijk, P. L.** (2017). The balance between Gα_i-Cdc42/Rac and Gα_{12/13}-RhoA pathways determines endothelial barrier regulation by sphingosine-1-phosphate. *Mol. Biol. Cell* **28**, 3371–3382.
- Reiter, E. and Lefkowitz, R. J.** (2006). GRKs and beta-arrestins: roles in receptor silencing, trafficking and signaling. *Trends Endocrinol. Metab.* **17**, 159–65.
- Reiter, E., Ahn, S., Shukla, A. K. and Lefkowitz, R. J.** (2012). Molecular mechanism of β-arrestin-biased agonism at seven-transmembrane receptors. *Annu. Rev. Pharmacol. Toxicol.* **52**, 179–97.
- Rekas, A., Alattia, J.-R., Nagai, T., Miyawaki, A. and Ikura, M.** (2002). Crystal structure of venus, a yellow fluorescent protein with improved maturation and reduced environmental sensitivity. *J. Biol. Chem.* **277**, 50573–8.
- Rens-Domiano, S. and Hamm, H. E.** (1995). Structural and functional relationships of heterotrimeric G-proteins. *FASEB J.* **9**, 1059–66.
- Ridley, A. J.** (2003). Cell Migration: Integrating Signals from Front to Back. *Science (80-)*. **302**, 1704–1709.
- Ridley, A. J.** (2015). Rho GTPase signalling in cell migration. *Curr. Opin. Cell Biol.* **36**, 103–112.

- Ridley, A. J., Paterson, H. F., Johnston, C. L., Diekmann, D. and Hall, A.** (1992). The small GTP-binding protein rac regulates growth factor-induced membrane ruffling. *Cell* **70**, 401–10.
- Riento, K. and Ridley, A. J.** (2003). ROCKs: multifunctional kinases in cell behaviour. *Nat. Rev. Mol. Cell Biol.* **4**, 446–456.
- Riobo, N. A. and Manning, D. R.** (2005). Receptors coupled to heterotrimeric G proteins of the G12 family. *Trends Pharmacol. Sci.* **26**, 146–154.
- Rojas, R. J., Yohe, M. E., Gershburg, S., Kawano, T., Kozasa, T. and Sondek, J.** (2007). Galphaq directly activates p63RhoGEF and Trio via a conserved extension of the Dbl homology-associated pleckstrin homology domain. *J. Biol. Chem.* **282**, 29201–10.
- Rosenbaum, D. M., Cherezov, V., Hanson, M. A., Rasmussen, S. G. F., Thian, F. S., Kobilka, T. S., Choi, H.-J., Yao, X.-J., Weis, W. I., Stevens, R. C., et al.** (2007). GPCR engineering yields high-resolution structural insights into beta2-adrenergic receptor function. *Science* **318**, 1266–73.
- Roth, B. L. and Kroeze, W. K.** (2015). Integrated Approaches for Genome-wide Interrogation of the Druggable Non-olfactory G Protein-coupled Receptor Superfamily. *J. Biol. Chem.* **290**, 19471–7.
- ## S
- Sabariegos, R., Picazo, F., Domingo, B., Franco, S., Martinez, M.-A. and Llopis, J.** (2009). Fluorescence resonance energy transfer-based assay for characterization of hepatitis C virus NS3-4A protease activity in live cells. *Antimicrob. Agents Chemother.* **53**, 728–34.
- Sadok, A. and Marshall, C. J.** (2014). Rho GTPases: masters of cell migration. *Small GTPases* **5**, e29710.
- Sah, V. P., Seasholtz, T. M., Sagi, S. A. and Brown, J. H.** (2000). The role of Rho in G protein-coupled receptor signal transduction. *Annu. Rev. Pharmacol. Toxicol.* **40**, 459–89.
- Saito, Y., Oikawa, M., Nakazawa, H., Niide, T., Kameda, T., Tsuda, K. and Umetsu, M.** (2018). Machine-Learning-Guided Mutagenesis for Directed Evolution of Fluorescent Proteins. *ACS Synth. Biol.* **7**, 2014–2022.
- Sakaue-Sawano, A., Kurokawa, H., Morimura, T., Hanyu, A., Hama, H., Osawa, H., Kashiwagi, S., Fukami, K., Miyata, T., Miyoshi, H., et al.** (2008). Visualizing spatiotemporal dynamics of multicellular cell-cycle progression. *Cell* **132**, 487–98.
- Salahpour, A.** (2012). BRET biosensors to study GPCR biology, pharmacology, and signal transduction. *Front. Endocrinol. (Lausanne)*. **3**, 105.
- Satake, H., Matsubara, S., Aoyama, M., Kawada, T. and Sakai, T.** (2013). GPCR Heterodimerization in the Reproductive System: Functional Regulation and Implication for Biodiversity. *Front. Endocrinol. (Lausanne)*. **4**, 100.
- Saulière, A., Bellot, M., Paris, H., Denis, C., Finana, F., Hansen, J. T., Altié, M.-F., Seguelas, M.-H., Pathak, A., Hansen, J. L., et al.** (2012). Deciphering biased-agonism complexity reveals a new active AT1 receptor entity. *Nat. Chem. Biol.* **8**, 622–30.
- Schaefer, A. and Hordijk, P. L.** (2015). Cell-stiffness-induced mechanosignaling - a key driver of leukocyte transendothelial migration. *J. Cell Sci.* **128**, 2221–2230.

- Schifferer, M. and Griesbeck, O.** (2012). A dynamic FRET reporter of gene expression improved by functional screening. *J. Am. Chem. Soc.* **134**, 15185–8.
- Schultz, C., Schleifenbaum, A., Goedhart, J. and Gadella Jr, T. W. J.** (2005). Multiparameter imaging for the analysis of intracellular signaling. *Chembiochem* **6**, 1323–30.
- Schwille, P., Haupts, U., Maiti, S. and Webb, W. W.** (1999). Molecular dynamics in living cells observed by fluorescence correlation spectroscopy with one- and two-photon excitation. *Biophys. J.* **77**, 2251–65.
- Scott, B. L. and Hoppe, A. D.** (2015). Optimizing fluorescent protein trios for 3-Way FRET imaging of protein interactions in living cells. *Sci. Rep.* **5**, 10270.
- Seachrist, J. L. and Ferguson, S. S. G.** (2003). Regulation of G protein-coupled receptor endocytosis and trafficking by Rab GTPases. *Life Sci.* **74**, 225–35.
- Shaner, N. C., Campbell, R. E., Steinbach, P. A., Giepmans, B. N. G., Palmer, A. E. and Tsien, R. Y.** (2004). Improved monomeric red, orange and yellow fluorescent proteins derived from *Discosoma* sp. red fluorescent protein. *Nat. Biotechnol.* **22**, 1567–72.
- Shaner, N. C., Lin, M. Z., McKeown, M. R., Steinbach, P. A., Hazelwood, K. L., Davidson, M. W. and Tsien, R. Y.** (2008). Improving the photostability of bright monomeric orange and red fluorescent proteins. *Nat. Methods* **5**, 545–51.
- Shaner, N. C., Lambert, G. G., Chamma, A., Ni, Y., Cranfill, P. J., Baird, M. A., Sell, B. R., Allen, J. R., Day, R. N., Israelsson, M., et al.** (2013). A bright monomeric green fluorescent protein derived from *Branchiostoma lanceolatum*. *Nat. Methods* **10**, 407–9.
- Shanker, N. and Bane, S. L.** (2008). Basic aspects of absorption and fluorescence spectroscopy and resonance energy transfer methods. *Methods Cell Biol.* **84**, 213–42.
- Shcherbakova, D. M., Hink, M. A., Joosen, L., Gadella Jr, T. W. J. and Verkhusha, V. V.** (2012). An orange fluorescent protein with a large Stokes shift for single-excitation multicolor FCCS and FRET imaging. *J. Am. Chem. Soc.* **134**, 7913–23.
- Shcherbo, D., Murphy, C. S., Ermakova, G. V., Solovieva, E. A., Chepurnykh, T. V., Shcheglov, A. S., Verkhusha, V. V., Pletnev, V. Z., Hazelwood, K. L., Roche, P. M., et al.** (2009). Far-red fluorescent tags for protein imaging in living tissues. *Biochem. J.* **418**, 567–74.
- Shi, L., Liapakis, G., Xu, R., Guarnieri, F., Ballesteros, J. A. and Javitch, J. A.** (2002). Beta2 adrenergic receptor activation. Modulation of the proline kink in transmembrane 6 by a rotamer toggle switch. *J. Biol. Chem.* **277**, 40989–96.
- Shimozono, S. and Miyawaki, A.** (2008). Engineering FRET constructs using CFP and YFP. *Methods Cell Biol.* **85**, 381–93.
- Shimozono, S., Hosoi, H., Mizuno, H., Fukano, T., Tahara, T. and Miyawaki, A.** (2006). Concatenation of cyan and yellow fluorescent proteins for efficient resonance energy transfer. *Biochemistry* **45**, 6267–71.
- Shrestha, D., Jenei, A., Nagy, P., Vereb, G. and Szöllösi, J.** (2015). Understanding FRET as a research tool for cellular studies. *Int. J. Mol. Sci.* **16**, 6718–56.
- Shui, B., Wang, Q., Lee, F., Byrnes, L. J., Chudakov, D. M., Lukyanov, S. A., Sondermann, H. and Kotlikoff, M. I.** (2011). Circular Permutation of Red Fluorescent Proteins. *PLoS One* **6**, e20505.

- Siehler, S.** (2009). Regulation of RhoGEF proteins by G12/13-coupled receptors. *Br. J. Pharmacol.* **158**, 41–9.
- Siemerling, K. R., Golbik, R., Sever, R. and Haseloff, J.** (1996). Mutations that suppress the thermosensitivity of green fluorescent protein. *Curr. Biol.* **6**, 1653–63.
- Siflinger-Birnboim, A., del Vecchio, P. J., Cooper, J. A., Blumenstock, F. A., Shepard, J. M. and Malik, A. B.** (1987). Molecular sieving characteristics of the cultured endothelial monolayer. *J. Cell. Physiol.* **132**, 111–117.
- Smrcka, A. V.** (2008). G protein $\beta\gamma$ subunits: central mediators of G protein-coupled receptor signaling. *Cell. Mol. Life Sci.* **65**, 2191–214.
- Snapp, E. L.** (2009). Fluorescent proteins: a cell biologist's user guide. *Trends Cell Biol.* **19**, 649–655.
- Snapp, E. L., Hegde, R. S., Francolini, M., Lombardo, F., Colombo, S., Pedrazzini, E., Borgese, N. and Lippincott-Schwartz, J.** (2003). Formation of stacked ER cisternae by low affinity protein interactions. *J. Cell Biol.* **163**, 257–269.
- Spangler, S. M. and Bruchas, M. R.** (2017). Optogenetic approaches for dissecting neuromodulation and GPCR signaling in neural circuits. *Curr. Opin. Pharmacol.* **32**, 56–70.
- Strange, P. G.** (2010). Use of the GTP γ S ([³⁵S]GTP γ S and Eu-GTP γ S) binding assay for analysis of ligand potency and efficacy at G protein-coupled receptors. *Br. J. Pharmacol.* **161**, 1238–1249.
- Subach, F. V., Subach, O. M., Gundorov, I. S., Morozova, K. S., Piatkevich, K. D., Cuervo, A. M. and Verkhusha, V. V.** (2009). Monomeric fluorescent timers that change color from blue to red report on cellular trafficking. *Nat. Chem. Biol.* **5**, 118–26.
- Sun, Y., Booker, C. F., Kumari, S., Day, R. N., Davidson, M. and Periasamy, A.** (2009). Characterization of an orange acceptor fluorescent protein for sensitized spectral fluorescence resonance energy transfer microscopy using a white-light laser. *J. Biomed. Opt.* **14**, 54009.
- Sun, X., Zhang, A., Baker, B., Sun, L., Howard, A., Buswell, J., Maurel, D., Masharina, A., Johnsson, K., Noren, C. J., et al.** (2011). Development of SNAP-tag fluorogenic probes for wash-free fluorescence imaging. *Chembiochem* **12**, 2217–26.
- Swaminathan, R., Hoang, C. P. and Verkman, A. S.** (1997). Photobleaching recovery and anisotropy decay of green fluorescent protein GFP-S65T in solution and cells: cytoplasmic viscosity probed by green fluorescent protein translational and rotational diffusion. *Biophys. J.* **72**, 1900–7.
- Syrovatkina, V., Alegre, K. O., Dey, R. and Huang, X.-Y.** (2016). Regulation, Signaling, and Physiological Functions of G-Proteins. *J. Mol. Biol.* **428**, 3850–68.
- Szymczak, A. L., Workman, C. J., Wang, Y., Vignali, K. M., Dilioglou, S., Vanin, E. F. and Vignali, D. A. A.** (2004). Correction of multi-gene deficiency in vivo using a single “self-cleaving” 2A peptide-based retroviral vector. *Nat. Biotechnol.* **22**, 589–94.

T

- Takefuji, M., Wirth, A., Lukasova, M., Takefuji, S., Boettger, T., Braun, T., Althoff, T., Offermanns, S. and Wettschureck, N.** (2012). G 13 -Mediated Signaling Pathway Is Required for Pressure Overload-Induced Cardiac Remodeling and Heart Failure. *Circulation* **126**, 1972–1982.

- Terskikh, A., Fradkov, A., Ermakova, G., Zaraisky, A., Tan, P., Kajava, A. V., Zhao, X., Lukyanov, S., Matz, M., Kim, S., et al.** (2000). "Fluorescent timer": protein that changes color with time. *Science* **290**, 1585–8.
- Thestrup, T., Litzlbauer, J., Bartholomäus, I., Mues, M., Russo, L., Dana, H., Kovalchuk, Y., Liang, Y., Kalamakis, G., Laukat, Y., et al.** (2014). Optimized ratiometric calcium sensors for functional in vivo imaging of neurons and T lymphocytes. *Nat. Methods* **11**, 175–82.
- Topell, S., Hennecke, J. and Glockshuber, R.** (1999). Circularly permuted variants of the green fluorescent protein. *FEBS Lett.* **457**, 283–9.
- Toseland, C. P.** (2013). Fluorescent labeling and modification of proteins. *J. Chem. Biol.* **6**, 85–95.
- Trzaskowski, B., Latek, D., Yuan, S., Ghoshdastider, U., Debinski, A. and Filipek, S.** (2012). Action of molecular switches in GPCRs—theoretical and experimental studies. *Curr. Med. Chem.* **19**, 1090–109.
- Tsien, R. Y.** (1998). The green fluorescent protein. *Annu. Rev. Biochem.* **67**, 509–44.
- Tsutsui, H., Karasawa, S., Okamura, Y. and Miyawaki, A.** (2008). Improving membrane voltage measurements using FRET with new fluorescent proteins. *Nat. Methods* **5**, 683–685.
- Tyas, L., Brophy, V. A., Pope, A., Rivett, A. J. and Tavaré, J. M.** (2000). Rapid caspase-3 activation during apoptosis revealed using fluorescence-resonance energy transfer. *EMBO Rep.* **1**, 266–70.

V

- van der Krogt, G. N. M., Ogink, J., Ponsioen, B. and Jalink, K.** (2008). A comparison of donor-acceptor pairs for genetically encoded FRET sensors: application to the Epac cAMP sensor as an example. *PLoS One* **3**, e1916.
- van Hinsbergh, V. W. M., Eringa, E. C. and Daemen, M. J. A. P.** (2015). Neovascularization of the atherosclerotic plaque. *Curr. Opin. Lipidol.* **26**, 405–411.
- van Hooren, K. W. E. M., van Breevoort, D., Fernandez-Borja, M., Meijer, A. B., Eikenboom, J., Bierings, R. and Voorberg, J.** (2014). Phosphatidylinositol-3,4,5-triphosphate-dependent Rac exchange factor 1 regulates epinephrine-induced exocytosis of Weibel-Palade bodies. *J. Thromb. Haemost.* **12**, 273–281.
- van Munster, E. B. and Gadella Jr., T. W.** (2004). Suppression of photobleaching-induced artifacts in frequency-domain FLIM by permutation of the recording order. *Cytom. A* **58**, 185–194.
- Van Munster, E. B. and Gadella Jr, T. W. J.** (2004). phiFLIM: a new method to avoid aliasing in frequency-domain fluorescence lifetime imaging microscopy. *J. Microsc.* **213**, 29–38.
- Van Munster, E. B. and Gadella Jr, T. W. J.** (2005). Fluorescence lifetime imaging microscopy (FLIM). *Adv. Biochem. Eng. Biotechnol.* **95**, 143–75.
- Van Munster, E. B., Kremers, G. J., Adjobo-Hermans, M. J. W. and Gadella, T. W. J.** (2005). Fluorescence resonance energy transfer (FRET) measurement by gradual acceptor photobleaching. *J. Microsc.* **218**, 253–62.
- van Unen, J., Woolard, J., Rinken, A., Hoffmann, C., Hill, S. J., Goedhart, J., Bruchas, M. R., Bouvier, M. and Adjobo-Hermans, M. J. W.** (2015a). A Perspective on Studying G-Protein-Coupled Receptor Signaling with Resonance Energy Transfer Biosensors in Living Organisms. *Mol. Pharmacol.* **88**, 589–595.

- van Unen, J., Reinhard, N. R., Yin, T., Wu, Y. I., Postma, M., Gadella, T. W. J. and Goedhart, J.** (2015b). Plasma membrane restricted RhoGEF activity is sufficient for RhoA-mediated actin polymerization. *Sci. Rep.* **5**, 14693.
- van Unen, J., Yin, T., Wu, Y. I., Mastop, M., Gadella Jr, T. W. J. and Goedhart, J.** (2016a). Kinetics of recruitment and allosteric activation of ARHGEF25 isoforms by the heterotrimeric G-protein Gαq. *Sci. Rep.* **6**, 36825.
- van Unen, J., Rashidfarrokhi, A., Hoogendoorn, E., Postma, M., Gadella, T. W. J. and Goedhart, J.** (2016b). Quantitative Single-Cell Analysis of Signaling Pathways Activated Immediately Downstream of Histamine Receptor Subtypes. *Mol. Pharmacol.* **90**, 162–76.
- van Unen, J., Stumpf, A. D., Schmid, B., Reinhard, N. R., Hordijk, P. L., Hoffmann, C., Gadella, T. W. J. and Goedhart, J.** (2016c). A New Generation of FRET Sensors for Robust Measurement of Gai1, Gai2 and Gai3 Activation Kinetics in Single Cells. *PLoS One* **11**, e0146789.
- Vassilatis, D. K., Hohmann, J. G., Zeng, H., Li, F., Ranchalis, J. E., Mortrud, M. T., Brown, A., Rodriguez, S. S., Weller, J. R., Wright, A. C., et al.** (2003). The G protein-coupled receptor repertoires of human and mouse. *Proc. Natl. Acad. Sci.* **100**, 4903–4908.
- Vázquez-Prado, J., Bracho-Valdés, I., Cervantes-Villagrana, R. D. and Reyes-Cruz, G.** (2016). Gβγ Pathways in Cell Polarity and Migration Linked to Oncogenic GPCR Signaling: Potential Relevance in Tumor Microenvironment. *Mol. Pharmacol.* **90**, 573–586.
- Verkhusha, V. V and Lukyanov, K. A.** (2004). The molecular properties and applications of Anthozoa fluorescent proteins and chromoproteins. *Nat. Biotechnol.* **22**, 289–96.
- Vermeer, J. E. M., Van Munster, E. B., Vischer, N. O. and Gadella, T. W. J.** (2004). Probing plasma membrane microdomains in cowpea protoplasts using lipidated GFP-fusion proteins and multimode FRET microscopy. *J. Microsc.* **214**, 190–200.
- Vilardaga, J.-P., Bünemann, M., Feinstein, T. N., Lambert, N., Nikolaev, V. O., Engelhardt, S., Lohse, M. J. and Hoffmann, C.** (2009). GPCR and G proteins: drug efficacy and activation in live cells. *Mol. Endocrinol.* **23**, 590–9.
- Vinkenborg, J. L., Evers, T. H., Reulen, S. W. A., Meijer, E. W. and Merckx, M.** (2007). Enhanced sensitivity of FRET-based protease sensors by redesign of the GFP dimerization interface. *Chembiochem* **8**, 1119–21.
- Virant, D., Traenkle, B., Maier, J., Kaiser, P. D., Bodenhöfer, M., Schmees, C., Vojnovic, I., Pisak-Lukáts, B., Endesfelder, U. and Rothbauer, U.** (2018). A peptide tag-specific nanobody enables high-quality labeling for dSTORM imaging. *Nat. Commun.* **9**, 930.
- von Stetten, D., Noirclerc-Savoie, M., Goedhart, J., Gadella, T. W. J. and Royant, A.** (2012). Structure of a fluorescent protein from *Aequorea victoria* bearing the obligate-monomer mutation A206K. *Acta Crystallogr. Sect. F Struct. Biol. Cryst. Commun.* **68**, 878–882.
- Vroon, A., Heijnen, C. J. and Kavelaars, A.** (2006). GRKs and arrestins: regulators of migration and inflammation. *J. Leukoc. Biol.* **80**, 1214–21.

W

- Wachter, R. M. and Remington, S. J.** (1999). Sensitivity of the yellow variant of green fluorescent protein to halides and nitrate. *Curr. Biol.* **9**, R628–9.

- Wachter, R. M., Watkins, J. L. and Kim, H.** (2010). Mechanistic diversity of red fluorescence acquisition by GFP-like proteins. *Biochemistry* **49**, 7417–27.
- Waeber, C., Blondeau, N. and Salomone, S.** (2004). Vascular sphingosine-1-phosphate S1P1 and S1P3 receptors. *Drug News Perspect.* **17**, 365–82.
- Wall, M. A., Coleman, D. E., Lee, E., Iñiguez-Lluhi, J. A., Posner, B. A., Gilman, A. G. and Sprang, S. R.** (1995). The structure of the G protein heterotrimer Gi alpha 1 beta 1 gamma 2. *Cell* **83**, 1047–58.
- Wedegaertner, P. B., Wilson, P. T. and Bourne, H. R.** (1995). Lipid modifications of trimeric G proteins. *J. Biol. Chem.* **270**, 503–6.
- Welch, H. C.** (2015). Regulation and function of P-Rex family Rac-GEFs. *Small GTPases* **6**, 49–70.
- Wennerberg, K. and Der, C. J.** (2004). Rho-family GTPases: it's not only Rac and Rho (and I like it). *J. Cell Sci.* **117**, 1301–12.
- Wettschureck, N. and Offermanns, S.** (2005). Mammalian G proteins and their cell type specific functions. *Physiol. Rev.* **85**, 1159–204.
- Wirth, A., Benyó, Z., Lukasova, M., Leutgeb, B., Wettschureck, N., Gorbey, S., Örsy, P., Horváth, B., Maser-Gluth, C., Greiner, E., et al.** (2008). G12-G13–LARG–mediated signaling in vascular smooth muscle is required for salt-induced hypertension. *Nat. Med.* **14**, 64–68.
- Wisler, J. W., Xiao, K., Thomsen, A. R. B. and Lefkowitz, R. J.** (2014). Recent developments in biased agonism. *Curr. Opin. Cell Biol.* **27**, 18–24.
- Wlodarczyk, J., Woehler, A., Kobe, F., Ponimaskin, E., Zeug, A. and Neher, E.** (2008). Analysis of FRET Signals in the Presence of Free Donors and Acceptors. *Biophys. J.* **94**, 986–1000.
- Woehler, A.** (2013). Simultaneous quantitative live cell imaging of multiple FRET-based biosensors. *PLoS One* **8**, e61096.
- Worzfeld, T., Wettschureck, N. and Offermanns, S.** (2008). G12/G13-mediated signalling in mammalian physiology and disease. *Trends Pharmacol. Sci.* **29**, 582–589.
- Wu, P. and Brand, L.** (1994). Resonance energy transfer: methods and applications. *Anal. Biochem.* **218**, 1–13.

X

- Xie, X.-Q. and Chowdhury, A.** (2013). Advances in methods to characterize ligand-induced ionic lock and rotamer toggle molecular switch in G protein-coupled receptors. *Methods Enzymol.* **520**, 153–74.
- Xiong, Y. and Hla, T.** (2014). S1P Control of Endothelial Integrity. In *Current topics in microbiology and immunology*, pp. 85–105.
- Xu, X., Gerard, A. L., Huang, B. C., Anderson, D. C., Payan, D. G. and Luo, Y.** (1998). Detection of programmed cell death using fluorescence energy transfer. *Nucleic Acids Res.* **26**, 2034–5.

Y

- Yang, F., Moss, L. G. and Phillips, G. N.** (1996). The molecular structure of green fluorescent protein. *Nat. Biotechnol.* **14**, 1246–1251.
- Yao, X., Parnot, C., Deupi, X., Ratnala, V. R. P., Swaminath, G., Farrens, D. and Kobilka, B.** (2006). Coupling ligand structure to specific conformational switches in the beta2-adrenoceptor. *Nat. Chem. Biol.* **2**, 417–22.

- Yatomi, Y., Igarashi, Y., Yang, L., Hisano, N., Qi, R., Asazuma, N., Satoh, K., Ozaki, Y. and Kume, S.** (1997). Sphingosine 1-phosphate, a bioactive sphingolipid abundantly stored in platelets, is a normal constituent of human plasma and serum. *J. Biochem.* **121**, 969–73.
- Yung, Y. C., Stoddard, N. C. and Chun, J.** (2014). LPA receptor signaling: pharmacology, physiology, and pathophysiology. *J. Lipid Res.* **55**, 1192–214.

Z

- Zacharias, D. A., Violin, J. D., Newton, A. C. and Tsien, R. Y.** (2002). Partitioning of lipid-modified monomeric GFPs into membrane microdomains of live cells. *Science* **296**, 913–6.
- Zapata-Hommer, O. and Griesbeck, O.** (2003). Efficiently folding and circularly permuted variants of the Sapphire mutant of GFP. *BMC Biotechnol.* **3**, 5.
- Zhu, H. and Roth, B. L.** (2014). DREADD: a chemogenetic GPCR signaling platform. *Int. J. Neuropsychopharmacol.* **18**, pyu007-pyu007.
- Zimmermann, T.** (2005). Spectral imaging and linear unmixing in light microscopy. *Adv. Biochem. Eng. Biotechnol.* **95**, 245–65.
- Zimmermann, T., Rietdorf, J. and Pepperkok, R.** (2003). Spectral imaging and its applications in live cell microscopy. *FEBS Lett.* **546**, 87–92.



Nederlandse Samenvatting

Cellen communiceren met elkaar via signaal moleculen. Signaal moleculen binden aan de buitenkant van een cel aan een transmembraan-receptor. Een transmembraan-receptor bestaat uit 3 delen: 1) het extra-cellulaire deel dat, aan de buitenkant van de cel, signaal moleculen kan binden, 2) het deel in het celmembraan wat de binnenkant en buitenkant van de cel met elkaar verbind, en 3) het intra-cellulaire deel dat aan de binnenkant van de cel interacteert met moleculen die het signaal doorgeven zodat de cel kan reageren op signalen van buiten.

G-eiwit-gekoppelde receptoren (GPCRs) vertegenwoordigen de grootste familie van transmembraan-receptoren. Medicijnen werken ook als signaal moleculen en een aanzienlijk deel van de goedgekeurde medicijnen werkt via GPCRs. Hoe de signaal-transductie via GPCRs precies wordt gereguleerd is echter nog niet volledig begrepen. Verdere opheldering van GPCR-signalering is vereist om de specificiteit van geneesmiddelen die op deze receptoren aangrijpen te verbeteren.

Het onderzoek dat is beschreven in dit proefschrift was gericht op verdere opheldering van intracellulaire signalering via GPCRs. We hebben fluorescentiemicroscopie gebruikt om GPCR-signalering in te bestuderen in levende cellen.

Om details in GPCR-signalering op te helderen, bestuderen we eiwit-eiwit interacties. Deze eiwit-eiwit interacties zijn vaak van korte duur en wanneer interactie plaatsvindt, is de afstand tussen de eiwitten minder dan 10nm. Hierdoor is een hoge resolutie in tijd en ruimte vereist. De ruimtelijke resolutie van conventionele microscopie is uiterlijk ongeveer 250nm. Om visualisatie van eiwit-eiwit interacties mogelijk te maken, wordt de techniek Förster Resonance Energy Transfer (FRET) gebruikt, in zogenaamde fluorescente biosensoren. FRET is energieoverdracht tussen twee fluoroforen. FRET treedt op als de fluoroforen dicht bij elkaar zijn (<10nm). De fluorescente biosensoren bestaan uit twee fluorescente eiwitten (FPs), dit is het zogenaamde FRET-paar, en een 'sensing' domein. Het 'sensing' domein moet specifiek zijn voor een bepaalde moleculair biologische gebeurtenis waarvoor de sensor is ontworpen. Wanneer de moleculair biologische gebeurtenis optreedt, zal het 'sensing' domein, interacteren, dissociëren of van conformatie veranderen. Dit leidt tot een verandering in de afstand en/of oriëntatie tussen het FRET-paar, waardoor de efficiëntie van de energieoverdracht verandert. Het FRET-paar rapporteert zo indirect dat de specifieke biologische gebeurtenis plaatsvindt. Het is van groot belang dat deze biosensoren de moleculair biologische gebeurtenissen naar waarheid rapporteren. Een aanzienlijk deel van mijn onderzoek was daarom gericht op de ontwikkeling en optimalisatie van biosensoren en de fluorescente eiwitten die het FRET-paar vormen.

Hoofdstuk 2 bevat een discussie over belangrijke kenmerken van fluorescente eiwitten en hun effect op de prestaties van een FRET-paar, met betrekking tot het FRET-contrast tussen de "aan" en de "uit" -stand van de sensor, de intensiteit van het uitgezonden licht en de omgevingsgevoeligheid van de fluorescente eiwitten. Een FRET-paar bestaat uit een FRET-donor en een FRET-acceptor. De FRET donor draagt energie over aan de FRET acceptor wanneer deze binnen een bepaalde afstand en oriëntatie van de donor verkeerd. We evalueerden de prestaties van verschillende FRET-acceptoren in combinatie met de recent gerapporteerde mTurquoise2 als FRET-donor. Het best presterende FRET-paar was mTurquoise2-mNeonGreen, toegepast in een bimoleculaire FRET-sensor die Gq activatie rapporteerd. **Hoofdstuk 3** is gericht op het verbeteren van de prestaties van een unimoleculaire FRET-sensor. Geoptimaliseerde FPs kunnen bijdragen aan een hogere lichtintensiteit, FRET-efficiëntie of fotostabiliteit van een sensor. De toepassing van deze geoptimaliseerde FPs leidt echter vaak tot een verminderd FRET-contrast tussen de "aan" -stand en de "uit" -stand van de sensor, omdat de FPs beperkt zijn tot bepaalde conformaties in een unimoleculaire sensor. Gepubliceerde unimoleculaire sensoren zijn vaak het resultaat van tijdrovende optimalisatie van de relatieve oriëntaties en afstand van het FRET-paar in de sensor. Een kleine wijziging in een dergelijk sterk geoptimaliseerde sensor, resulteert vaak in een afname van het FRET-contrast. Wij evalueerden het effect van FP 'stickiness', een zwakke neiging tot heterodimerisatie, en de relatieve oriëntaties van FPs op het FRET-contrast van een unimoleculaire sensor voor RhoA activatie. RhoA is een effector in de GPCR-signalering, welke een belangrijke rol speelt in de regulatie van het cytoskelet. De relatieve oriëntatie van de FPs en hun 'stickiness' beïnvloeden het FRET contrast van de sensor maar meer onderzoek is nodig om de optimale oriëntatie van de FPs te vinden en een duidelijk verband te kunnen leggen tussen Fp 'stickiness' en FRET contrast van de sensor. Het doel van het onderzoek besproken in **hoofdstuk 4** was het ontwikkelen van een op FRET gebaseerde G13 activatie biosensor. Gα13 vertegenwoordigt een van de vier klassen van Gα-subunits, als deel van een heterotrimeer G-eiwit, samen met een Gβ en een Gy subunit. Het heterotrimeer G-eiwit koppelt aan de binnenkant van de cel aan de GPCR en induceert verder signaal transductie naar effector eiwitten. Wij hebben meerdere fluorescent gelabelde Gα13-varianten gemaakt en de functionaliteit en lokalisatie van deze varianten geanalyseerd. Uiteindelijk hebben we drie G13 activatie biosensoren geconstrueerd en beoordeeld. De sensor laat zien dat G13 activatie geremd wordt wanneer het P115-RGS-domein tot expressie wordt gebracht in menselijke navelstreng endotheelcellen (HUVECs). Bovendien werd de sensor gebruikt om te evalueren welke GPCRs G13 activeren. De G13 activatie biosensor maakt het mogelijk onderscheid te maken tussen Gαq- en Gα13-signalering. Deze heterotrimeer G-eiwit klassen worden vaak geactiveerd door dezelfde GPCRs en leiden vaak tot soortgelijke signalering via verschillende effectoren. De ontwikkeling van een G13 activatie biosensor was cruciaal in het pad naar verdere opheldering van GPCR-signalering.



In **hoofdstuk 5** werden sensoren ontwikkeld gericht op duaal of multiplex FRET experimenten, welke naast de in overvloed beschikbare op CFP-YFP (cyaan-geel) gebaseerde sensoren toegepast kunnen worden. mT-Sapphire werd verder geoptimaliseerd tot LSS-SGFP2, welke werd gekarakteriseerd en toegepast als FRET donor in een bimoleculaire Gq of G13 activatie biosensor en een unimoleculaire RhoA activatie biosensor, waarbij mCherry en mScarlet-I als FRET-acceptoren werden bestudeerd. Een duaal FRET experiment werd uitgevoerd, waarbij tegelijkertijd de Gq- en G13-activatie werd gerapporteerd. Circulaire permutatie van de FPs, met als doel de relatieve oriëntatie van de dipolen van de FPs te variëren, werd toegepast op de unimoleculaire RhoA activatie biosensor. Deze methode werd toegepast om het FRET contrast van deze sensor verdert e verbeteren.

Hoofdstuk 6 richt zich op de barrière regulatie in endotheelcellen (EC). S1P activeert GPCRs die koppelen aan Gi- of G13-heterotrimere G-eiwit klassen, respectievelijk leidend tot barrière bescherming en barrière verstoring. Dit hoofdstuk heeft betrekking op de S1PR1-Gi-CDC42-signalering en heeft tot doel de moleculaire basis van CDC42-gemedieerde EC-spreiding te onderzoeken en meer betrokken signalerings componenten te identificeren. De studie onthult dat G β y-signalering vereist is voor CDC42-activering en pRex1 is voorgesteld als GEF voor de activatie van CDC42.

Het werk beschreven in dit proefschrift draagt bij aan de aanhoudende opbouw van kennis over hoe GPCR-signalering wordt gereguleerd. Bovendien kunnen de ontwikkelde en geoptimaliseerde FPs, biosensoren en andere hulpmiddelen voor het ontrafelen van signalerings interacties worden toegepast in toekomstige studies over GPCR-signalering of verwante onderzoeksgebieden.



Dankwoord

Het boekje is af, nu kan ik met plezier terug kijken op mijn tijd als PhD-er. Dat ik het leuk vind om op deze tijd terug te kijken heeft te maken met mijn interesse in en de wetenschappelijke waarde van mijn onderzoeksonderwerp, maar daarnaast ook met de goede begeleiding, behulpzame en gezellige collega's en alle leuke activiteiten die werden georganiseerd. Ik heb veel geleerd en veel plezier gehad. Dit boek is het resultaat van de inspanningen van vele mensen en ik wil hen dan ook enorm bedanken.

Allereerst wil ik graag mijn supervisor en co-promotor Joachim bedanken voor alle enthousiasme, ideeën, feedback en peptalks. Bedankt voor jouw geduld en jouw positieve instelling. Ik ben erg blij met jou als supervisor.

Dan wil ik graag mijn promotor Dorus bedanken dat ik bij moleculaire cytologie mocht werken aan dit promotie onderzoek. Bedankt voor de feedback op mijn teksten en experimenten en natuurlijk ook voor de lessen in meteorologie.

Merel and Cristiane, thanks for the collaboration on the development and characterization of the G13 sensor and for reviewing the manuscript. Nathan Shaner, thanks for the collaboration on the characterization of FRET acceptors for mTurquoise2 and for reviewing the manuscript. Bedankt, Marten, voor het analyseren van de spectrale imaging en multiplex FRET data. Nathalie, bedankt voor de leuke samenwerkingen op het gebied van G13 en Gi signalering, voor het uitlenen van je maxipreps, voor de uitleg over experimenten met HUVECs en voor de uitwisseling van recepten voor thuis in de keuken. Daphne en Lindsay, bedankt voor het uitlenen van alle rode fluorescente eiwitten en natuurlijk uiteindelijk voor het uitlenen van jullie eigen mScarlet serie, die ik zo gelijk kon gebruiken voor mijn eerste publicatie. Ook bedankt voor de hulp met fluorescente eiwitten zuiveren en apparatuur zoals de spectrophotometer, fluorimeter en het bacterie-agar-petrischaal-imaging-systeem en natuurlijk ook voor het organiseren van de vet coole speurtocht door Haarlem als labuitje. Nathalie, Daphne, Lindsay, Anoeska and Stephanie thanks for the dancing, singing, talking, eating and drinking, I am so happy that we stay in touch! Bedankt, Kobus, voor het fungeren als vraagbaak, voor alle goede adviezen en bedankt dat ik jouw werk aan het G13/Gs sensor project kon voortzetten. Ronald bedankt voor alle hulp met de microscopen. Anna P., thanks for all the relevant feedback after my presentations and all the suggestions in the work discussions. Linda, Laura, Amber en Anna C., bedankt voor alle hulp in het laboratorium. Verder wil ik ook graag mijn studenten Fenna, Amber, Emma, Sanne en Nikki bedanken, jullie waren allen erg gemotiveerd en gezellig en jullie hebben belangrijke bijdragen geleverd aan de inhoud van dit boekje. Dorus, Joachim, Mark, Renee, Marten, Kobus, Ada, Tim, Giulia,

Rick, Eelco, Laura, Daphne, Lindsay, Linda, Anoeska, Amber, Christiaan, Nathalie, Stephanie, Orry, Nika, Susanne, Saskia, Sergei, Anna P., Anna C., Ronald, Katrin, Yorick, Larissa, Franka, Eike en alle studenten bedankt voor de gemoedelijke sfeer op werk. Iedereen is altijd bereid om elkaar te helpen, iets voor elkaar te doen en alle successen en verjaardagen worden gevierd met taart of koekjes. De vele activiteiten buiten werk zoals labuitjes, sinterklaas en het kerst/nieuwjaars diner waren altijd erg gezellig. Ik keek ernaar uit en denk er met plezier aan terug.

Mijn nieuwe collega's bij plant physiology aan de UvA ook bedankt voor de interesse en de motivatie en tijd die ik gekregen heb om het boekje ook echt af te maken.

Ik wil ook graag mijn niet-collega vrienden, Carlijn, Martine, Kelli, Madelon, Esther, Ingrid, Loes, Lucy, Diana (ookal ben je nu wel collega je hoort nog steeds meer in deze categorie), Corine en Tom bedanken voor alle gezelligheid, jullie boden mij mogelijkheden om even te ontspannen en op te laden. Bedankt dat jullie al zo lang mijn vrienden zijn en dat het altijd gezellig is wanneer we elkaar weer spreken. Diana, Corine en Tom, bedankt voor alle gezellige citytrips/housewarming uitjes, steun en motivatie. Bedankt, Lucy, voor alle gezelligheid tijdens feestjes, festivals, concerten en creatieve uitjes.

Iris, Julian, Melissa, Jonne, Nick, Wouter L., Lisa, Roel, Veerle, Michiel, Tjeerd, Merel, Thijn, Noëmie, Wouter H., Luuk en Cas bedankt voor de leuke feestjes en uitjes.

Natuurlijk wil ik ook graag mijn familie bedanken. Mama en Papa ik kan altijd bij jullie terecht en jullie hebben altijd begrip, goede raad en heel veel gezelligheid, bedankt voor alles. Bedankt ook voor alle leuke dingen die we samen doen. Hilde, bedankt voor je gezelligheid en enthousiasme. Rianne en Bas jullie zijn de beste broer en zus die ik me kan wensen. Alle feestjes, festivals, uitjes en spelletjes avonden zijn altijd zeer geslaagd. Ik wil ook graag mijn schoonfamilie, Riek, Wim, Theresa, Arjan, Myrthe, Winston en Sam, bedanken voor alle interesse en gezelligheid. Amber en Odin, bedankt dat jullie iedere dag zorgen dat ik genoeg frisse lucht en beweging krijg, dat jullie altijd willen knuffelen, altijd blij zijn om me te zien en me op kunnen vrolijken als geen ander.

Ten slotte, wil ik graag mijn man Chris bedanken omdat hij geweldig is. Chris, bedankt voor al je interesse en meedenken en alle steun en motivatie als ik even een minder optimistisch momentje had.

List of Publications

A FRET-based biosensor for measuring Ga13 activation in single cells (2018), Marieke Mastop, Nathalie R. Reinhard, Cristiane R. Zuconelli, Fenna Terwey, Theodorus W. J. Gadella Jr., Jakobus van Unen, Merel J. W. Adjobo-Hermans, Joachim Goedhart. PLoS ONE 13(3): e0193705.

The balance between Gai-Cdc42/Rac and Ga12/13-RhoA pathways determines endothelial barrier regulation by Sphingosine-1-Phosphate (2017), Nathalie R. Reinhard, Marieke Mastop, Taofei Yin, Yi Wu, Esmeralda K. Bosma, Theodorus W. J. Gadella Jr., Joachim Goedhart, and Peter L. Hordijk. Molecular biology of the cell.

Characterization of a spectrally diverse set of fluorescent proteins as FRET acceptors for mTurquoise2 (2017), Marieke Mastop, Daphne S. Bindels, Nathan C. Shaner, Marten Postma, Theodorus W. J. Gadella Jr. & Joachim Goedhart. Scientific Reports, vol. 7, Article number: 11999.

Robust and Bright Genetically Encoded Fluorescent Markers for Highlighting Structures and Compartments in Mammalian Cells (2017), Chertkova, Anna; Mastop, Marieke; Postma, Marten; van Bommel, Nikki; van der Niet, Sanne; Batenburg, Kevin Llewelyn; Joosen, Linda; W.J. Gadella Jr, Theodorus; Okada, Yasushi; Goedhart, Joachim. BioRxiv.

mScarlet: a bright monomeric red fluorescent protein for cellular imaging (2017), Daphne S Bindels, Lindsay Haarbosch, Laura van Weeren, Marten Postma, Katrin E Wiese, Marieke Mastop, Sylvain Aumonier, Guillaume Gotthard, Antoine Royant, Mark A Hink, Theodorus W J Gadella Jr. Nature Methods, Vol. 14, Issue 1, pg 53–56.

siFLIM: single-image frequency-domain FLIM provides fast and photon-efficient lifetime data (2016), Marcel Raspe, Katarzyna M Kedziora, Bram van den Broek, Qiaole Zhao, Sander de Jong, Johan Herz, Marieke Mastop, Joachim Goedhart, Theodorus W J Gadella, Ian T Young, Kees Jalink. Nature Methods, Vol. 13, Issue 6, pg 501–504.

Kinetics of recruitment and allosteric activation of ARHGEF25 isoforms by the heterotrimeric G-protein Gαq (2016), Jakobus van Unen, Taofei Yin, Yi I. Wu, Marieke Mastop, Theodorus W. J. Gadella Jr. & Joachim Goedhart. Scientific Reports, Vol. 6, Article number: 36825.

H-NS mediated repression of CRISPR-based immunity in Escherichia coli K12 can be relieved by transcription activator LeuO (2010), Edze R. Westra, Ümit Pul, Nadja

Heidrich, Matthijs M. Jore, Magnus Lundgren, Thomas Stratmann, Reinhild Wurm, Amanda Raine, Melina Mescher, Luc van Heereveld, Marieke Mastop, E. Gerhart H. Wagner, Karin Schnetz, John van der Oost, Rolf Wagner, Stan J. J. Brouns. *Molecular Microbiology*, Vol. 77, Issue 6, pg 1380–1393.

